

**TOWARDS THE CONTROL OF ELECTROPHOTOGRAPHIC-BASED 3-DIMENSIONAL
PRINTING: IMAGE-BASED SENSING AND MODELING OF SURFACE DEFECTS**

A dissertation presented to the dissertation committee

by

Alvaro J. Rojas Arciniegas

B.S. Mechatronics Engineering, Universidad Autonoma de Occidente, 2003

M.S. Industrial Engineering, Rochester Institute of Technology, 2008

M.S. Systems Engineering, University of Illinois at Urbana Champaign, 2010

In partial fulfillment of the requirements for the
degree of *Doctor of Philosophy* in Imaging Science

at

CHESTER F. CARLSON CENTER FOR IMAGING SCIENCE

COLLEGE OF SCIENCE

ROCHESTER INSTITUTE OF TECHNOLOGY

ROCHESTER, NEW YORK, USA

2013

Signature of the Author _____

Accepted by _____

Prof. John Kerekes, Coordinator, Ph.D. Degree Program Date

CHESTER F. CARLSON CENTER FOR IMAGING SCIENCE
COLLEGE OF SCIENCE
ROCHESTER INSTITUTE OF TECHNOLOGY
ROCHESTER, NEW YORK, USA

CERTIFICATE OF APPROVAL

PH.D. DEGREE DISSERTATION

The Ph.D. Degree Dissertation of Alvaro J. Rojas Arciniegas has
been examined and approved by the following dissertation
committee as satisfactory for a Ph.D. degree in Imaging Science

PROF. MARCOS ESTERMAN, DISSERTATION ADVISOR	DATE
---	------

PROF. CARL SALVAGGIO, COMMITTEE MEMBER	DATE
--	------

PROF. DENIS CORMIER, COMMITTEE MEMBER	DATE
---------------------------------------	------

PROF. JUAN C. COCKBURN, COMMITTEE CHAIR	DATE
---	------

ABSTRACT

Electro-Photography (EP) has been used for decades for fast, cheap, and reliable printing in offices and homes around the world. It has been shown that extending the use of EP for 3D printing is feasible; multiple layered prints are already commercially available (color laser printers) but only for a very limited number of layers. Many of the advantages of laser printing make EP 3D printing desirable including: speed, reliability, selective coloring, ability to print a thermoplastic, possibilities for multi-material printing, ability to print materials not amenable to liquid ink formulations. However, many challenges remain before EP-based 3D printing can be commercially viable. A limiting factor in using the same system architecture as a traditional laser printer is that as the thickness of the part increases, material deposition becomes more difficult with each layer since the increased thickness reduces the field strength. Different system configurations have been proposed where the layer is printed on intermediate stations and are subsequently transferred to the work piece. Layer registration and uniform transfer from the intermediate station become crucial factors in this architecture.

At the Print Research and Imaging Systems Modeling (PRISM) Lab preliminary tests have confirmed the feasibility of using EP for Additive Manufacturing (AM). However, similar issues were encountered to those reported in literature as the number of layers increased, resulting in non-uniform brittle 3D structures. The defects were present but not obvious at each layer, and as the part built up, the defects add up and became more obvious. The process, as in many printers, did not include a control system for the ultimate system output (print), and the actuation method (electrostatic charge) is not entirely well characterized or sensed to be used in a control system. This research intends to help the development of a model and an image-based sensing system that can be used for control of material deposition defects for an EP 3D printing process. This research leverages from the expertise at RIT and the Rochester area in Printing, Electrophotography, Rapid Prototyping, Control, and Imaging Sciences.

ACKNOWLEDGEMENTS

The work presented in this dissertation was only possible because of the guidance, contribution, and support from many different people, and there are no words to thank them enough.

First the staff and professors from the Chester F. Carlson Center for Imaging Science who provided a knowledge base and constant support for the work developed. The center director, Prof. Stefi Baum, who believed in the value of our work and provided funding to complete it through the micro-grant for student innovative research.

The professors and staff from the Industrial and Systems Engineering who had to deal with the exceptions and issues of working with a graduate student from a different college, but always include me in the activities of the department and supported this work. I have a special gratitude to Marilyn Houck who was instrumental for me to have a timely stipend and was always helpful while ordering components and equipment for the lab.

The Universidad Autónoma de Occidente who partially supported my studies in the US through the program of academic development for faculty.

The classmates and friends of the graduate program in imaging science with whom I shared the experience of going through very tough classes, long projects, strange seminars, talks and discussions, and above all an impossible comprehensive exam; I wouldn't have made it through without your support. The lab companions and fellow TAs for Engineering of Systems who provided great feedback to my work and were patient to listen on topics and experiments that were not directly relevant for them.

Dr. John Knapp (retired Xerox scientist) who came multiple times to RIT to explain the intricate details of the EP process, providing a foundation to the work developed in this area. Similarly, Prof. Jon Arney (retired) who frequently came to review our progress and provided valuable input into direction to explore.

Robert Semple who came to the lab as a voluntary high school summer intern and was of great help to construct multiple samples despite the tedious and repetitive nature of the process.

The dissertation committee members, Prof. Denis Cormier, Prof. Carl Salvaggio, and Prof. Juan Cockburn who were always flexible to accommodate the meetings in their schedule and provided guidance at times when it was hard to see the end of the road. Also Prof. Shu Chang who was always willing to help and contribute.

The friends made along the way of my graduate education, first in Rochester (Carlos, Mariolga, Mariela, Ivan, Ignacio, Rosa, Lio, and Melissa), later in Urbana-Champaign (Andres Ortiz, Meredith, Emerson, Andres Salas, Beatriz, Camilo, and Laura), and back in Rochester (Ruth, Burt, Leidy, Harold, Libby, Alison, Javier, and Gary); it has been great to share this amazing journey with you, to have you in our life and we will treasure your friendship forever, you will be greatly missed and we hope to see you in Colombia soon. The long-lasting friends in Colombia (Juan, Monica, Andres, Adriana) thank you for your visits, keeping in touch, and all the support throughout this process. When talking about friends I will always remember something that Juan wrote in our yearbook: “friends are the family we choose”, thank you for being that!

My deepest gratitude towards my advisor, mentor, and above all friend Prof. Marcos Esterman. I wouldn't have reached my goals without your support. Thanks for believing in me, for reaching out when things were not working out in Illinois, for being there when I needed it the most, for jumping through hoops and making things work out. I look forward to continue working with you and have you visit Colombia, but above all continue with our friendship.

To my family who has always supported the pursuit of my dreams, specially my dad who has been a role model in many ways and a lifesaver when life has thrown curved balls at us; also my sister who shared most of her summers with us and learned to take advantage of having his brother in the US, with occasional remainders that I had “abandoned her” when she was only nine.

Lastly, I want to thank my wife Victoria for being so supportive and putting up for so many years with the long nights and the ups and downs that come with being a graduate student. Thank you for coming along in this crazy rollercoaster, for being my best friend, my confident, my rock, my lover... for building our family together, first with Ramon and now with Alejandro who has changed our world and is constantly giving us more reasons to laugh, cry and love each other. Thank you also for listening and understanding even when you didn't understand, for being right next to me providing me a hand to stand up, a shoulder to cry, and a hug to celebrate. Thank you for being who you are, for putting a spark in my life, for being full of energy and for teaching me to enjoy little things from life because it is happening and we cannot let it pass.

*To my wife Victoria, love of my life and companion in this incredible journey;
to my son Alejandro, constant motivation to be a good role model and a better human being;
to my dad and sister who constantly supported me from the distance;
to the memory of my mom who is still greatly missed.*

TABLE OF CONTENTS

Abstract.....	i
Chapter 1. Introduction	1
1.1. EP printing working principle	2
1.2. EP-based 3D printing attempts.....	3
1.3. Surface defect sensing.....	6
Chapter 2. Literature Review	9
2.1. Electro-Photographic Process Physics	9
2.1.1. EP Process Overview	10
2.1.2. EP Development Process Modeling.....	18
2.2. EP-based 3D printing attempts.....	23
2.2.1. Bynum’s Patent (1992)	24
2.2.2. University of Florida (2000)	26
2.2.3. NC State – RIT (2002)	27
2.2.4. De Montfort University (Active).....	28
2.2.5. Printed Electronics (2010-2012).....	29
2.2.6. Kodak NexPress Dimensional Printing (2009)	30
2.3. Control of EP3D printed surface	32
2.4. Surface reconstruction by Image Processing	34
2.4.1. Shape-from-Shading	36
2.4.2. Shape-from-Focus	38
2.4.3. Shape-from-Specularity	39
2.4.4. Reflectance Transformation Imaging (RTI)	41
2.4.5. GelSight.....	42
Chapter 3. Research Objectives	45
3.1. Identified challenges to overcome towards EP-based 3D printing.....	45
3.2. Scope of Research: Areas of contribution	46
3.2.1. Surface defect characterization.....	46
3.2.2. Modeling of EP3D printing for control	47
3.2.3. Development of preliminary control strategy for EP3D printing.....	47

3.2.4. Surface imaging for compensation of defects	47
Chapter 4. Research Methodology.....	48
4.1. Surface defects characterization	49
4.1.1. EP3D Sample Generation Methodology	49
4.1.2. Design of Experiments (DOE) approach.....	50
4.1.3. Layer-by-layer measurements	50
4.2. Modeling of EP3D printing for control.....	50
4.2.1. EP Development static model understanding and simulation.....	50
4.2.2. Dynamic system identification experiments and model inference.....	51
4.2.3. Model validation.....	51
4.3. Preliminary control of the EP3D printed surface.....	51
4.3.1. Passive approach based on a more compliant interface	51
4.3.2. Feedback control	52
4.4. Surface imaging for compensation of defects.....	52
4.4.1. Preliminary testing and hardware configurations.....	52
4.4.2. Image Processing Algorithm Development	53
4.4.3. Validation	53
Chapter 5. Surface Defects Characterization	55
5.1. EP-based 3D Printed Sample Generation Methodology	55
5.2. Surface measurement	57
5.3. Design of Experiment (DOE) Approach	61
5.3.1. Experimental Design	61
5.3.2. Analysis of Response Variables.....	63
5.3.3. Analysis of Significant Effects.....	65
5.4. Layer-by-layer measurements.....	71
5.5. Conclusion.....	75
Chapter 6. Modeling of EP3D printing for control	77
6.1. Static Model of EP Development Process	77
6.2. System Identification and Modeling	78
6.2.1. Layer printing	79
6.2.2. Fusing the new layer to the part under construction	80

6.2.3. Simulation Model	82
6.3. Results and model validation	83
6.4. Conclusion.....	88
Chapter 7. Control of EP3D printed surface	90
7.1. A passive approach through a more compliant interface.....	90
7.2. Feedback control approach	95
7.3. Conclusion.....	99
Chapter 8. Surface imaging for compensation of defects	100
8.1. Preliminary testing	100
8.2. Reflectance Transformation Imaging (RTI).....	101
8.3. Creating compensation images for feedback control.....	105
8.4. GelSight	110
8.5. Conclusion.....	112
Chapter 9. Conclusions and Future Work.....	114
9.1. Contributions to the state of the art	114
9.1.1. Surface defects characterization	114
9.1.2. Modeling of EP3D printing for control	115
9.1.3. Development of preliminary control strategy for EP3D printing.....	115
9.1.4. Surface imaging for compensation of defects	116
9.2. Areas for future work.....	117
9.2.1. Understand further the root causes of surface defects	117
9.2.2. Relaxation of constraints and assumptions of simulation.....	118
9.2.3. 3D extension of the simulation model.....	119
9.2.4. Testing different materials for intermediate substrate.....	120
9.2.5. Explore materials for printing and their properties	120
9.2.6. Develop and validate a 3D surface map through image processing techniques	122
9.2.7. Implementation of feedback control.....	122
9.2.8. Automate the transfuse process.....	123
Appendix A. Simulation Code	125
A.1. Static Simulation of EP Development Process.....	125

A.2. Simulation of the EP3D printing process	126
A.3. Simulation of feedback control strategy applied to the EP3D printing process.....	130
A.4. Light direction estimation from reflecting sphere	134
A.5. Edge detection and image fusing for compensation image.....	135
Appendix B. Results of DOE analysis.....	137
B.1. Ra – Leading edge.....	137
B.2. Rq – Leading edge.....	139
B.3. Ra – Trailing edge.....	141
B.4. Rq – Trailing edge.....	143
B.5. Unfiltered profile Pa – Leading edge	145
B.6. Pq – Leading edge	147
B.7. Pa – Trailing edge	149
B.8. Pq – Trailing edge	151
B.9. Height at curling.....	153
B.10. Material Transferred	155
B.11. Surface quality	157
B.12. Height Adjusted to discount base substrate.....	159
B.13. Analysis blocked by printed pattern	162
B.13.1. C-100%-Yes	162
B.13.2. CM-100%-Yes.....	164
B.13.3. C-50%-Yes	166
B.13.4. CM-50%-Yes.....	168
B.13.5. C-100%-No.....	170
B.13.6. CM-100%-No	172
B.13.7. C-50%-No.....	174
B.13.8. CM-50%-No	176
Appendix C. Plots and raw data from layer-by-layer analysis	178
C.1. Sample fused face up – leading edge.....	178
C.2. Sample fused face up – trailing edge	180
C.3. Sample fused face down – leading edge	182
C.4. Sample fused face down – trailing edge.....	184
C.5. Compiled raw measurements	186

Appendix D. Images captured by GelSight.....	188
D.1. 25-layer sample.....	188
D.2. 30-layer sample fused face up	190
D.3. 30-layer sample fused face down.....	191
D.4. 30-layer sample belt interface	193
D.5. 100-layer 1-toner sample	194
Bibliography.....	196

LIST OF FIGURES

Figure 1. Schematic of electro-photographic printing process.....	2
Figure 2. Schematic of Kumar's device for EP-based 3D printing, from [3]	4
Figure 3. Self-insulating nature of EP-based 3D printing, adapted from [1]	4
Figure 4. Surface defects, from [1]	5
Figure 5. Transferring method by heating the top layer of the pile to facilitate adherence, adapted from [1]	5
Figure 6. Surface measurement with a contact profilometer at the PRISM Lab.....	7
Figure 7. a., b. Images of orange skin illuminated from different angles; c. reconstructed 3D surface of the orange skin, from [16].....	8
Figure 8. Rendering of the captured geometry from a \$20 bill, from [17]	8
Figure 9. Commemorative images of Carlson's original work on display at the Chester F. Carlson Center for Imaging Science of RIT	9
Figure 10. Organic photoreceptor structure: a. four layers from [18], b. six layers, from [19]	10
Figure 11. Schematic of charging devices: Corotron (top), Scorotron (bottom), from [18]	12
Figure 12. Laser exposure structure, from [20]	13
Figure 13. Comparative schematic between two-component development and mono-component development, from [21]	14
Figure 14. Schematic of mono-component development systems, a. magnetic toner (Canon), b. non-magnetic toner, a soft supply roller is used (Ricoh), from [18].....	14
Figure 15. Carrier bead with toner stuck to its surface, from [22].....	15
Figure 16. Schematics of two-component magnetic brush development systems, a. single development roller, from [18]; b. multiple development rollers, from [22]	15
Figure 17. Schematic of a Hybrid development system, from [23].....	16
Figure 18. a. Schematic of direct transfer, from [1]; b. Schematic of intermediate transfer, from [24].....	17
Figure 19. Fusing stations at the PRISM Lab: a. roller based with desktop printer rollers, b. roller based with more robust rollers, and c. stamp-based	18

Figure 20. Solid area development curve, from [23]	20
Figure 21. Block diagram of the control oriented model, from [23].....	23
Figure 22. Schematic of the EP-based 3D printer from Bynum's patent [2]	25
Figure 23. a. Photograph of the test-bed for ELM at the University of Florida, b. Parts produced by corona top charging of 3 mm thickness, from [5].	26
Figure 24. a. Schematic of the Color 3D laser printer configuration proposed, b. 30 layer sample result, c. Color compensation scheme, from [4]	27
Figure 25. a. Test-bed for SLP at DMU, b. Thick preliminary sample (~10 mm), c. Thickest sample obtained in the test-bed (~1.6 mm), from [1]	28
Figure 26. a. Copper lines printed by selective laser melting (SLM), from [36]; b. conductive silver line after four prints by EP and "firing", from [37]	29
Figure 27. Applications of EP in the production of PCB: a. printed conductive tracks, 10 layers of silver particles, b. conductive tracks etched using a laser printed mask (2 layers), c. legends printed with UV-cured toner; from [38]	30
Figure 28. a. Kodak NexPress 2500, one of the digital presses capable of dimensional printing, from [42]; b. detail diagram, from [43]; c. and d. dimensional printing feature, from [40].....	31
Figure 29. Section of a 3D printed sample under the microscope changing focus: a. peaks on focus, b. valleys on focus, from [45]	33
Figure 30. a. Vision system to monitor the 3D printing process, b. test target for one of the studies conducted, from [46]	33
Figure 31. Light reflection model	35
Figure 32. Surface reconstruction of synthetic images Vase and Mozart using a local approach (Lee and Rosenfeld's method) having light source at (0,0,1) for (a. and b.) and (1,0,1) for (c. and d.), from [14]	37
Figure 33. a. Conceptual diagram of the shape-from-focus methodology; Surface reconstruction of a ball by direct assignment of height (b.) and Gaussian interpolation (c.), from [15].....	39
Figure 34. Set up used to reconstruct structure from specularity, from [16]	40
Figure 35. RTI representation of the Sennedjem Lintel, with color information (bottom) and specular enhancement (top), from [89].....	42

Figure 36. GelSight system configurations: a. Bench-top, b. Portable; Samples of reconstructed images, detail of a US quarter coin: c. Using metal-flake coating, d. Using silver powder coating, from [17]	43
Figure 37. Research Roadmap.....	48
Figure 38. Initial configurations for image based sensing: a. Two side linear illumination, b. One point source used at different positions	53
Figure 39. Preliminary testing for EP-based 3D printing: a. 15 layers, b. 25 layers	55
Figure 40. EP3D printing sample generation methodology.....	56
Figure 41. Printed samples from initial testing (3, 20,50 layers).....	57
Figure 42. Initial set-up for surface measurements with laser profilometer.....	57
Figure 43. Initial trials of surface readings with laser profilometer.....	58
Figure 44. Trials of surface readings using the NI DAQ	58
Figure 45. Trials of surface reading comparing a bare plate and a 25-layer sample	59
Figure 46. Surface measurements using a Mitutoyo SJ-401 contact profilometer for the 25-layer sample.....	60
Figure 47. Measurement of a EP3D printed sample with the Mitutoyo SJ-210 profilometer a. handheld instrument; b. driving unit and sensor; c. 16 mm measurement paths for leading and trailing edges.....	61
Figure 48. Patterns used for the experimental setup: 2 toners (C & M) on the first two columns, 1 toner (C) on the last two columns; top row use a 50% graded transitions a. and c. from 100% to 50%, b. and d. from 50% to 0; bottom row were solid fill patterns e. and g. 100%, f. and h. 50%.	63
Figure 49. 30-layer samples from the experimental design.....	63
Figure 50. Residual plots for surface roughness Ra(1)	66
Figure 51. Main effects plot for surface roughness Ra(1)	67
Figure 52. Interaction plot for surface roughness Ra(1)	67
Figure 53. Residual plots for material transferred, for case 2: CM-100%-Yes	70
Figure 54. Residual Plot for Height Adj. [mil] for Cyan-100%-No transition.....	71
Figure 55. a. 16 mm measurement paths for leading and trailing edges; b. 30-layer samples fused face up (top) and face down (bottom); c. surface roughness evolution summary chart.....	72
Figure 56. Surface profiles for sample fused face up, leading edge.....	74
Figure 57. Autocorrelation function for sample fused face up, leading edge	74

Figure 58. Histograms of measurements on sample fused face-up, leading edge at several layers.....	75
Figure 59. Development curves using the static model from section 2.1.2.1	77
Figure 60. Linear Test-bed for EP at the PRISM Lab, RIT	78
Figure 61. Unfused EP printed sample observed through a confocal microscope, multiple layers of particles are detected	80
Figure 62. a. Fuser testbed used for EP3DP; b. Diagram of fuser used for modeling; c. Diagram of equivalent dynamic system	81
Figure 63. Flow diagram of simulation algorithm	83
Figure 64. Simulation profiles: reaction force applied on the sample (top); sample as input to the fuser (middle), the measurement regions are marked by the dotted lines, leading edge in red and trailing edge in blue; response of the roller (bottom)	84
Figure 65. Section of the simulated EP3D print for a sample fused face up trailing edge ...	85
Figure 66. Comparison of profiles for a 30-layer sample fused face-up, leading edge: (top) measurement in the direction of travel, (middle) measurement across the direction of travel, (bottom) simulated profile.....	86
Figure 67. Autocorrelation function for simulated layers of a sample fused face up leading edge	87
Figure 68. Ra for measured and simulated data at various threshold levels.....	88
Figure 69. Simulated sample for 80 μ m threshold	89
Figure 70. Ra comparison up to layer 50	89
Figure 71. Failed attempts to perform EP3D printing using transfuse belt material as intermediate substrate: a. toner not fused to final substrate after going through fuser, b. toner fused to the intermediate substrate while preheating to 130 C, c. sample got caught in the fuser at layer 6.	91
Figure 72. a. Transfuse belt material after being used as intermediate substrate; b. 14-layer sample; c. 100-layer sample.....	91
Figure 73. Ra evolution for 100-layer sample fused using transfuse belt material as intermediate substrate and compared to readings from samples using Mylar as intermediate substrate.....	92
Figure 74. 100-layer samples constructed using Mylar as intermediate substrate: a. 1 toner (M) at 100% fill; b. 2 toner (CM) at 100% fill.....	93

Figure 75. Comparison of measured profiles for 100-layer samples: (top) 2-toner produced with Mylar interface, (bottom) 1-toner using belt interface	94
Figure 76. Flow diagram of the simulation algorithm with compensation.....	96
Figure 77. Simulated profiles of force, and sample generated without compensation.....	97
Figure 78. Simulated profiles of force and sample generated with compensation	97
Figure 79. Comparison on Ra for 30 layers from simulated data with no compensation, with compensation and the measurements on sample fused face down.....	98
Figure 80. 2-layer sample imaged on the setup with line source illumination from the right (a.) and the left (b.).....	101
Figure 81. Sample images taken from different illumination angles	102
Figure 82. Images of the 25-layer sample recreated from the PTM representation: a. lighted from top-right; b. specular enhancement; c. diffuse gain.....	102
Figure 83. Imaging set up with PointGrey camera	103
Figure 84. Compiled images of a reflecting sphere with the different light directions and the detected edges for: a. 8 directions, b. 24 directions	104
Figure 85. 100-layer 2-toner sample recreated using the PTM file generated with 8 light directions: a. illuminated from top, b. illuminated towards the center of the sample, c. illuminated towards the center enhancing specular reflections.....	104
Figure 86. 100-layer 2-toner sample recreated using the PTM file generated with 24 light directions: a. illuminated from top, b. illuminated towards the center of the sample, c. illuminated towards the center enhancing specular reflections.....	104
Figure 87. Images of 100-layer 2-toner sample: a. original, b. grayscale, histogram adjusted, c. compensation image extracted.....	106
Figure 88. Images of 30-layer sample fused face down: a. original, b. grayscale, histogram adjusted, c. compensation image extracted	107
Figure 89. Edge detection and image fusing approach: a. 100-layer 2-toner sample illuminated from the top; b. edges detected and fused from 8 images; c. compensation image after applying morphological operators	108
Figure 90. Detailed image of the edge detection approach: a. original image illuminated from the bottom; b. edges detected for this image only; c. edges from 8 images (8 illumination angles) fused; d. compensation image after applying morphological operators.	109
Figure 91. GelSight Benchtop Beta System, from [96]	111

Figure 92. a. 30-layer sample fused face up imaged with a flatbed scanner; b. 22.3 x 14.9 mm section of the 30-layer sample imaged using GelSight, c. 8 x 8 mm detail, d. 3D reconstruction of the detail area.....	112
Figure 93. Residual plots for Ra - leading edge.....	138
Figure 94. Main effects plot for Ra - leading edge.....	138
Figure 95. Interaction plot for Ra - leading edge.....	139
Figure 96. Residual plots for Rq - leading edge.....	140
Figure 97. Main effects plot for Rq - leading edge.....	140
Figure 98. Interaction plot for Rq - leading edge.....	141
Figure 99. Residual plots for Ra - trailing edge.....	142
Figure 100. Main effects plot for Ra - trailing edge	142
Figure 101. Interaction plots for Ra - trailing edge.....	143
Figure 102. Residual plots for Rq - trailing edge.....	144
Figure 103. Main effects plot for Rq - trailing edge	144
Figure 104. Interaction plots for Rq - trailing edge.....	145
Figure 105. Residual plots for Pa - leading edge	146
Figure 106. Main effects plot for Pa - leading edge.....	146
Figure 107. Interaction plot for Pa - leading edge.....	147
Figure 108. Residual plots for Pq - leading edge	148
Figure 109. Main effects plot for Pq - leading edge.....	148
Figure 110. Interaction plot for Pq - leading edge.....	149
Figure 111. Residual plots for Pa - trailing edge.....	150
Figure 112. Main effects plot for Pa - trailing edge.....	150
Figure 113. Interaction plot for Pa - trailing edge	151
Figure 114. Residual plots for Pq - trailing edge.....	152
Figure 115. Main effects plot for Pq - trailing edge.....	152
Figure 116. Interaction plot for Pq - trailing edge	153
Figure 117. Residual plots for Height at curling.....	154
Figure 118. Main effects plot for Height at curling.....	154
Figure 119. Interaction plot for Height at curling.....	155
Figure 120. Residual plots for Material transferred	156
Figure 121. Main effects plot for Material transferred	156
Figure 122. Interaction plot for Material transferred.....	157

Figure 123. Residual plots for Surface quality	158
Figure 124. Main effects plot for Surface quality	158
Figure 125. Interaction plot for Surface quality	159
Figure 126. Residual plots for Height adjusted.....	160
Figure 127. Main effects plot for Height adjusted.....	160
Figure 128. Interaction plot for Height adjusted	161
Figure 129. Residual plots for Material transferred	162
Figure 130. Residual plot for Height Adjusted.....	163
Figure 131. Residual plot for Material transferred.....	164
Figure 132. Residual plots for Height adjusted.....	165
Figure 133. Residual plots for Material transferred	166
Figure 134. Residual plots for Height adjusted.....	167
Figure 135. Residual plots for Material transferred	168
Figure 136. Residual plots for Height adjusted.....	169
Figure 137. Residual plots for Material transferred	170
Figure 138. Residual plots for Height adjusted.....	171
Figure 139. Residual plots for Material transferred	172
Figure 140. Residual plots for Height adjusted.....	173
Figure 141. Residual plots for Material transferred	174
Figure 142. Residual plots for Height adjusted.....	175
Figure 143. Residual plots for Material transferred	176
Figure 144. Residual plots for Height adjusted.....	177
Figure 145. Plot of measurements at each layer (shifted up to avoid overlap)	178
Figure 146. Histogram of measurements at layers 0 (base substrate), 1, 5, 10, 15, 20, 25, and 30.....	179
Figure 147. Plot of measurements at each layer (shifted up to avoid overlap)	180
Figure 148. Histogram of measurements at layers 0 (base substrate), 1, 5, 10, 15, 20, 25, and 30.....	181
Figure 149. Plot of measurements at each layer (shifted up to avoid overlap)	182
Figure 150. Histogram of measurements at layers 0 (base substrate), 1, 5, 10, 15, 20, 25, and 30.....	183
Figure 151. Plot of measurements at each layer (shifted up to avoid overlap)	184

Figure 152. Histogram of measurements at layers 0 (base substrate), 1, 5, 10, 15, 20, 25, and 30.....	185
Figure 153. 22.3 x 14.9 mm section of the sample.....	188
Figure 154. 8 x 8 mm detail of the sample.....	189
Figure 155. 3D reconstruction of the detail of the sample.....	189
Figure 156. 22.3 x 14.9 mm section of the sample.....	190
Figure 157. 8 x 8 mm detail of the sample.....	190
Figure 158. 3D reconstruction of the detail of the sample.....	191
Figure 159. 22.3 x 14.9 mm section of the sample.....	191
Figure 160. 8 x 8 mm detail of the sample.....	192
Figure 161. 3D reconstruction of the detail of the sample.....	192
Figure 162. 22.3 x 14.9 mm section of the sample.....	193
Figure 163. 8 x 8 mm detail of the sample.....	193
Figure 164. 3D reconstruction of the detail of the sample.....	194
Figure 165. 22.3 x 14.9 mm section of the sample.....	194
Figure 166. 8 x 8 mm detail of the sample.....	195
Figure 167. 3D reconstruction of the detail of the sample.....	195

LIST OF TABLES

Table 1. Experimental design.....	62
Table 2. Paired T-Test for Ra(1) [μm] - Ra(2) [μm]	64
Table 3. Analysis of Variance for Ra(1) [μm], using Adjusted SS for Tests	65
Table 4. ANOVA for Height at curling [in], using Adjusted SS for Tests	68
Table 5. ANOVA for Material transferred [g], using Adjusted SS for Tests.....	69
Table 6. ANOVA for Height Adj. [mil], using Adjusted SS for Tests	69
Table 7. Conditions blocked for further analysis on the responses.....	70
Table 8. ANOVA for Material Transferred [g] for case 2: CM-100%-Yes	70
Table 9. ANOVA for Height Adj. [mil] for Cyan-100%-No Transition	70
Table 10. Ra measurements for 100-layer samples.....	93
Table 11. Analysis of Variance for Ra(1) [μm], using Adjusted SS for Tests	137
Table 12. Analysis of Variance for Rq(1) [μm], using Adjusted SS for Tests	139
Table 13. Analysis of Variance for Ra(2) [μm], using Adjusted SS for Tests	141
Table 14. Analysis of Variance for Rq(2) [μm], using Adjusted SS for Tests	143
Table 15. Analysis of Variance for Pa(1) [μm], using Adjusted SS for Tests	145
Table 16. Analysis of Variance for Pq(1) [μm], using Adjusted SS for Tests	147
Table 17. Analysis of Variance for Pa(2) [μm], using Adjusted SS for Tests	149
Table 18. Analysis of Variance for Pq(2) [μm], using Adjusted SS for Tests	151
Table 19. Analysis of Variance for Height at curling [in], using Adjusted SS.....	153
Table 20. Analysis of Variance for Material Transferred [g], using Adjusted SS	155
Table 21. Analysis of Variance for Surface quality [qual], using Adjusted SS.....	157
Table 22. Analysis of Variance for Height Adj. [mil], using Adjusted SS.....	159
Table 23. Analysis of Variance for Material Transferred [g], using Adjusted SS	162
Table 24. Analysis of Variance for Height Adj. [mil], using Adjusted SS.....	163
Table 25. Analysis of Variance for Material Transferred [g], using Adjusted SS	164
Table 26. Analysis of Variance for Height Adj. [mil], using Adjusted SS.....	165
Table 27. Analysis of Variance for Material Transferred [g], using Adjusted SS	166
Table 28. Analysis of Variance for Height Adj. [mil], using Adjusted SS.....	167

Table 29. Analysis of Variance for Material Transferred [g], using Adjusted SS	168
Table 30. Analysis of Variance for Height Adj. [mil], using Adjusted SS	169
Table 31. Analysis of Variance for Material Transferred [g], using Adjusted SS	170
Table 32. Analysis of Variance for Height Adj. [mil], using Adjusted SS	171
Table 33. Analysis of Variance for Material Transferred [g], using Adjusted SS	172
Table 34. Analysis of Variance for Height Adj. [mil], using Adjusted SS	173
Table 35. Analysis of Variance for Material Transferred [g], using Adjusted SS	174
Table 36. Analysis of Variance for Height Adj. [mil], using Adjusted SS	175
Table 37. Analysis of Variance for Material Transferred [g], using Adjusted SS	176
Table 38. Analysis of Variance for Height Adj. [mil], using Adjusted SS	177
Table 39. Measurements for sample fused face up.....	186
Table 40. Measurements for sample fused face down	187

Chapter 1. INTRODUCTION

The use of Electro-Photography (EP) as an additive manufacturing process has been seen as a promising approach since this technology transfers dry particles instead of relying on a liquid medium to suspend and transfer particles onto a media/substrate. This enables the manufacture of parts from materials that may not be compatible with liquid ink formulations such as metals, ceramics, or plastics. It also holds the promises for faster deposition rates, higher reliability and less expensive parts as has been demonstrated in document printing in home and office environments for decades [1]. Multi-material parts and selectively colored parts are also possibilities envisioned through the use of EP similar to color copiers and printers which already achieve placement of at least three layers of toner (each one with different characteristics) to reproduce color. Bynum [2] and Kumar [3] were among the first to demonstrate the feasibility of creating 3D structures using EP. Since then, multiple approaches have been taken to adapt traditional EP-based printing for additive manufacturing [4-6]. These approaches have confirmed the feasibility of the principle but have struggled to create parts thicker than a few tenths of a millimeter due to process limitations as well as surface and structural defects that arise by not having uniform layers fixed on top of each other.

In order to be able to successfully develop 3D printing technologies, the control of layer uniformity seems to be a key consideration. Many factors contribute to the uniformity of a layer, such as: toner particle size distribution, particle shape, charge control agents, pigment and flow additives in the toner, the charge generation process, the development process, mixing processes, halftoning, toner cycling, aging, and relative humidity [7]. While the process has been used for decades, some of the parameters of the process are not fully understood or characterized. Static models used in the document printing industry rely on empirically derived constants to capture the behavior of the material being used [7]. A dynamic model in which the behavior of every particle can be determined is simply not available or not realistic. In fact, the EP process is set up in a way in which there is no direct control over a specific particle but rather conditions are created to attract (or push)

particles to a desired location up to an acceptable level but there is no certainty on the actual number of particles being transferred at a given time.

1.1. EP printing working principle

As reviewed in Hoshino et al. 2010 [8], EP is the process by which charged toner particles are controlled and transferred through the application of electrostatic forces. EP was invented by Carlson in 1938 and has been the basis for copying and laser printing [9]. The process can be characterized by six processes or stations: charge, exposure, development, transfer, fusing, and cleaning. A schematic of the process can be seen in Figure 1.

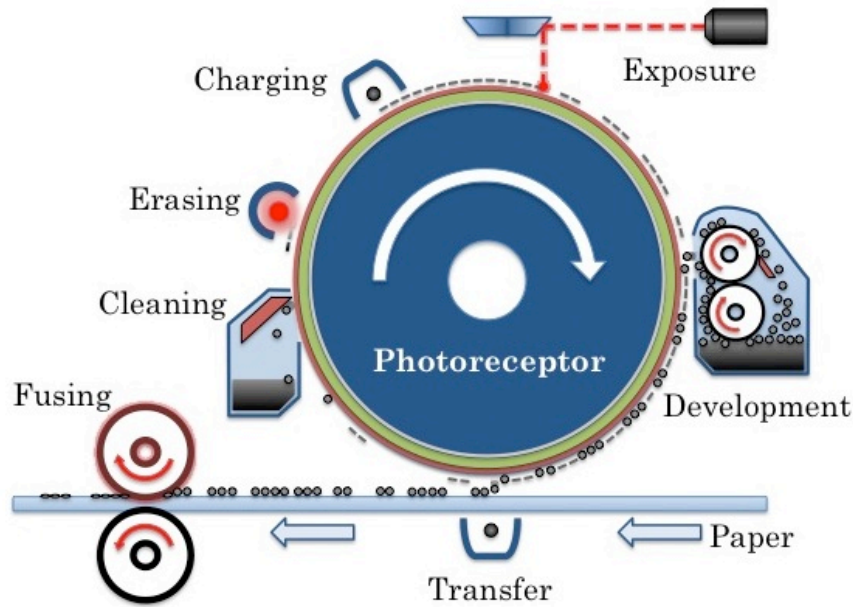


Figure 1. Schematic of electro-photographic printing process

The system is largely based on the photoconductor drum (or belt), which retains electrostatic charge in the dark and discharges as it is exposed to light. In this way a uniform field is generated on the photoconductor in the first station (*charge*), and then it is selectively discharged at the *exposure* station to create a field representative of the image that is desired to print (i.e. latent image). The latent image is taken to the *development* station where toner particles are attracted to the photoconductor due to the difference in potential across the field on the photoconductor forming a real image to print. The real image is then *transferred* to the media (e.g. paper) using opposite electrostatic forces and then the toner is fused (*fixed*) to the media by means of heat and pressure. The

photoconductor is then *cleaned* from residual toner particles and all remaining charges are "erased" by a uniform exposure to light, resetting the system for a new cycle.

It is important to highlight that the exposure is the only phase in which there is a "point-by-point" control; although it cannot be considered as a true digital process with binary states, there is an indication on a desired state for each location on the photoreceptor. However, the analog nature of the photoreceptor and the process, blur those desired states and each addressable point in the photoreceptor cannot be related to just one toner particle. Such levels of uncertainty make EP a challenging technology to use for additive manufacturing. Additionally, expecting a direct transition from document printing to 3D printing or the adaptation of commercial printers into 3D printers has proven unrealistic and unsuccessful to date.

1.2. EP-based 3D printing attempts

Bynum's patent from 1992 [2] included four processes for layered manufacturing, one of which used EP to selectively deposit toner onto a Teflon coated belt that would later be heated until the layer of toner would become "tacky", and the layer would be transferred by applying pressure to a pile of previously deposited layers forming the 3D part. This was the first concept to use EP for 3D printing ever documented but no working device was built or developed further based on this patent.

Kumar in 1999 [3] described a process in which a photo conducting belt was used to retain charge (i.e. latent image), develop the layer attracting the toner particles to the belt, and then transferred that layer onto a building platform charged in the opposite polarity to attract the particles (see Figure 2). This process resembled the regular implementation of EP printing for documents found in many laser printers. This system was later patented in 2000 [10], and a test-bed was constructed at the University of Florida, but there was a clear limitation on the thickness of the parts produced, the registration between layers, and a control system was not implemented.

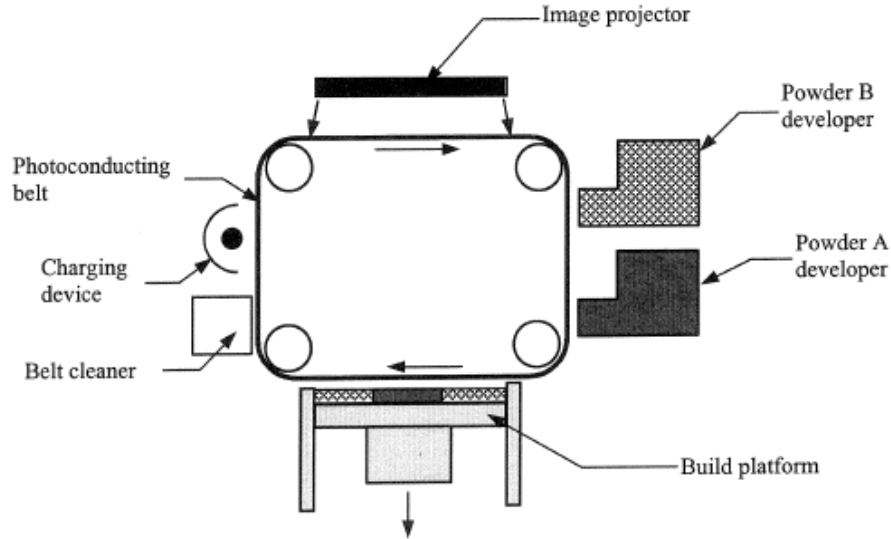


Figure 2. Schematic of Kumar's device for EP-based 3D printing, from [3]

Cormier et al. in 2000 [4, 11] experimented using commercial toner cartridges and laser printers to produce 3D parts using both regular toner and HDPE powder. The process was successful for parts of ~30-layer thickness, encountering problems to reliably deposit material much further since the force that pushes particles onto the building platform decreased as the part grew thicker (see Figure 3).

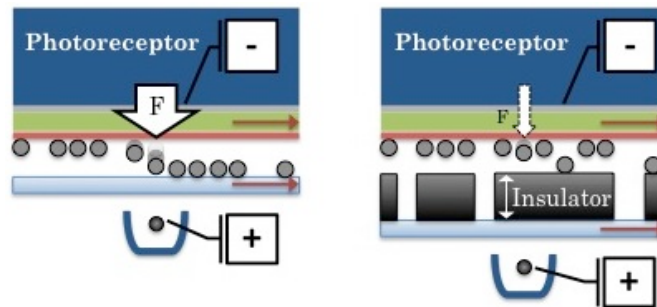


Figure 3. Self-insulating nature of EP-based 3D printing, adapted from [1]

This self-insulating nature of the implementation has been the most significant barrier to manufacture thicker parts using EP. Kumar and Dutta [5] reported improvements in their process by applying a charge to the top-most layer of the part being printed. This saturated the top layer with electrostatic charge, facilitating the transfer of toner onto the pile. The approach successfully increased the thickness of the produced part up to ~2 mm; however, surface defects appeared and accumulated, producing unsatisfactory parts. It was determined that the reason for the failure, even with the top charging mechanism, was

residual charges on the top layer that accumulated over time and could not be discharged between the transfer of layers [12].

Recently, Jones et al. [1, 13] have been working on a device that uses EP and a transferring mechanism similar to the one presented by Bynum. Parts of greater thickness have been achieved (up to ~10 mm in manual trials and ~2 mm in an automated rig) but it is still limited as the part grows thicker and experiences surface defects that ultimately produce unsatisfactory parts (see Figure 4).

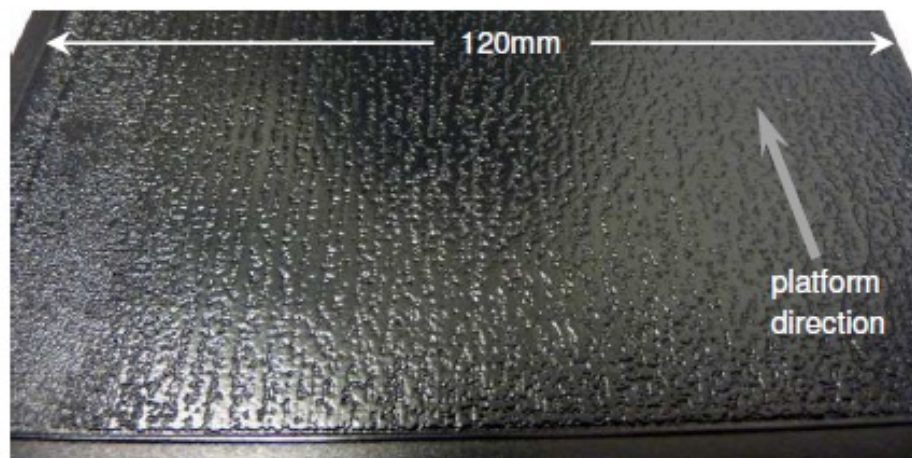


Figure 4. Surface defects, from [1]

In their approach, they try to circumvent the limitation by heating up the top of the part being printed so that the new toner particles would adhere easily (see Figure 5); however, surface defects continue to appear at ~1 mm. In the manual process, multiple stops were required to heat the part in an oven, allowing the part to relax from residual stresses and charges that were producing curling and other artifacts.

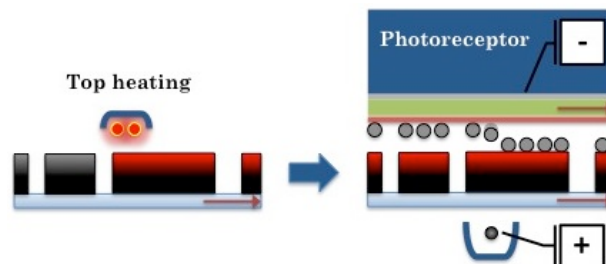


Figure 5. Transferring method by heating the top layer of the pile to facilitate adherence, adapted from [1]

None of the attempts reviewed included an active control method to mitigate the defects or irregularities within the 3D structure being created. Adjustments of bias voltage, surface

charge, surface temperature and fusing temperature, have been tried but defects still appear and ultimately produce an unsatisfactory part as these defects tend to accumulate. Instead of pursuing an open-loop approach for a system to produce consistently uniform layers, it is being proposed that the process needs to acknowledge the current system limitations, including the defects and irregularities that it may contain, and compensate with subsequent layers to minimize those defects.

1.3. Surface defect sensing

In order to compensate for surface defects, one must be able to detect them. However, surface measurement in the range of microns is a difficult task, particularly if the information extracted needs to be used within a process to make in-line decisions. Traditional methods based on contact with the surface require sample preparation; can result in some disruption of the surface; is typically taken over a very limited field; and can be very expensive. Many times the information provided is limited to a point or line of measurements, a statistical average of the variation of the surface, or simply a plot. These limitations make it very difficult to implement real-time (or close to real-time) decisions based on that information.

Contact profilometers are examples of such devices which are very expensive due to the highly sensitive probes, exotic materials (ruby is commonly found on the tips of the probes) and the same measurement is difficult to replicate (see Figure 6). Similarly, laser distance sensors provide a non-contact alternative but they are very sensitive to any surface variation, giving reliable measurements only when the surface is perpendicular to the laser beam.



Figure 6. Surface measurement with a contact profilometer at the PRISM Lab

Optically-based measurements present a very attractive alternative since they do not rely on the contact of a probe to the surface, but instead extract geometry information from the properties of the reflected light. However, the measurement of the surface at this scale is challenging. Traditional microscopy, such as confocal microscopy and electron-microscopy, do provide similar information at the required scale, but not only is it prohibitively expensive for commercial applications, it usually has an extremely narrow range of coverage.

Image processing techniques like shape-from-shading [14], shape-from-focus [15], or shape-from-specularity [16] aim to recover the 3D structure of an object from images. Many of them rely on multiple frames in which either the camera has moved, the source of illumination has changed (see Figure 7), or the object to image has changed. For many applications, taking several images from a fixed point with different illumination sources is not only feasible but realistic for a commercial implementation. In fact cameras and LED's are fairly inexpensive and are small enough to be included in many processes without a significant cost increase.

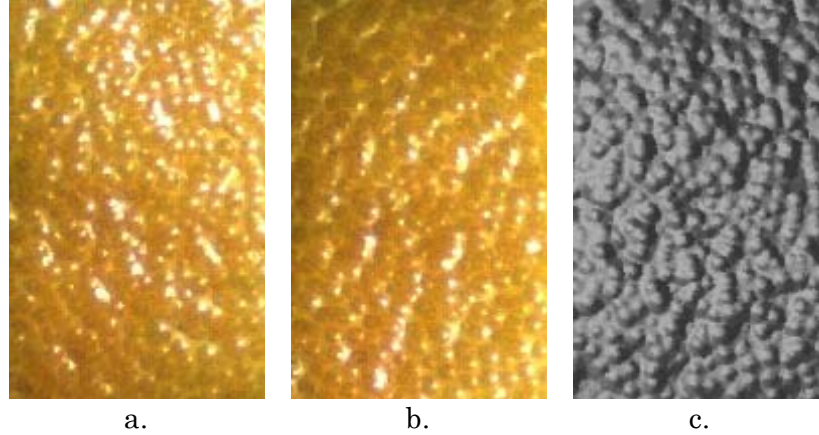


Figure 7. a., b. Images of orange skin illuminated from different angles; c. reconstructed 3D surface of the orange skin, from [16]

However, many of these methods have been shown for larger objects, shadows for example are not as apparent when the features to detect are just a few microns tall. An encouraging approach was taken by an MIT group in which a gel coated with a uniform (well characterized) material was used as an interface to easily capture surface measurements [17]. This system has become the basis of the start-up company GelSight. The system has proven useful and versatile and is able to generate 3D reconstructions of surfaces like coins, human skin, and even letters printed on a \$20 bill (see Figure 8).

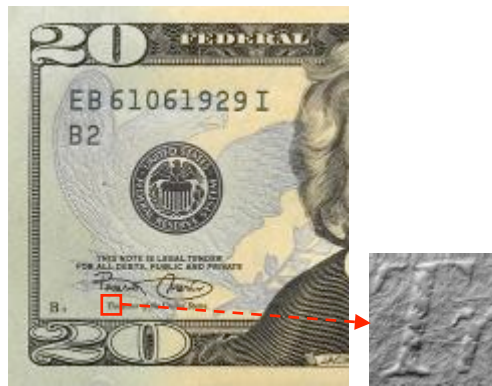


Figure 8. Rendering of the captured geometry from a \$20 bill, from [17]

This research intends to explore the ways in which EP-based 3D printing may be enabled by successfully modeling the EP process, characterizing and imaging the surface defects to achieve a uniform surface of the part being produced.

The remainder of this document reviews the related work in each area, formally describes the research problem of interest, describes the research methodology proposed to achieve the research goals, and presents some preliminary results in each of the proposed areas.

Chapter 2. LITERATURE REVIEW

This research relies on a knowledge base from four areas: Electro-photographic process physics, modeling and control, additive manufacturing, and image-based techniques for extracting geometric information from objects. This section reviews the work most relevant to the research goals of this thesis and identifies areas of opportunities.

2.1. Electro-Photographic Process Physics

The Electro-Photographic (EP) process used in document printing is based on transferring thermo-set powder particles (toner) through the use of electric fields. This process was first proposed by Carlson, who in 1938 developed an image on a plate with fine powder after charging the plate with a cloth and exposing it to light with the desired image pattern. Electrophotography was patented in 1942 and later became the basis for copying and laser printing.

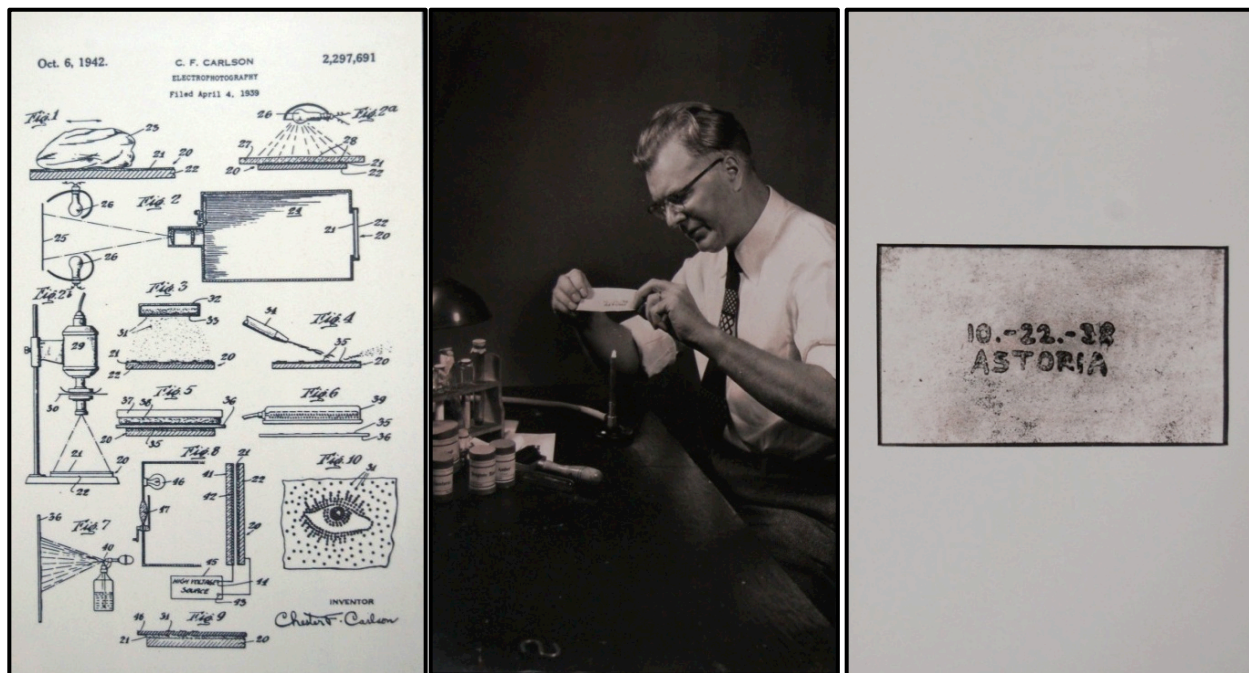


Figure 9. Commemorative images of Carlson's original work on display at the Chester F. Carlson Center for Imaging Science of RIT

2.1.1. EP Process Overview

The EP process consists of six different stages which were briefly described above and will be described in greater details below (refer to Figure 1 for reference):

2.1.1.1. The Photoreceptor

In commercial systems, a photoreceptor drum (or belt) is the core of the system since it retains electric charge while in dark, allowing for selective discharges that form the images to print.

The photoreceptor is usually formed by four to six different layers: A base layer, a ground plane, a charge generator layer, and a charge transport layer (see Figure 10.a.) [18].

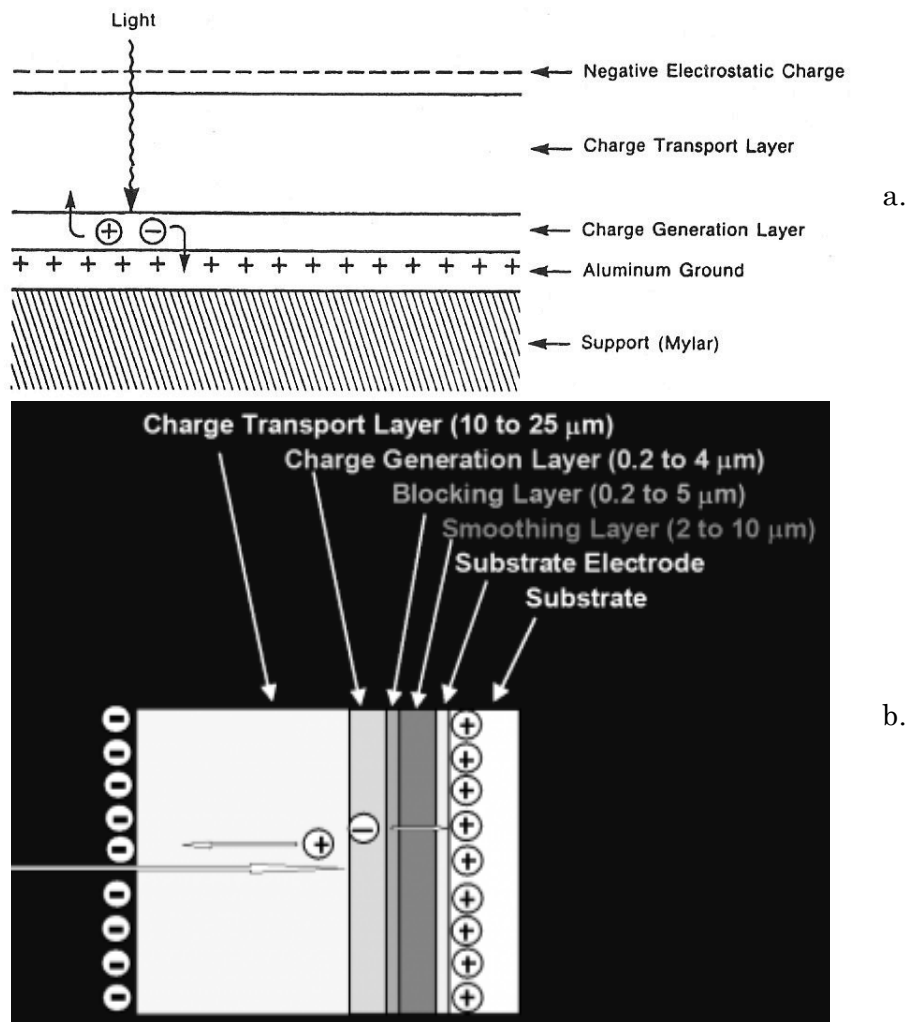


Figure 10. Organic photoreceptor structure: a. four layers from [18], b. six layers, from [19]

The base layer provides support and dimensional stability for either the drum or the belt. In metallic drums, the metal itself would act as a base; in belts, a base of Mylar or some type of Polyethylene is used.

The ground plane provides charges to neutralize the charges created on the surface of the photoreceptor. Usually is made of Aluminum or Titanium.

The charge generator layer reacts to light producing electron-hole pairs, which are then separated by the internal electric field and the holes travel through the transport layer. This layer distinguishes two type of photoreceptors, organic and inorganic. The inorganic are usually made of amorphous selenium alloys (reddish brown in color), while the organic usually use a Gallium compound giving a distinctive blue color.

The transport layer is much thicker in contrast to the charge generation layer and usually allows only the holes to travel, which is why the surface is charged negatively. This layer is usually made of some doped polycarbonate.

Two additional layers may be used to optimize the performance of the photoreceptor: a blocking layer and an interface layer may be placed between the ground plate and the charge generation layer to prevent charges to travel from the ground plate to the transport layer (see Figure 10.b.).

The behavior of the photoreceptor is usually modeled as an ideal capacitor. Despite the effectiveness of the process, residual charge gets trapped in the transport layer that light cannot dissipate, this causes a residual potential (different than 0) which will become the discharge level in the exposure phase. In general, organic photoreceptors are less expensive but also have a shorter life [18].

2.1.1.2. Charging

The photoreceptor is exposed to a constant voltage charge device (e.g. corotron or scorotron), which puts down charge on the surface of the photoreceptor until the field between the charge device and the photoreceptor is neutralized. These devices are based on corona discharges, which occur by ionizing the air surrounding a thin wire with a high electric potential and a nearby shield. The electric field pushes the ions towards the shield and the photoreceptor, ultimately charging its surface. The distance between the wire and the

shield (and photoreceptor) is critical to create corona discharges instead of arcing which is given by Paschen sparking breakdown voltage [18]. If the charging device only has the wire and the shield is known as corotron; if a screen is added between the corona wire and the photoreceptor the device is known as scorotron (see Figure 11). The voltage on the surface of the photoreceptor will match the voltage of the charge device (usually around 700 V).

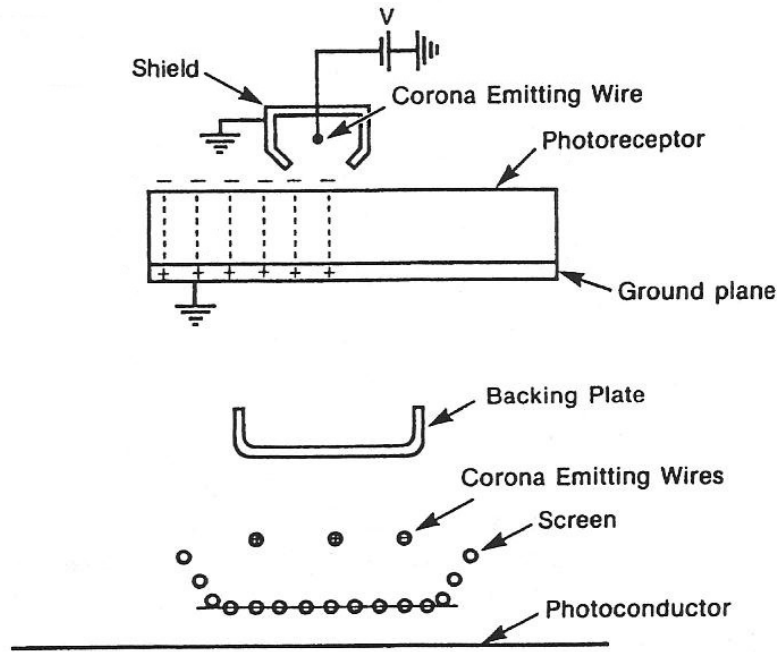


Figure 11. Schematic of charging devices: Corotron (top), Scorotron (bottom), from [18]

2.1.1.3. Exposure

The nature of the photoreceptor is such that it retains electric charge in the absence of light, therefore, the EP process is conducted in the dark and a laser beam is usually used to selective expose the photoconductor to light in the areas where toner is ultimately desired for marking (hence the common term of laser printers)¹. The negative charge on the surface of the photoreceptor of the unexposed areas remains at the voltage level achieved during the charging step (typically ~700V), while the exposed areas discharge to a much lower voltage (usually less than 100V). This process creates a latent image on the photoreceptor,

¹ This exposure approach is referred to as Discharge and Development. Depending on the polarity of the toner, there are also systems that discharge the area where marking is not desired.

² This architecture is known as toner accumulation on intermediate belt; two other alternatives for

which results in an electric field pattern that will attract toner particles in the development step.

The laser beam is directed to the different points across the photoreceptor through the use of scanning mirrors and beam alignment lenses (see Figure 12). The digital ‘on’ and ‘off’ patterns of the desired image are approximated by turning the laser on and off as the mirror face is rotating. The multiple facets of the mirror allows for multiple scan lines per rotation of the mirror. This arrangement is widely used in commercial devices and can achieve very fine resolution of up to 2400 dots per inch (dpi). Alternatively, LED arrays have also been used, eliminating the need for the moving parts since each one of the LEDs addresses a point in the photoreceptor. The challenge is then to pack enough LEDs to provide a comparable resolution to the laser and mirror arrangement. For the LED arrangement, resolutions of 600 and 1200 dpi are not uncommon.

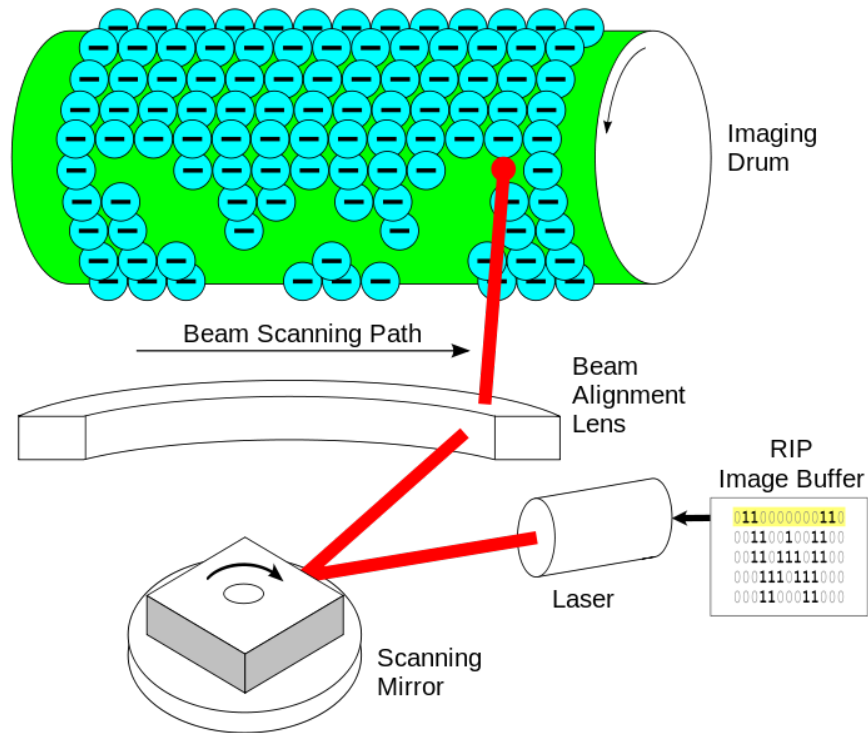


Figure 12. Laser exposure structure, from [20]

2.1.1.4. Development

In the development phase, the photoreceptor and the toner particles come in close proximity to one another and the electric field patterns that result from the latent image serves to attract the toner particles producing a real, developed image on the photoreceptor.

In general there are two types of development systems, single- or two-component development systems (see Figure 13).

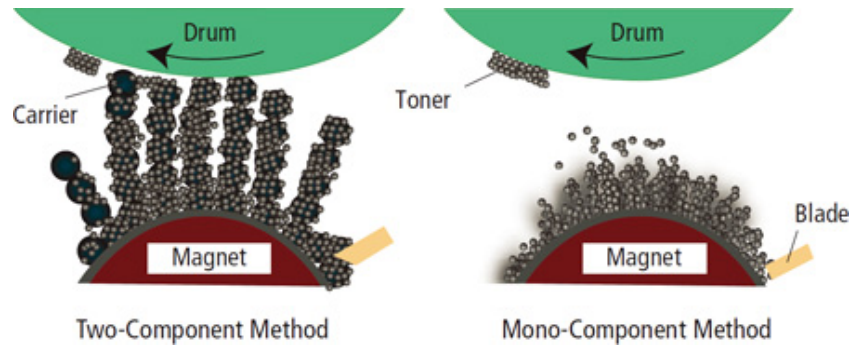


Figure 13. Comparative schematic between two-component development and mono-component development, from [21]

In the single-component (also referred as mono-component), the toner is agitated and brought in contact with a charging blade and the surface of the rollers to achieve the toner charging. This system is less expensive but less efficient, thence its usually found in low speed machines. Among mono-component development systems a main distinction is whether the toner is magnetic or not. If the toner is magnetic, magnetic forces are used to pick up the toner and a doctor blade regulates the amount of toner that is taken by the roller to the development gap. Non-magnetic systems rely on contact and compliant rollers to provide toner to the roller from which the development will be done. Schematics of both strategies can be seen in Figure 14.

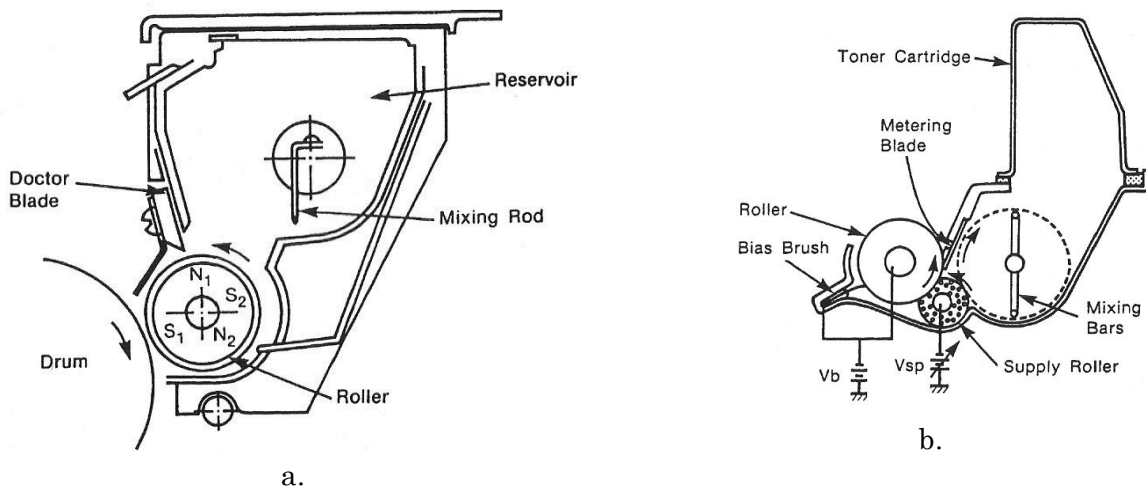


Figure 14. Schematic of mono-component development systems, a. magnetic toner (Canon), b. non-magnetic toner, a soft supply roller is used (Ricoh), from [18]

In the two-component system larger beads (usually magnetic) known as carriers are used and are agitated against the toner, charging it up and causing the toner to stick to it (see Figure 15). The carriers are then picked up by rollers with magnetic cores and directed into the proximity of the photoreceptor so the toner can be picked up. Then the carrier beads and the remaining toner are released back into the reservoir (see Figure 16). In many development systems multiple development rollers can be placed to achieve higher printing speeds, making the carrier jump from one roller to the next, allowing more toner to be picked up by the photoreceptor. The two-component system is more efficient charging the toner and provides an easier way to move the toner in the developer (using magnetic force), which is why it is widely use for mid-size and larger printers and copiers [18].

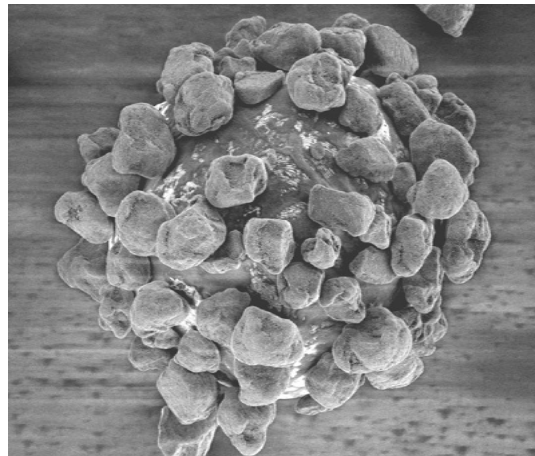


Figure 15. Carrier bead with toner stuck to its surface, from [22]

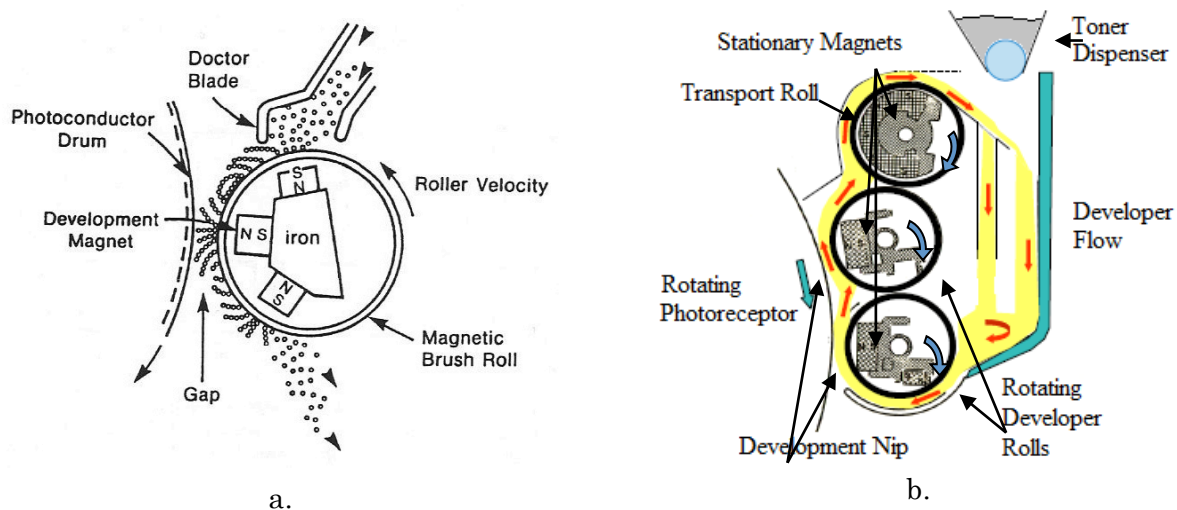


Figure 16. Schematics of two-component magnetic brush development systems, a. single development roller, from [18]; b. multiple development rollers, from [22]

In both cases (mono or two-component), the toner gets charged using the tribo-electric effect of putting in contact two dissimilar materials. The charge in the toner (about the same as the photoreceptor $\sim 700\text{V}$) and the potential difference in the areas of the photoreceptor that have been exposed, create a force that is enough to make the toner jump a gap (and detach from the carrier) only in those exposed areas, creating a developed image on the photoreceptor (see Figure 13).

One last type of development system is a hybrid two-component development system. The hybrid has characteristics of both the mono-component and the two-component system because it does contain carrier beads that charge the toner and are used to move the toner easily, but the toner is transferred to a donor roll that ultimately provides the toner for development to the photoreceptor. A schematic of the hybrid system can be seen in Figure 17.

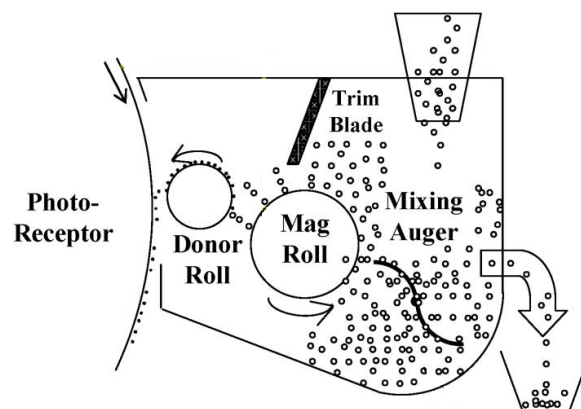


Figure 17. Schematic of a Hybrid development system, from [23]

2.1.1.5. Transfer

Once the image has been developed on the photoreceptor, the toner needs to get to the media. The developed image, also referred as real image, is passed onto the desired media (usually paper) by means of an opposite electrostatic force that repel the toner from the photoreceptor (or support drum/belt) onto the media. A transfer corona or biased transfer rollers with opposite polarity are placed behind the media and the media is thin enough that the electric field created can move the toner, making it to stick to the media [18].

Two configurations are common, direct transfer and intermediate transfer. In the direct transfer configuration, the toner passes from the photoconductor directly to the media while in the intermediate transfer, the toner passes first to a supporting drum or belt and from it

to the ultimate media. This last configuration is commonly used in color printers where four developments are required (cyan, magenta, yellow, and black - CMYK) to form the color image², therefore, each development is carried independently and the toner is stacked in the supporting drum/belt and finally passed all together as one image to the media.

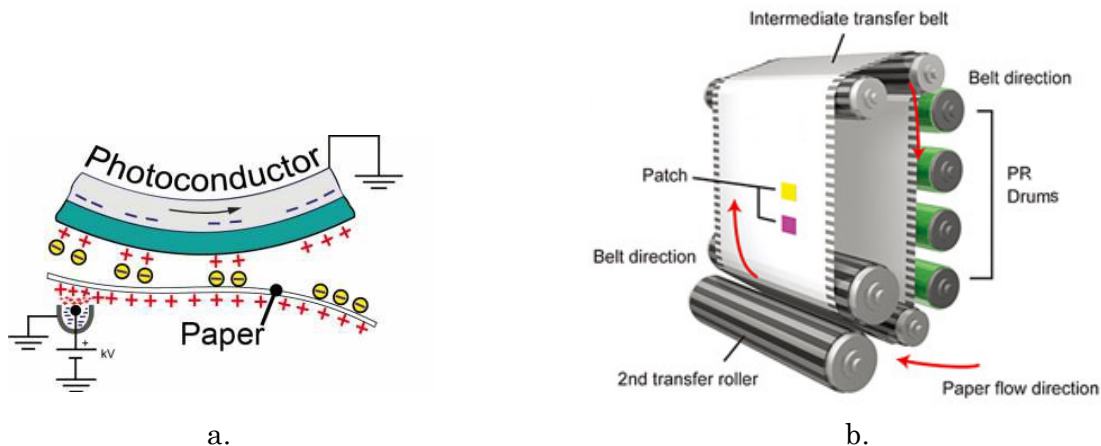


Figure 18. a. Schematic of direct transfer, from [1]; b. Schematic of intermediate transfer, from [24]

While the direct transfer may be more compact and may require less hardware (only one transfer vs. transferring from the photoconductor to the supporting drum/belt and from there to the media), the intermediate transfer allows for more flexible systems in which multiple development stations can be arranged, a shorter paper path and higher speeds can be achieved [25].

2.1.1.6. Fixing

The toner that has been transferred onto the media needs to be permanently attached to it. Pressure and heat are applied to bring the toner to a crystallization point in which the toner is not completely liquid but is melted enough to attach to the fibers of the media. This phase of the process typically does not involve the photoreceptor and can be done offline (see Figure 19). In fact, in color printing, four separate developments (CMYK) are carried away and transferred to the media before fusing it. This step of the process changes the properties and shape of the toner particles, giving the final appearance to the print in terms of color, brightness and gloss [26].

² This architecture is known as toner accumulation on intermediate belt; two other alternatives for toner accumulation have been implemented in commercial systems, accumulation on paper, and accumulation on photoreceptor, each one with technical advantages and challenges.

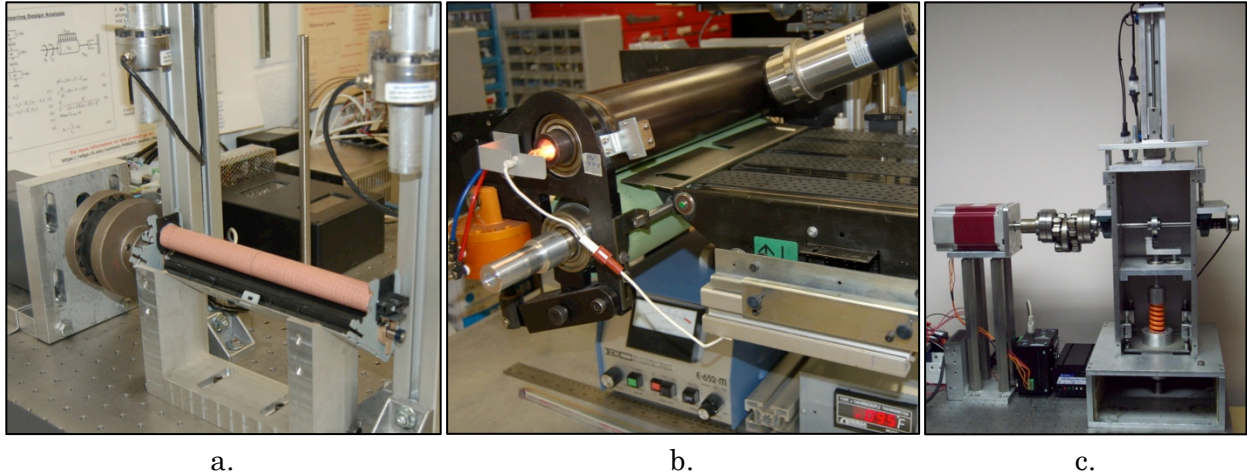


Figure 19. Fusing stations at the PRISM Lab: a. roller based with desktop printer rollers, b. roller based with more robust rollers, and c. stamp-based

2.1.1.7. *Cleaning/Erasing*

After development, the photoreceptor needs to be prepared for another printing cycle. The photoreceptor is cleaned from toner that was not transferred, usually by mechanical means either with blades or brushes and vacuum. This step prevents unintended marking in the following print. Residual charges that may remain on the surface are also erased from the photoreceptor by a corona or a uniform exposure to light, leaving the photoreceptor ready for another printing cycle.

2.1.2. EP Development Process Modeling

This section explores the models used to describe the behavior of the development systems and its applicability towards the control of the material being transferred. The first approach has been widely used in industry to model toner development while the second formulates a dynamic model for toner aging, describing how the changes in the toner properties affect the performance of the system.

2.1.2.1. Static Model for Solid Area Development

A development system is very complex, there are many factors that affect the amount of toner being transferred to the photoreceptor. In a two component system for example, its behavior depends on the materials used (toner, carrier, photoreceptor) and its properties (toner charge density $\frac{q_t}{m_t}$, dielectric constants for the toner k_t , photoreceptor k_{pr} , developer k_d (this term refers to the mixture of carrier and toner used for development), the developer mass density P_d), the toner concentration C (fraction of mass of toner relative to the mass

of the developer $C = (M_t/M_d)$, the velocities of the rotating elements (photoreceptor v_{pr} and rollers v_r), the number of developer rollers N , the geometrical constraints (gap between the photoreceptor and the roller L , the active gap for development l , the trim blade gap l_t , thickness of the photoreceptor t_{pr} and the toner layer t_t , the developer packing fraction P_f), the effectiveness of development f_n , the permittivity ϵ_0 and the voltages for development (bias voltage V_{bias} , image discharge voltage V_{low}) among others. Many of these factors are determined or can only be estimated experimentally. The following model has been used in industry to capture the behavior of the solid area development for a two-component system [7, 22] under static/steady state conditions:

$$DMA = K_{SAD} \cdot V_{devel} \cdot \left(1 - e^{-C/C_o}\right) \quad (2.1)$$

$$K_{SAD} = \frac{K_{cond} - K_{ins}}{2} \left(\frac{e^x - e^{-x}}{e^x + e^{-x}} \right) + \frac{K_{cond} + K_{ins}}{2} \quad (2.2)$$

$$K_{ins} = \frac{\epsilon_o \cdot N \cdot (v_r/v_{pr})}{\frac{t_{pr}}{k_{pr}} + \frac{t_t}{2k_t} + \frac{L-l}{k_{dev}}} \quad (2.3)$$

$$K_{cond} = \frac{\epsilon_o}{\frac{t_{pr}}{k_{pr}} + \frac{t_t}{2k_t}} \quad (2.4)$$

$$V_{devel} = V_{bias} - V_{low} \quad (2.5)$$

$$C_o = \frac{K_{SAD} \cdot f_n \cdot V_{devel} \cdot l_t}{P_d \cdot P_f \cdot L \cdot l \cdot N \cdot \left(\frac{v_r}{v_{pr}}\right) \left(\frac{q_t}{m_t}\right)} \quad (2.6)$$

A simplified version of it is described in [23] where the developed mass per unit area (DMA) can be described by:

$$DMA = \alpha \left(1 - \exp - \frac{\gamma(V_{dev} - V_{D0})}{\alpha} \right) \quad (2.7)$$

where α is the maximum achievable toner mass, V_{dev} is the applied development voltage, γ is the slope of the development curve and V_{D0} is a bias voltage of development. The development curve can be seen in Figure 20, where DMA^* and V_{dev}^* are the desired operating point and γ_L is the slope at that point.

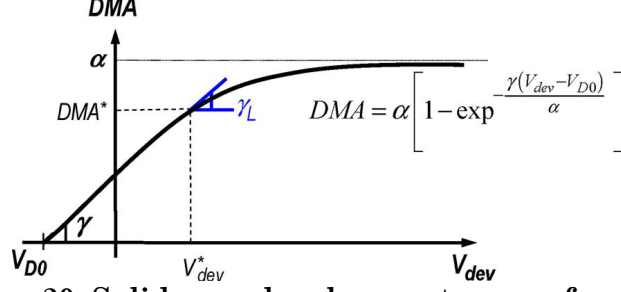


Figure 20. Solid area development curve, from [23]

Similarly, Anzai and Hoshi in [27] presented a model for toner flow for a dual component magnetic brush development system. For the development of solid areas, the model for the mass of deposited toner is:

$$M = M_0 (1 - \exp(-H/\phi)) \quad (2.8)$$

$$M_0 = \kappa E_e / q \quad (2.9)$$

$$H = \frac{a + puW}{|S|} \quad (2.10)$$

where M_0 is the saturation level for developed mass, H is the toner flow mass, ϕ is a coefficient, κ is a coefficient, E_e is the effective electrostatic field, q is the toner charge, a is the toner weight per unit area, p is a perturbation parameter of the agitation of carrier beads and toner forming the magnetic brush, u is the toner weight per unit volume, W is the brush nip, and S is the speed ratio between the brush and the photoreceptor. Clearly equations 2.7 and 2.8 are very similar and capture the same type of behavior in slightly different manners.

A model introduced by Takeda et al. in [28] captured the influence of electrostatic field and magnetic field to the development of toner in a mono-component system that uses a magnet roller with a sleeve as the development roller. In it, the Electrostatic field within a toner layer is modeled by:

$$E(x) = \frac{V_S - V_B}{\epsilon_b \left(\frac{d}{\epsilon} + \frac{d_b}{\epsilon_b} + \frac{d_e}{\epsilon_e} \right)} + \frac{\rho_b}{\epsilon_b} x \quad (2.11)$$

$$\rho_b = \frac{Q}{M} \rho_t (1 - Pt) \quad (2.12)$$

where x is the coordinate going from the photoreceptor to the sleeve of the development roll, V_S is the surface potential of the photoreceptor, V_B is the bias voltage for development, ϵ is

the dielectric constant of the photoreceptor, ϵ_b is the dielectric constant of the toner layer, ϵ_e is the dielectric constant of the dielectric layer (gap between photoreceptor and sleeve), d is the thickness of the photoreceptor, d_b is the thickness of the toner layer, d_e is the thickness of the dielectric layer, Q/M is the charge of toner per unit mass, ρ_b is the volume charge density of the toner layer, ρ_t is the density of a toner particle, and P_t is the porosity of the toner layer.

The electric force that acts on the toner particle is modeled by:

$$F_e(x) = \left(q + 4\pi r^3 \frac{\epsilon_t - \epsilon_0}{\epsilon_t + 2\epsilon_0} \epsilon_0 \frac{\rho_b}{\epsilon_b} \right) E(x) \quad (2.13)$$

where q is the electric charge of the toner particle, r is the radius of the toner particle, ϵ_0 is the dielectric constant of free space, and ϵ_t is the dielectric constant of the toner particle. Similarly, the magnetic force is modeled by:

$$F_m = 4\pi r^3 \mu_0 \left(\frac{\rho_m}{2\mu_0} \right)^2 \left(\frac{\mu_t - \mu_0}{\mu_t + 2\mu_0} \right) \left(\frac{R_0^{2k+2}}{R^{2k+3}} \right) (k+1) \quad (2.14)$$

where μ_0 is the permeability of vacuum, μ_t is the permeability of a toner particle, ρ_m is the maximum magnetic charge density on the magnetic roller, k is the number of magnetic poles on the magnetic roller, R_0 is the radius of the magnetic roller, and R is the distance between the center of the magnetic roller and the toner particle.

These models are very specific to each technology and hardware, which makes them difficult to find in the literature and hard to translate for different hardware configurations.

2.1.2.2. Dynamic Model for Toner Aging

Ramesh [29] and Gross and Ramesh [30] introduced a dynamic model of the toner behavior in the EP process for toner aging and was further explored by Liu et al. [23]. In this model two time scales are considered in the EP process, one is the time in which development occurs (which is extremely fast) and a longer time that considers how the toner age in the developer system, changing its properties. The first type of time is disregarded for this analysis and the dynamic model presented describes the behavior of the hybrid two-component system (see section 2.1.1.4) as the toner ages. The model starts with the toner mass balance, for which the mass of toner $M_t(t + dt)$ at any given time depends on the previous amount of toner $M_t(t)$ plus the new toner being dispensed at the rate $D_t(t)$ minus

the toner being developed at the rate $C_t(t)$ and the toner being discarded as waste at the rate $R_w(t)$. The model establishes that a particle of toner has a certain development probability $P(\tau, t)$ that depends on its residence time τ (time that this particle has been in the developer) and the time t . The toner age distribution also changes but it is different at the sump $g_s(\tau, t)$ and at the donor roll $g_d(\tau, t)$. The dynamics can be expressed as follows:

$$M_t(t + dt) = M_t(t) + (D_t(t) - C_t(t) - R_w(t))dt \quad (2.15)$$

$$P(\tau + dt, t + dt) = \frac{p_0(t)}{1 + p_0(t)} + e^{-\beta dt} \frac{P(\tau, t)}{1 + p_0(t)} \quad (2.16)$$

$$M_t(t + dt)g_s(\tau + dt, t + dt) = M_t(t).g_s(\tau, t) - C_t(t)dt. \frac{P(\tau, t).g_s(\tau, t)}{\sum_{\tau=0}^t P(\tau, t)g_s(\tau, t)} - R_w(t)dt.g_s(\tau, t) \quad (2.17)$$

$$M_d.g_d(\tau + dt, t + dt) = M_d.g_d(\tau, t) - C_t(t)dt. \frac{P(\tau, t).g_d(\tau, t)}{\sum_{\tau=0}^t P(\tau, t)g_d(\tau, t)} + C_t(t)dt. \frac{P(\tau, t).g_s(\tau, t)}{\sum_{\tau=0}^t P(\tau, t)g_s(\tau, t)} \quad (2.18)$$

where:

$$p_0(t) = p_a. \frac{D_t(t)dt}{M_t(t + dt)} \quad (2.19)$$

$$M_t(t + dt).g_s(0, t + dt) = D_t(t)dt \quad (2.20)$$

$$M_d.g_d(0, t + dt) = C_t(t)dt. \frac{D_t(t)dt}{M_t(t + dt)} \quad (2.21)$$

with p_a being the fraction of additives dispensed, and β being the time constant for natural decay. Equations **Error! Reference source not found.** and **Error! Reference source not found.** are derived by mass balance of the controlled volume. Ultimately, average toner developabilities can be defined for the sump and donor as:

$$\gamma_s(t) = \sum_{\tau=0}^t P(\tau, t)g_s(\tau, t) \quad (2.22)$$

$$\gamma_d(t) = \sum_{\tau=0}^t P(\tau, t)g_d(\tau, t) \quad (2.23)$$

These variables are the used to redefine the dynamic model towards a more control oriented:

$$\gamma_s(t + dt) = \sum_{\tau=0}^{t+dt} P(\tau, t + dt)g_s(\tau, t + dt) \quad (2.24)$$

which in turn gets simplified to:

$$\dot{\gamma}_s(t) = \frac{D_t(t)}{M_t(t)}(1 + p_a)(1 - \gamma_s(t)) - \beta \cdot \gamma_s(t) \quad (2.25)$$

$$\dot{\gamma}_d(t) = \frac{D_t(t)}{M_t(t)}p_a(1 - \gamma_d(t)) + \lambda \frac{C_t(t)}{M_d}(\gamma_s(t) - \gamma_d(t)) - \beta \gamma_d(t) \quad (2.26)$$

$$\dot{M}_t(t) = D_t(t) - C_t(t) - R_w(t) \quad (2.27)$$

where λ is an experimental value. The state variables are then $X(t) = [M_t(t), \gamma_s(t), \gamma_d(t)]^T$, the control input is the dispensing rate $D_t(t)$. This aging model was put together with a linearized version of the static model of development to control the DMA at a constant level for color consistency. Linearizing the development curve around DMA^* and V_{dev}^* :

$$DMA = f_1(DMA^*, \gamma_L, V_{dev}, V_{dev}^*) = DMA^* + \gamma_L(V_{dev} - V_{dev}^*) \quad (2.28)$$

then the local slope of development curve and the desired development voltage depends on the mass of toner, the developability of the toner at the donor roll and the relative humidity $\gamma_L = f_2(M_t, \gamma_d, RH)$ and $V_{dev}^* = f_3(M_t, \gamma_d, RH)$. An overall diagram of the control model can be seen in Figure 21.

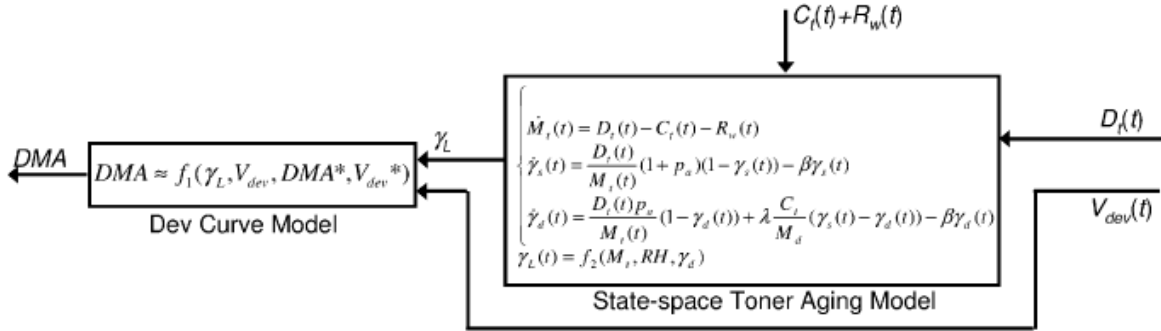


Figure 21. Block diagram of the control oriented model, from [23]

2.2. EP-based 3D printing attempts

The intent to extend document printing to create three-dimensional parts has been reported for over two decades. Most of the approaches have used existing printers modified up to a certain extent to accept different materials or printing conditions that would enable stacking multiple layers of toner. Although success has been limited, all have shown feasibility and have highlighted areas where further study is required. The following are the most significant attempts to date to perform three-dimensional printing using Electrophotography:

2.2.1. Bynum's Patent (1992)

The first patent granted that suggested the use of EP for 3D printing was proposed by David K. Bynum in 1992 [2] and contemplated four different technologies for additive manufacturing, one of which involved EP. The patent suggested that each layer was formed using EP onto a support belt, and before transferring, the new layer should be heated until it became “tacky” to facilitate the addition to the previous stack of layers. The stack of layers that form the part would be kept on a platform that adjust its position to accommodate for new layers (see Figure 22). The patent suggested the use of multiple development stations, each one with different materials that may serve as support material for more complex parts, to achieve different colors, or other combinations of materials to achieve the desired properties for the part.

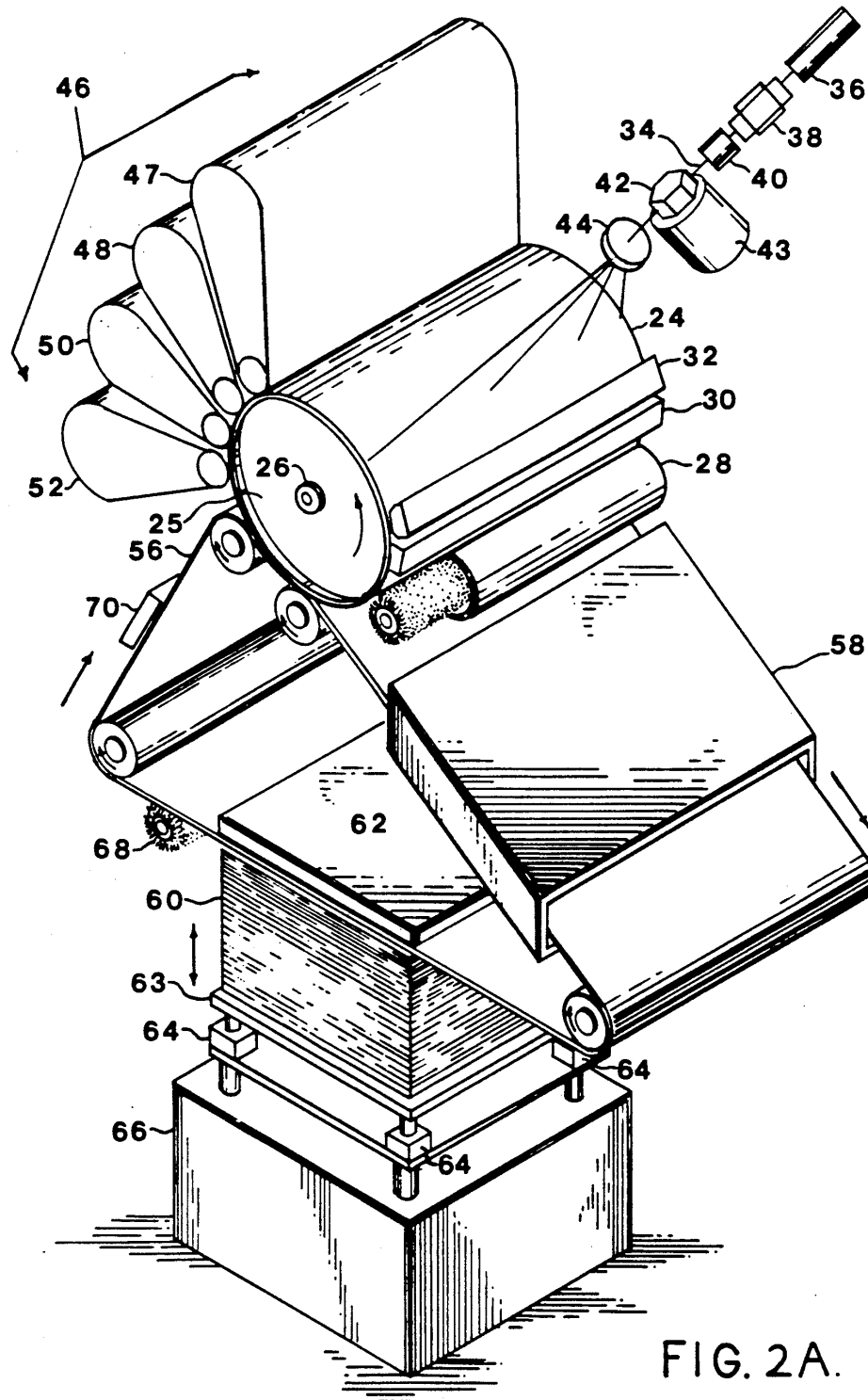


Figure 22. Schematic of the EP-based 3D printer from Bynum's patent [2]

Although the patent was granted, and the approach suggested seemed feasible, there was never an actual working device built from this patent.

2.2.2. University of Florida (2000)

Research lead by Prof. Ashok Kumar from the University of Florida proposed a two powder method (support material and part material) [3] and was later patented [10]. The powders were handled by EP to form a layer and fused/sintered to form an actual part (see Figure 2). The process was later referred as Electrophotographic Layered Manufacturing (ELM) and Electrophotographic Solid Freeform Fabrication (ESFF). A test-bed was built (see Figure 23.a.) and preliminary tests showed feasibility; however, it was reported that many challenges remained in order to produce thicker parts. In fact, transferring new layers after a certain thickness (~ 40 layers) was a real concern, and achieving a uniform surface was not easy [31, 32]. The surface of the stack of layers was charged with a corona before transferring a new layer to facilitate the transfer of material and mitigate the decrease in strength of the electric field due to the insulating nature of the growing part. A compaction step was introduced before fusing to obtain better adhesion and a smooth surface. Although further layers were printed, other challenges manifested. Of particular concern was the charge and the interaction between the photoconductor and the stack surface. In the end parts of up to 575 layers (~ 3 mm) were produced [5] (see Figure 23.b.). Further analysis showed that growing parts thicker was unfeasible because the corona used for top charging, ceased to put charge on the surface as the part grows thicker and the platform which serve as electrode was further away from the corona wire [12].

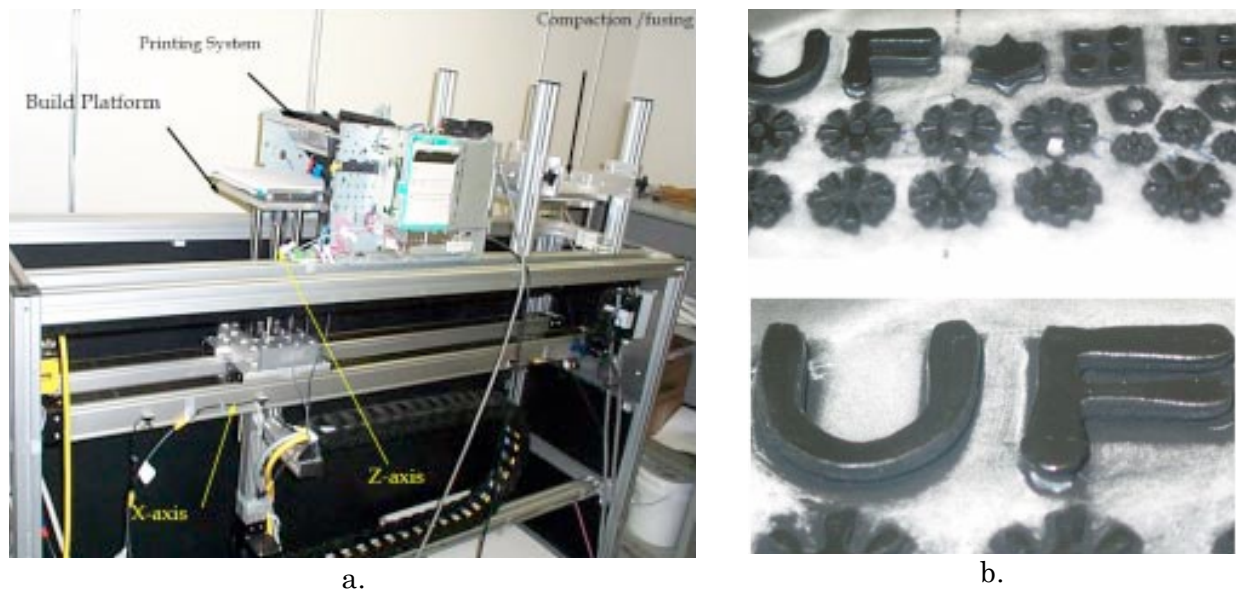


Figure 23. a. Photograph of the test-bed for ELM at the University of Florida, b. Parts produced by corona top charging of 3 mm thickness, from [5].

2.2.3. NC State – RIT (2002)

Prof. Denis Cormier then at NC State led the research efforts that explored not only multiple layers of toner but also selective coloring with EP in 3D structures [4, 11]. A structure was proposed for the "3D laser printer" (see Figure 24.a.) and preliminary testing was done using a commercial printer HP LaserJet 4500, obtaining satisfactory results for 30 layer parts (see Figure 24.b.). It was reported that a test-bed was built to assess the transfer method which used only heat and pressure [33], but the research effort did not continue much after.

During those preliminary tests, it was observed that the color of the printed part changed as a function of the number of layers. It is known in document printing that the final color of the print is dependent on the base substrate; therefore, as the part grows thicker, the base substrate or plate would be obscured by the multiple layers of material, resulting in a darkening effect. A compensating scheme was proposed that involved printing a white base material and only printing color material in the final layers of the part to achieve the desired color reproduction (see Figure 24.c.). This area of research has become active recently at RIT where a master's thesis was done on a preliminary study for color reproduction in 3D prints [34] and further research is underway.

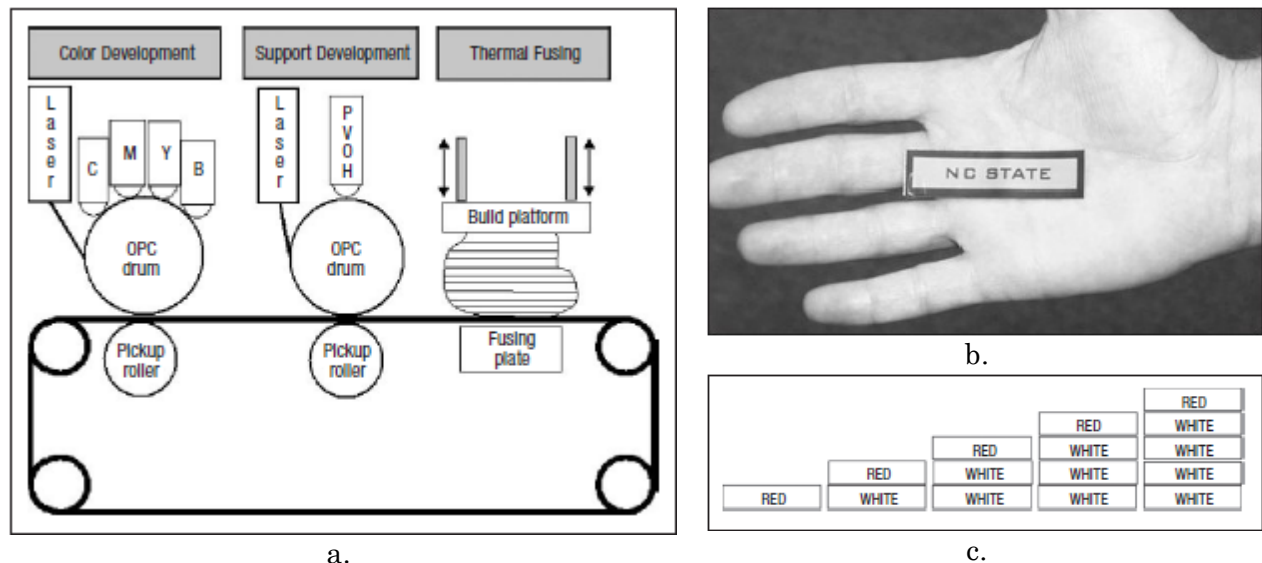


Figure 24. a. Schematic of the Color 3D laser printer configuration proposed, b. 30 layer sample result, c. Color compensation scheme, from [4]

2.2.4. De Montfort University (Active)

The most recent work in this area has come from the UK where research led by Prof. David Wimpenny at De Montfort University have developed a test-bed for Additive Manufacturing by EP. The test-bed includes two industrial monochrome printers CTG-1C17-600 from CTG PrintTEC, Germany, a moving platform where the layers are transferred and stacked, and an infrared heater to fuse the layers (see Figure 25.a.) [1, 13]. The process was referred as Selective Laser Printing (SLP). Although preliminary manual tests had shown that parts as thick as ~10 mm were achievable (see Figure 25.b.), the automated rig was only able to produce samples of up to ~1.6 mm (see Figure 25.c.). Those unsatisfactory results had motivated further studies on ways to increase the part thickness and the effect of residual charges on creating a 3D part [35] which is believed to be the reason for surface defects to appear.

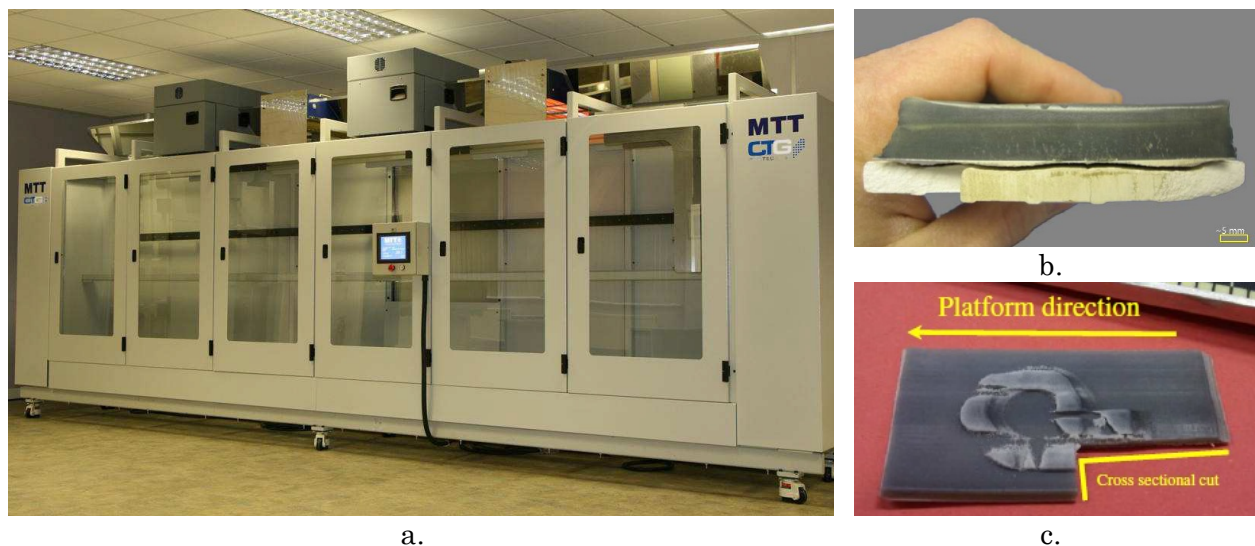


Figure 25. a. Test-bed for SLP at DMU, b. Thick preliminary sample (~10 mm), c. Thickest sample obtained in the test-bed (~1.6 mm), from [1]

The preliminary tests that yielded significantly thicker samples were conducted over a ceramic substrate and the entire sample would be heated for 5 minutes in an oven at 150 C before adding a new layer. The new layer was transferred applying heat and pressure at a level considerably higher than what is used for document printing. The difference in the results obtained has led to the conclusion that those longer waiting/relaxation times between layers (about 10 minutes compared to less than a minute in the automated rig) played a key role allowing the surface to completely discharge before accepting a new layer of toner.

A complementary research was conducted within the group to establish a better toner for EP-based 3D printing since it has been clear that the nature of the toner used for document printing produced extremely brittle parts [33].

2.2.5. Printed Electronics (2010-2012)

A related area of research has been extending the use of EP and laser printing to print electronic circuit boards. Both copper [36] and silver lines [37] have been printed showing some encouraging results. Although conductive toner has been used since the early days of EP [18], printing metal powders like copper or silver is not an easy task, in fact, the trials with copper reported in [36] showed limited success and showed greater potential on selectively melting the copper particles with a high power laser where the conductive lines were desired (see Figure 26.a.). In [37], silver particles were used but needed to be coated with a polymer to make it non-conductive, facilitating its movement through the EP process. Several layers needed to be deposited in order to achieve conductivity. The sample was then "fired" which meant heating the sample until the polymer coating was melted and the silver particles adhere to each other, obtaining actual conductive lines (see Figure 26.b.). Despite these results, the technique performs poorly when compared to inkjet.

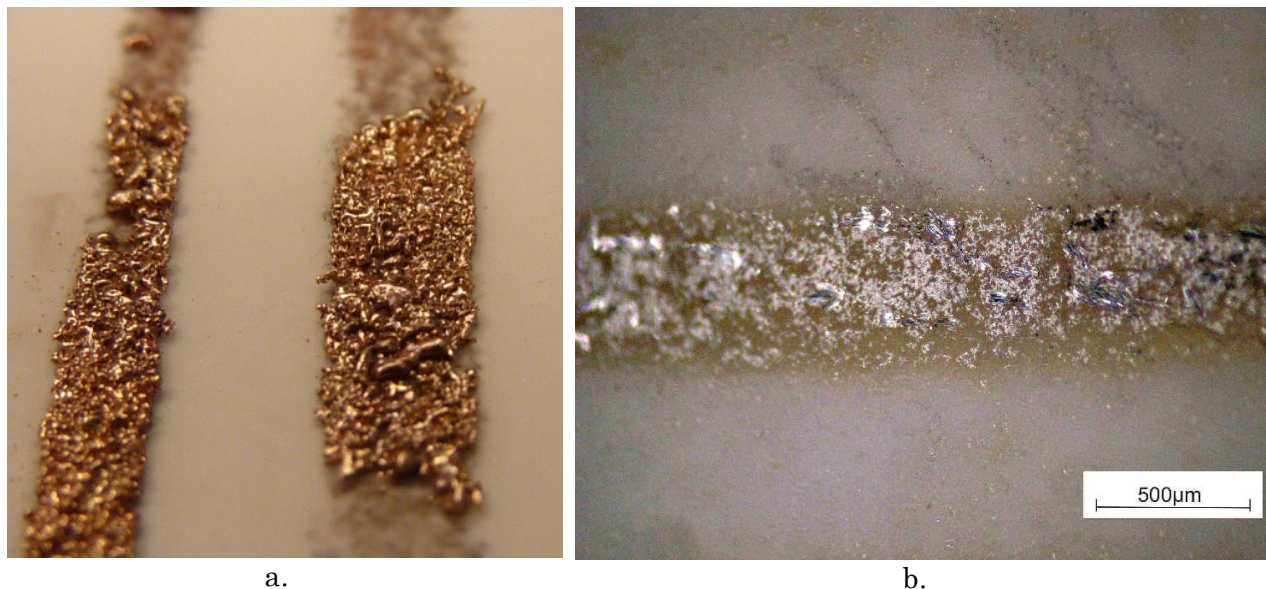
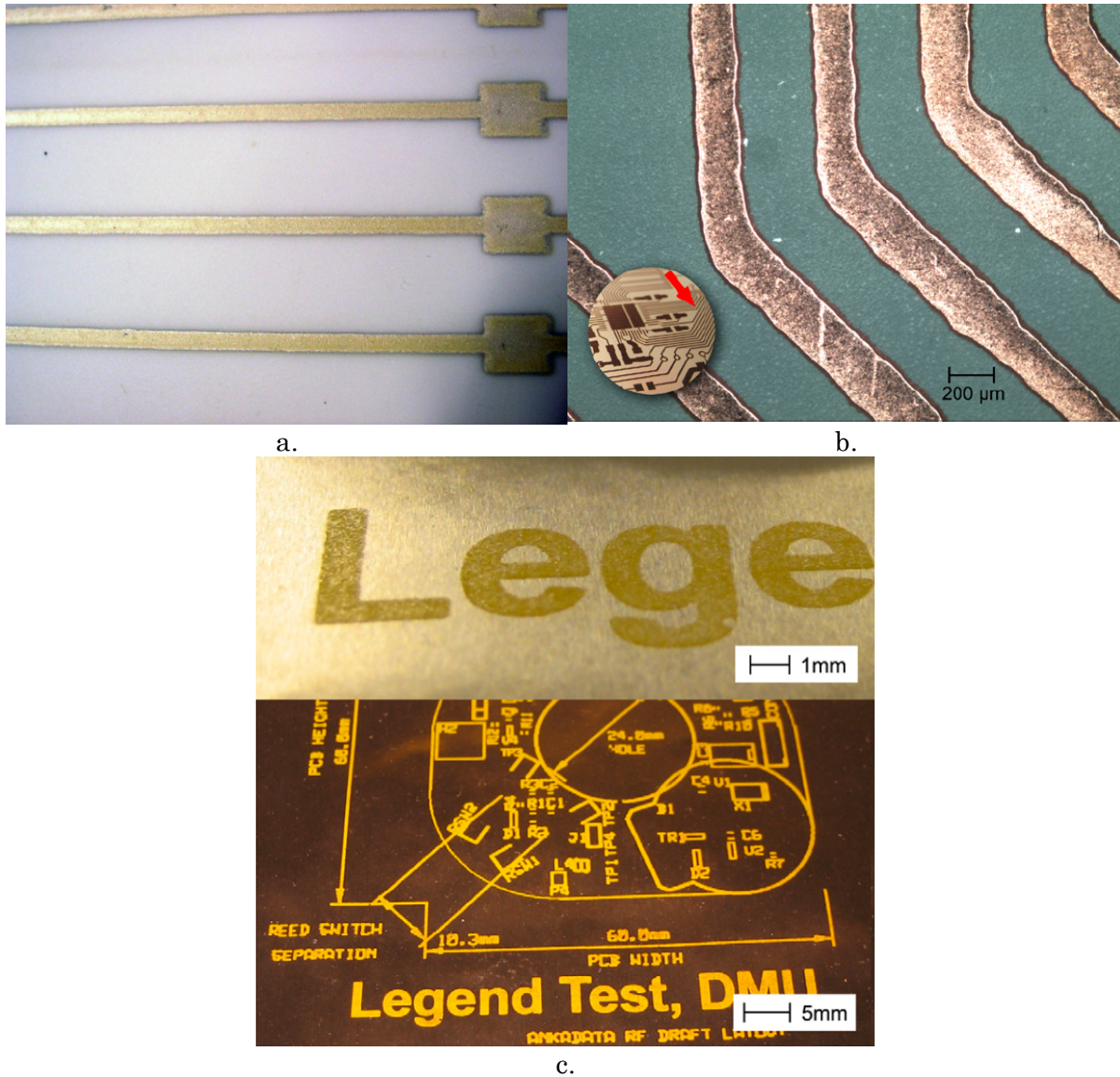


**Figure 26. a. Copper lines printed by selective laser melting (SLM), from [36];
b. conductive silver line after four prints by EP and "firing", from [37]**

Subsequent work indicated that EP could be used in the production of circuit boards and electronics not only to deposit conductive materials but also as a way to streamline the

overall workflow, eliminating the need for artwork masks, and for legend printing on the circuit boards [38]. Sample images of the different applications identified for EP in the production of circuit boards can be seen in Figure 27.



the first four are targeted for the traditional CMYK stations while the fifth one is targeted for customized colors, gloss enhancers, coatings, and as one of the options a clear coating to achieve what they refer as dimensional printing [40]. The NexPress uses clear toner to produced a clear 3D structure of up to 28 μm tall that enable the reproduction of textures and patterns that enhance the printed content [41]. Images of the Kodak NexPress and the dimensional printing feature can be seen in Figure 28.

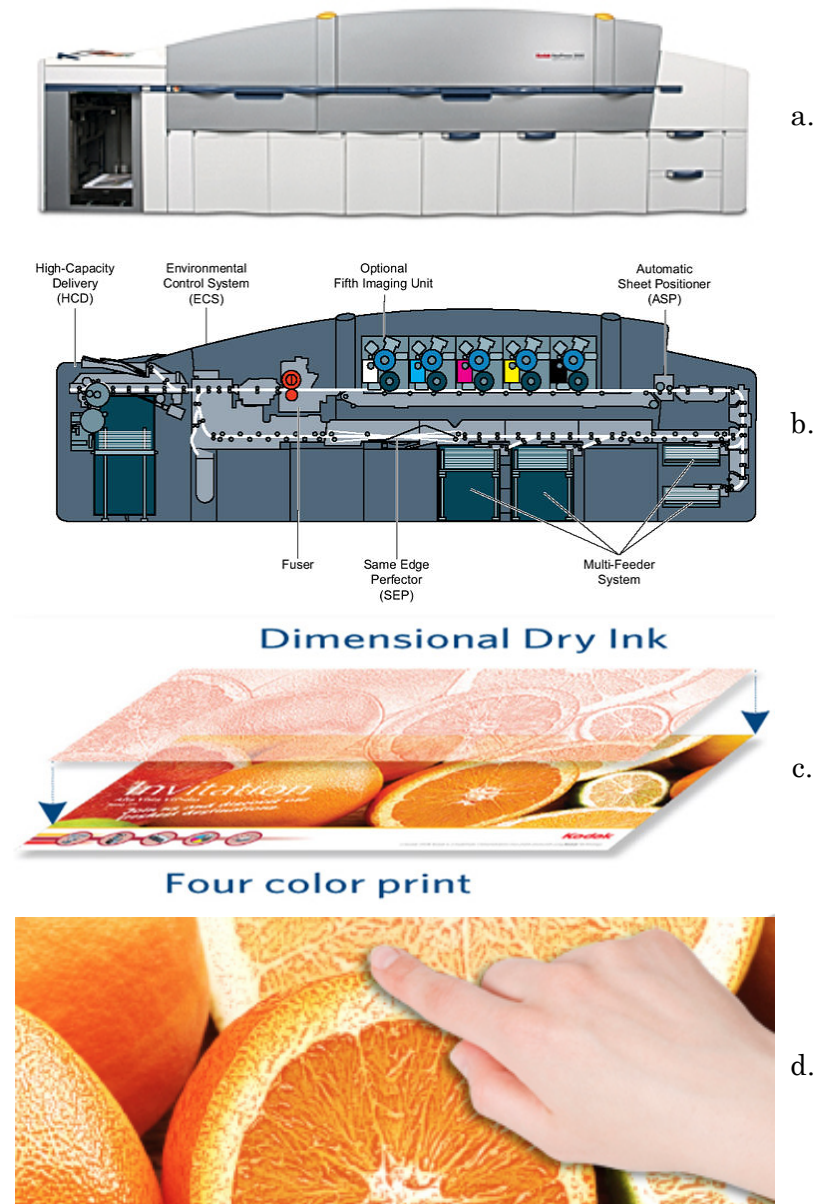


Figure 28. a. Kodak NexPress 2500, one of the digital presses capable of dimensional printing, from [42]; b. detail diagram, from [43]; c. and d. dimensional printing feature, from [40]

Although the dimensional printing feature is not intended to reproduce tall three-dimensional structures, it is a commercial application of EP-based 3D printing to reproduce thin structures, incorporating those into traditional printing methods.

2.3. Control of EP3D printed surface

Process modeling and closed-loop control have been identified as key areas needed for further advancement of additive manufacturing technologies [44]. The vast majority of printing processes run “open-loop”, meaning there is no specific control on the final outcome of the process, which is the amount of material deposited on a substrate or base structure. This does not imply that other control strategies are not implemented. Multiple local controllers handle different parameters to make the processes work, such as control of voltages, position of printheads, temperature, speed of rollers, etc. Additionally, printers include calibration routines and control patches to maintain good performance but there is no real feedback throughout the printing process. Similarly, 3D printers maintain operating conditions and tight control on x, y, z, positioning but there is little feedback on the final output of the system.

To examine registration between layers in a 3D printing process, a vision system was suggested to take measurements after each layer [45]. The study showed that there was an oscillating nature in the placement of each layer that needed further control to guarantee an accurate reproduction of the intended geometry (see Figure 29, layers are outlined by the dashed lines). This work was presented as a first step towards developing a closed-loop control for a metal-based additive manufacturing process.

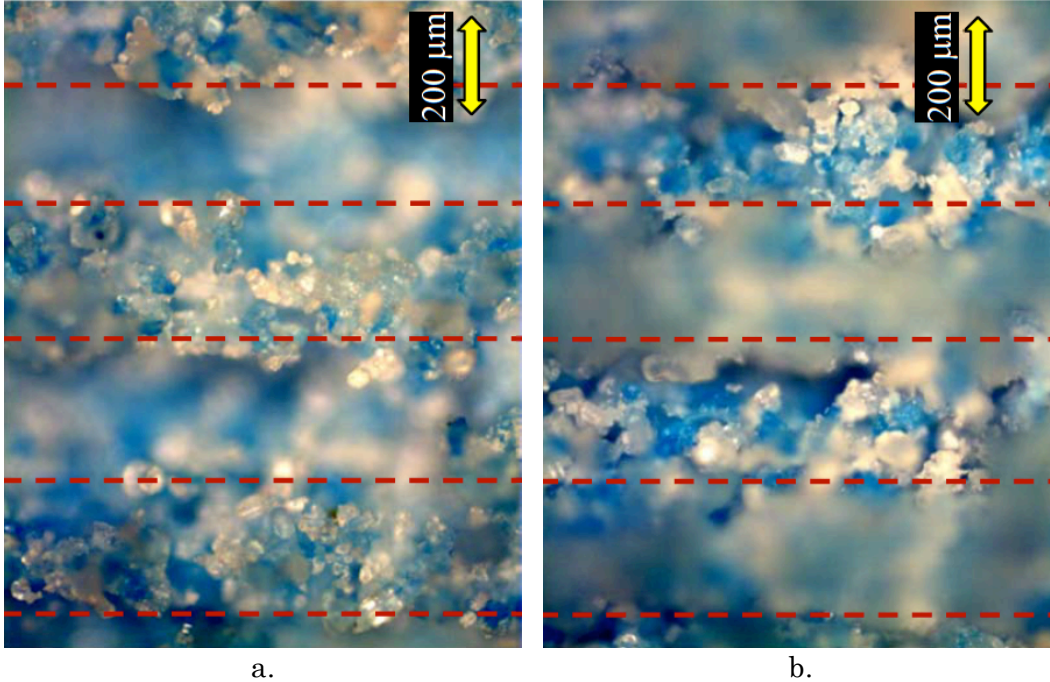


Figure 29. Section of a 3D printed sample under the microscope changing focus: a. peaks on focus, b. valleys on focus, from [45]

Another study suggested the use of image processing to examine internal structure of 3D printed parts [46]. Once again the imaging system proved effective to extract information from images taken every layer to monitor the process; however, the use of this information for control purposes was envisioned but not implemented. The implementation of the imaging system and one of the test targets used for the study can be seen in Figure 30.

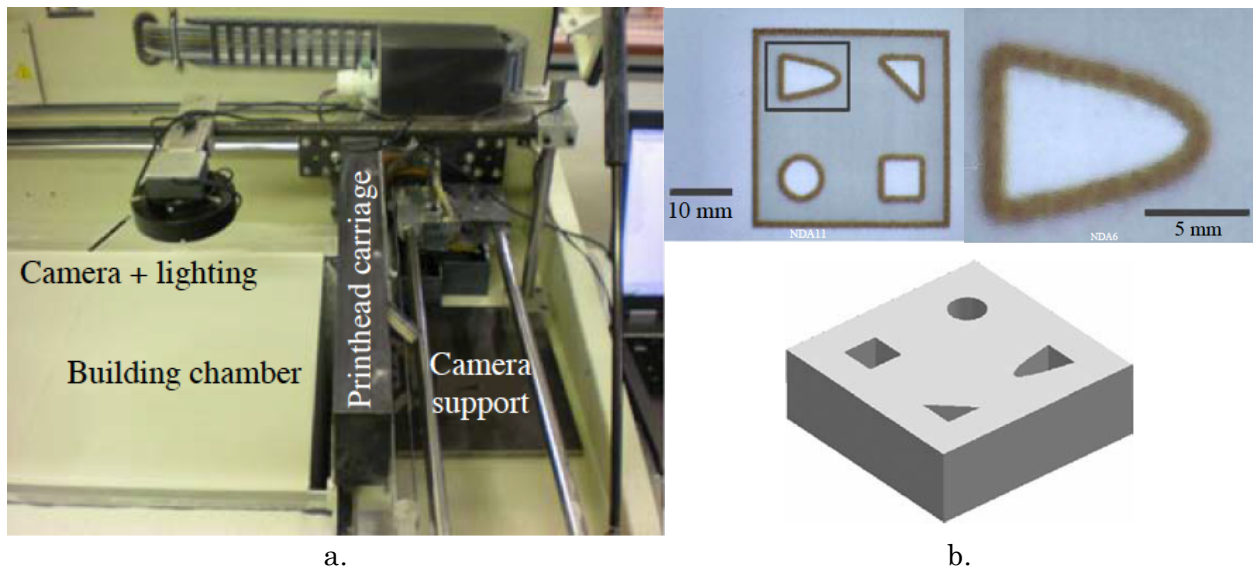


Figure 30. a. Vision system to monitor the 3D printing process, b. test target for one of the studies conducted, from [46]

Both of these studies were implemented on commercial powder-bed 3D printers. No control (or monitor) system has been reported that is implemented on an EP-based 3D printer.

In terms of the control strategy, the 3D printing processes impose a limitation to perform real-time control of the material deposited. These processes create a three-dimensional structure by printing multiple layers; each layer is created either by selectively depositing new material or by selectively binding the particles together. Acting on the material deposition process to control the amount of material at each location of each layer seems extremely difficult and impractical. Instead, the nature of the process suggests controlling it by layer or passes.

Traditional control methodologies (e.g. PID, modern control) do not seem well suited to handle the problem since they rely on a fixed reference (or a trajectory) over time which would have to be applied for every point (x,y) of the structure having a time scale dependent on the number of layers. An adaptive control strategy that would take into account the progress of the 3D print and process changes may be required [44]. A control methodology that seems promising for repetitive processes is Iterative Learning Control (ILC) in which the system learns from the performance of the previous iteration to improve and achieve the desired outcome [47]. This methodology has been developed further and major approaches have been summarized in various surveys [48, 49]. A particularly interesting track is Terminal Iterative Learning Control (ILC) in which only the end point of the system is tracked; this method has been applied to control deposition thickness of wafer fabrication [50] and thermoforming ovens [51]. Further developments have include multiple intermediate pass points to obtain better tracking [52].

2.4. Surface reconstruction by Image Processing

Extracting geometric information from images is a common need; in fact, our visual system does it constantly. The underlying principle is that light is reflected from a surface in two ways: specularly and diffusely [53] (see Figure 31). The specular reflection is the component of the light that gets reflected as if the surface acted as a mirror; therefore, the angle between the incident light (S) and the normal of the surface (N), is the same as the angle between the specular reflection (R) and the normal (N), following Snell's law. The diffuse

reflection is the component of light that is reflected in all directions from the surface of interest, as expressed in the Lambertian model [54]:

$$I_r = (I_s k_d / d^2) \cos(\theta) \quad (2.29)$$

where I_s is the point light source intensity, k_d is the diffuse reflectance coefficient, and d is the distance of view.

When viewing any point in a surface, the light reflected from the surface can be modeled as a mixture of both reflections, as expressed in Phong's model [53, 55]:

$$I_r = k_a I_a + \frac{I_s}{d} [k_d (N \cdot S) + k_s (V \cdot R)^m] = k_a I_a + \frac{I_s}{d} [k_d \cos(\theta) + k_s \cos^m(\gamma)] \quad (2.30)$$

where k_a is the ambient light coefficient, I_a is the ambient light intensity, k_s is the specular reflectance coefficient, and m is the shininess constant which is dependent on the material. Notice that d instead of d^2 is used as a common approximation.

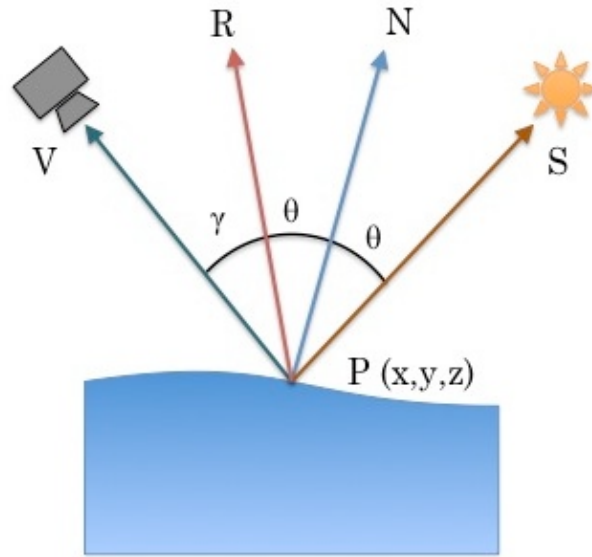


Figure 31. Light reflection model

Understanding the geometric relations between the elements (light source, surface, and viewing point) has allowed extracting information and reconstructing a three-dimensional model of the scene from two-dimensional images. The following are some of the most relevant methods that have been proposed to recover the surface structure by image processing.

2.4.1. Shape-from-Shading

This technique is based on inferring the surface structure from the shadows generated under one or several points of view or illumination conditions. The idea that the shadows convey information on the shape of an object has been around for a long time. One of the earlier efforts was to extract the topography of the moon from images in 1929 [56], and similar efforts were reported in 1966 [57]. These efforts use the shades on the Moon to extract features of the surface by modeling the light source position (the Sun), the viewing point (the Earth), and the reflectivity of the lunar surface. The singularities of those approaches were later summarized in 1975 by Horn [58] (who introduced the term “Shape from Shading” in 1970 [59]), and described more general solutions, explaining that the surface of the moon was just one application.

In 1999, a survey was carried on the most common methods for recovering shape-from-shading using single images with known light source directions [14]. Four types of approaches were identified: minimization of an energy function, propagation of the shape information from a reference point where the shape is known, local surface assumption, and a linearization of the reflectance map. Representative algorithms for each approach were tested with synthetic and real images, obtaining generally poor results.

For minimization of energy the work by Ikeuchi and Horn in 1981 [60], Brooks and Horn in 1985 [61], and Horn in 1990 [62], were some of the most representatives. For propagation, the seminal work by Horn in 1970 [59] and those by Dupuis and Oliensis in 1992 and 1993 [63, 64] were some of the most representatives. For local approaches Pentland in 1984 [65] and Lee and Rosenfeld in 1985 [66] used spherical point assumptions to recover the surfaces. Lastly for linear approaches Pentland in 1988 [67] and Tsai and Shah in 1994 [68] used linear approximations of the reflectance to recover the geometry. Some algorithms performed better for smooth, simple images (like a vase) but ultimately failed for real, more complex images like a human face (see Figure 32).

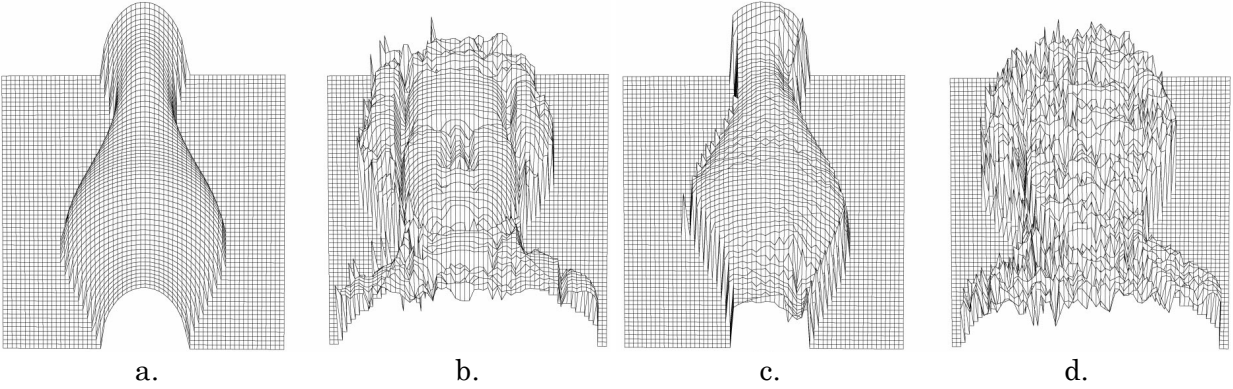


Figure 32. Surface reconstruction of synthetic images Vase and Mozart using a local approach (Lee and Rosenfeld's method) having light source at $(0,0,1)$ for (a. and b.) and $(1,0,1)$ for (c. and d.), from [14]

Prados and Faugeras [69] also presented a review of the most common approaches to solve SFS from one image, in particular implementing propagation by numerical methods and partial derivatives equations, showing some promising results. They particularly explored viscosity solutions to the Hamilton-Jacobi equations [70], since they guarantee the existence of (weak) solutions but have difficulties with the boundaries of the image that were later addressed by singular discontinuous viscosity solutions (SDVS) [71]. More importantly, it is acknowledged that from a single image, the problem is ill-posed and there is no unique solution, there is room for ambiguities and errors based on the assumptions used to recover the information, especially in the dark areas (or shadows), because very little information is being gathered from those regions of the image and important features of the surface may be lost; however, under certain conditions like knowing the distance of the light source to the object, the problem becomes well-posed [72].

On the other hand multi-view and stereo approaches have been successful in recovering the shape and texture of an object. Approaches like the one presented by Jin et al. in 2008 [73] performed scene reconstructions under the assumptions of unknown illumination conditions, while Yoon et al. in 2009 and 2010 [74, 75] considered known illumination, and Prados et al. in 2009 [76] considered ambient lighting. Having known illumination provided better results and proved that applying shape-from shading methods to multiple views of a scene was not a trivial problem. A successful approach to combine stereo vision and shape-from-shading was presented by Chenglei et al. in 2011 [77] in which the reconstruction is performed under arbitrary illumination conditions.

2.4.2. Shape-from-Focus

This technique was introduced by Nayar in 1989 [78] and developed further by Nayar and Nakagawa in 1994 [15], relies on creating a height map of the surface by changing the focus plane on the camera and determining the areas that are sharper (see Figure 33.a.). The change of focus is done in a systematic way that reflects in increments Δd in the height/depth of the element to image. For each point, the "best focus" is found and the respective height is assigned either by directly taking the distance that produced that "best focus" or by Gaussian interpolation, creating a height map. Complementarily, Noguchi and Nayar in 1994 [79] used structured lighting to enhance the detection of focus in very smooth surfaces.

The measure of quality of focus is perhaps the biggest challenge of this technique. An operator was proposed in [15] that respond to high-frequency variations, a high-pass filter, for which the sum of a modified Laplacian was ultimately selected. It evaluates the quality of focus for each pixel by analyzing a small neighborhood at each location. Results showed a good reconstruction of the surface imaged, especially after performing Gaussian interpolation (see Figure 33 b. and c.), but highlighted that the effectiveness of the method depended on the depth of field, the surface texture and the resolution of displacements Δd . It was also noted that it required a fine control of the focus plane, for their implementation an electronic microscope was used (Nikon Alphaphot-2 microscope and CCD camera) and the z-axis of the microscope was driven by a stepper motor with a resolution of 0.02 μm .

Since then multiple approaches have introduced other metrics for focus. In 2009, Shim et al. [80] proposed the use of not only neighboring pixels on a given frame but on adjacent image frames to establish the focus level. In 2011, Minhas et al. [81] proposed the use of the fast discrete curvelet transform (FDCT) to establish the high frequency content of the image. Lee et al. in 2013 [82] explored the effect of the window size used to evaluate the focus level on an image.

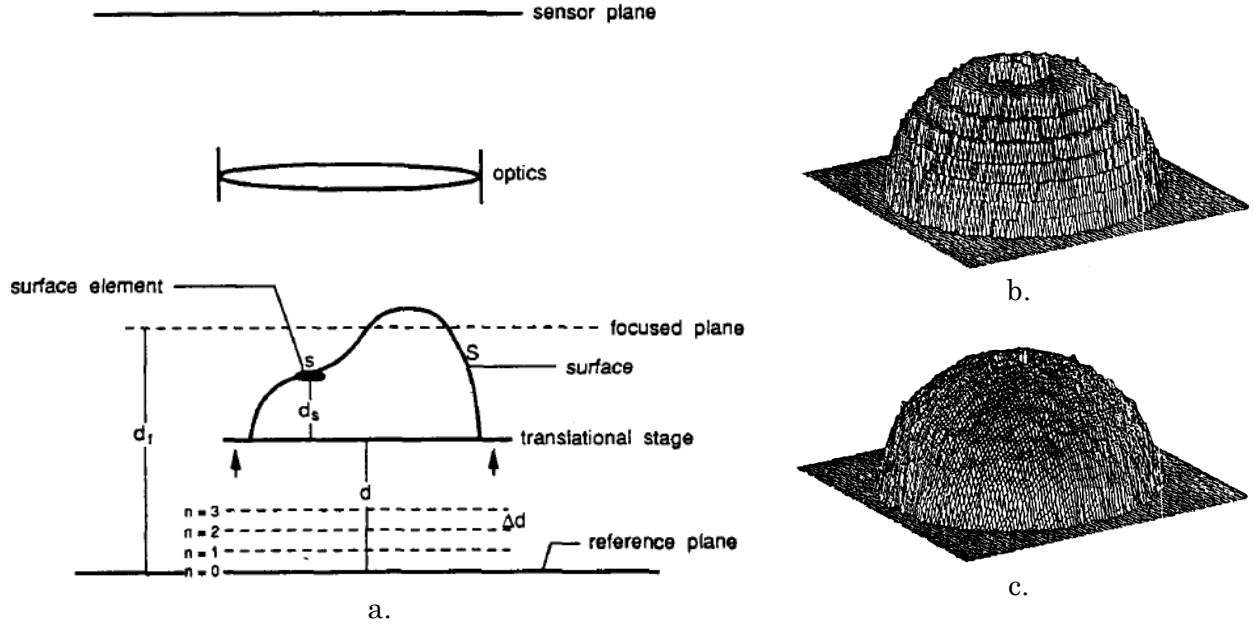


Figure 33. a. Conceptual diagram of the shape-from-focus methodology; Surface reconstruction of a ball by direct assignment of height (b.) and Gaussian interpolation (c.), from [15]

Pertuz et al. in 2013 [83] presented an analysis that cover thirty six focus measure operators grouped in six different types, used for shape-from-focus: gradient-based operators, laplacian-based operators, wavelet-based operators, statistics-based operators, DCT-based operators, and miscellaneous operators. The first two groups rely on finding edges on the image through the use of the first or second derivatives of the image. The wavelet and discrete cosine transforms (DCT) approaches try to establish the high frequency content of the image and in this way the areas at focus. The statistic operators use image statistics as texture descriptors that allow then computing a focus level. In the end, Laplacian-based operators seem to performed better under general conditions while the others were better suited for particular conditions of noise, contrast, and/or saturation and therefore particular capturing devices.

2.4.3. Shape-from-Specularity

Previous approaches had used or assumed lambertian properties for the surface and the specular component has been neglected or treated as an undesirable effect that occludes the underlying surface. Healey and Binford in 1988 [84] and Blake and Bulthoff in 1991 [85] did the seminal work in which the specular reflection was used to uncover the geometry of the surface. Rather than treating specular reflections as anomalies, Chen et al. in 2006 [16]

proposed to recover the surface normals by identifying the light direction and the viewing angle for each pixel at which maximum reflectance is observed. This derives from Snell's law and the law of specular reflection which tell us that the light reflected (specularly) on a surface forms an equal but opposite angle from the normal than the incoming light (see Figure 31). This implies that if the viewing angle is fixed and the direction of a single illumination source can be determined, one can recover the surface normal for those points where the maximum reflection is observed.

This method works particularly well for non-lambertian surfaces where the specular reflection is dominant. In [16], the light direction is estimated from four spheres placed in the scene, and the light source is moved around to cover different illumination angles while a camera records the scene (see Figure 34). The method proposed, then analyzed each frame for the brightest pixels and determined the light direction to infer the normal direction of the surface for those pixels. At the end, a normal field of the surface can be created from where a 3D surface model can be constructed.

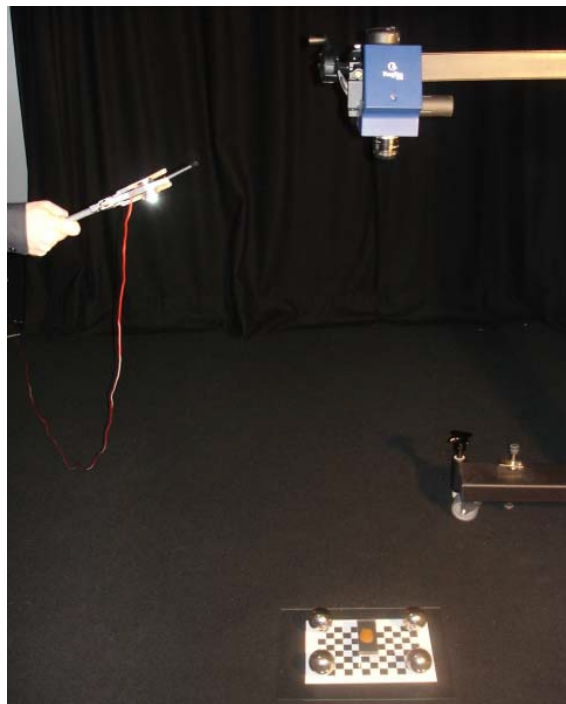


Figure 34. Set up used to reconstruct structure from specularity, from [16]

The methodology was tested with orange skin (see Figure 7), chocolate, human skin, dried apricot, jelly candy and black leather, showing good reconstructions in all the cases, although the jelly candy proven more difficult for being translucent. This approach was

further explored by Francken et al. in 2008 [86] showing an improvement in speed and resolution of the reconstruction.

Other approaches have exploited the specular reflections to extract the shape of an object by providing known environments and analyzing the distortions on the reflection on a specular surface [87, 88].

2.4.4. Reflectance Transformation Imaging (RTI)

The method referred as Reflectance Transformation Imaging (RTI) consists in taking several images under different lighting directions and extract information on how the surface shape and color changes. A model of the surface is created and it allows for interactive visualization in which other lighting conditions can be recreated [89]. This technique has been used to aid the visualization and study of artistic and cultural pieces, revealing multiple details that are otherwise lost in single image analysis.

The method is based on Polynomial Textural Maps (PTM) [90], which recover the normal information of a surface imaged under different illumination conditions and records a model of it for each pixel of the image along with the color information. Having the surface normal allows for simulating how the surface would react to light coming from any direction, and multiple image enhancements that enable further analysis of objects. An example of an image obtained/enhanced with this method is shown in Figure 35.

The Cultural Heritage Imaging (CHI), a nonprofit corporation, has been promoting this technique, using it for multiple studies, and improving the algorithms. They provide guides and open-source software to capture, compile and visualize RTIs on your own [89] with a basic setup that includes a DSLR camera, reflectance balls to determine the light direction and an external light source.



Figure 35. RTI representation of the Sennedjem Lintel, with color information (bottom) and specular enhancement (top), from [89]

2.4.5. GelSight

A team at MIT working on surface reconstruction acknowledge that the reconstruction process would be much simpler if the entire surface was from the same material or had known reflectance properties. This observation motivated the development of a sensor that used a translucent gel as an interface to image a surface. One side of the gel would be coated with a known material of well characterized reflectance properties, and at the other side a detector would image the surface. The gel, being compliant, would adapt to the surface topography, and light sources would shine through the gel from three different angles to capture different shades that allow for the surface to be reconstructed. The results from this system were reported in 2009 [91], and further improvements were shown in 2011 [17], in which a new composition for the coating using silver powder (vs. metal-flakes) allowed for better resolution of approximately 1 micron. This work has resulted in a start-up company called GelSight (www.gelsight.com) that is currently seeking to develop further this system towards commercialization. Two different configurations for the system as well as sample images can be seen in Figure 36.

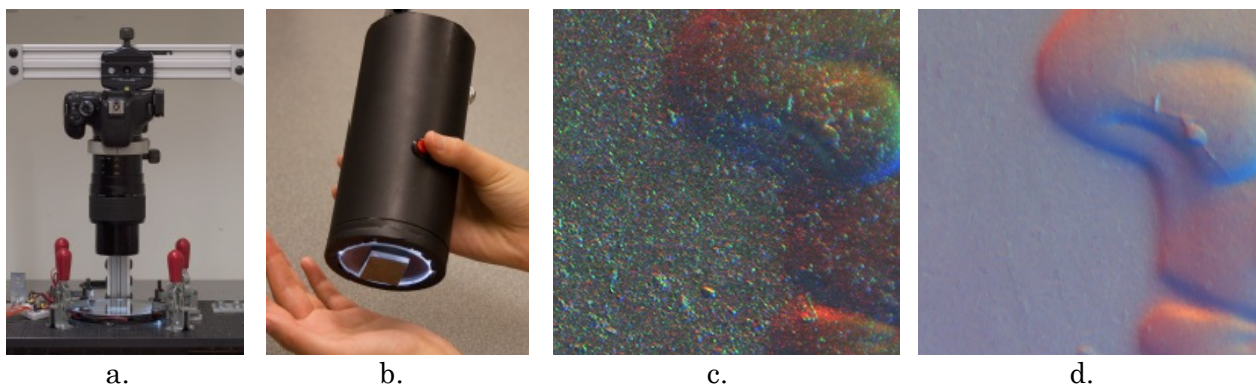


Figure 36. GelSight system configurations: a. Bench-top, b. Portable; Samples of reconstructed images, detail of a US quarter coin: c. Using metal-flake coating, d. Using silver powder coating, from [17]

Chapter 3. RESEARCH OBJECTIVES

From the literature reviewed, it seems clear that there are still many factors to consider before achieving a reliable EP-based printing process. This section reviews the most significant challenges that were identified and establishes the scope of this research work by defining the areas where contribution is expected.

3.1. Identified challenges to overcome towards EP-based 3D printing

Many technical challenges still prevent the commercialization of EP-based 3D printing. The most prevalent issues identified from the literature review are:

3.1.1.1. Transfer of new material as the part grows thicker

The main concern is being able to continuously stack layers beyond the limited number achieved so far. The limitation is inherent in the self-insulating nature of the process (see Figure 3), which prevents the use of electrostatics to transfer particles or to charge the surface after a given thickness has been achieved. This characteristic suggests that an intermediate step is required in which the new layer is transferred from the photoreceptor to a support structure which can be used later to transfer the new layer onto the stack by mechanical means (heat and pressure).

Although this approach has been suggested since Bynum's patent in slightly different forms, there has not been a successful implementation yet that can reliably achieve thick parts.

3.1.1.2. Achieving a smooth surface

As it was noted in the literature review, all attempts to produce 3D parts with EP have experienced surface defects. It is still unclear why the surface defects appear; it seems like the stochastic nature of the EP process produces irregularities that are amplified as layers accumulate. Other factors may also contribute, like the residual charges on the surface

which may prevent some particles or regions of toner to transfer, or the halftoning patterns which may produce non-uniform layers.

Some of the approaches to date have proposed a compaction step or preheating the surface to facilitate transfer and to smooth the surface but with partial success; however, ultimate control of the surface topography has yet to be achieved.

3.1.1.3. Appropriate materials to use

Another concern that has been identified is the selection of materials to use that would produce desired characteristics in a part. This involves selecting the powders to form the part and to act as support material, the appropriate particle size distribution, the material for a base substrate or platform on which the part can grow, the material for the intermediate support of new layers that allow for mechanical transfer, etc.

3.1.1.4. An automated implementation

Some of the test-beds that have been used by the different research groups have a certain degree of automation but they have shown limited successes, and in some cases the results have been worse than those obtained manually. In order to have a successful EP-based 3D printing implementation, an automated system is required that can register the successive layers and is able to compensate for the surface defects.

3.2. Scope of Research: Areas of contribution

After reviewing the most significant challenges to overcome, the following areas were identified as the areas to focus this research effort towards the goal of enabling EP3D printing:

3.2.1. Surface defect characterization

Understanding how the surface defects appear is an important step toward a successful implementation of EP-based 3D printing. Identifying the effect of each main factor of the process on the surface of the print enables the establishment of the appropriate methodology to produce samples and to select materials and operating conditions. A proper understanding and description of how the surface defects form and evolve as more layers are aggregated would provide insights into what the best strategy to compensate for them may be.

3.2.2. Modeling of EP3D printing for control

There has been no model of the EP3D printing process reported in the literature so far. The models found in literature for traditional EP printing are mainly focused on the development of solid areas and they are static, limited, and rely heavily on parameters found experimentally. These types of models are not well suited for use in control. Instead, a dynamic model that captures the evolution of the 3D print as a function of time would enable the design of a control strategy. This model would be specific to a given hardware, but many of the principles used to derive it may apply to similar systems.

3.2.3. Development of preliminary control strategy for EP3D printing

Traditional document printing and 3D printers work in open loop; there is no direct feedback on the amount of material being deposited or the quality of the output. The development of a control strategy for the overall EP3D printing process would provide a mean to overcome intrinsic difficulties and open the door for closed loop systems in 3D printing.

3.2.4. Surface imaging for compensation of defects

In order to correct the surface defects, being able to detect them is key. However, it is also important to do it in a way that it can be integrated into the process without significant disruption to the process. The development of an image-based sensing system, capable of detecting the irregularities in the surface from multiple frames captured under different illumination conditions, seems feasible given the approaches reported in the literature. The identification of areas where more material/toner is required would enable a compensation system that ultimately leads towards uniform surfaces and appropriate reproduction of three-dimensional parts.

Chapter 4. RESEARCH METHODOLOGY

This chapter describes the methodology used to achieve the research objectives set in the previous chapter. An overview is presented in the research roadmap in Figure 37. A detailed description of each major track is presented in the following sections of this chapter, identifying the major tasks and milestones.

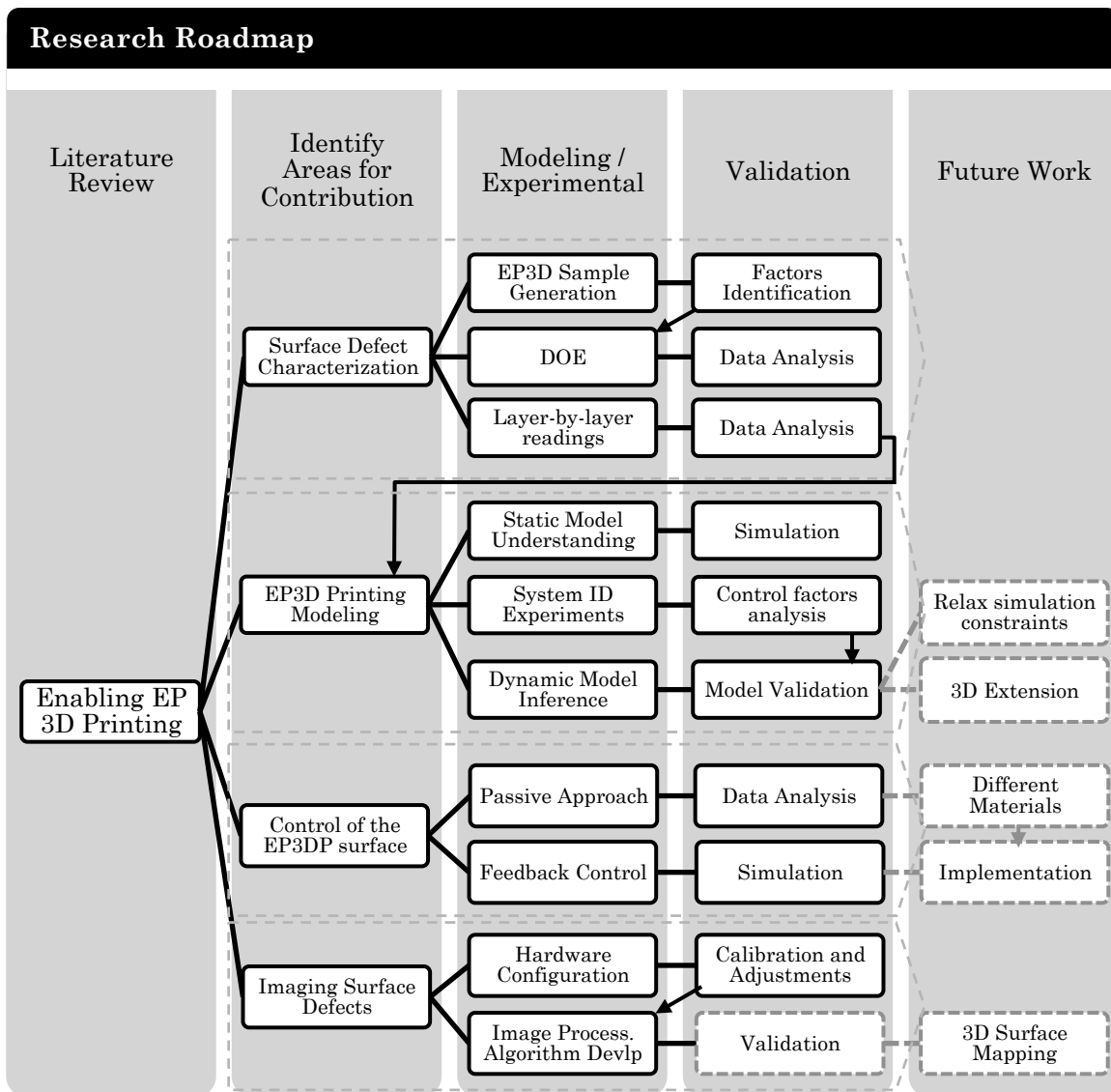


Figure 37. Research Roadmap

4.1. Surface defects characterization

An experimental methodology was used to perform the characterization of surface defects in EP-based 3D printing. The theoretical foundation for EP was reviewed and summarized in section 2.1; however, the interaction of multiple layers of toner is not well understood. An empirical approach was used to gaze into the details of what factors affected the surface topography and how the surface defects develop.

4.1.1. EP3D Sample Generation Methodology

The first endeavor of this track was to establish a methodology to create samples and ultimately to create EP3D prints. The methodology needed to circumvent the self-insulating nature of EP reported in literature and provide consistent results even if the implementation require manual steps.

4.1.1.1. Preliminary tests and establishment of methodology

In the first trials in which surface defects were observed, a pattern changing from pure cyan to pure magenta was printed. 15 and 25 layers were accumulated in two different samples, observing how the surface defects amplified as the number of layers increased. Different factors were proposed as the reasons for the surface defects to appear, ranging from charging issues to halftoning. Nonetheless, the samples provided encouraging results since the transfer of material occurred consistently, showing that the methodology for generating samples was effective.

4.1.1.2. Main Factors Identification

The preliminary tests for EP3D printing were done with complex patterns that varied many factors, making it difficult to identify why surface defects appear. More controlled tests were done to reduce the complexity of the process and to be able to gather meaningful data. This exploration phase indicated which factors affected more the surface of the 3D print and which direction to pursue for further research.

4.1.1.3. Surface Measurement

In order to characterize the surface of the EP3D prints and the defects observed on it, it was necessary to establish ways to measure the surface. Multiple contact and non-contact alternatives were evaluated until reaching a consistent methodology that provided sufficient data for further analysis.

4.1.2. Design of Experiments (DOE) approach

The factors highlighted by the exploratory phase were investigated further following an experimental approach. The experimental design allowed studying the effect of four factors on several aspects of the 3D print as the number of layers increased. The conclusions from this work validated assumptions and observations from the preliminary experiments with EP3D printing while pursuing the identification for optimal operating conditions that could lead to a more automated implementation.

4.1.3. Layer-by-layer measurements

The ultimate goal is to be able to understand how the surface changes as the number of layers increase. Data gathered from previous experiments were taken at the final structure or after 10 layers had been deposited, making it difficult to clearly see how the surface evolved. Taken measurements of the sample at every layer as more layers were built would enable to characterize better the process and understand the evolution of the surface. Further analysis was done on the surface profiles to extract the frequency response and model how the particles interact as the part grows thicker.

4.2. Modeling of EP3D printing for control

Modeling of any EP system for control purposes is a daunting task if the right supporting tools and expertise are not available. For this reason, the modeling of development systems relies on the vast expertise in EP in the greater Rochester area and the information available in the literature to form a knowledge base in EP that facilitate the understanding of the factors involved in the development of toner for powder marking.

4.2.1. EP Development static model understanding and simulation

Dr. John Knapp and Dr. Shu Chang, former Xerox scientists, have provided insights into the physics and material properties of the different components involved in the EP printing process. Particularly for the development phase, a detailed static model of a magnetic-brush two-component development system (see section 2.1.2.1) was shared and explained by Dr. Knapp. An understanding of this model and the many factors involved, as well as being able to replicate the results by simulations in Matlab, provided a base ground to continue the research in this area.

4.2.2. Dynamic system identification experiments and model inference

A broader look was taken to establish a model of the overall EP3D printing process; the measurements taken layer-by-layer provided insights into the probabilistic nature of the process. Analyzing also the progression of measurements shed light into ways to develop a model for how the layers stack together forming the 3-dimensional structure. The transfusing step had been identified as critical for the surface; a dynamic model of the fuser was developed and incorporated into the overall EP3D printing model. The parameters that characterize the fuser were established through direct and indirect measurement and by analyzing the system response to a known input of a series of steps, captured using pressure sensitive paper. The model developed was coded into Matlab to allow for tuning, further refinement, and simulation.

4.2.3. Model validation

The results of the simulations with the model developed were validated against the datasets of the layer-by-layer measurements. Part of the dataset was used to tune the parameters of the model to match the conditions of the process in which real samples had been created. The remaining of the dataset was used to verify the consistency of the results. Other samples measured only at the final stage were used for further verification.

4.3. Preliminary control of the EP3D printed surface

Most printing systems do not control the final output in terms of amount of material deposited nor compensate for surface irregularities, relying only on local controllers of the various process variables. For EP3D printing, early on the characterization of surface defects, it became clear that a control strategy was needed in order to achieve a satisfying surface quality, otherwise the surface defects would inevitably appear.

4.3.1. Passive approach based on a more compliant interface

Previous trials demonstrated that having a more compliant interface for transfusing was desirable; therefore, a material from a transfuse belt of an HP indigo printer was selected as an interface for transfusing. Samples of up to 100 layers were constructed exhibiting a much smoother surface; however, the transfer efficiency decreased significantly and the heat transfer through the thick interface was much more difficult. The process became much more labor intensive requiring to preheat each layer and to clean the interface

afterwards from residual toner. A different material may be needed to improve both the transfer efficiency of the layers which would also helped with the cleaning process, but also the heat transfer necessary to achieve fusing.

4.3.2. Feedback control

A two-passes approach was proposed in which after printing each layer the surface is evaluated and a compensation layer is also printed, intending to correct imperfections by depositing material in the locations where it seems needed.

Nonetheless, the control of the surface implies sensing it to provide feedback on the current state of the surface to take a corrective action. A contact profilometer provides only a line profile of the surface; commercial 3D scanners do not provide enough resolution to be useful at the scale of the process; confocal microscopy provides great detail on a very limited region. Furthermore, many of these processes are prohibitive in terms of cost, time or methodology to be considered for a future commercialization of an EP3D printer. Image-based sensing seems like a promising alternative and an exploration of this approach constituted another area of this research. However a solution for the specific needs of the process has to be developed and a proper way to validate the results is still needed.

Having the limitation on sensing the structure, the simulation model not only provided a starting point for the design of the controller but also a quick way to demonstrate the effectiveness of the control strategy. The implementation of the control strategy fell out of the scope of this work and would depend on establishing a sensing strategy and validation.

4.4. Surface imaging for compensation of defects

Since the ultimate goal for an EP-based 3D printing system is to be commercialized, an image-based sensing seems like the most reasonable way to detect imperfections and extract information that would enable a compensation method. Different imaging techniques have been proposed to estimate the structure of a surface. Shape-from-shading and shape-from-specularity seem particularly applicable to the research task at hand.

4.4.1. Preliminary testing and hardware configurations

The main objective is to be able to sense the surface defects and determine accurately regions that require the addition of further material to compensate and make the surface

smooth. A full reconstruction of the surface is beyond the scope of this research. A fixed camera and various illumination conditions seems the most appropriate strategy to perform this task. Several configurations were tested, especially in regard to type of illumination needed, number of images to capture, and position of the light source (see Figure 38).

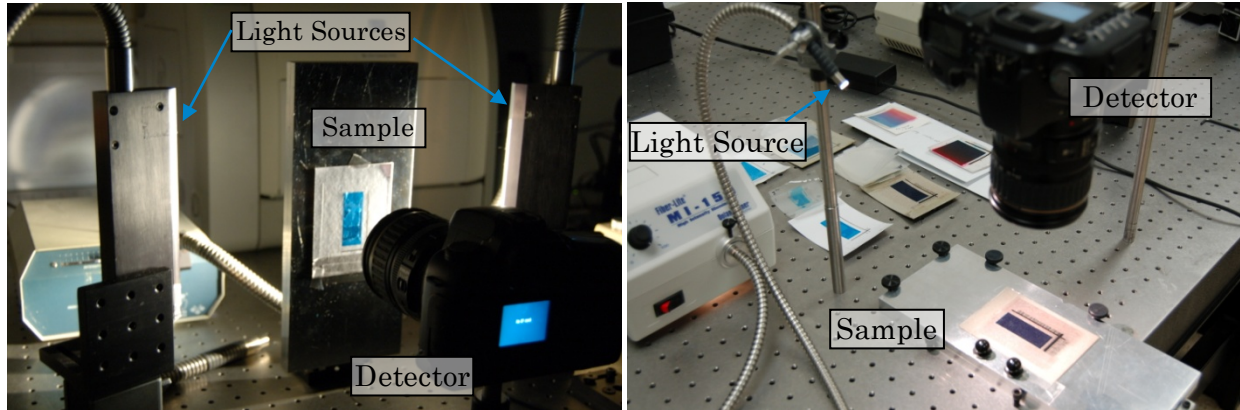


Figure 38. Initial configurations for image based sensing: a. Two side linear illumination, b. One point source used at different positions

4.4.2. Image Processing Algorithm Development

Based on the literature review, a few alternatives for shape-from-shading and shape-from-specularity seem to have provided good results for shape reconstructions on larger scale than the required for EP-based 3-D printing. Gel-sight [17] and RTI [89] have shown real applications in which the visualization of certain objects have been aided by taking several images under different illuminations and reconstructing the surface normals. Therefore, an appropriate strategy is needed and the development of the image-processing algorithm that would enable the detection of the surface defects. The output of this algorithm may serve for control purposes of the layer uniformity, identifying areas where more material is needed.

4.4.3. Validation

The accuracy of the estimation can be determined by comparison to surface measurements taken by contact methods. However, contact methods (e.g. profilometer readings) take readings over a line of the surface while the image-based approach sense the entire area at different resolution, making the comparison extremely difficult. Third party sensing was done using Gel-sight and served as a starting reference. A more rigorous measurement is being explored for future stages with special equipment for 3D surface analysis such as a

Nanovea optical profiler in collaboration with Professor Andres Carrano from Auburn University (former RIT Professor).

Chapter 5. SURFACE DEFECTS CHARACTERIZATION

This section presents the work done to characterize the surface defects reported in literature and observed in preliminary tests of EP3D printing.

5.1. EP-based 3D Printed Sample Generation Methodology

As mentioned throughout the document, early feasibility tests were carried out to produce multilayer samples printed through EP in order to verify the results reported in literature. Samples of 15 and 25 layers were created (see Figure 39) and a process was defined for successful EP3D printing. The process consisted on printing an un-fused pattern on a sheet of silicon coated Mylar using a HP LaserJet 4700 printer where the fuser has been disabled. The sheet of Mylar was placed on top of the substrate (for the first layer) or the previous layers and was temporary secured to prevent relative movement. The sample was fused in a fusing station (see Figure 19.b.) achieving transfer of material from the Mylar sheet onto the stack of layers. This process of transferring while fusing is also referred as transfusing.

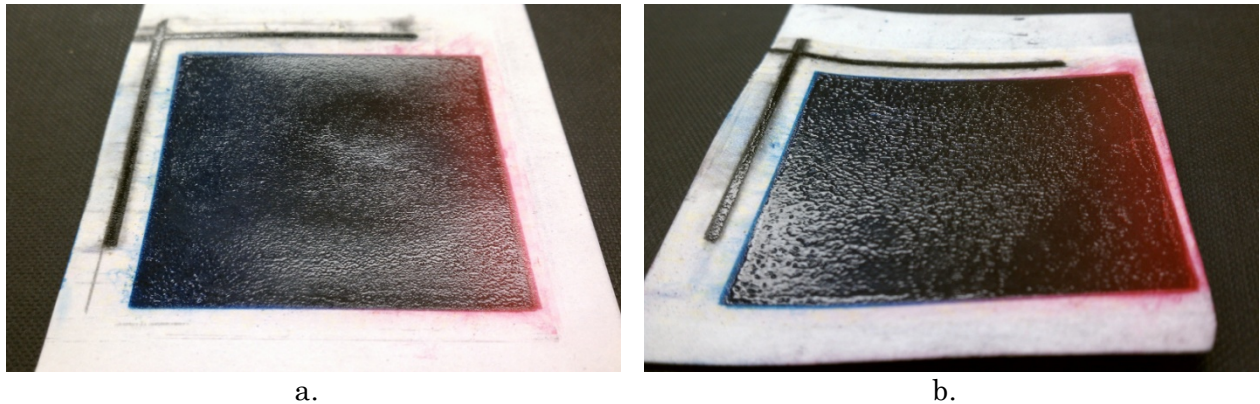


Figure 39. Preliminary testing for EP-based 3D printing: a. 15 layers, b. 25 layers

Using the Mylar sheet as an intermediate step has avoided the inherent limitation of the decay of the electric field for transferring particles as the number of layers increase. However, significant curling of the sample has been experienced as a result of the substrate going through the fusing station multiple times. Another important issue in this approach has been the manual registration of multiple layers. So far only manual care has been

employed to place and secure the Mylar sheet on top of the previous layers before sending it through the fuser. Registration marks are printed each time to aid the process but ultimately an automated process is required in order to achieve better results.

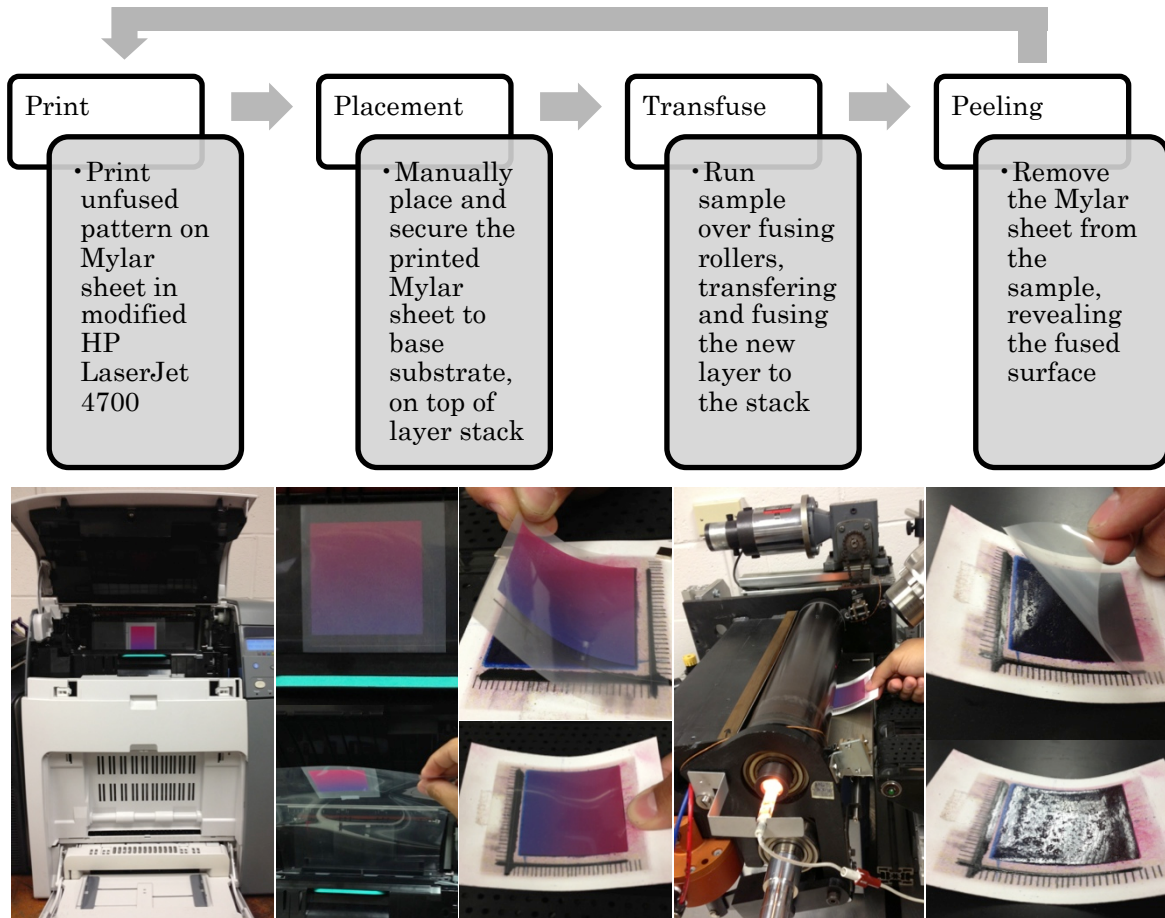


Figure 40. EP3D printing sample generation methodology

Subsequently, multiple samples were printed on different base substrates, having one or two toner colors, solid fills or graded transitions between colors. These exploratory trials reached heights of up to 50 layers. The results varied significantly but ultimately showed that surface defects appear on the sample regardless of the configuration. Some of the samples printed can be seen below:

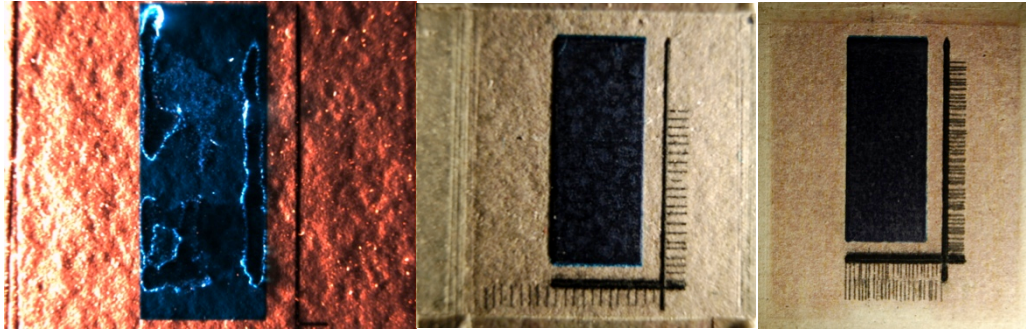


Figure 41. Printed samples from initial testing (3, 20,50 layers)

5.2. Surface measurement

Multiple methods were tested for measuring the surface and follow the surface defects. The first method to try was a laser profilometer that took measurements as the sample moved in a linear slide controlled by a stepper motor (see Figure 42).



Figure 42. Initial set-up for surface measurements with laser profilometer

Three main issues arose with this method: noise, aliasing and light reflection artifacts. The first one was related to the way the sensor was providing the data to the computer, the sensor was transmitting the data through serial connection that was interpreted in the computer as keystrokes which in many cases cause missing data and losing resolution. In Figure 43, three different readings of the same surface can be seen. Note how trial 2 is much shorter even when the readings were taken under the same conditions. Note also the difference in readings for the same sample.

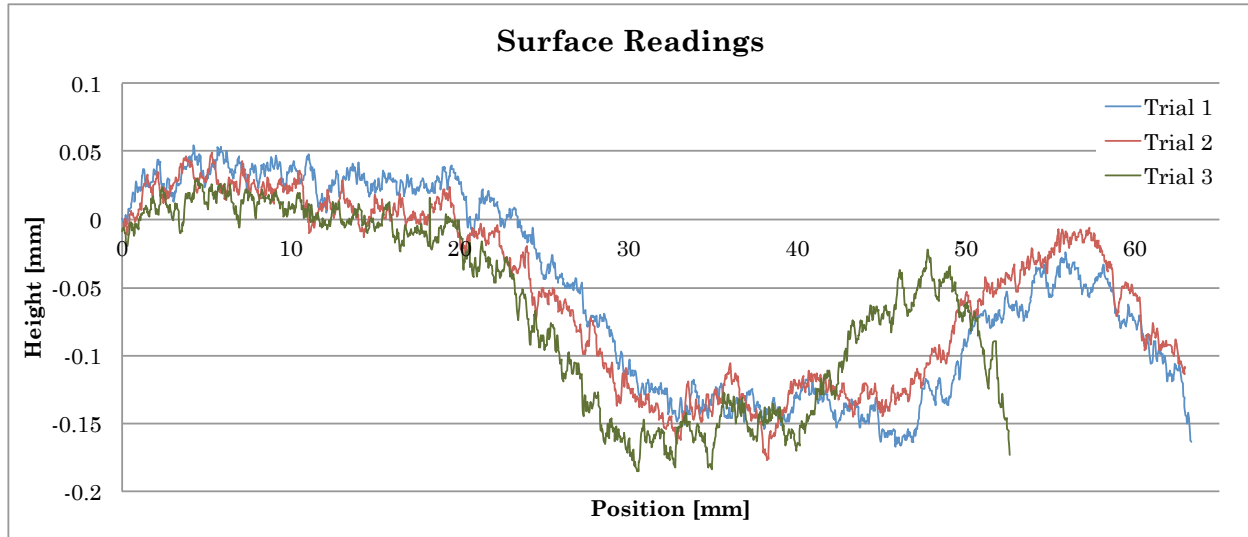


Figure 43. Initial trials of surface readings with laser profilometer

This issue was solved by changing the connection between the sensor and the computer. The sensor provided an analog output that was read through a data acquisition card (DAQ) NI USB-6009 that enable to take readings much faster and reliably. Figure 44 shows a set of readings taken with the new set-up. Note how the readings are much more consistent.

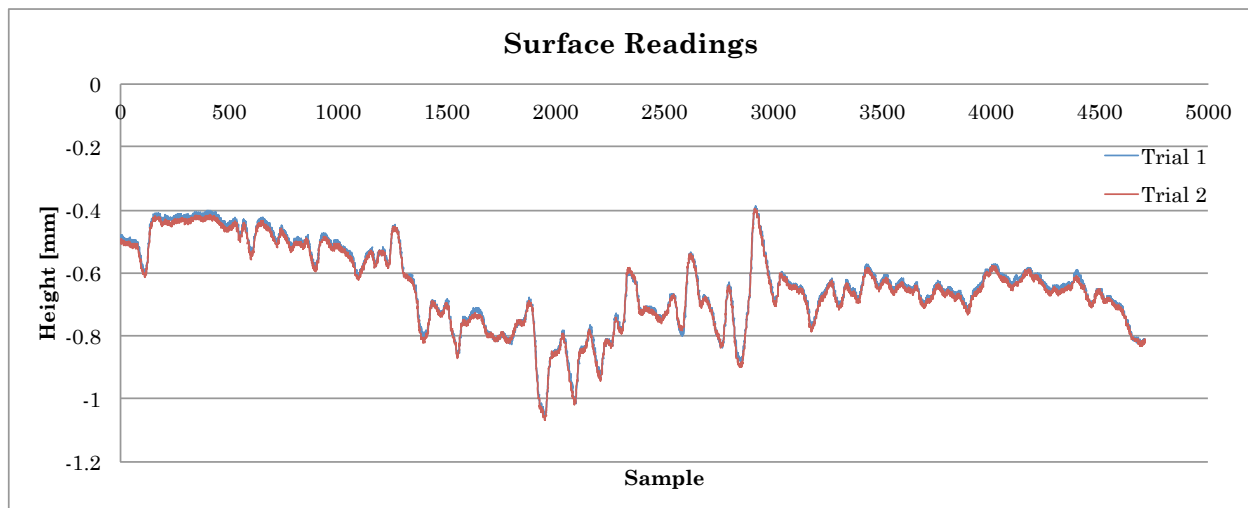


Figure 44. Trials of surface readings using the NI DAQ

The second issue was related to the sampling frequency used with respect to the speed of the motor. Readings appeared to contain a low frequency sinusoidal type of interference that quickly pointed towards the aliasing effect. The speed used for the stepper motor was reviewed and the sampling frequency was adjusted to the Nyquist frequency to avoid aliasing. Figure 45 shows readings taken after those improvements.

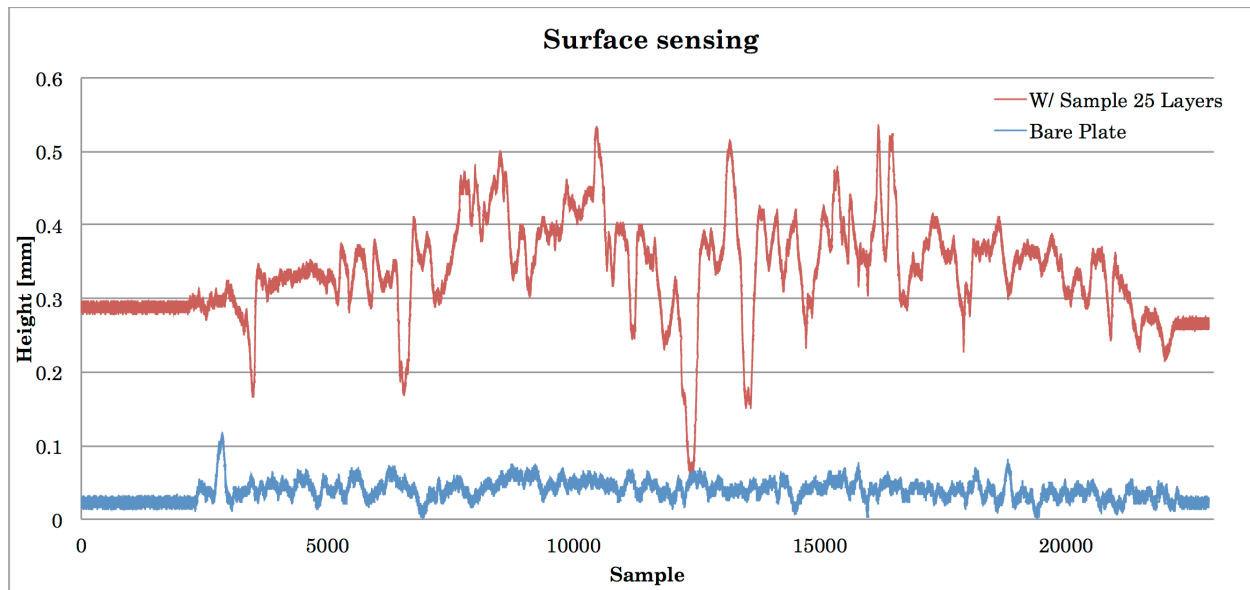


Figure 45. Trials of surface reading comparing a bare plate and a 25-layer sample

Although the readings were much more consistent and did not exhibit aliasing, random peaks and dips were evident that did not seem to correlate with reality. Note how in Figure 45 a pronounced dip in the center suggested a hole in the sample which was not there. Further examination suggested that the peaks were artifacts due to the light from the laser bouncing at the surface and interacting with it, especially where edges were present.

After experiencing disappointing results with the laser profilometer, a contact profilometer was used to measure the surface (see Figure 6). A Mitutoyo Surftest SJ-401 was used to take readings. The instrument has a stylus tip that slides on top of the surface as it retracts towards the body of the instrument, recording the variation in height. It has a maximum range of travel of 25 mm, therefore only a section of the original samples of 25 layers (50 x 50 mm) was recorded at each time. Figure 46 shows three initial trials of measuring the surface on a section of the 25-layer sample. Notice how much variation is observed in the readings. One source of variation in the readings is the lateral travel of the stylus as is moving through the surface. Although it is clear that some shift of the data may place them on similar planes and relative comparisons could be done, there are many other shifts and variations, particularly evident in trial 3, that suggest that this instrument required calibration and perhaps repair.

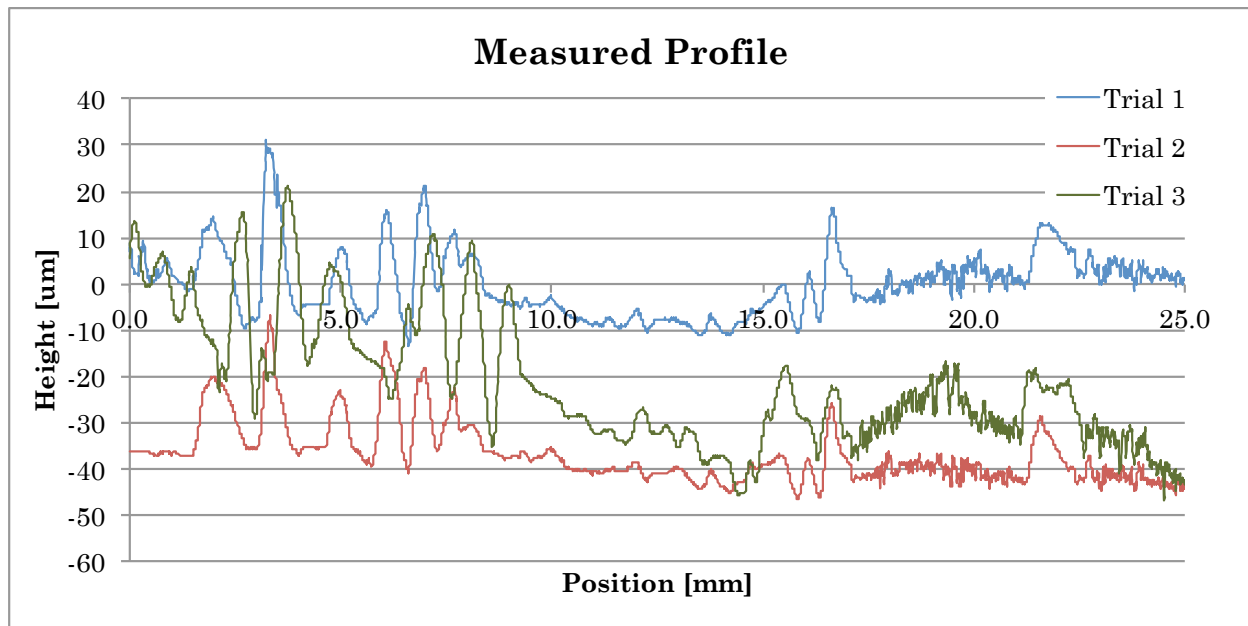


Figure 46. Surface measurements using a Mitutoyo SJ-401 contact profilometer for the 25-layer sample

The Mitutoyo SJ-401 contact profilometer was sent for calibration and repair; however, it was determined that it could not be repaired since the model had been discontinued from the market several years ago and the repair parts were no longer manufactured. This forced to replace it with a newer but more compact instrument, the Mitutoyo SJ-210; the new instrument provides a measurement travel range of 16 mm instead of 25 mm and a sampling resolution of 1.5 $\mu\text{m}/\text{sample}$. Those specifications provided confidence in the measurements since the toner particles are larger than the resolution and the travel was long enough to capture low-frequency variations on the surface. The device also included a USB interface and controlling software that enables exporting the measurements into excel that made easier the data collection process.

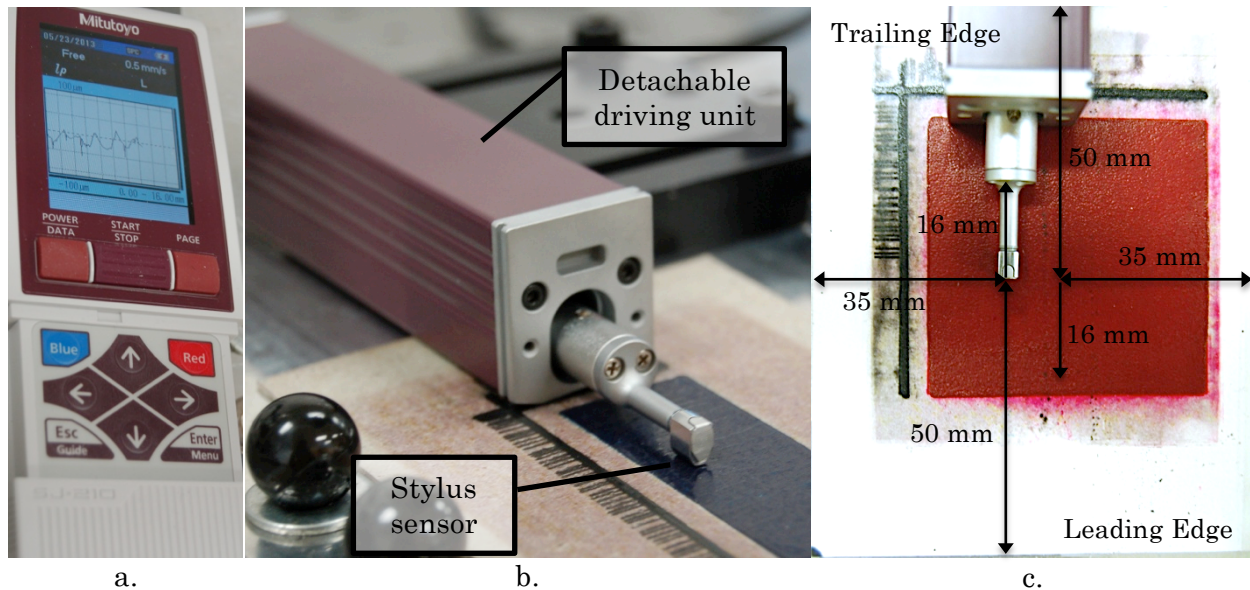


Figure 47. Measurement of a EP3D printed sample with the Mitutoyo SJ-210 profilometer a. handheld instrument; b. driving unit and sensor; c. 16 mm measurement paths for leading and trailing edges

5.3. Design of Experiment (DOE) Approach

Although the preliminary tests showed significant surface defects, the patterns used and the unstructured testing made it difficult to investigate if the defects appeared only because multiple layers were stacking, or because two materials were being combined (cyan and magenta toner), or because of the base substrate chosen for the tests, or because the halftoning patterns were creating more complex, non-uniform structures.

5.3.1. Experimental Design

From the preliminary tests it seems like the most significant factors that affected the surface under the current approach were:

- Number of layers
- Base substrate
- Number of materials / colors
- The use of halftoning

As result, the experimental design consisted of five control parameters and five dependent response parameters. The control parameters consisted of the number of layers at three levels (10, 20, and 30), substrate type at three levels (paper, cardboard, metallic paper), the number of materials printed at two levels (1, 2), the use of halftoning at two levels (100%

fill, 50% halftone), and the use graded transitions at two levels (if no transition it was either a 50% halftone or a 100% fill, if there was a transition it would start at either 100% on one edge to 50% on the opposite edge or 50% on one edge to 0% on the opposite edge).

The main response variable was the surface roughness (arithmetic mean of roughness Ra) although full profiles were recorded for further analysis. These measurements were taken on a range of 16 mm starting from inside the sample towards the leading edge (1) and towards the trailing edge (2), using a contact profilometer (Mitutoyo Surftest SJ-210).

Additional metrics were recorded to see the progress of the process: root mean squared of roughness Rq, unfiltered roughness indicators Pa and Pq (the Ra and Rq indicators are calculated after applying a high pass filter to the measurement profile – PC75 in this case), weight of material transferred, maximum height of the sample discounting the base substrate, height of curl, and a qualitative assessment of surface quality. The experiment with these control factors was carried out as full factorial (i.e. 24 samples of 30 layers, with measurements made at 10, 20 and 30 layers). A summary table of the experimental design is presented below:

Table 1. Experimental design

Factors	Levels
A. Base Substrate	1. Paper (4×10^{-3} in \cong 0.102 mm thick, 75 g/m ²) 2. Cardboard (9×10^{-3} in \cong 0.229 mm thick, 200 g/m ²) 3. Metallic Paper (3×10^{-3} in \cong 0.076 mm thick, 109 g/m ²)
B. Number of Materials	1. Cyan Toner 2. Cyan and Magenta Toner
C. Halftoning	1. No Halftoning (100% fill) 2. Halftoning at 50% fill
D. Graded Transitions	1. No transition (constant fill) 2. 50% gradient transition applied (100% to 50% or 50% to 0% depending on the halftoning level)
Response variable	Ra: Arithmetic mean of roughness. Full profile stored Rq: Root mean squared of roughness. Pa & Pq: Unfiltered roughness indicators. Weight of material transferred. Maximum height of printed sample (adjusted for substrate). Height of curl. Qualitative assessment of surface quality.
Blocks	Number of layers for evaluation: 10, 20, 30.
Number of runs	24 x 3 blocks = 72

The patterns used can be seen next:

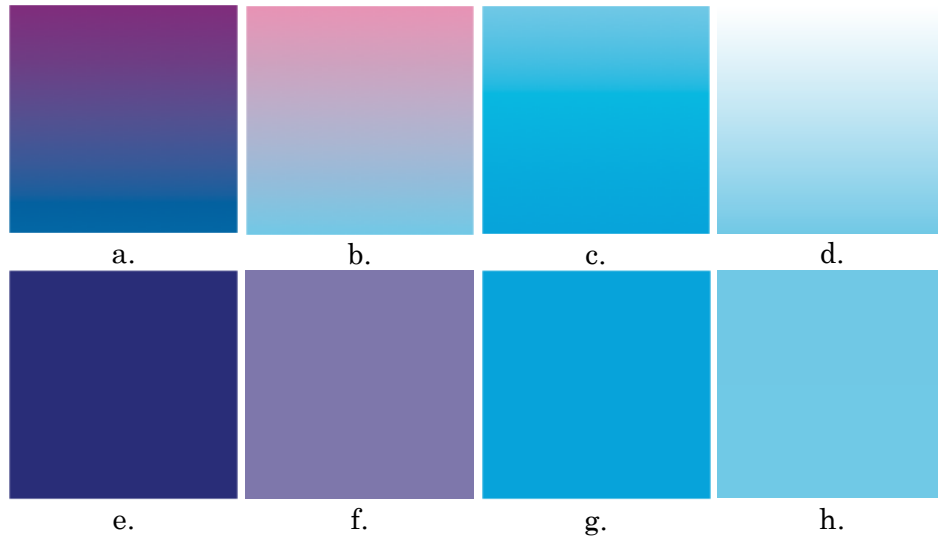


Figure 48. Patterns used for the experimental setup: 2 toners (C & M) on the first two columns, 1 toner (C) on the last two columns; top row use a 50% graded transitions a. and c. from 100% to 50%, b. and d. from 50% to 0; bottom row were solid fill patterns e. and g. 100%, f. and h. 50%.

5.3.2. Analysis of Response Variables

24 samples of 30 layers each were generated according to the experimental design described above; measurements were taken at intervals of 10, 20 and 30 layers. The resulting 30 layer samples can be seen in Figure 49. Curling and registration errors due to the manual process are clearly evident.

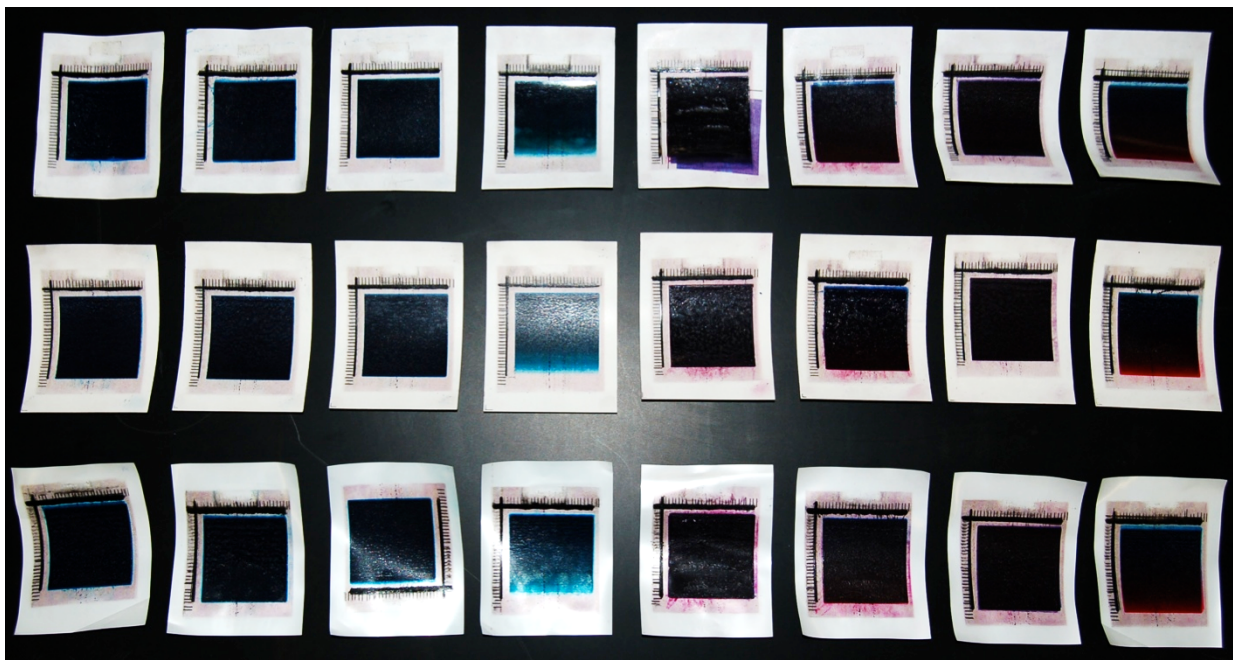


Figure 49. 30-layer samples from the experimental design

There were four roughness measurements that were taken, as indicated above. In order to establish if the information provided from these measurements was consistent, the following analyses were performed.

The first item that was analyzed was the difference between the leading and trailing edges. The arithmetic mean of roughness measured from inside of the sample towards the leading edge (parallel but opposite to the process direction) on a range of 16 mm was represented by Ra(1). Measurements were also taken from the inside of the sample towards the trailing edge (parallel to the process direction) and this was represented by Ra(2). The correlation between the two responses was high: Pearson correlation of Ra(1) [μm] and Ra(2) [μm] = 0.739, P-Value < 0.001. Since the samples seemed rougher on the leading edge, a paired t-test was performed to establish if the readings were significantly different:

Table 2. Paired T-Test for Ra(1) [μm] - Ra(2) [μm]

	N	Mean	StDev	SE Mean
Ra(1) [μm]	72	9.992	6.349	0.748
Ra(2) [μm]	72	6.849	3.359	0.396
Difference	72	3.143	4.479	0.528
95% CI for mean difference: (2.091, 4.196)				
T-Test of mean difference = 0 (vs not = 0):				
T-Value = 5.95; P-Value < 0.001				

These results confirmed that the results obtained from the readings on the leading edge are indeed significantly different (higher roughness) from those taken on the trailing edge of the samples.

In addition, the difference between the four roughness measurements was explored. First the two filtered responses, Ra and Rq, were examined (recall that it was established that Ra(1) and Ra(2) are correlated). There was a strong correlation between Ra and Rq: Pearson correlation of Ra(1) [μm] and Rq(1) [μm] = 0.987 P-Value < 0.001. Next the correlation with the unfiltered responses and between the unfiltered responses was examined. The unfiltered response variable Pa was also strongly correlated with the selected response Ra: Pearson correlation of Ra(1) [μm] and Pa(1) [μm] = 0.967, P-Value < 0.001. Likewise, the correlation between the unfiltered responses Pa and Pq was very strong: Pearson correlation of Pa(1) [μm] and Pq(1) [μm] = 0.992, P-Value < 0.001.

Similarly, the correlation between the arithmetic roughness and the qualitative assessment of the surface was explored: Pearson correlation of Ra(1) [μm] and Surface quality [qual] = -

0.796; P-Value < 0.001. The result shows that there is indeed a high negative correlation which seems to indicate that the readings Ra(1) seems to correspond to the qualitative assessment of the surface. It is negative due to the nature of the responses: in the qualitative assessment 10 is very good and 1 is very poor quality of the surface, while in Ra a higher value corresponds to a rougher surface.

As a result, the main response variable for surface roughness was selected to be Ra(1). The curling height, the weight of material transferred, and the height of sample were also analyzed further to understand better the effect of the different factors on the 3D printed sample.

5.3.3. Analysis of Significant Effects

The responses were used to analyze the experiment and determine the significant factors that affect each aspect of the EP-based 3D-printed samples. The resulting ANOVAs and factorial plots are presented in the following pages:

Table 3. Analysis of Variance for Ra(1) [μm], using Adjusted SS for Tests

Source	DF	Seq SS	Adj SS	Adj MS	F	P
Layers (x10)	2	1195.75	1195.75	597.88	52.28	<0.001
Substrate	2	27.76	27.76	13.88	1.21	0.305
Colors/Materials	1	188.99	188.99	188.99	16.53	<0.001
Halftoning	1	628.00	628.00	628.00	54.92	<0.001
Graded	1	33.19	33.19	33.19	2.90	0.094
Substrate*Colors/Materials	2	13.98	13.98	6.99	0.61	0.546
Substrate*Halftoning	2	1.11	1.11	0.56	0.05	0.953
Substrate*Graded	2	69.71	69.71	34.85	3.05	0.056
Colors/Materials*Halftoning	1	68.60	68.60	68.60	6.00	0.018
Colors/Materials*Graded	1	0.01	0.01	0.01	0.00	0.980
Halftoning*Graded	1	5.60	5.60	5.60	0.49	0.487
Error	55	628.96	628.96	11.44		
Total	71	2861.66				
S = 3.38166 R-Sq = 78.02% R-Sq(adj) = 71.63%						

This analysis highlights that the number of colors/materials, the halftoning level and the interaction between colors and halftoning are the most significant factors that affect the surface quality. It is important to note that graded transitions and different base substrates do not seem to affect significantly the surface quality.

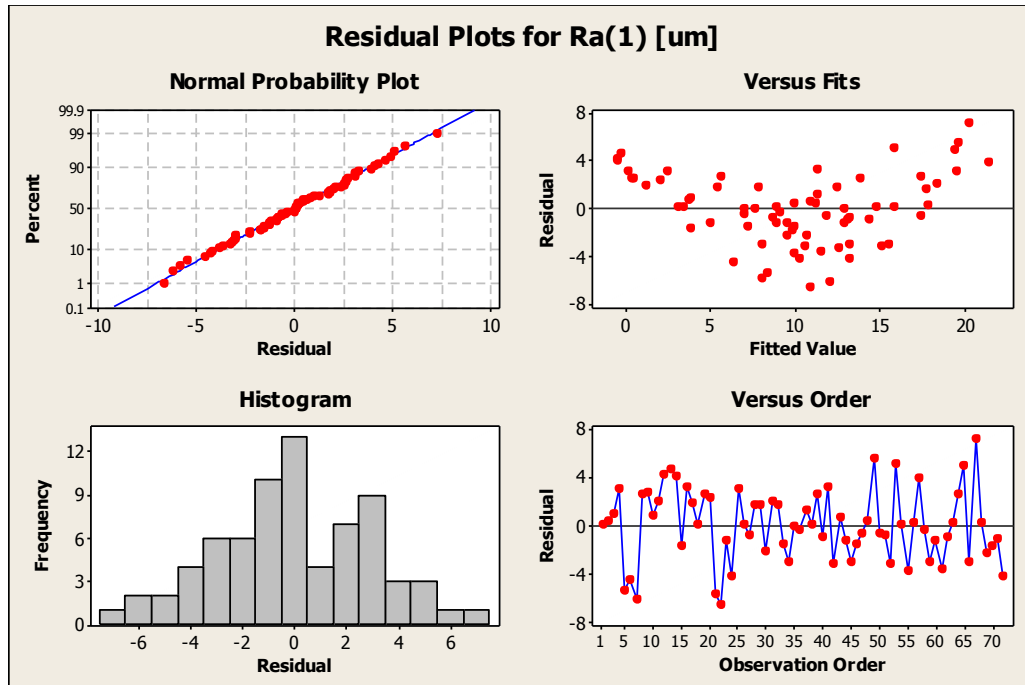


Figure 50. Residual plots for surface roughness Ra(1)

The residual plots shown in Figure 50 validate the normality assumptions for the model and provide confidence in the conclusions extracted from it. Although the plot of residuals versus fit shows a trend, a log and a square root transformation were applied to the data obtaining slightly better plots at the expense of worsening the histogram but conveying the same conclusion in terms of significant factors; in the end, the original data was selected for the analysis.

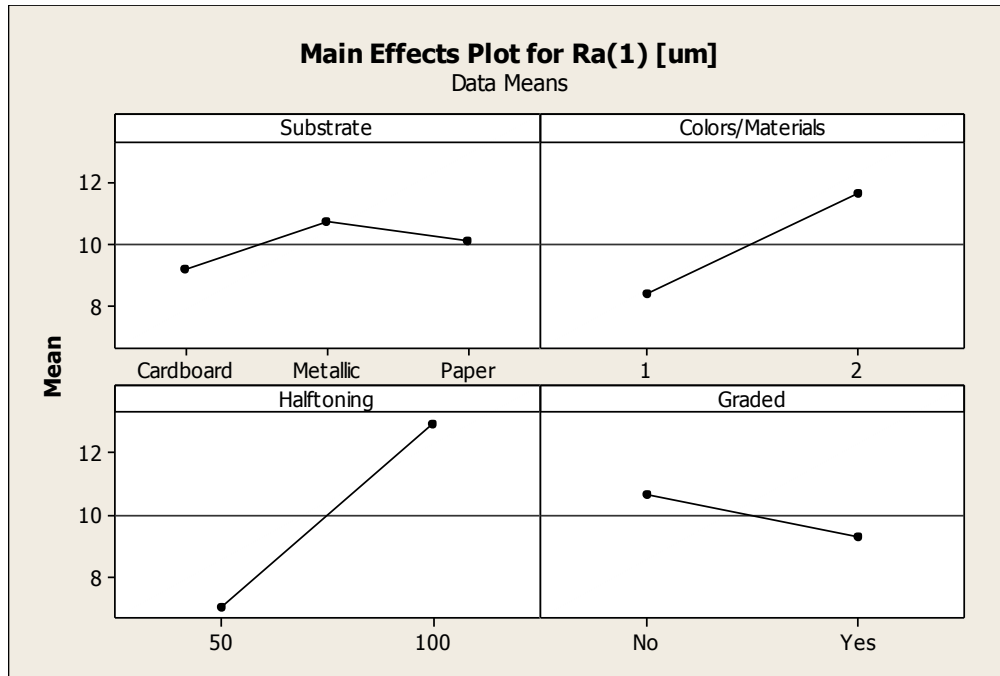


Figure 51. Main effects plot for surface roughness Ra(1)

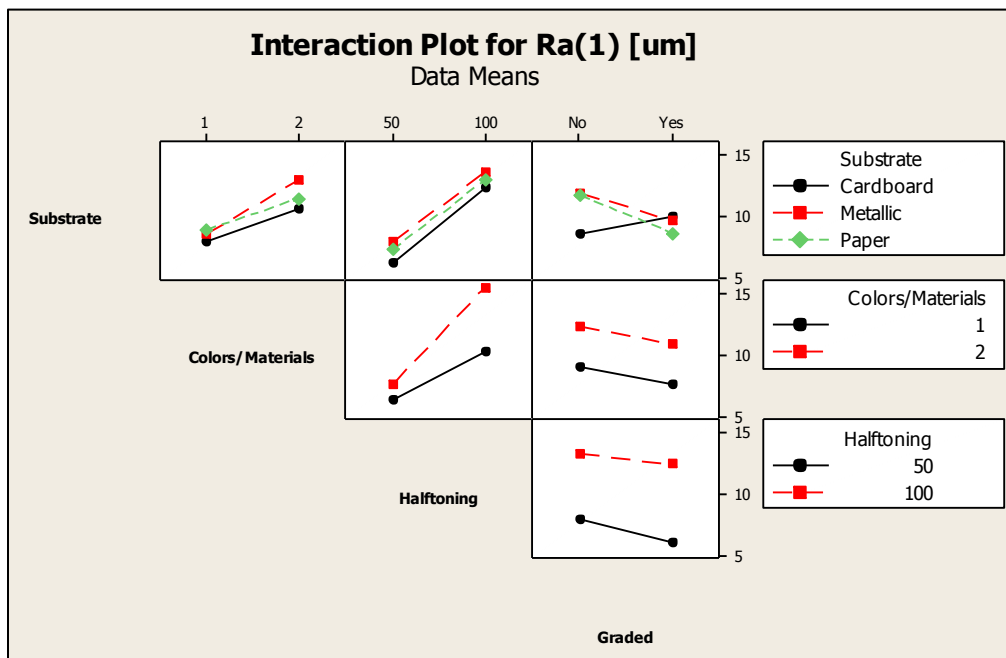


Figure 52. Interaction plot for surface roughness Ra(1)

The main effect plot in Figure 51 shows the trend for each level of each factor, and the interaction plot in Figure 52 allows for more detailed examination of the behavior of the factors and their effect on the surface quality. The most significant interaction was between Colors/Materials and Halftoning; however, the plot shows that using 2 toners tend to produce a rougher surface but the difference is more dramatic when printing at 100% fill. A

more interesting observation is that the interaction between substrate and graded transitions was just above the threshold for significance ($p = 0.056$). The interaction plot shows that when using the cardboard as the base substrate it is better not to use graded transitions to produce a smoother surface, while it seems better to use them when using the other base substrates. At this time, this behavior is not understood, but perhaps this suggest that interactions between a rougher substrate and the layers can lead to smoother surfaces. This is something that will have to be explored further.

Other response variables also shed light into the matter. The analysis for height at curling can be seen in Table 4. The results highlight that number of layers, substrate, number of colors/materials, and halftoning level, as well as the interactions between substrate and number of colors/materials and between substrate and halftoning level affect significantly the amount of curling. From the main effect and interaction plots (not shown due to space limitations) it can be concluded that the metallic substrate tends to curl less than the other substrates, and when more material is placed on the sample, the more the sample will curl.

When examining the material transferred response, the main insight gained was that neither the number of layers nor the base substrate affect significantly the amount of material to transfer. The ANOVA can be seen in

Table 5. Similarly, when examining the height of the sample as a response (see Table 6), the base substrate was not a significant factor after adjusting for the initial substrate thickness.

Table 4. ANOVA for Height at curling [in], using Adjusted SS for Tests

Source	DF	Seq SS	Adj SS	Adj MS	F	P
Layers (x10)	2	0.19971	0.19971	0.09986	5.51	0.007
Substrate	2	0.57470	0.57470	0.28735	15.85	<0.001
Colors/Materials	1	0.46561	0.46561	0.46561	25.68	<0.001
Halftoning	1	0.29287	0.29287	0.29287	16.15	<0.001
Graded	1	0.04993	0.04993	0.04993	2.75	0.103
Substrate*Colors/Materials	2	0.27502	0.27502	0.13751	7.58	0.001
Substrate*Halftoning	2	0.12108	0.12108	0.06054	3.34	0.043
Substrate*Graded	2	0.04736	0.04736	0.02368	1.31	0.279
Colors/Materials*Halftoning	1	0.01003	0.01003	0.01003	0.55	0.460
Colors/Materials*Graded	1	0.00130	0.00130	0.00130	0.07	0.790
Halftoning*Graded	1	0.02880	0.02880	0.02880	1.59	0.213
Error	55	0.99741	0.99741	0.01813		
Total	71	3.06382				
S = 0.134665 R-Sq = 67.45% R-Sq(adj) = 57.98%						

Table 5. ANOVA for Material transferred [g], using Adjusted SS for Tests

Source	DF	Seq SS	Adj SS	Adj MS	F	P
Layers (x10)	2	0.000066	0.000066	0.000033	0.99	0.377
Substrate	2	0.000183	0.000183	0.000092	2.74	0.073
Colors/Materials	1	0.036302	0.036302	0.036302	1085.43	<0.001
Halftoning	1	0.106514	0.106514	0.106514	3184.80	<0.001
Graded	1	0.019837	0.019837	0.019837	593.13	<0.001
Substrate*Colors/Materials	2	0.000034	0.000034	0.000017	0.51	0.602
Substrate*Halftoning	2	0.000079	0.000079	0.000040	1.18	0.314
Substrate*Graded	2	0.000002	0.000002	0.000001	0.04	0.966
Colors/Materials*Halftoning	1	0.008075	0.008075	0.008075	241.45	<0.001
Colors/Materials*Graded	1	0.002430	0.002430	0.002430	72.66	<0.001
Halftoning*Graded	1	0.000217	0.000217	0.000217	6.48	0.014
Error	55	0.001839	0.001839	0.000033		
Total	71	0.175580				

S = 0.00578313 R-Sq = 98.95% R-Sq(adj) = 98.65%

Table 6. ANOVA for Height Adj. [mil], using Adjusted SS for Tests

Source	DF	Seq SS	Adj SS	Adj MS	F	P
Layers (x10)	2	261.444	261.444	130.722	68.77	<0.001
Substrate	2	2.965	2.965	1.483	0.78	0.463
Colors/Materials	1	56.889	56.889	56.889	29.93	<0.001
Halftoning	1	260.681	260.681	260.681	137.15	<0.001
Graded	1	32.000	32.000	32.000	16.84	<0.001
Substrate*Colors/Materials	2	0.007	0.007	0.003	0.00	0.998
Substrate*Halftoning	2	0.340	0.340	0.170	0.09	0.915
Substrate*Graded	2	0.438	0.438	0.219	0.12	0.892
Colors/Materials*Halftoning	1	21.125	21.125	21.125	11.11	0.002
Colors/Materials*Graded	1	18.000	18.000	18.000	9.47	0.003
Halftoning*Graded	1	2.347	2.347	2.347	1.23	0.271
Error	55	104.542	104.542	1.901		
Total	71	760.778				

S = 1.37868 R-Sq = 86.26% R-Sq(adj) = 82.26%

The nature of the patterns used posed a question on whether the effect of the different factors was being overshadowed by other sources of variation for these responses. For instance, when graded transitions were used with only one material, the sample was “unbalanced” generating a ramp instead of a “flat” structure. This was an oversight on the experimental design and it may be necessary to explore if changing the orientation of the ramp at each layer may “balance out” the ramping effect on the total part. To validate the conclusions gained, the data was blocked by number of colors, halftoning level, and the use of graded transitions (see Table 7). Eight separate ANOVAs were constructed for each response (material transferred and sample height) as a function of number of layers and substrate. The results were consistent with the initial conclusions for all 8 cases, but a much smaller estimate of error was obtained (~2 orders of magnitude less). A representative ANOVA and residual plot is shown for each response variable (see Table 8

and Figure 53, and Table 9 and Figure 54 respectively); the remaining 14 are shown in the appendices, but were very similar with the residuals behaving different.

Table 7. Conditions blocked for further analysis on the responses

Factor \ Case	1	2	3	4	5	6	7	8
Colors/Materials	C	CM	C	CM	C	CM	C	CM
Halftoning Level	100%	100%	50%	50%	100%	100%	50%	50%
Graded Transition	Yes	Yes	Yes	Yes	No	No	No	No

Table 8. ANOVA for Material Transferred [g] for case 2: CM-100%-Yes

Source	DF	Seq SS	Adj SS	Adj MS	F	P
Layers (x10)	2	0.0002055	0.0002055	0.0001028	0.95	0.461
Substrate	2	0.0000615	0.0000615	0.0000307	0.28	0.768
Error	4	0.0004347	0.0004347	0.0001087		
Total	8	0.0007017				
S = 0.0104250 R-Sq = 38.05% R-Sq(adj) = 0.00%						

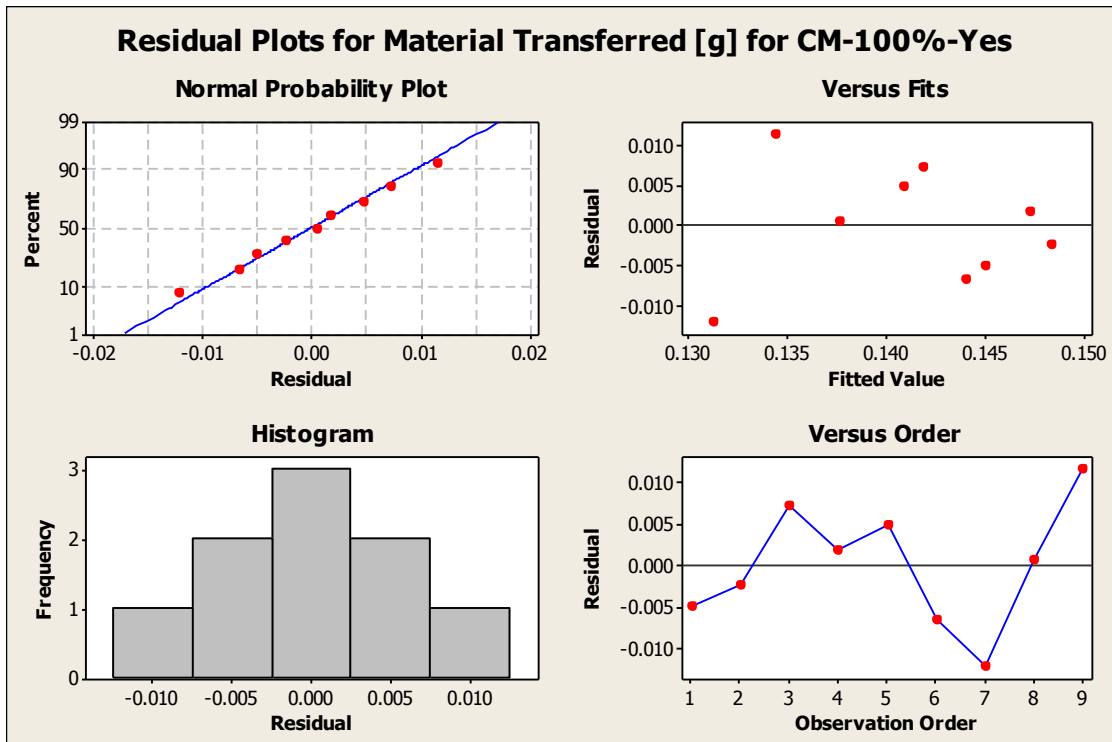


Figure 53. Residual plots for material transferred, for case 2: CM-100%-Yes

Table 9. ANOVA for Height Adj. [mil] for Cyan-100%-No Transition

Source	DF	Seq SS	Adj SS	Adj MS	F	P
Layers (x10)	2	35.1667	35.1667	17.5833	42.20	0.002
Substrate	2	0.6667	0.6667	0.3333	0.80	0.510
Error	4	1.6667	1.6667	0.4167		
Total	8	37.5000				
S = 0.645497 R-Sq = 95.56% R-Sq(adj) = 91.11%						

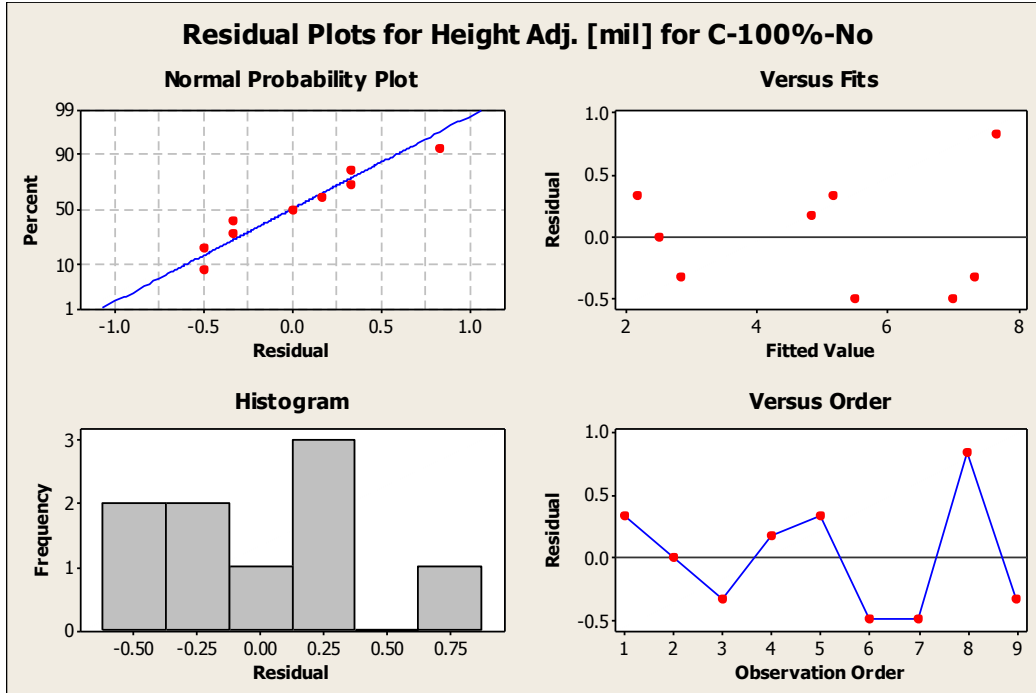


Figure 54. Residual Plot for Height Adj. [mil] for Cyan-100%-No transition

It is reassuring that neither the transfer of material nor the height of the print were dependent on the base substrate; but more importantly, the transfer of material did not depend on the number of layers, which indicates that the process established is indeed circumventing the limitation of transferring new material for EP3D printing.

However, in the process of building over 720 layers it was noted that the fusing process plays a key role in the generation of the 3D structure. Up until this point, the fusing parameters (temperature, pressure, and speed) have remained constant based on values that have worked well for traditional document printing ($170 \pm 5^\circ\text{C}$, ~ 85 psi on the nip, ~ 80 mm/s). It is necessary to establish if these conditions are appropriate for EP3D printing as the number of layers increases. A more detailed study is needed to understand better how the surface changes with an increasing number of layers and what role does the fuser play.

5.4. Layer-by-layer measurements

The characterization of surface defects in EP3D prints require a deep understanding on how the surface changes as more layers are stacked on top of each other. Previous studies had analyzed the final state of the print or had taken measurements of the surface roughness every 10 layers [92]; those studies proved to be useful to determine the effect of some factors on the final surface, but they lack of sufficient resolution to show the evolution

of the surface. A study of a 30 layer sample was conducted where measurements were taken at each layer in two distinct locations: one from the leading edge towards the center of the sample, and other from the center towards the trailing edge of the sample. Each measurement was taken with a contact profilometer (Mitutoyo Surftest SJ-210), sampling a line 16 mm in length with a sampling rate of $1.5\ \mu\text{m}$ (see Figure 47.c.). This is comparable to the particle size of the toner used in the experiment, which typically ranges from 4-6 μm .

The sample was constructed following the methodology shown in Figure 40, fusing at half the speed of previous trials (250 rpm \sim 37 mm/s). A more uniform surface was observed both visually and in the measurement readings. A second sample was constructed by fusing it face down, which put the topmost layer (and the intermediate transfer substrate) in contact with the soft pressure roller of the fuser (instead of the hard heated roller), which is more compliant. Both samples can be seen in Figure 55.a. A comparison between the readings for both samples can be seen in Figure 55.b.

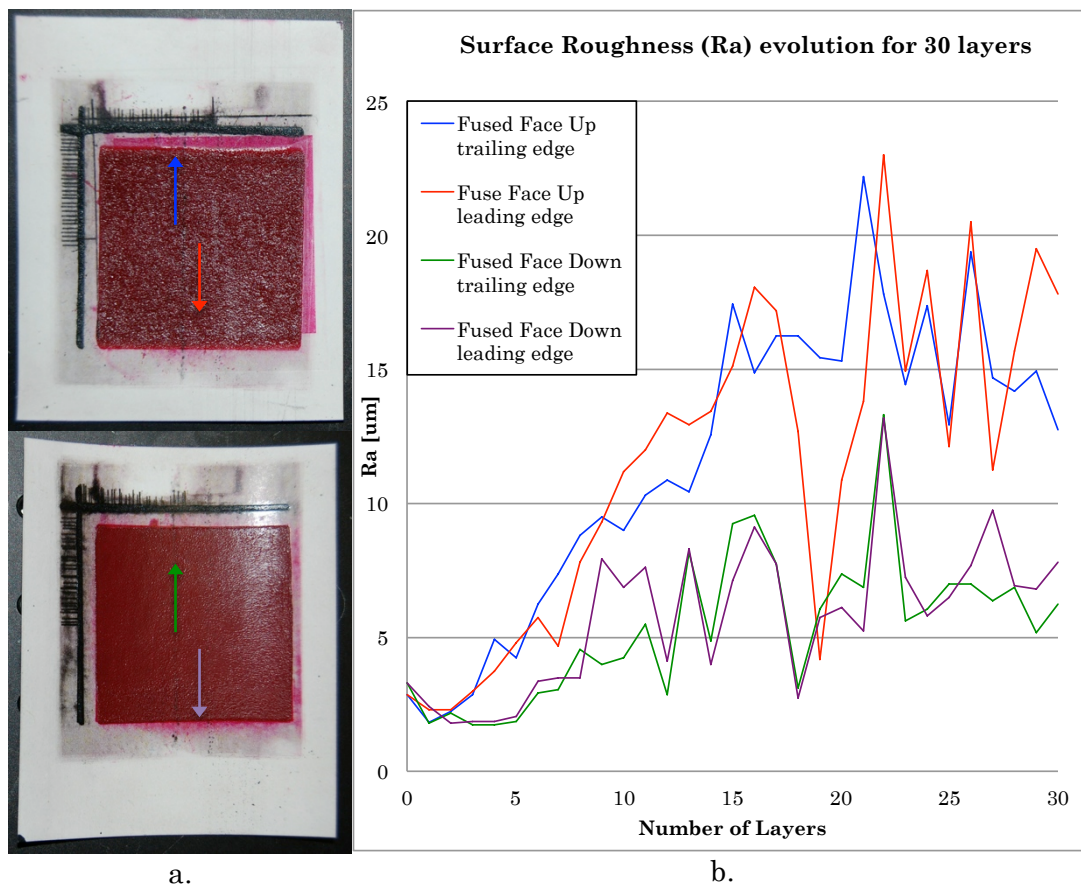


Figure 55. a. 16 mm measurement paths for leading and trailing edges; b. 30-layer samples fused face up (top) and face down (bottom); c. surface roughness evolution summary chart

The measurements showed that the sample fused face down had consistently lower roughness (Ra) values than the sample fused face up. This suggests that a more compliant interface is desirable in order to achieve a smoother surface. The trailing edge of the sample which was fused face-up had an anomalous reading on layer 19; the measured roughness was much lower than the measurement taken on the leading edge, even lower than the measurements taken on the sample fused face-down. It is unclear if this was only a local effect on the sample that quickly passed, if there was an obstruction on the contact needle of the profilometer, or some other artifact that may have caused the instrument to report a roughness much lower than what seems reasonable. Whatever the cause, this point seems to be an outlier and a general trend seems to prevail throughout the measurements of the samples. It is important to note that contrary to what had been observed in [92], both readings taken on either sample were comparable, showing no significant difference on the surface due to the orientation of the sample as it went through the fuser. As will be shown later, this is due the dynamics of the fusing process and the different fusing speed that was used in this study.

When the profiles recorded at each layer were examined, an autocorrelation study showed that the low frequency content tends to expand with the number of layers (i.e. the autocorrelation function becomes wider), and the process cannot be characterized by a single transfer function from these data. The profiles for the leading edge of the sample fused face up can be seen in Figure 56 (the profiles were shifted up for visualization purposes) and the autocorrelation function of the data from the different layers in Figure 57.

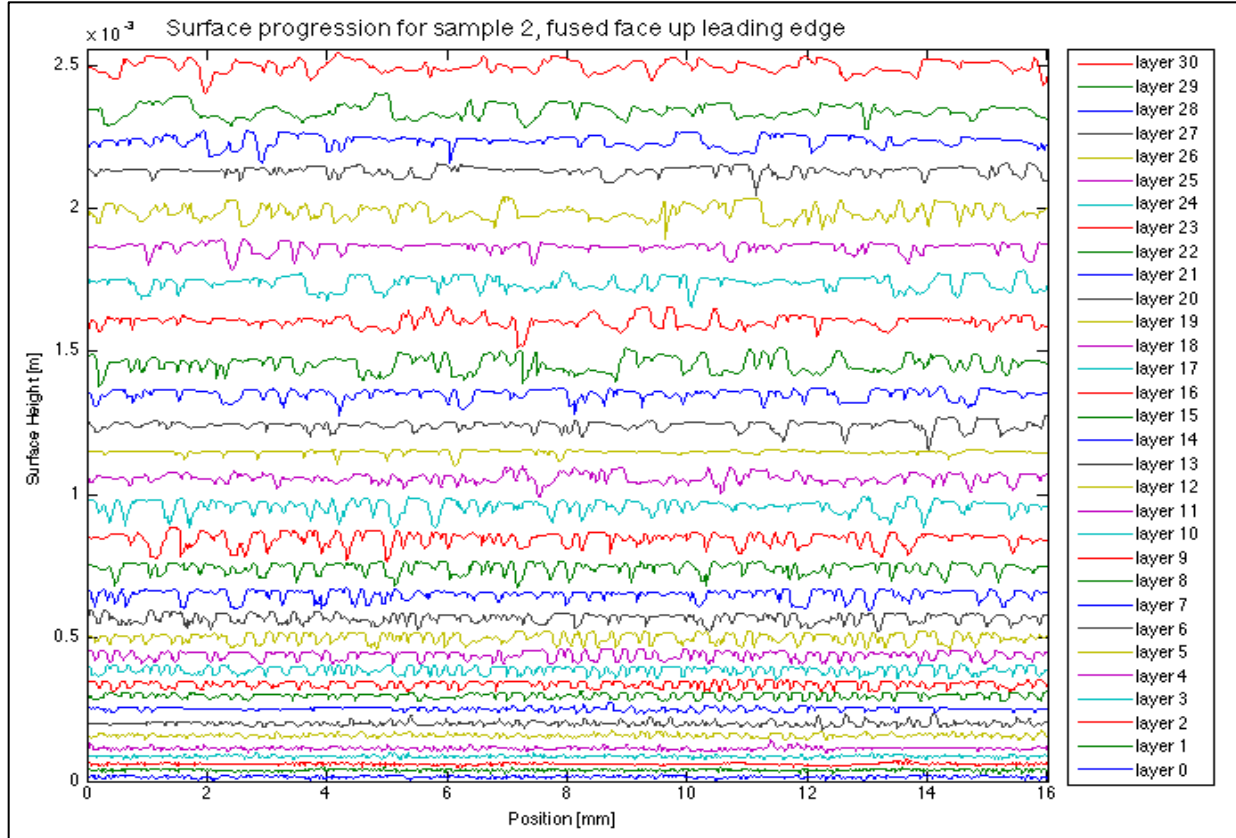


Figure 56. Surface profiles for sample fused face up, leading edge

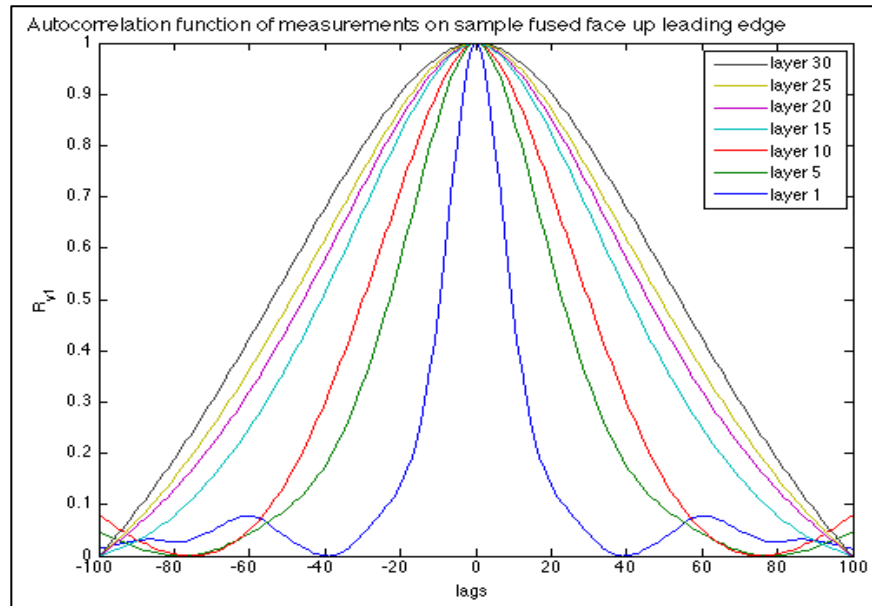


Figure 57. Autocorrelation function for sample fused face up, leading edge

The histogram of the measurements at several layers can be seen in Figure 58.

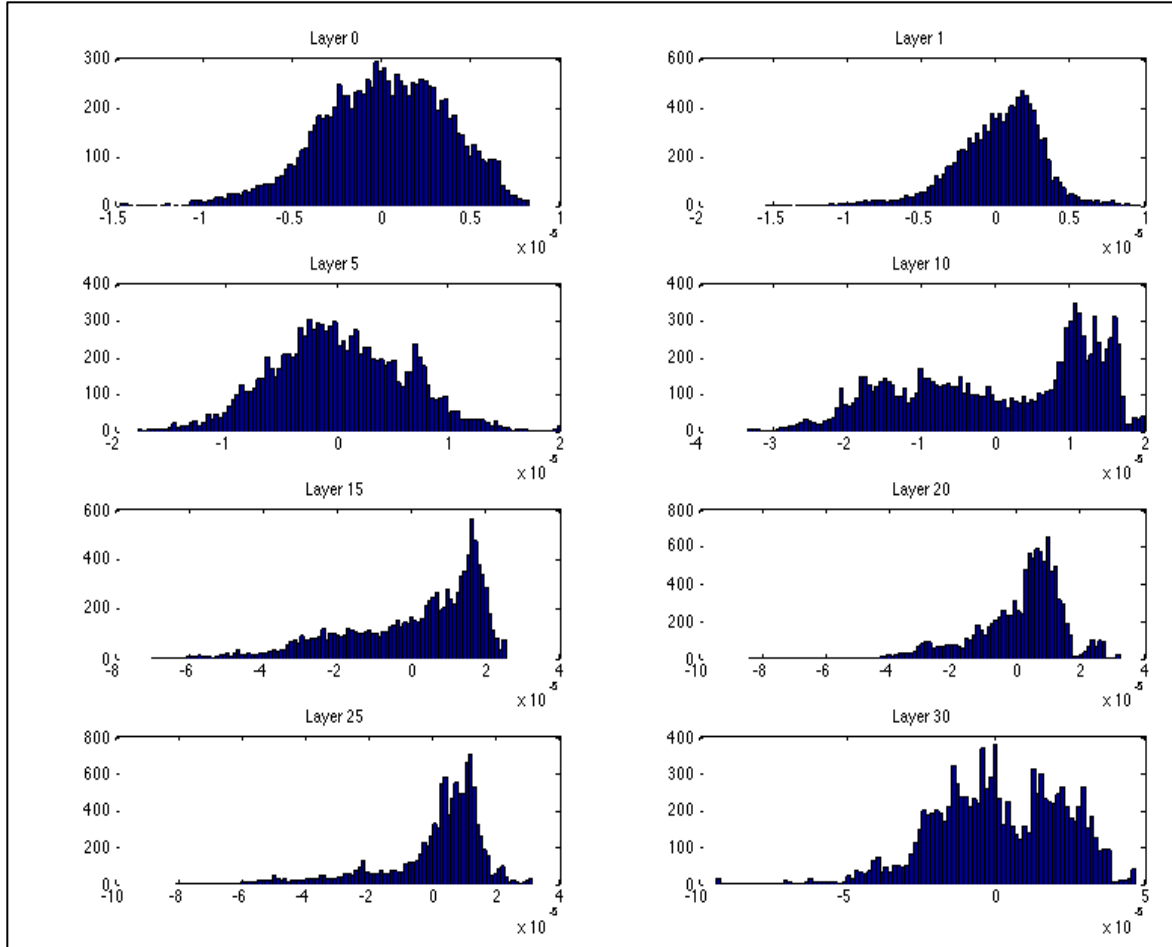


Figure 58. Histograms of measurements on sample fused face-up, leading edge at several layers

5.5. Conclusion

This exploratory study of surface defects in EP3D Printing has uncovered many of the challenges to overcome for this technology to become feasible on a larger scale. The effect of multiple factors on the surface quality of an EP3D printed part was studied through an experimental approach. The selected factors used in the experimental setup proved to be relevant for characterizing the surface quality.

The results suggest that the surface quality seems to be affected mostly by the number of materials printed, the halftoning level, and the growing number of layers. The base substrate does not seem to have a significant effect on the surface quality, nor the amount of material transferred, nor the height of the part. It only seems to play a significant role in the amount of curling of the sample for which a sturdy substrate seems desirable.

The fusing stage was highlighted as a crucial step for the surface quality. A more compliant interface on the transfusing process seems to provide better transfers and better surface quality. The variation of results between the leading edge and the trailing edge suggest that the transient response of the fuser to the changing profile as the sample goes through affects the structure. Furthermore, it is necessary to evaluate if the traditional roller fusing method is the most appropriate for this application and perhaps other architectures may be better suited for the task, such as a stamp-based fusing or a non-contact alternative.

The results also indicate that surface defects would appear regardless of the configuration of factors explored, suggesting that a feedback control strategy may be required in order to achieve uniform layers and ultimately an accurate reproduction of 3D structures. The measurements taken at every layer allowed observing changes in the structure that occur throughout the process, and provided insights to develop a model of the process that can be useful for control purposes.

Chapter 6. MODELING OF EP3D PRINTING FOR CONTROL

Modeling the EP3D printing process was seen as a way to achieve deeper understanding into the multi-layer printing process and would enable the design and simulation of control strategies. This chapter presents the advancements in this area starting with the most detailed model of the EP development process to our knowledge, following with the approach to obtain an overall model of the current EP3D printing process with the specific characteristics of the hardware used.

6.1. Static Model of EP Development Process

The static model summarized in section 2.1.2.1 was simulated using Matlab to verify the results reported in literature. The code can be seen in Appendix A.1

The results show the development curve relating toner concentration and the developed mass per unit area for the given parameters. Usually, more variables are evaluated; a sample plot can be seen below in Figure 59, where the development curves were obtained for different bias voltages.

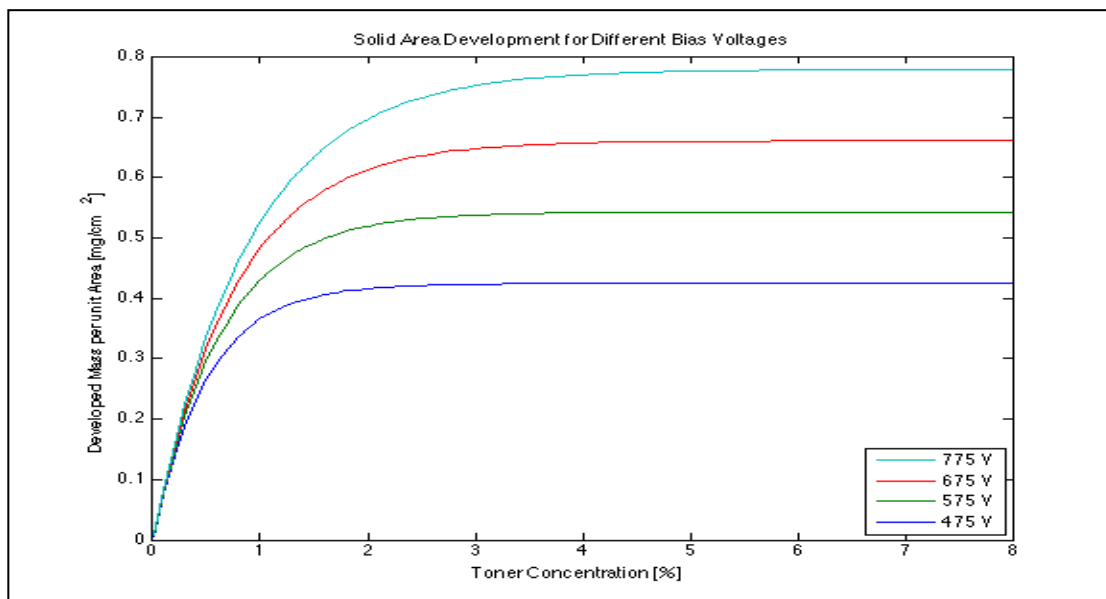


Figure 59. Development curves using the static model from section 2.1.2.1

These results provided guidance on the response of the development system to variations on voltages, gaps, speeds, etc., identifying opportunities to innovate towards 3D printing.

6.2. System Identification and Modeling

A linear test-bed for EP was donated by Kodak to the PRISM Lab in late 2008. Since then, the test-bed has gone through major updates and renovations, giving it full control through Labview and the ability to easily record data. This test-bed replicates all steps of the EP process except for cleaning and fusing which makes it ideal for testing new materials or process conditions since there is access to most of the parameters at each step of the process (see Figure 60).

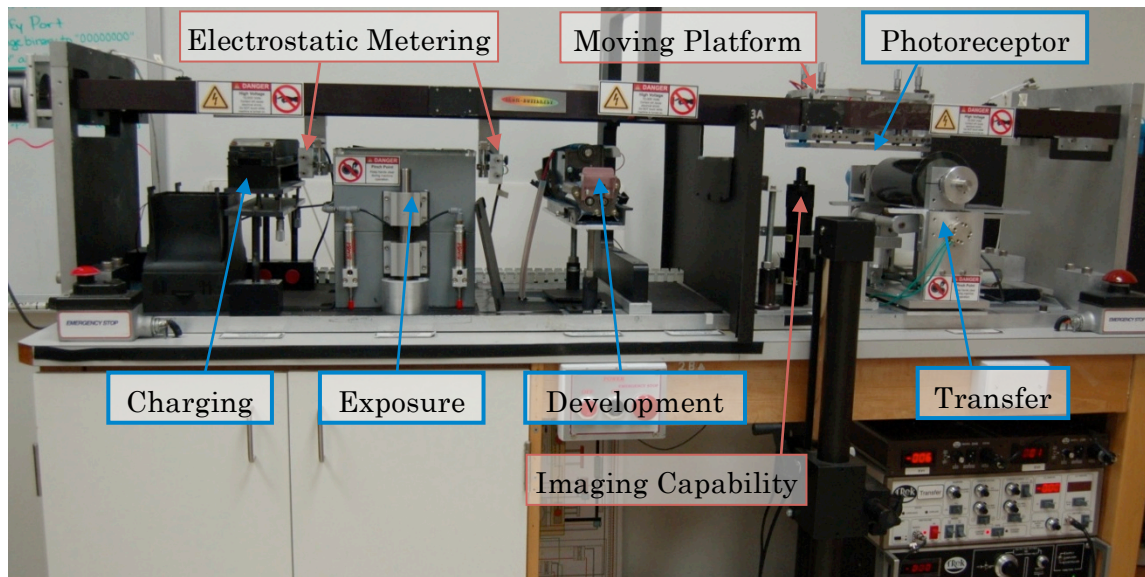


Figure 60. Linear Test-bed for EP at the PRISM Lab, RIT

Unfortunately, the test-bed does not have a programmable exposure system but rather a fixed exposure station based on a negative plate that is illuminated from below. This has limited the usability of the test-bed; however, plans are underway to adapt an LED bar exposure system to achieve greater flexibility.

Similarly, three off-line fusing stations at the PRISM lab allow for independent control of pressure, temperature, and dwell time of the fusing step (see Figure 19). The more robust fuser was used for the generation of EP3D printed samples and allowed for dynamic modeling of the fusing process of the multilayer structure. The system identification was

performed by direct and indirect measurement of some parameters and by deducting others from system level responses gathered using pressure sensitive paper.

As detailed in Figure 40, the EP3D printing process consisted of two stages, (1) creating a layer through EP, and (2) fusing the new layer to the part under construction. To model the EP3D printing process, both stages need to be considered since they affect the surface output.

6.2.1. Layer printing

The nature of the EP process is such that there is no direct control on the number of particles developed at a specific location. In the exposure stage, the latent image serves to create an electric field between the photoreceptor and the developer roller; this field attracts toner particles but there is no certainty on how many particles are transferred. Liu et al. [23] used a probabilistic approach to describe the development process of a hybrid two-component system, an approach which was corroborated in a personal communication with a development physics expert [22]. The measured surface height readings which were taken layer-by-layer also suggested that the substrate and each layer tended to follow a normal distribution. This information was used to make the following modeling assumptions:

- Each layer is generated by a normally distributed height, which physically correlates to a random accumulation of particles in a particular location
- but the resulting height is affected by the fusing process, which compresses the particles and makes them stick together

The number of particles at each location for each layer is drawn from a normal distribution with a mean of 3 and a standard deviation of 1 based on what has been reported but also from direct observations of unfused samples using confocal microscopy (see Figure 61).

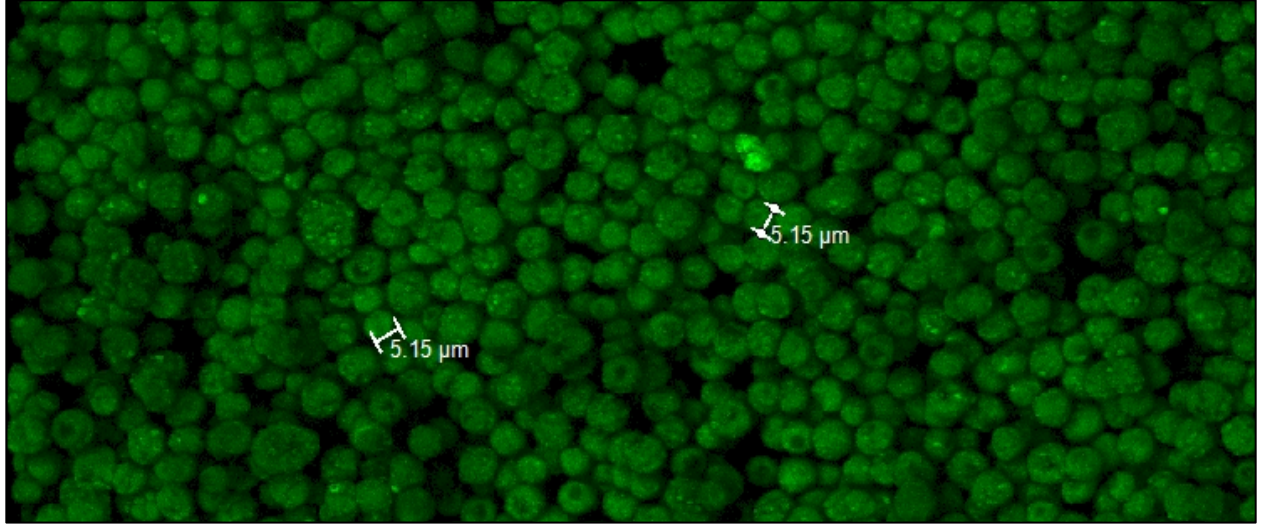


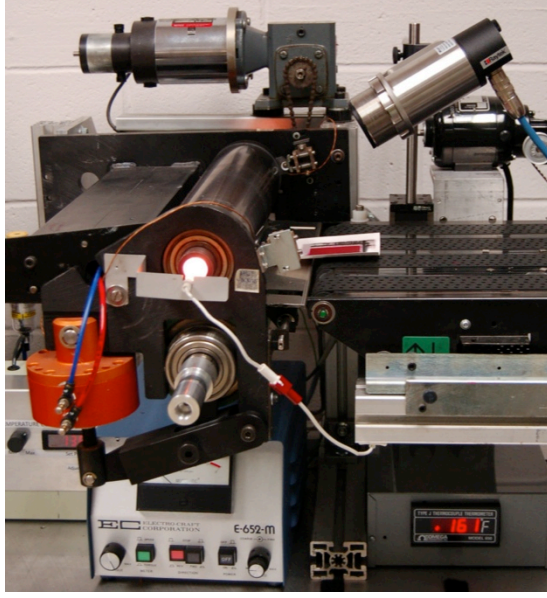
Figure 61. Unfused EP printed sample observed through a confocal microscope, multiple layers of particles are detected

6.2.2. Fusing the new layer to the part under construction

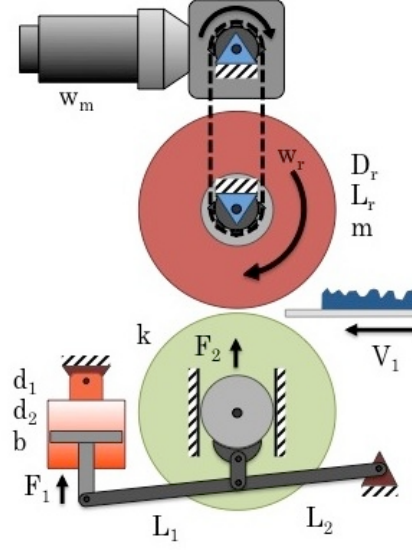
The new layer printed on the intermediate transfer sheet is transfused onto the top of the existing 3D structure by running both through fuser rollers. The term transfuse implies that the transfer of the new material happens while fusing it to the existing part by applying heat and pressure. In this technique the transfer is not done through electrostatics, which circumvents the “self-insulating nature” of EP3D printing [1].

In previous experiments reported in [92], it was observed that a significant difference existed between the surface roughness on the leading edge and the trailing edge of the samples. At the time it was unclear what was causing the difference in the readings, but it became clear that the transient response of the fuser was affecting the output when the speed of the fuser was reduced and the rougher area reduced significantly resulting in comparable readings on both edges. This motivated the modeling of the fuser as a dynamic system to study the effects of the transient response on the surface of the print.

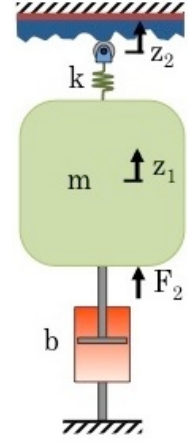
The fuser used for the experiments can be seen in Figure 62.a. A dynamic model of the fuser was developed and the specific parameters (dimensions, roller mass, spring constant, damping coefficient from the pneumatic actuators) were measured or identified examining the response of the system to known input parameters. A diagram of the system used for modeling purposes and the equivalent dynamic system can be seen in Figure 62.b and c.



a.



b.



c.

Figure 62. a. Fuser testbed used for EP3DP; b. Diagram of fuser used for modeling; c. Diagram of equivalent dynamic system

The equivalent dynamic system corresponds to a very well known second order mass-spring-dashpot system. The system identification was performed through a series of tests to capture the transient response of the rollers to a known input (series of steps) with the use of pressure sensitive paper. The mass of the model aggregates the mass of the pressure (bottom) roller and the elements that connect it with the pneumatic actuator. The spring constant corresponds to the compressibility of the roller around the operating condition (air pressure ranging from 15 to 25 psi). The damping constant considers only the resistance of the pneumatic actuator to change, and the external force (F_2) is the force of the actuator (F_1) transmitted and amplified through the lever arm to the pressure roller, remaining constant throughout the simulation. The displacement of the roller is modeled as z_1 and the displacement seen by the top of the roller as the sample goes through is z_2 .

The state space representation of the system can be seen below:

$$\begin{aligned} \dot{X}(t) &= \begin{bmatrix} 0 & 1 \\ -k/m & -b/m \end{bmatrix} X(t) + \begin{bmatrix} 0 & 0 \\ 1/m & k/m \end{bmatrix} U(t); & X(0) &= \begin{bmatrix} F_2/k \\ 0 \end{bmatrix}; \\ y(t) &= \begin{bmatrix} k & 0 \end{bmatrix} X(t) + \begin{bmatrix} 0 & -k \end{bmatrix} U(t); & U(t) &= \begin{bmatrix} F_2 \\ z_2 \end{bmatrix}; \end{aligned} \quad (6.1)$$

Notice that the output of the system is the force applied onto the surface by the compliant roller. This force leads to more or less compression of the toner particles as they are fused.

6.2.3. Simulation Model

The simulation is carried out in the following manner:

1. Initialize all the parameters: print size, particle size, number of points, number of layers, base substrate, fuser speed, pressure, etc.
2. Generate a new layer of particles to be deposited.
3. Add the new layer to the existing structure to create an input profile for the dynamic model of the fuser.
4. Simulate the reaction of the fuser to the input profile.
5. For each point calculate the height difference relative to the maximum point of the profile seen by the roller in the nip width.
6. Check if the height difference is within the compliance of the interface. The compliance of the fusing interface (thres) is a determinant factor because it ultimately enables more or less particles to stick to the existing structure because the interface conforms to the variation of the surface and is able to apply force to the new particles to make them fuse.
7. Generate a random number and check if it is below the probability of transfer; this is a parameter to model the probabilistic aspect of the transfer process.
8. Calculate the compression as a result of the force generated by the fuser as it reacts to the print. The model assumes that the particles compress linearly to the force applied at each location. The model also allows for further compression of the previous layers up to a certain depth; this depth is related to how much heat goes into the existing structure as the print is going through the fuser.
9. Establish the new height for the point in the simulation profile.
10. Go to step 5 and repeat sequence for the next point of the simulation profile.
11. Apply a low-pass filtering with the nearest neighbors. A Gaussian kernel of length 5 and standard deviation of 1 was used. This filtering effect resembles the evening action of the fuser at the nip, and correlates to the frequency response extracted from the measurements taken.
12. Go to step 2 and repeat sequence for the next layer.

An overview of the simulation structure can be seen in Figure 63.

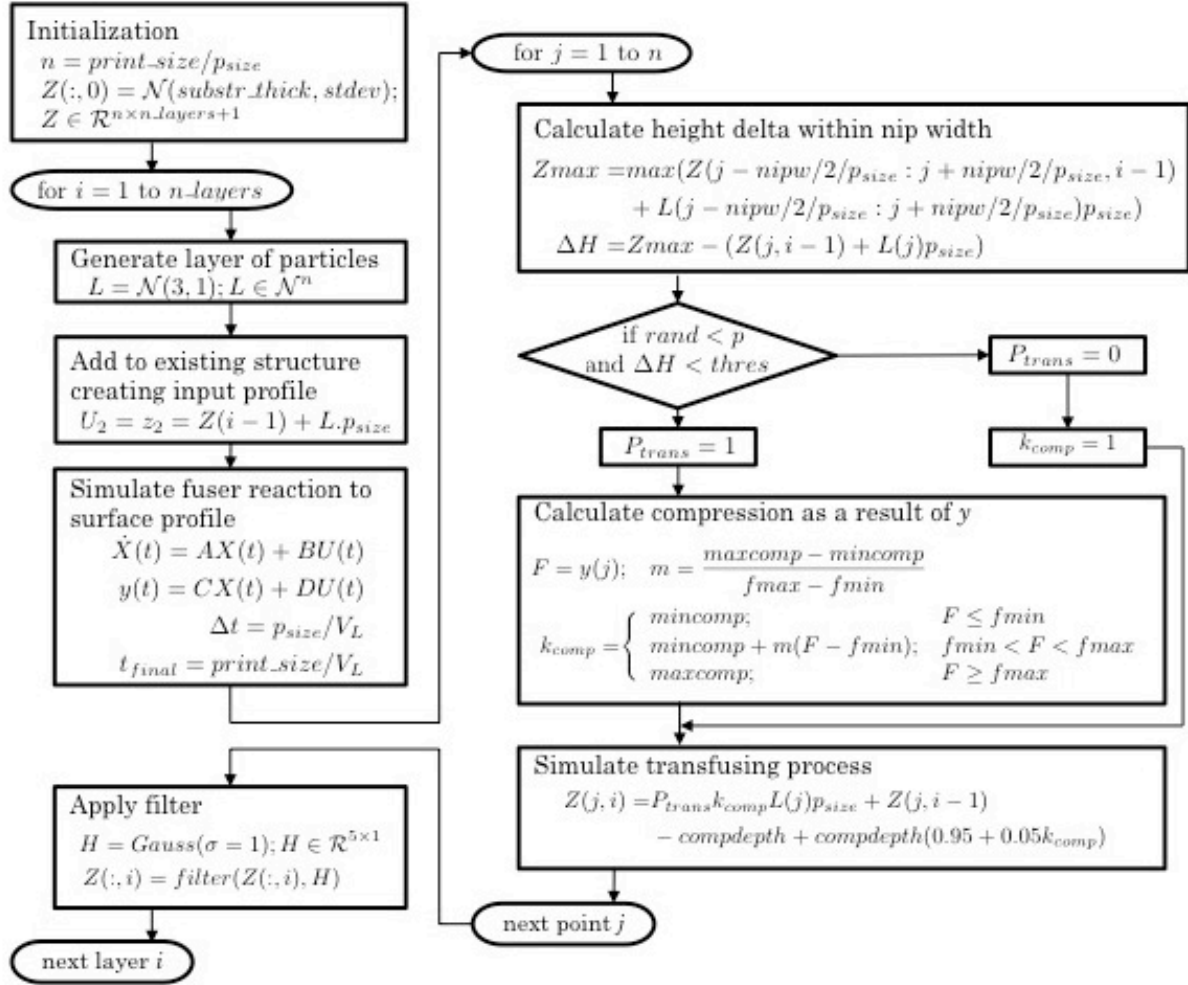


Figure 63. Flow diagram of simulation algorithm

6.3. Results and model validation

An entire cross-section of the 3D print is simulated. The dynamic response of the fuser is simulated for the entire length of the sample; the reaction force of the roller that is applied to each point of the simulation can be seen in the top of Figure 64, the profile of the entire print can be seen in the middle, while the position of the roller can be seen in the bottom. Notice how the transient response of the fuser affects the print compressing significantly the leading edge. It is also important to highlight that the simulation assumes perfect registration between the layers, which is why the trailing edge appears perfectly square.

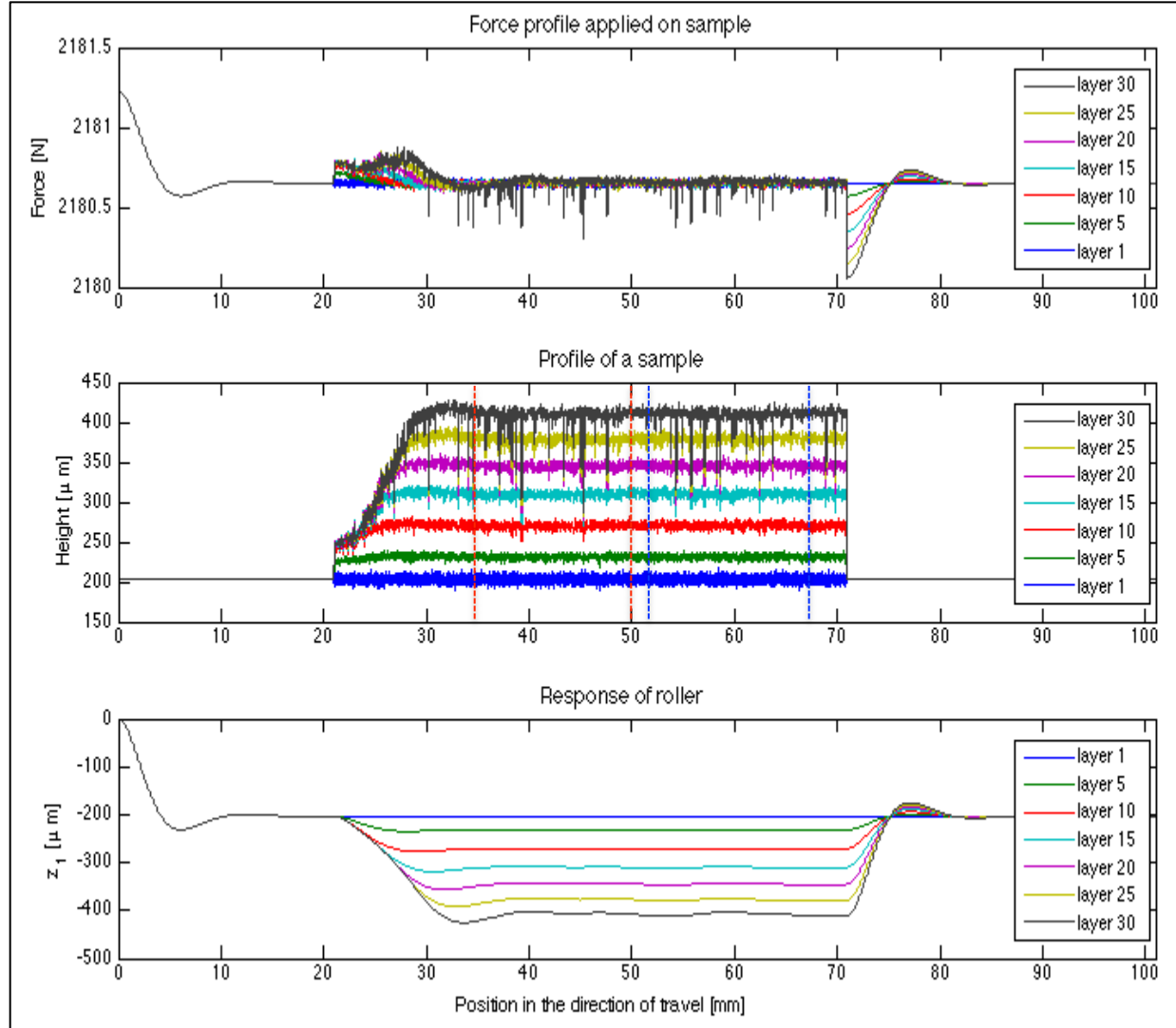


Figure 64. Simulation profiles: reaction force applied on the sample (top); sample as input to the fuser (middle), the measurement regions are marked by the dotted lines, leading edge in red and trailing edge in blue; response of the roller (bottom)

In order to compare to the data obtained through direct measurements with the profilometer, a specific region is sampled that correspond to the location in which the measurements occurred. The measurement regions are shown in Figure 64 (middle) enclosed by dotted lines, red for the leading edge and blue for the trailing edge. A section of the simulated EP3D print can be seen in Figure 65.

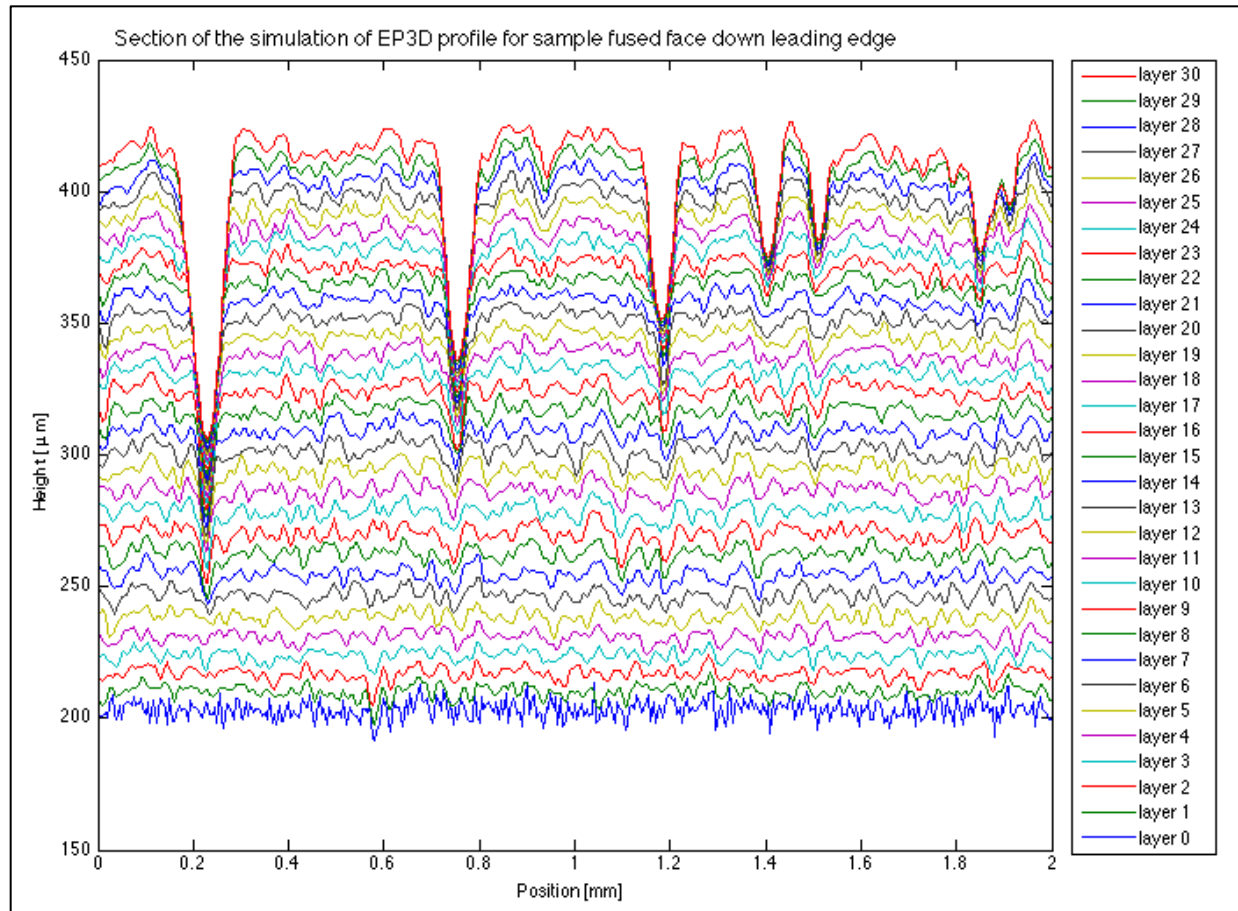


Figure 65. Section of the simulated EP3D print for a sample fused face up trailing edge

Similarly, measurements were taken across from the direction of travel to verify that the features observed in one direction were prevalent in the other. A comparison of the overall profile of a measurement taken in the direction of travel, the cross direction, and the simulated profile can be seen in Figure 66. Notice that the profile of the cross direction has similar features from the profile in the direction of travel, and the simulated profile has narrower features but of similar depth.

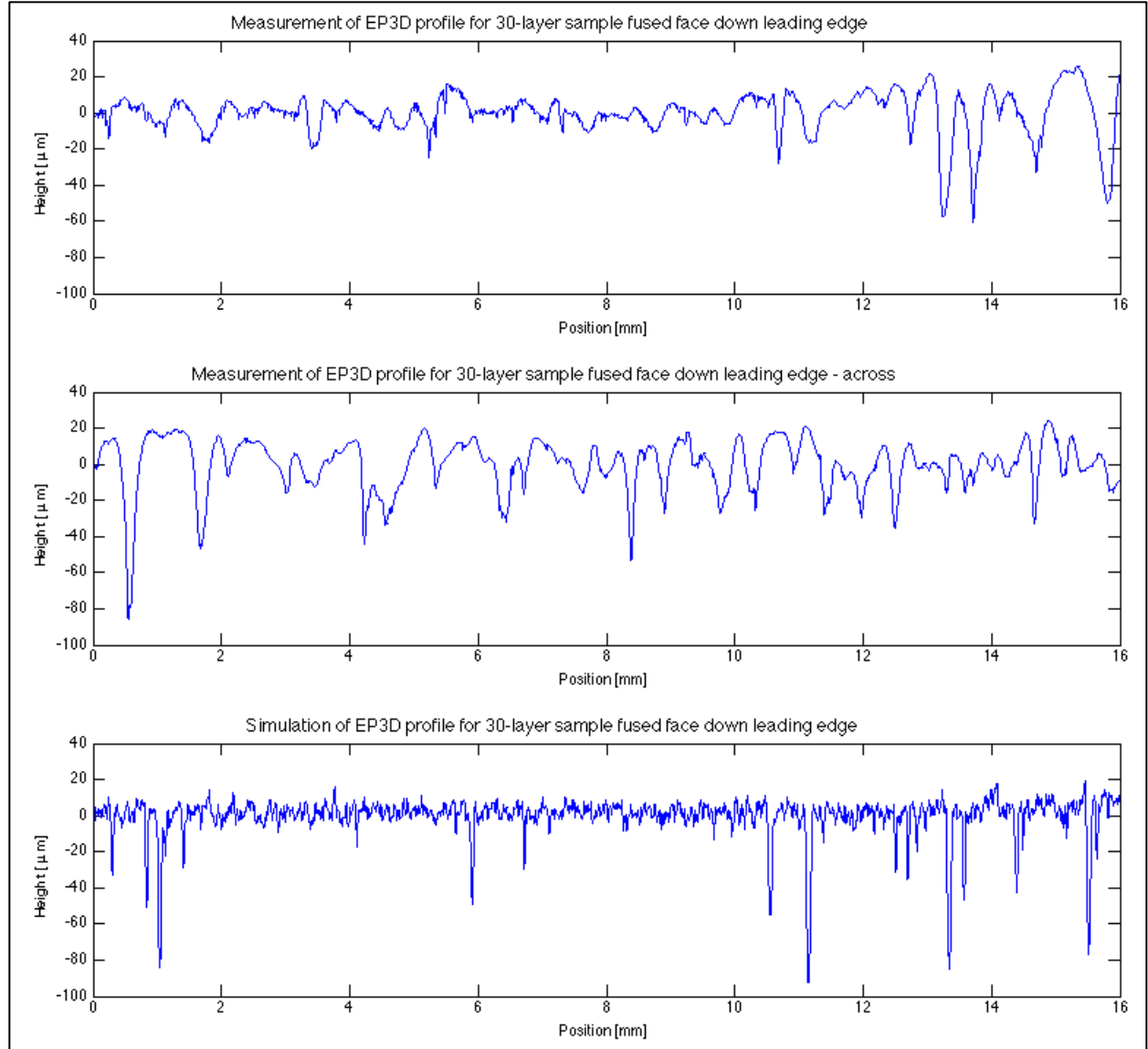


Figure 66. Comparison of profiles for a 30-layer sample fused face-up, leading edge: (top) measurement in the direction of travel, (middle) measurement across the direction of travel, (bottom) simulated profile

Due to the observation of the low-frequency content increasing with the number of layers (Figure 57), a low-pass filtering was applied after the transfusing step, each point is affected by its neighbors, a Gaussian kernel of length 5 and standard deviation of 1 was chosen based on the response observed in the data collected. The autocorrelation function for the simulated data can be seen in Figure 67.

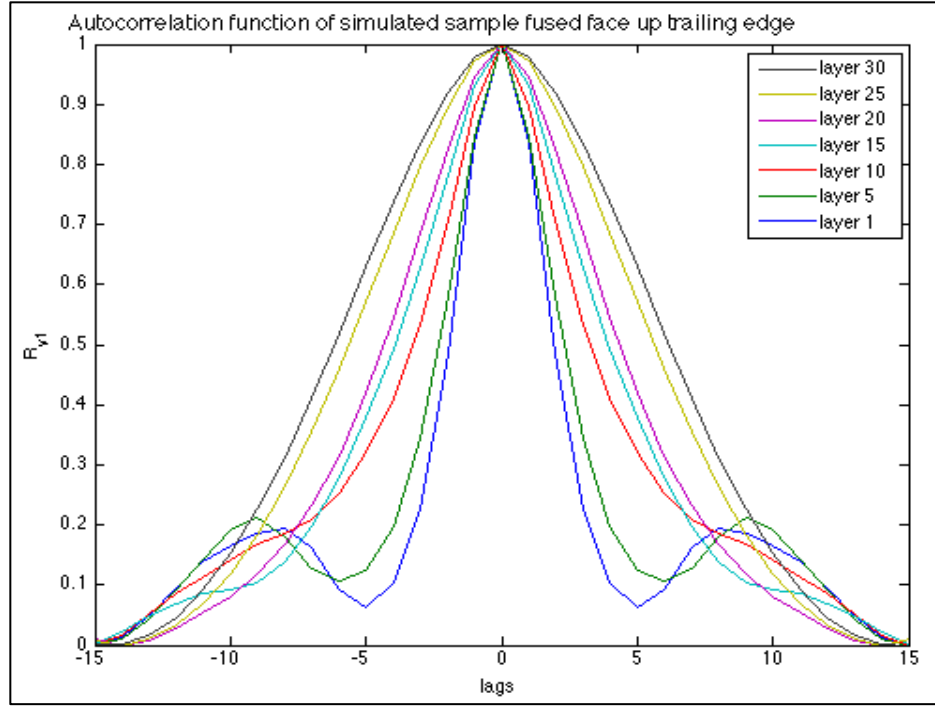


Figure 67. Autocorrelation function for simulated layers of a sample fused face up leading edge

The simulation model developed required significant tuning to find an appropriate threshold level that corresponded to the compliance of the interface. An optimization routine was used to find the appropriate threshold based on the roughness measurements from one side of the sample (e.g. leading edge) and validated against the data from the other side (e.g. trailing edge). A graph on the evolution of the Ra for the simulated data for various threshold levels, compared to the measurements taken from the trailing edge on samples fused face up and face down can be seen in Figure 68. Throughout the simulation it was observed that similar Ra values were achieved by very different structures (e.g. a profile with sharp spikes protruding from the base line and a profile with narrow holes into the structure). Since the Ra is a statistical measure (first order norm), a different metric may be needed to capture other aspects of the surface and the 3D printing process, similar to what was suggested by Boschetto et al. [93].

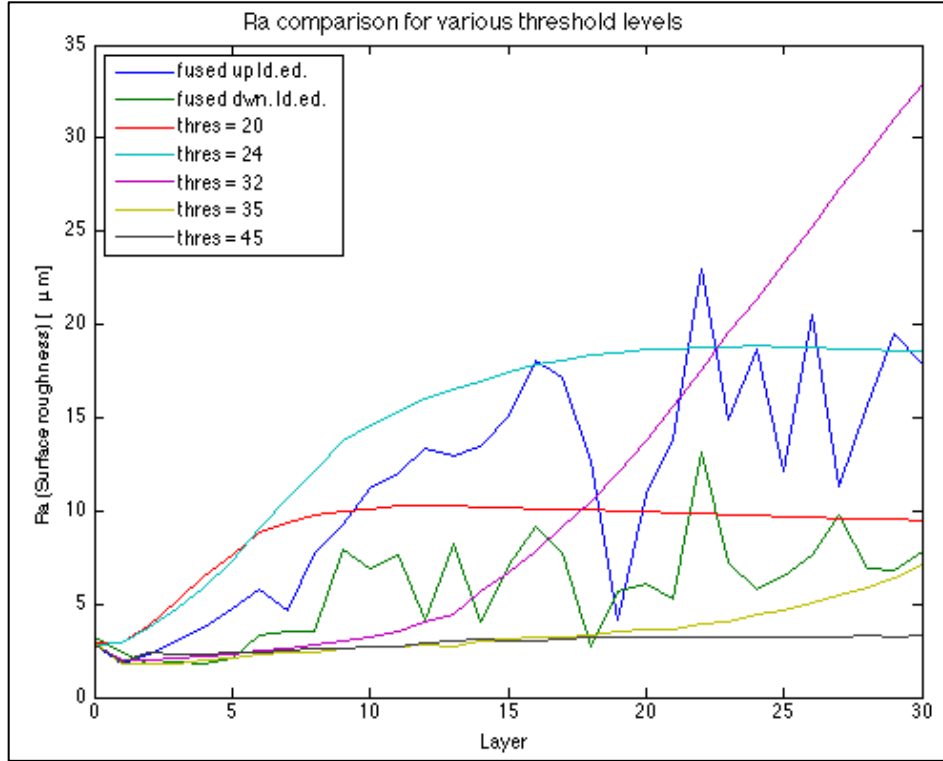


Figure 68. Ra for measured and simulated data at various threshold levels

6.4. Conclusion

The results indicate that the model provides a good approximation of the behavior of the EP3D printing process as the number of layers increase. The threshold variation showed that the surface roughness is dependent on the characteristics of the interface and a more compliant interface is desired; nonetheless, the surface roughness does not improve much above a threshold value of 45 μm for this number of layers. This implies that even having a very compliant interface that would perfectly conform to the surface to fuse newer particles, the surface would not improve any further. However, a more compliant interface is desirable and would significantly reduce the edge effect of the fuser transient response. A simulated surface profile for a higher threshold (80 μm) can be seen Figure 69. The evolution of the surface roughness can be estimated as the number of layers increase. An estimation of the evolution up to layer 50 can be seen in Figure 70. It is clear once again that even with a compliant interface, the surface roughness tends to increase as more layers are accumulated.

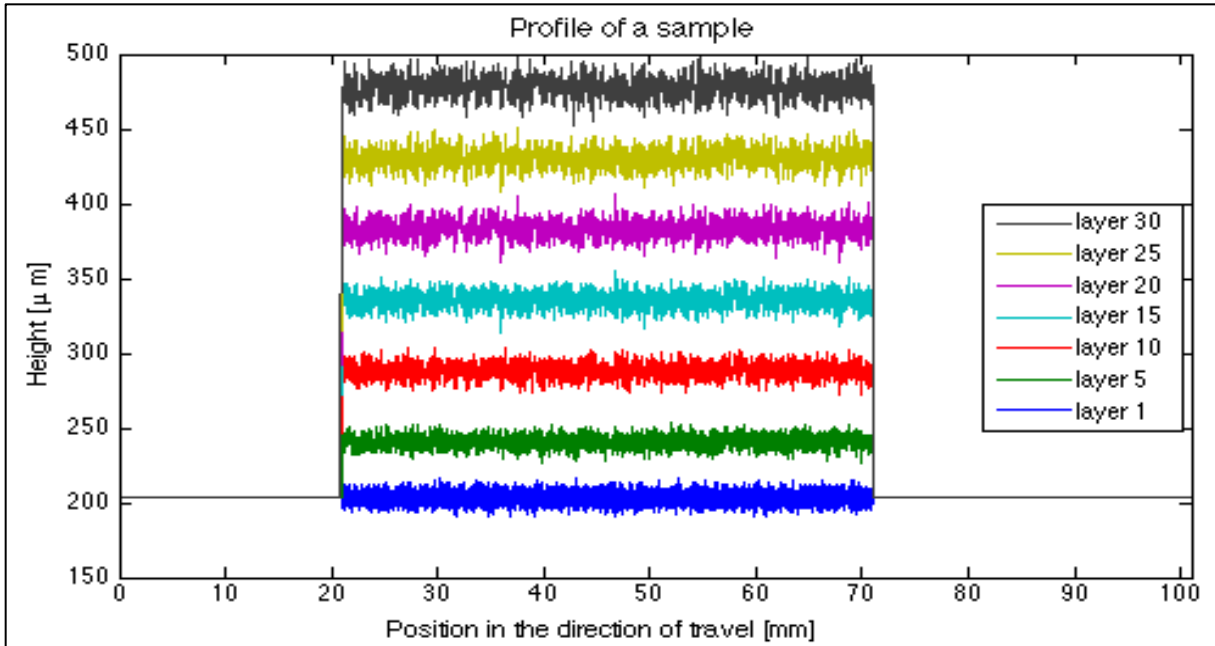


Figure 69. Simulated sample for 80 μm threshold

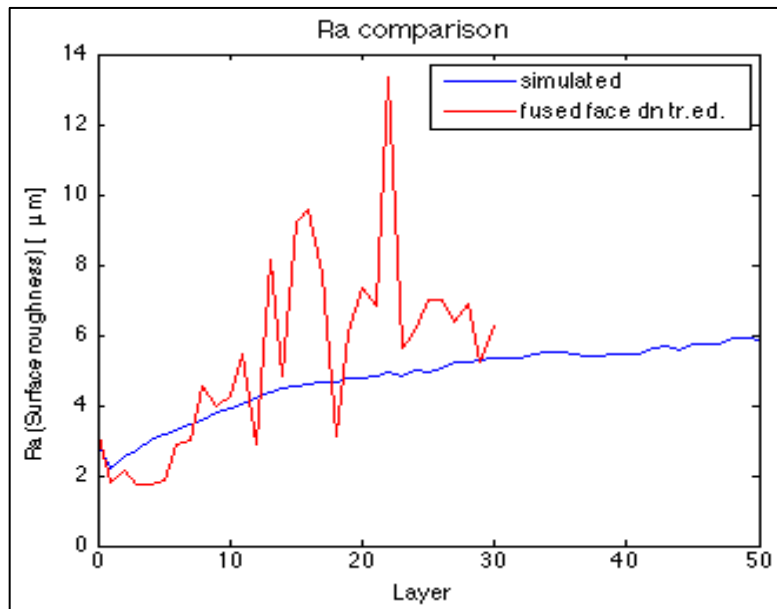


Figure 70. Ra comparison up to layer 50

This implies that an open loop implementation, even with perfect registration between layers and a compliant surface that had the desired release properties would still produce a rough surface. Considering the fact that envisioned applications would require thousands of layers, it is logical to conclude that this process would greatly benefit from a closed loop implementation in which the status of the surface is feedback to provide newer layers that would make the surface smoother.

Chapter 7. CONTROL OF EP3D PRINTED SURFACE

The control of surface defects has been seen as one of the main enablers of EP3D printing. This chapter presents the advances towards that goal based on the process characterization work and the insights developed for the evolution of defects described in previous chapters.

7.1. A passive approach through a more compliant interface

The layer-by-layer measurements and subsequent simulations indicated that a more compliant interface was desirable for the transfusing phase [94]. The samples fused face-down had smoother surfaces than the counterparts fused face-up which indicated that being in contact with the soft pressure roller was better than the hard heated roller of the fuser. The simulation suggested that having an interface that would conform to the structure would significantly reduce the surface roughness but ultimately increased surface roughness would still occur (see Figure 69).

A transfusing belt from an HP Indigo printer was selected as a suitable material for further trials. The rubber-like material was thin enough to go through the layer printing process without modifying the printer, it was more compliant than the soft pressure roller of the fuser, and it had decent release properties to enable its use as an intermediate substrate instead of the silicon coated Mylar.

Initial tests were unsuccessful because the material was too thick and did not allow for sufficient heat transfer resulting in very poor transfer and adhesion (see Figure 71.a.). The temperature of the fuser was increased and the speed was reduced but it was still insufficient to produce good transfection. The solution was to preheat the intermediate substrate after printing the new layer and before transfusing, that way the fuser only provided the final increment in temperature to make the particles stick to the previous layers. A first trial was done preheating the sample to 130 C, which fused the toner to the intermediate substrate (see Figure 71.b.); a temperature of 80 C was set for subsequent trials, which worked well to create a multi-layer structure. The transfer was not as good as the ones obtained with the Mylar (~60% for the Indigo belt vs. >90% for the Mylar) which

meant that a cleaning step was required to remove the toner left on the belt to prepare the intermediate substrate for printing a new layer since the amount of belt material was limited. Additionally the samples were more susceptible to jamming in the fuser, which damaged the structure (see Figure 71.c.). As a result, the fuser was modified to increase the gap and prevent sample damage.

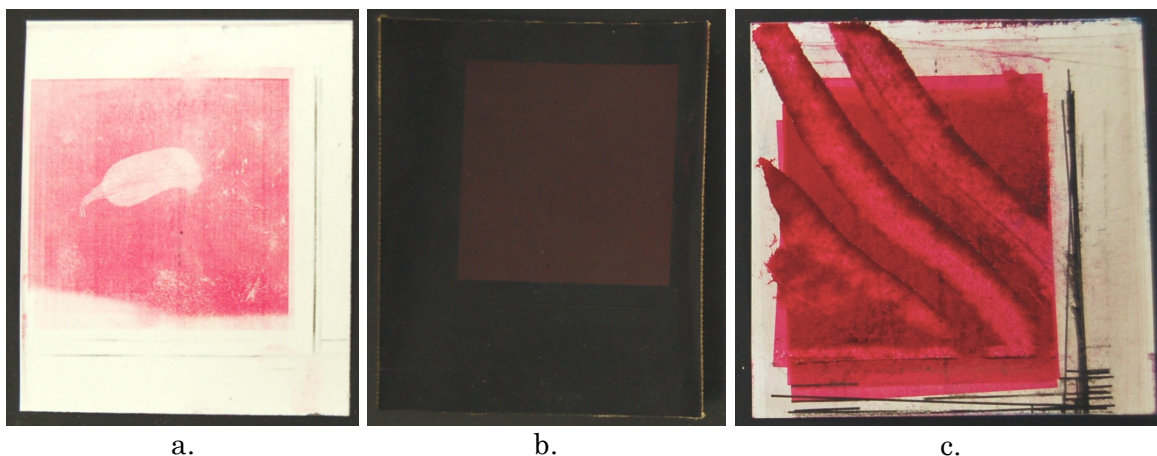


Figure 71. Failed attempts to perform EP3D printing using transfuse belt material as intermediate substrate: a. toner not fused to final substrate after going through fuser, b. toner fused to the intermediate substrate while preheating to 130 C, c. sample got caught in the fuser at layer 6.

After these modifications samples were produced of up to 100 layers with a smoother surface. However, because of the poorer transfer efficiency that was described above, less material was deposited which resulted on thinner structures than in the counterpart structure produced with the Mylar interface. The substrate used, as well as a 14-layer sample and a 100-layer sample can be seen in Figure 72.

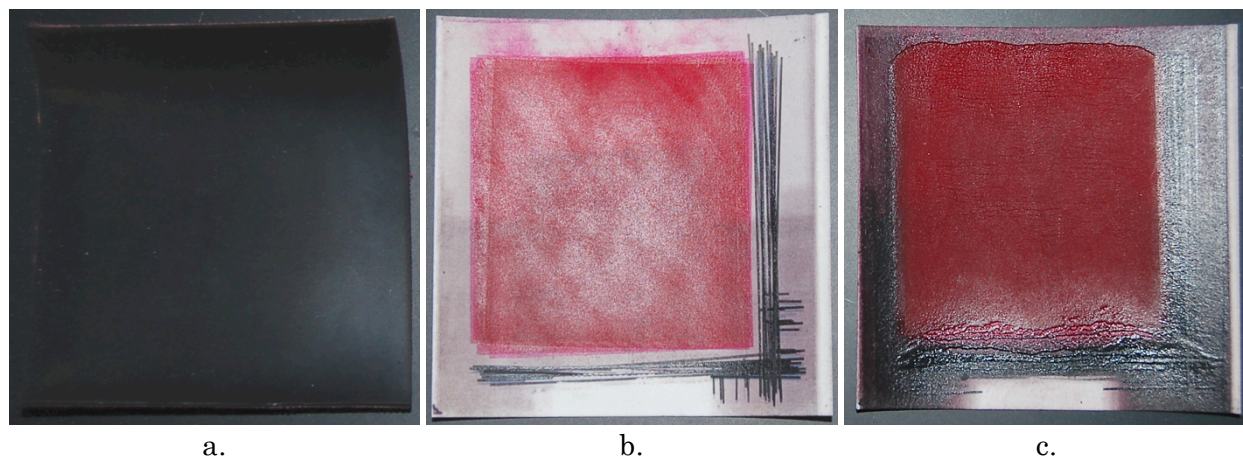


Figure 72. a. Transfuse belt material after being used as intermediate substrate; b. 14-layer sample; c. 100-layer sample

The 100-layer sample constructed under this methodology was measured every 10 layers. The results showed that the surface roughness certainly improves from the samples using Mylar as the intermediate substrate, especially from the ones fused face up (see Figure 73). In the range 0-30 layers, the results with the new interface are similar to those obtained by fusing face down. In addition, the sample did not exhibit significant difference between the leading edge and the trailing edge.

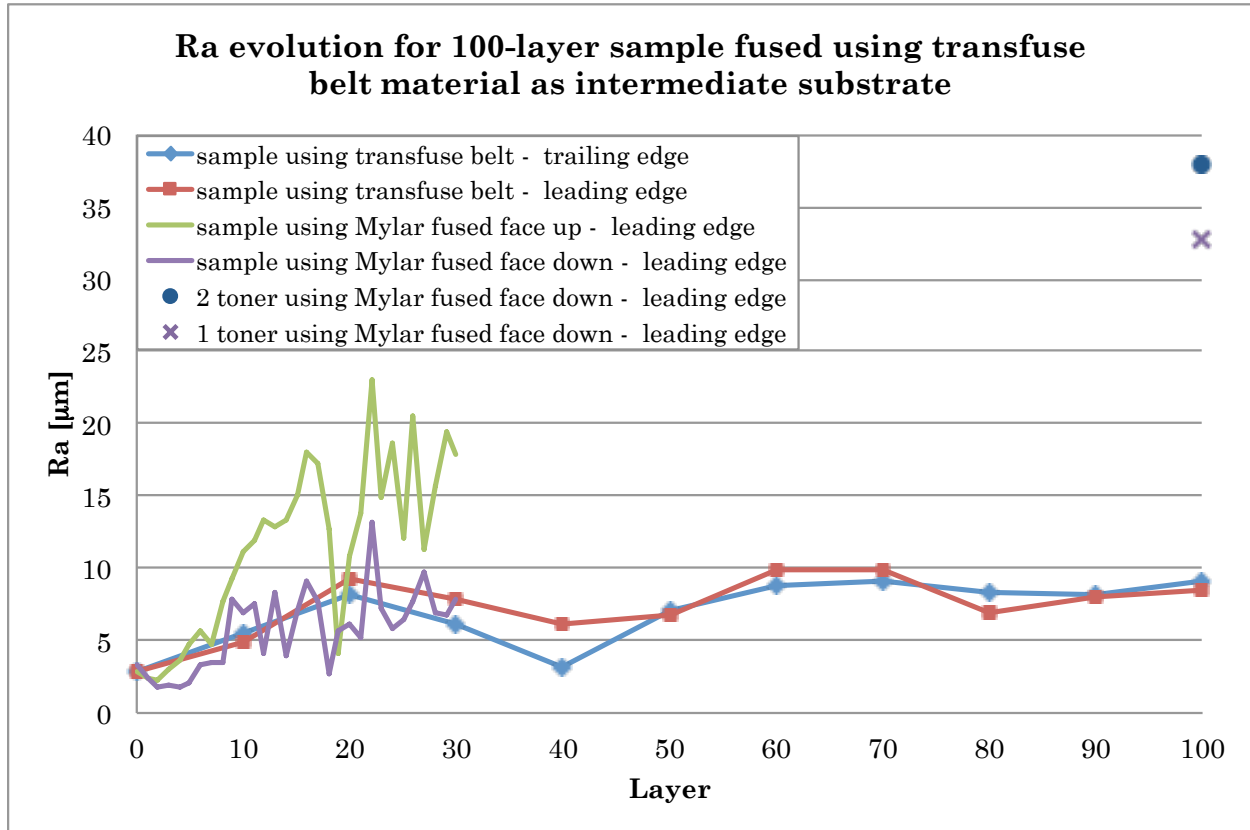


Figure 73. Ra evolution for 100-layer sample fused using transfuse belt material as intermediate substrate and compared to readings from samples using Mylar as intermediate substrate

Two 100-layer samples were constructed using Mylar as the intermediate substrate (see Figure 74) but were difficult to measure; many times the variation was beyond the measuring capabilities of the profilometer (variation greater than 400 μm). The samples were constructed fusing face down; when trying to build the samples fusing face-up, the surface would degrade very quickly resulting in damage to the sample. The highest structure built fusing face-up had 64 layers of 1 toner at 100% fill. The 100-layer sample with 2 toners built using the Mylar interface and fused face down is the thickest sample created so far at 0.82 mm (0.032 in) ignoring the base substrate thickness. Similarly, the

100-layer sample with 1 toner using the Mylar interface reached a height of 0.51 mm (0.020 in). In contrast, the 100-layer sample constructed using the more compliant interface only reached a height of 0.3 mm (0.012 in).

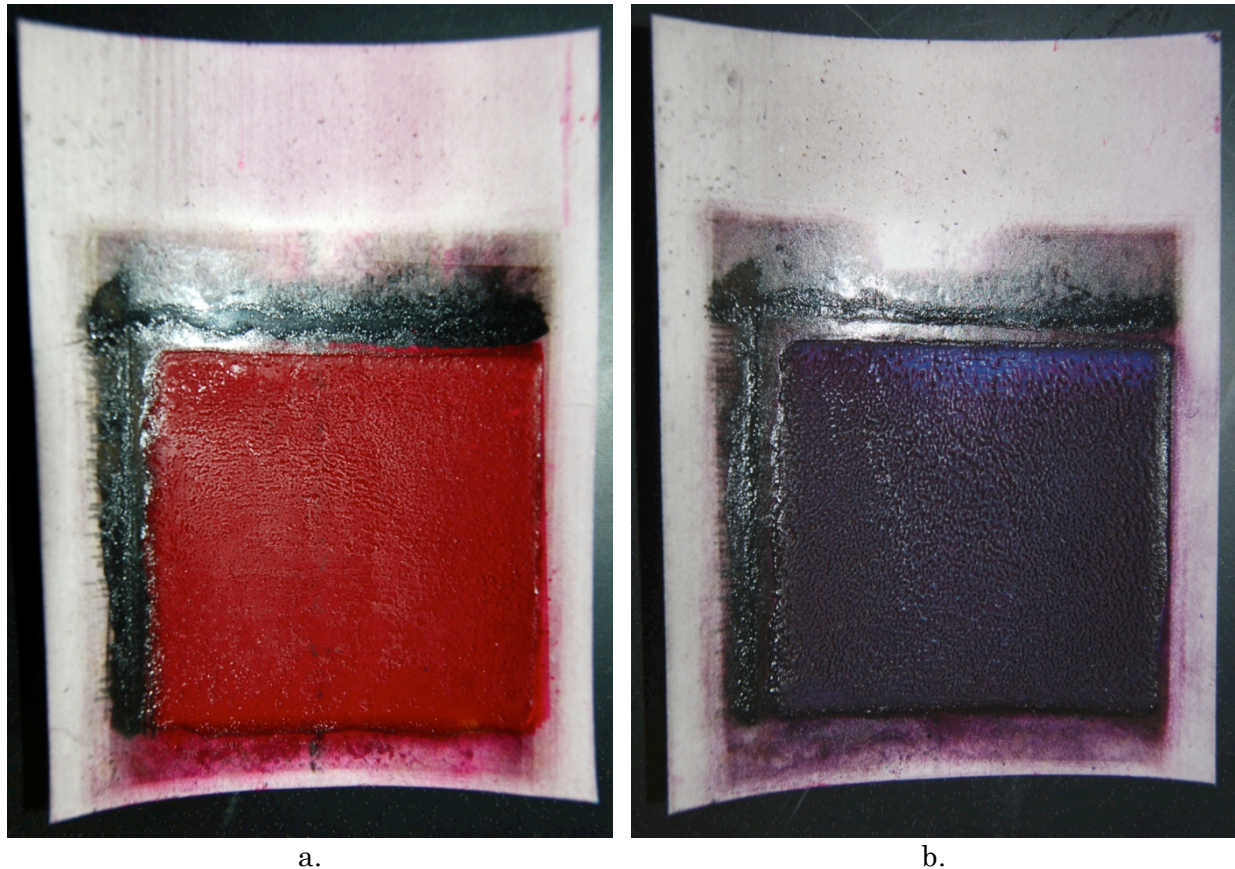


Figure 74. 100-layer samples constructed using Mylar as intermediate substrate: a. 1 toner (M) at 100% fill; b. 2 toner (CM) at 100% fill

Comparing the samples, it is clear that the sample produced using the belt material as an intermediate substrate is much smoother than the ones produced with the Mylar substrate and that is reflected in the Ra values (see Table 10). A comparison of the profiles can be seen in Figure 75; notice that the features in the surface of the sample produced with the belt material are significantly smaller than the ones in the sample produced using the Mylar interface. The mean level was subtracted in both to facilitate comparison.

Table 10. Ra measurements for 100-layer samples

Intermediate substrate	# Toner	Layer #	Height [mm]	Ra [μ m]	
				Leading edge	Trailing edge
Silicon coated Mylar	2 (CM)	100	0.82	37.829	33.700
Silicon coated Mylar	1(M)	100	0.51	32.794	32.098
HP Indigo Belt	1 (M)	100	0.30	8.471	9.107

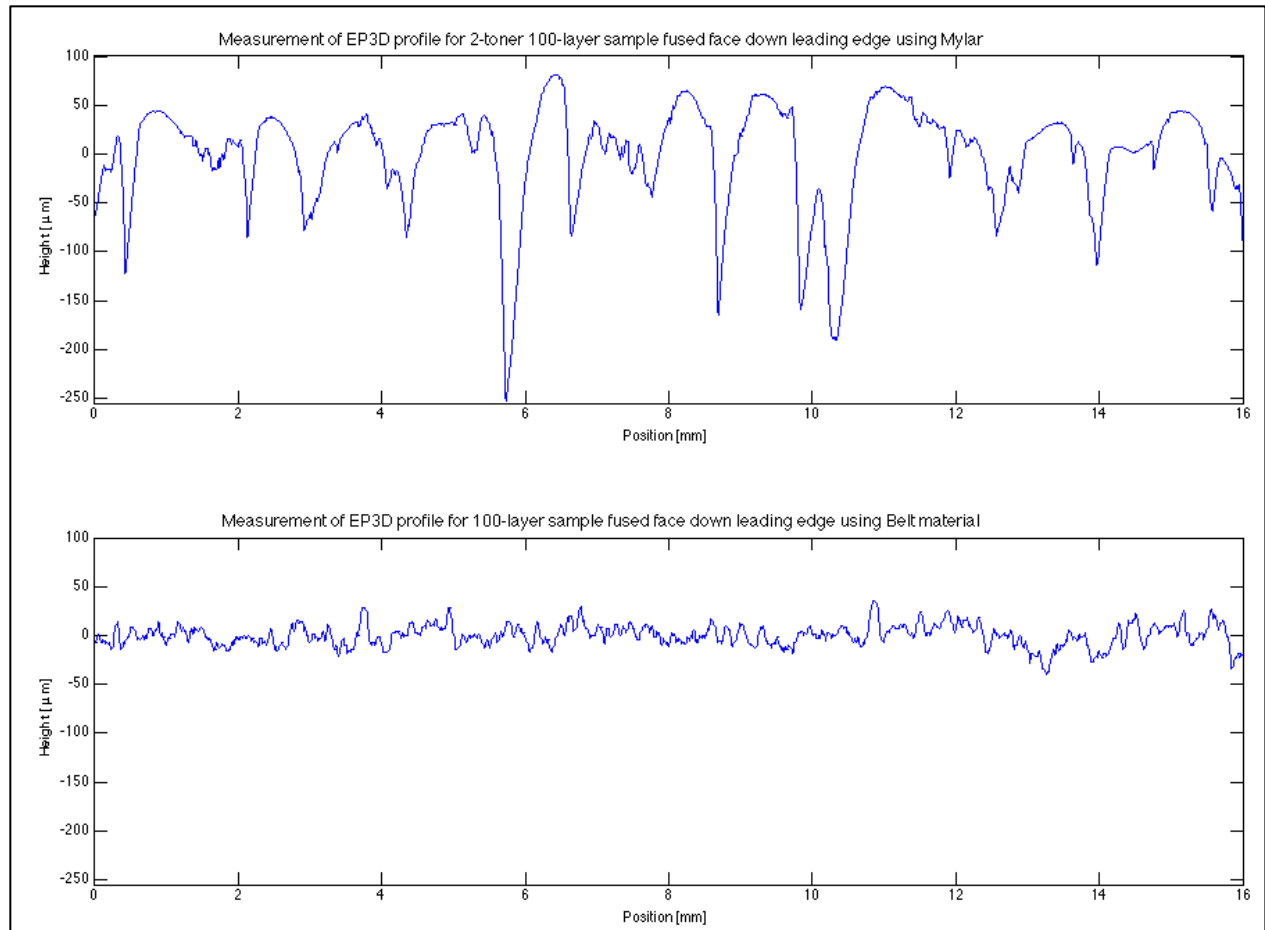


Figure 75. Comparison of measured profiles for 100-layer samples: (top) 2-toner produced with Mylar interface, (bottom) 1-toner using belt interface

It is important to acknowledge that the comparison is not really well posed since the structures are not of the same height; therefore, it is unclear if the smoothness achieved with the more compliant interface is due to the nature of the interface or having a thinner structure. Nonetheless, the 100-layer sample constructed with the Indigo belt was thicker than the 30-layer samples produced with the Mylar interface (~ 0.22 mm) and smoother, suggesting that the more compliant interface was indeed contributing to achieve a smoother structure.

The results with this passive approach are encouraging; however, the resulting samples are not ideal, surface defects still form although much smaller but the transfer efficiency decreased significantly. The next step is to use feedback to create a control strategy that may produce better results.

7.2. Feedback control approach

The initial approach to perform control using feedback is to complete each layer in two passes: the first pass is the layer, printed and transfused as usual; then the surface is sensed to determine the regions where more material is needed, and a new image of compensation is printed and transfused with material only in those regions that were identified, becoming the second pass. A flow diagram of the algorithm can be seen in Figure 76.

The compensation layer is constructed comparing each point with the maximum height of the structure and evaluating if the difference is above a threshold; if so, more material is required at that location. This creates a binary image that marks the locations to deposit more material. Then the development process is simulated as before by assuming that the number of particles developed comes from a normal distribution (for the points where more material is desired). This compensation layer is placed on top of the existing structure and the transfuse process is simulated as before. The process is repeated at each layer.

This strategy was chosen because the nature of the EP process would make very difficult to implement a real-time control strategy for the amount of material deposited at each location. Furthermore, the only step of the EP process where each point is addressed is during the exposure where light is modulated to create the latent image on the photoreceptor; at every other stage of the process the print is treated uniformly.

The simulation model developed for the EP3D printing process was used to evaluate the effectiveness of the strategy. A sample was simulated as a reference without applying any compensation (see Figure 77). Similarly, a sample was simulated applying a second pass for compensation at each layer (see Figure 78).

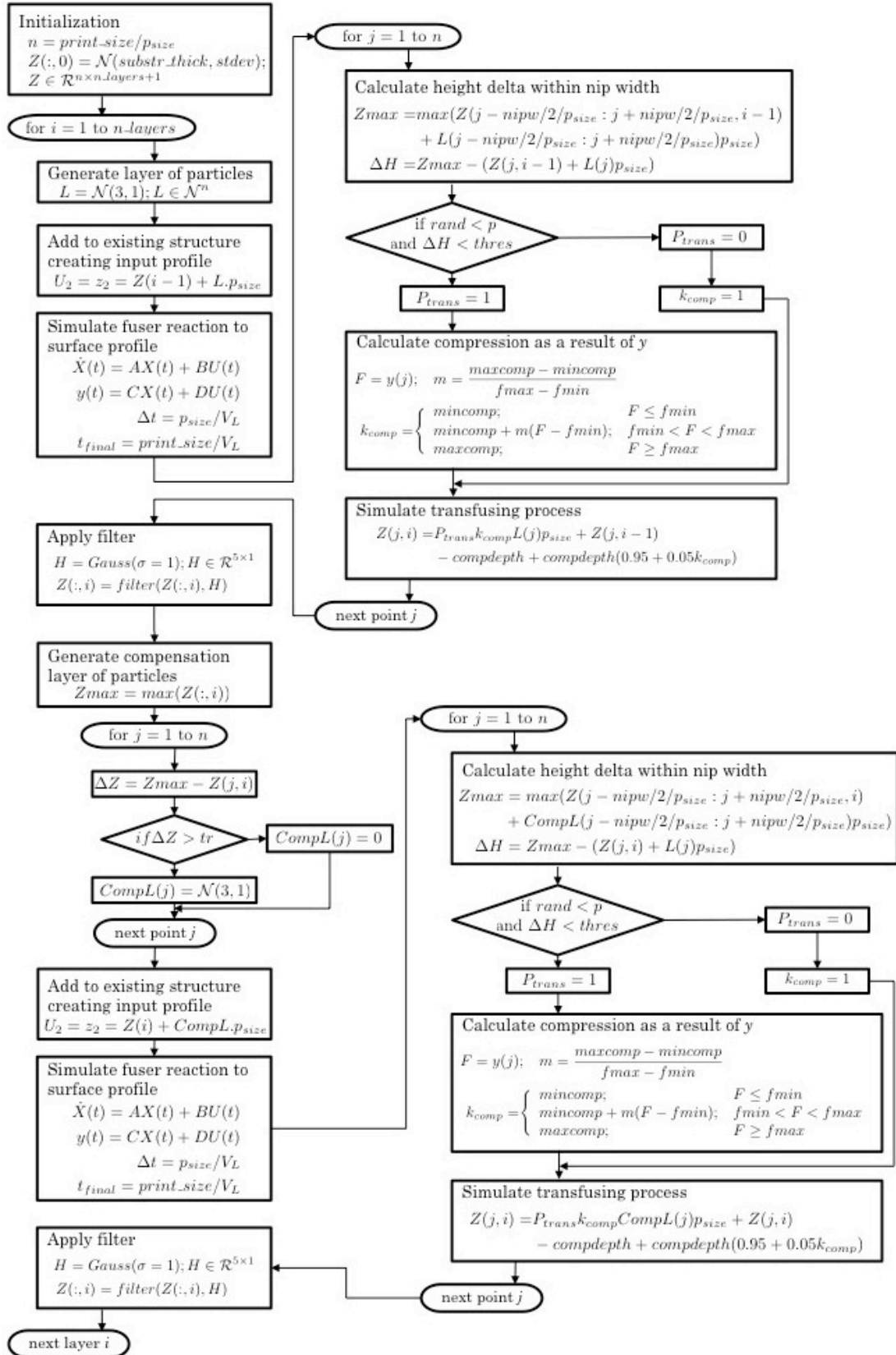


Figure 76. Flow diagram of the simulation algorithm with compensation

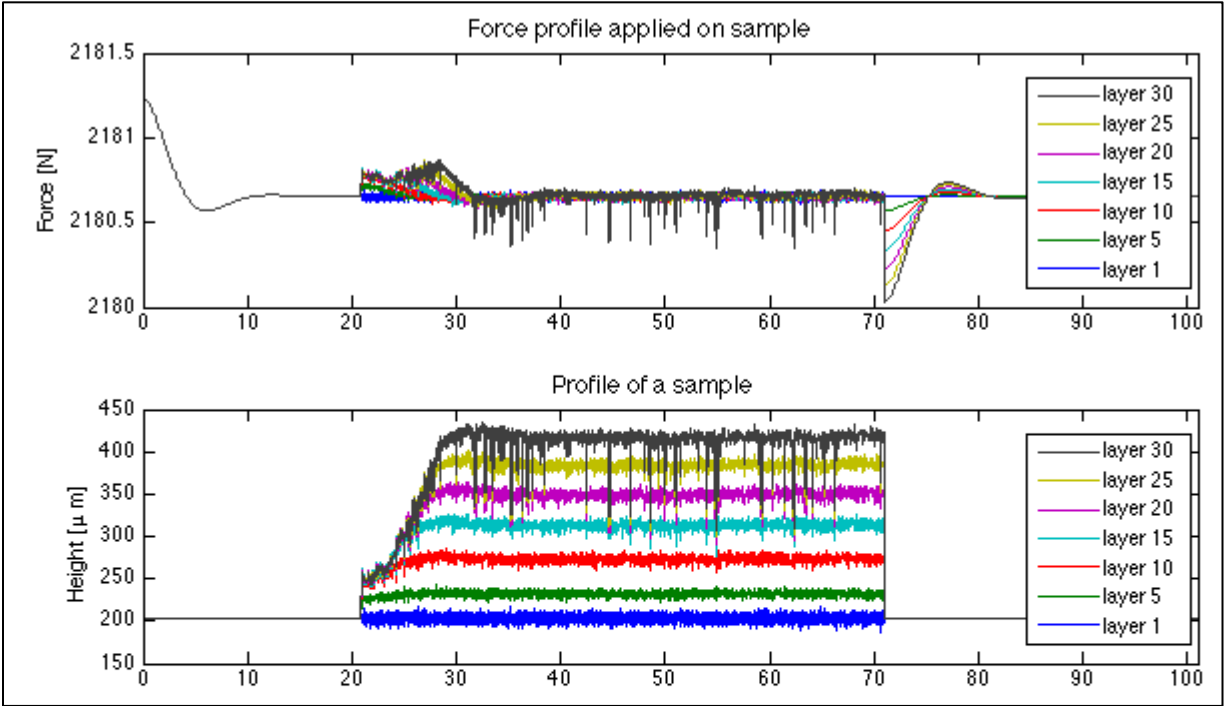


Figure 77. Simulated profiles of force, and sample generated without compensation

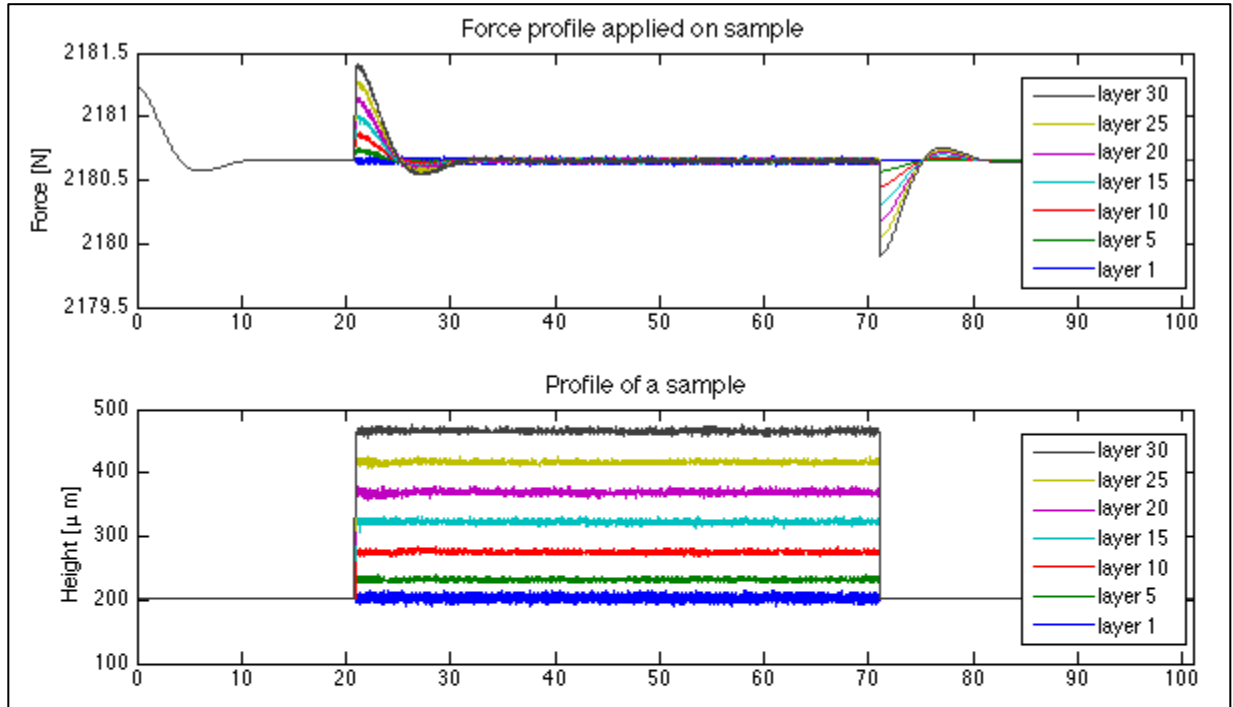


Figure 78. Simulated profiles of force and sample generated with compensation

The results show significant improvement, both in the edge of the sample as in the rest of the surface. The edge effect is dominated by the transient response of the fuser as it is seen

in the simulation without compensation; however, feeding back the status of the surface helps the printed structure to maintain the intended geometry. A comparison of Ra values that would be obtained from both simulations and the actual measurements taken on the 30-layer sample fused face down can be seen in Figure 79. The surface roughness on the simulated sample with compensation stayed below the surface roughness of the base substrate, showing that the feedback control would indeed work to reduce the surface defects in EP3D printing.

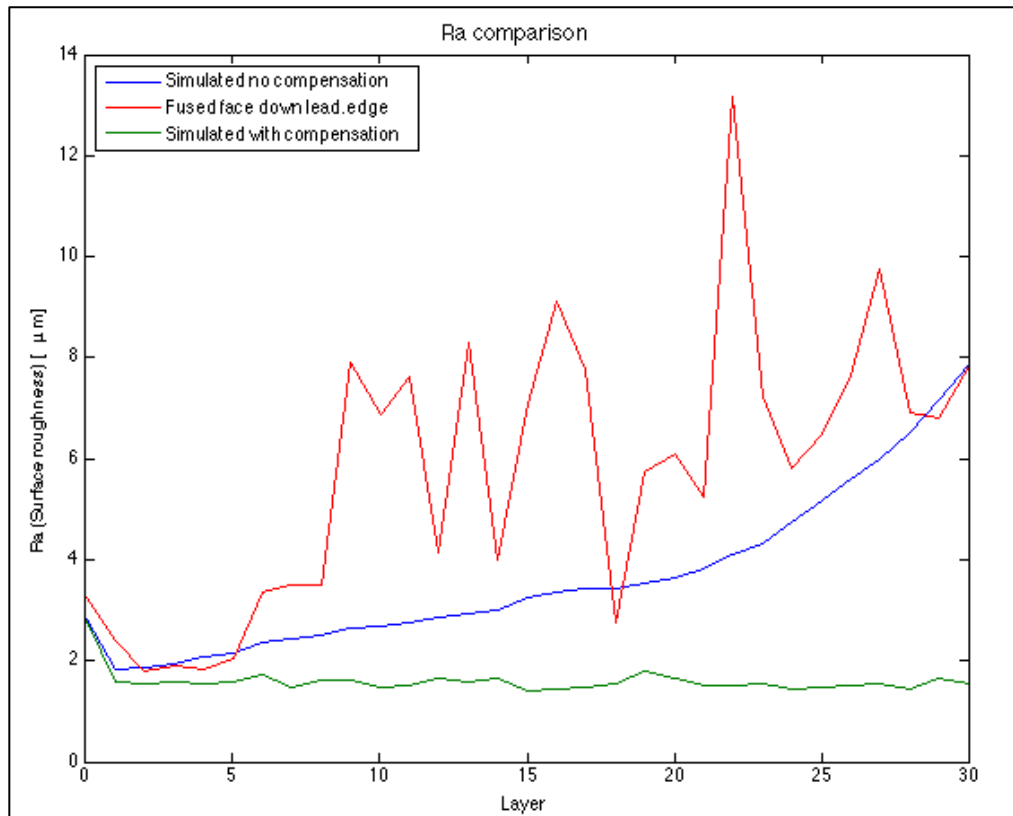


Figure 79. Comparison on Ra for 30 layers from simulated data with no compensation, with compensation and the measurements on sample fused face down

This control strategy relies on several assumptions that may not hold in an actual implementation, the most important are:

1. Perfect sensing: The simulation model has perfect information on the status of the surface. In a real implementation, the sensing capability would estimate the state of the surface with a certain degree of uncertainty based on the resolution of the sensor and the methodology.

2. Perfect registration between layers: The simulation assumes that the layers are all stacked perfectly on top of each other and the particles line up. In reality, it has been observed that particles organize differently and restructure in the process. Moreover, compensation layers would require perfect registration to indeed deposit material in the desired location and not somewhere else.
3. Very fine resolution for development: The simulation assumes that each point is addressable and the sample size corresponds to the average toner particle size. Real EP systems have a resolution of 600 dpi (or 1200 dpi), meaning that each addressable dot has a size of 42.3 μm (or 21.2 μm) while the particle size is only 5 μm approximately.

7.3. Conclusion

Two approaches to control the surface of the EP3D print were presented, one passive based on the compliance of the interface, and one active based on feedback and a two-pass methodology to construct and compensate for each layer.

The passive approach showed that a more compliant interface is desirable and creates a smoother surface; however, the thicker more compliant interface made more difficult the transfuse process due to poor heat transfer and poor transfer efficiency. Different materials may be needed to improve those aspects both in the intermediate substrate, the printing material, and the fuser.

The feedback approach seems promising but it has only been tested in simulations. There are several obstacles to overcome before this strategy can be implemented: automation of the process ensuring good registration between layers, and a 3-dimensional surface sensing capability.

Chapter 8. SURFACE IMAGING FOR COMPENSATION OF DEFECTS

Sensing the surface of the EP3D prints has proven to be challenging. The profilometer readings offer a lot of details on a line of the surface and it is unreal to try to use the same instrument to construct a 3D reading. Other instruments such as 3D scanners do not have the necessary resolution to distinguish the features on the EP3D prints. Imaging seems to be the more realistic approach, the entire sample can be analyzed and there is no need to contact the sample which may disturb the surface. However, extracting three-dimensional information from images that are inherently two-dimensional is not a trivial process, particularly at the scale of the features present on EP3D prints. This chapter summarizes the efforts in this area with the goal in mind of using the information extracted for control purposes.

8.1. Preliminary testing

Several techniques have been explored to image the surface. A 5 megapixel DSLR camera was used as the sensor. The first set-up (see Figure 38.a.) included a line source illumination on the side of the samples which highlighted its topography. Clamping the sample was a challenge because it was desired to have no obstruction of the light reaching the sample from the edge. In the end, a suction plate was selected to hold the sample flat without the need for further components to get in the way. Sample images from this setup can be seen in Figure 80. The images captured under this setup were encouraging since subtle features like pressure marks from the Mylar sheet used as an intermediate transfer can be seen in both the left and the right of the images. The setup worked especially well for features perpendicular to the light direction, the features parallel to the light direction were not highlighted. This last observation suggested that many more light directions should be used in order to detect all the features in the surface.

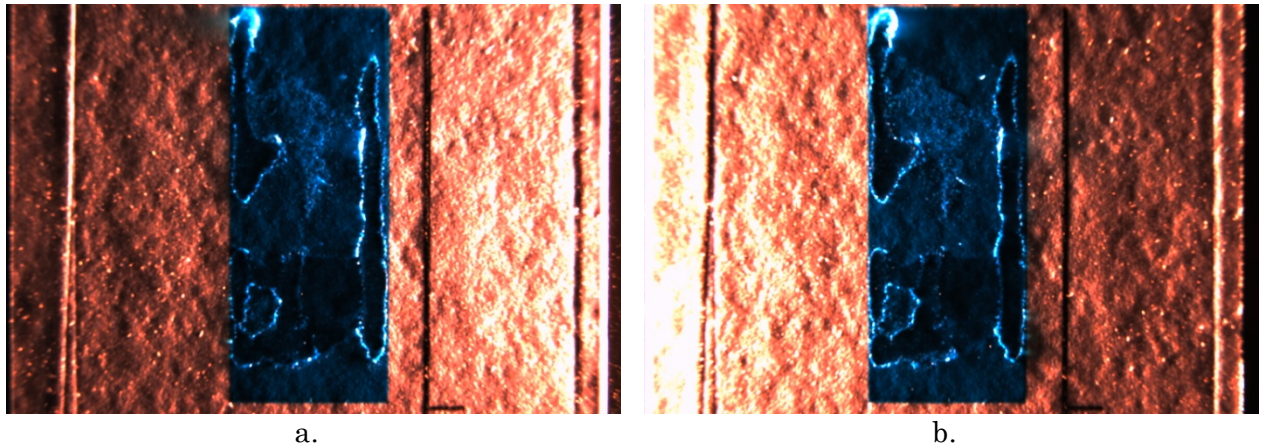


Figure 80. 2-layer sample imaged on the setup with line source illumination from the right (a.) and the left (b.)

8.2. Reflectance Transformation Imaging (RTI)

A technique that captures images with several illumination directions to improve the visualization of the object to image is called Reflectance Transformation Imaging (RTI), developed and promoted by the Cultural Heritage Imaging (CHI), a nonprofit organization, as a way to reveal further details from the surface of art/cultural pieces. This technique is based on Polynomial Textural Mapping (PTM) in which an image is converted into a structure in which each pixel contains not only color information (RGB) but also an additional dimension that describes of how light is reflected from it (LRGB). Those texture maps are generated from a set of images of distinct illumination directions from which the light direction is known or can be retrieved. The maps allow for interactive relighting of the object in the scene by interpolation of the known conditions, revealing more detail than traditional, static images. CHI provides open-source software to compile the images into PTMs and interactively display the resulting image.

A setup was created to capture images with different illumination direction; two reflecting spheres were included to allow for light direction estimation. The setup can be seen in Figure 38.b. and sample images can be seen below.

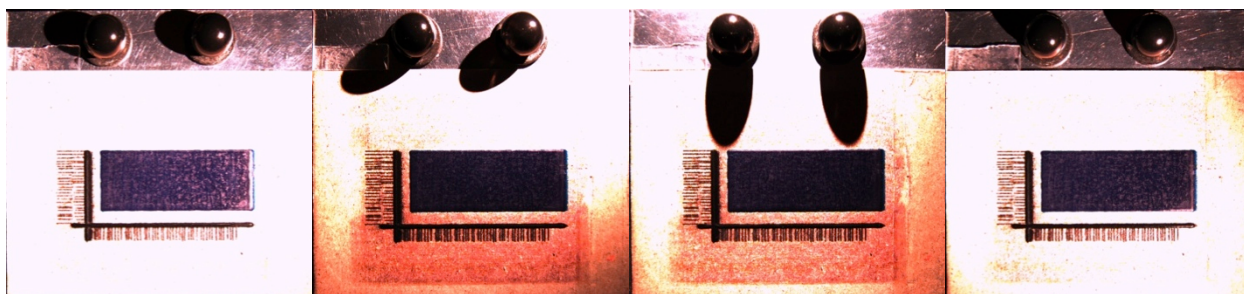


Figure 81. Sample images taken from different illumination angles

Similarly, a dome had been constructed at the Center for Imaging Science as a first year project. The dome contains 23 LEDs spread out to illuminate an object from different angles and uses a DSLR camera to capture the images. A controlling software was developed in Labview to sync the illumination and capture. The images were analyzed using the software from the CHI and a PTM version of the images can be obtained. The dome simplifies the process because the light positions are known and isolates other sources of light that may contribute to create unwanted effects on the outcome.

One of the preliminary samples of 25 layers was imaged under this dome and a PTM was constructed. The visualizing software has several enhancements or visualization modes; some sample images are shown below:

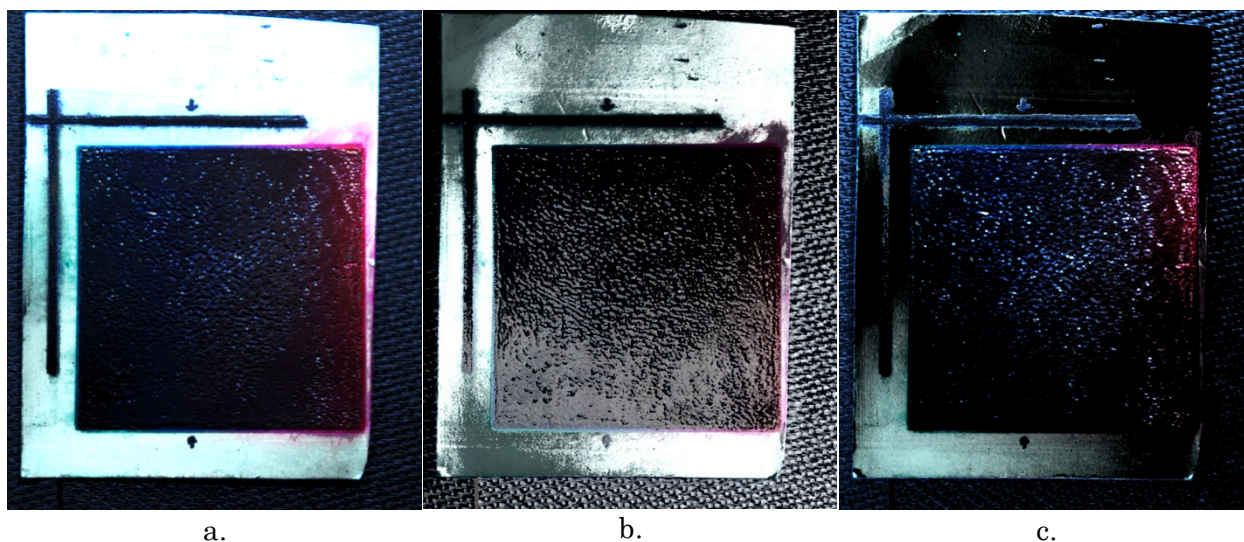


Figure 82. Images of the 25-layer sample recreated from the PTM representation: a. lighted from top-right; b. specular enhancement; c. diffuse gain

Although this is just a visualization tool, it shows how combining information from different illumination conditions can capture texture. Encouraged by these results, a more flexible

setup was built and a new camera was purchased to image the surface of the EP3D prints. The selected camera was the Flea 2G 5 MP Color from Point Grey with a Fujinon 12.5 mm lens due to the ease of interface with Matlab, good sensitivity, and 5 MP for a sample of 50 mm would offer a resolution of under 25 μm per pixel which is comparable to the 1200 dpi resolution of a laser printer.

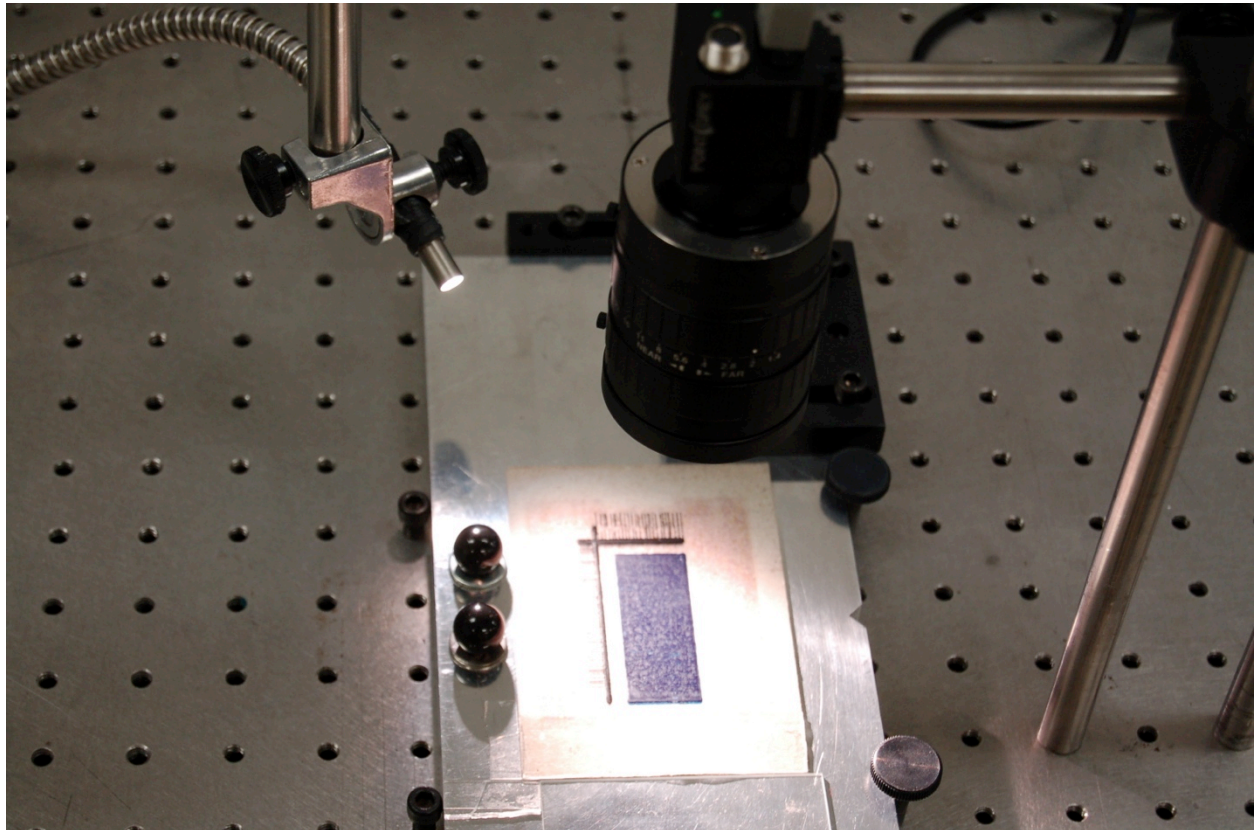


Figure 83. Imaging set up with PointGrey camera

The reflecting balls were used to determine the light direction, first simply placing them in the field of view of the camera along with the sample; later the spheres were placed by themselves and imaged with predetermined locations for the light source that were used also for imaging the sample (see Figure 84). This strategy provided more space in the image to focus on the sample with all the resolution available from the camera. The sample with 100 layers and 2 toners was imaged under this set up; some images can be seen in Figure 85 and Figure 86.

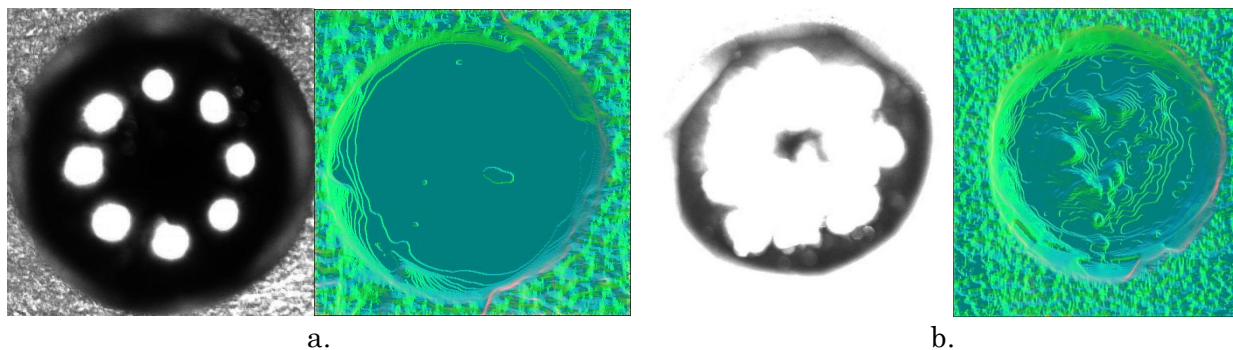


Figure 84. Compiled images of a reflecting sphere with the different light directions and the detected edges for: a. 8 directions, b. 24 directions

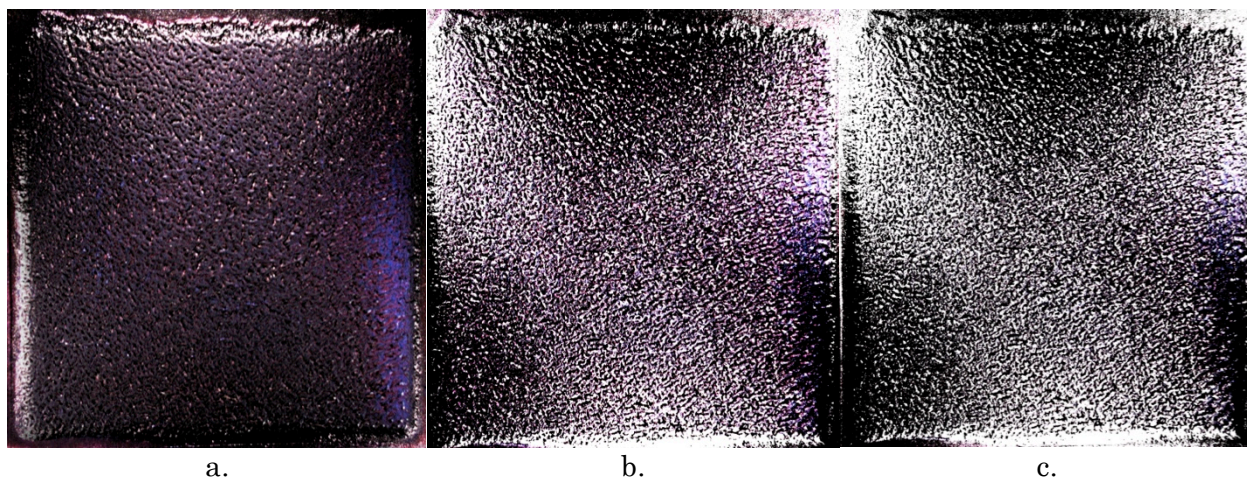


Figure 85. 100-layer 2-toner sample recreated using the PTM file generated with 8 light directions: a. illuminated from top, b. illuminated towards the center of the sample, c. illuminated towards the center enhancing specular reflections

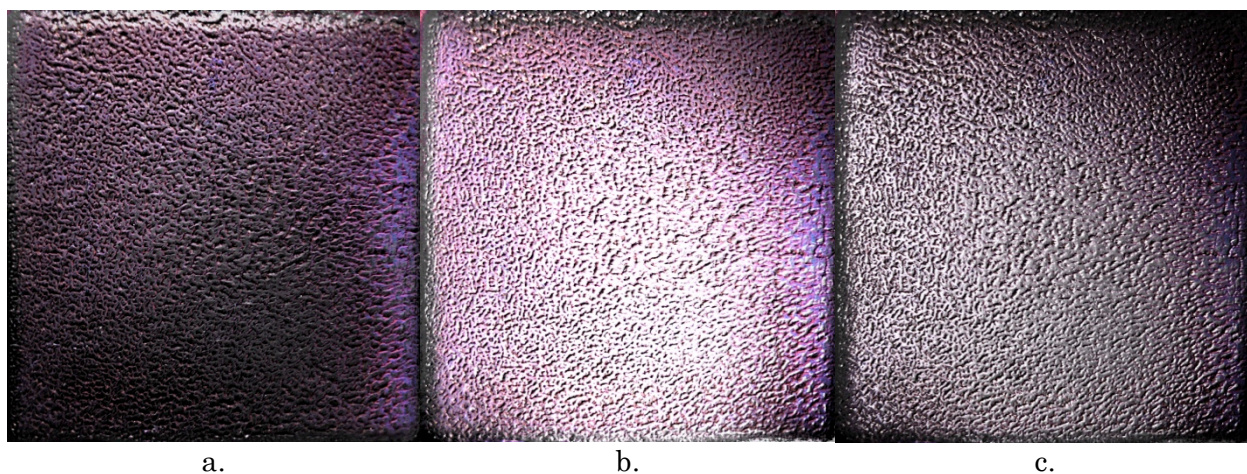


Figure 86. 100-layer 2-toner sample recreated using the PTM file generated with 24 light directions: a. illuminated from top, b. illuminated towards the center of the sample, c. illuminated towards the center enhancing specular reflections

Using more light directions allowed for better reproduction of the surface, especially under conditions when the light was coming straight from above the sample. This effect is related to the light directions used to capture the original images and the coverage can be seen in the reflections compiled on the reflecting ball presented in Figure 84.

Nevertheless, the PTM representation of the sample showed that the defects (namely cracks and holes) are not only visible but also highlighted by changing the illumination. Having light coming from more angles is desirable since it highlights different parts of the sample or different sections of the contours of the holes, making it easier to identify areas where more material is needed.

8.3. Creating compensation images for feedback control

A few tests have been conducted to determine areas where more material is needed and create an image to compensate for those imperfections. The first approach was to take an image of an EP3D printed sample and perform simple adjustments of its histogram (e.g. contrast, brightness, exposure) to allow for thresholding, creating a new binary image that dictates where more material is needed (i.e. where to fill the cracks and holes).

The sample with the more pronounced defects (100 layers 2 toners fused face down using Mylar) was scanned using a flatbed scanner (see Figure 87.a.). Then the image was converted to grayscale, the contrast, exposure, and gray levels were adjusted to highlight (darken) the holes on the surface, identifying areas where more material was needed (see Figure 87.b.). A binary image was created by thresholding this image (see Figure 87.c.)

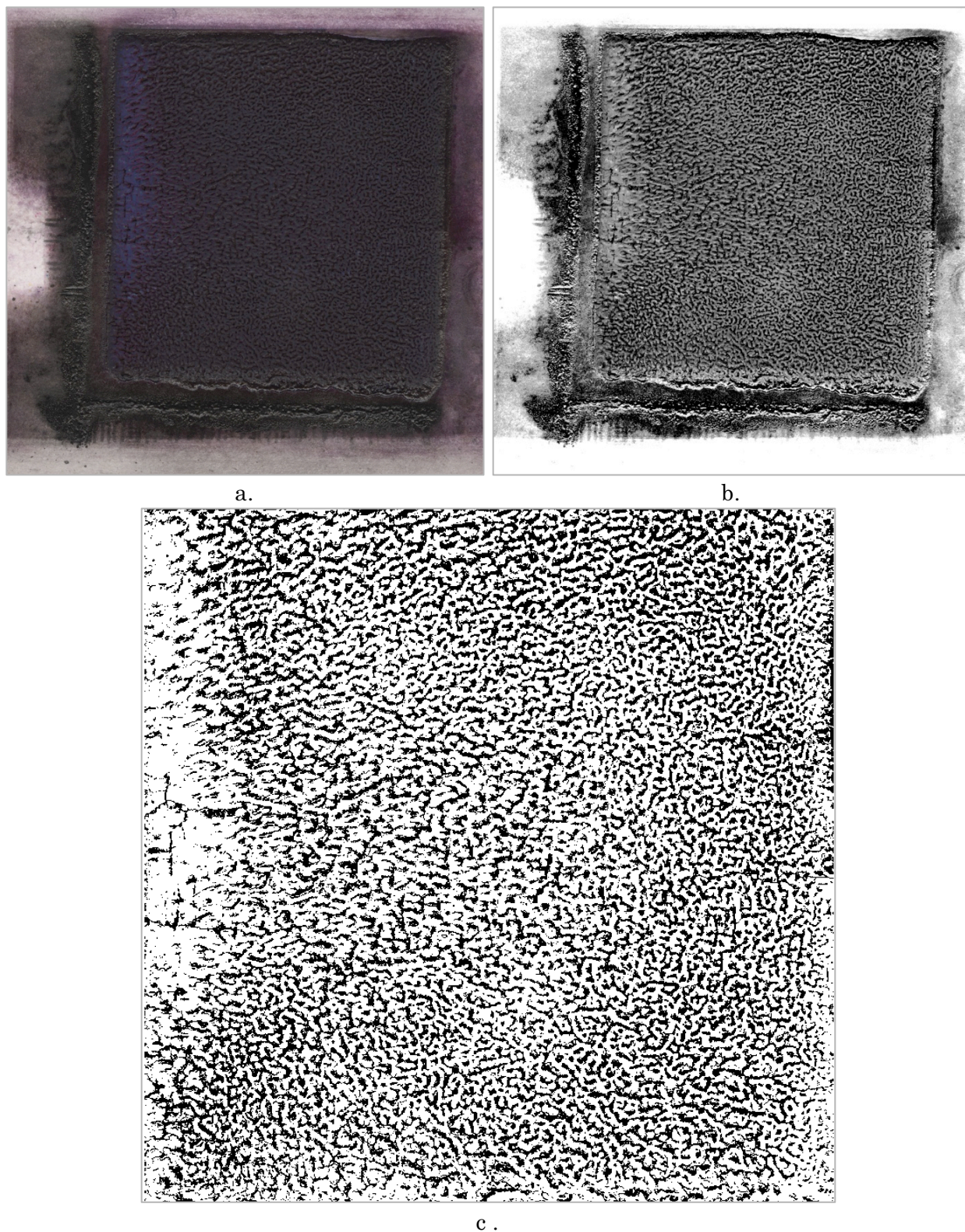


Figure 87. Images of 100-layer 2-toner sample: a. original, b. grayscale, histogram adjusted, c. compensation image extracted

A sample with less pronounced defects was then analyzed to evaluate if the same type of results could be obtained; a 30-layer sample fused face down was selected, see Figure 88.

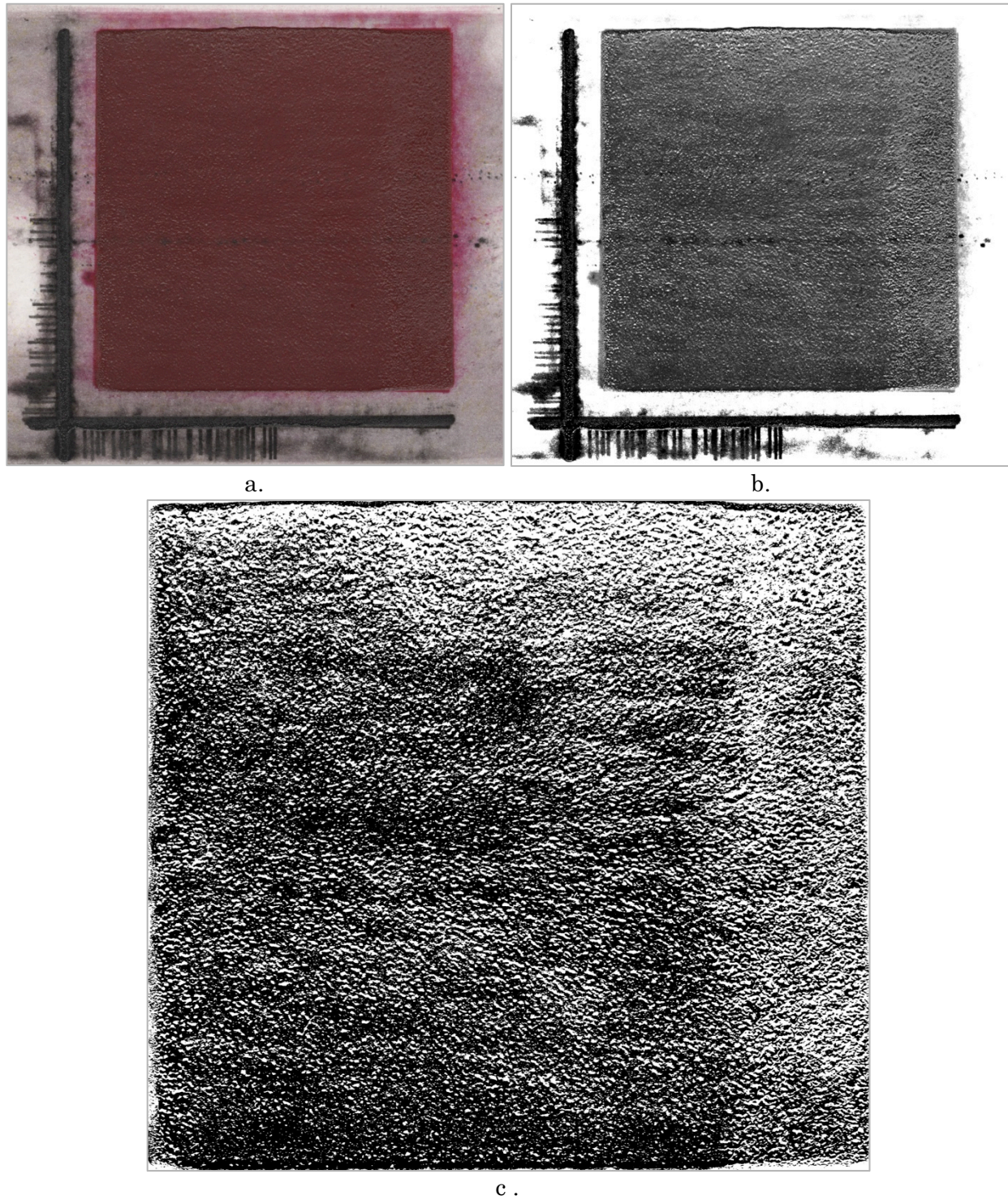


Figure 88. Images of 30-layer sample fused face down: a. original, b. grayscale, histogram adjusted, c. compensation image extracted

The results showed that the surface variation is indeed highlighted by these changes; however, since the features are less noticeable, it gets harder to tell if the generated image is indeed indicating the regions that require more material. This posed the problem of how to validate the sensing strategy. The profiles obtained with the contact profilometer are only lines of measurement that may not have the same alignment as the image and have different sampling resolution, making very difficult to compare the two.

Another issue was detected regarding the color of the material. The sample contained a strip of black dots towards the center of the sample that occurred due to slight damage to the photoreceptor of the black cartridge on the printer (HP 4700) used to create the sample. These dots were marked as regions to put more material when the image was thresholded due to the dominance of the black color of the toner, regardless of the actual geometry of the sample at that location.

A different approach was used to detect edges instead. It was noted from previous trials that having one or two illuminations would only highlight certain portions of the contour; therefore, eight directions (roughly every 45 degrees) were used to try to detect full edges on the holes and cracks of the samples.

The implementation consisted of converting the images to grayscale, applying a Sobel edge detector to each image, fusing all the edges by applying a logical 'or', and applying morphological operators (i.e. closing, dilation and erosion as described in [95]) to obtain a binary image of the regions to deposit more material. Sample images are shown below:

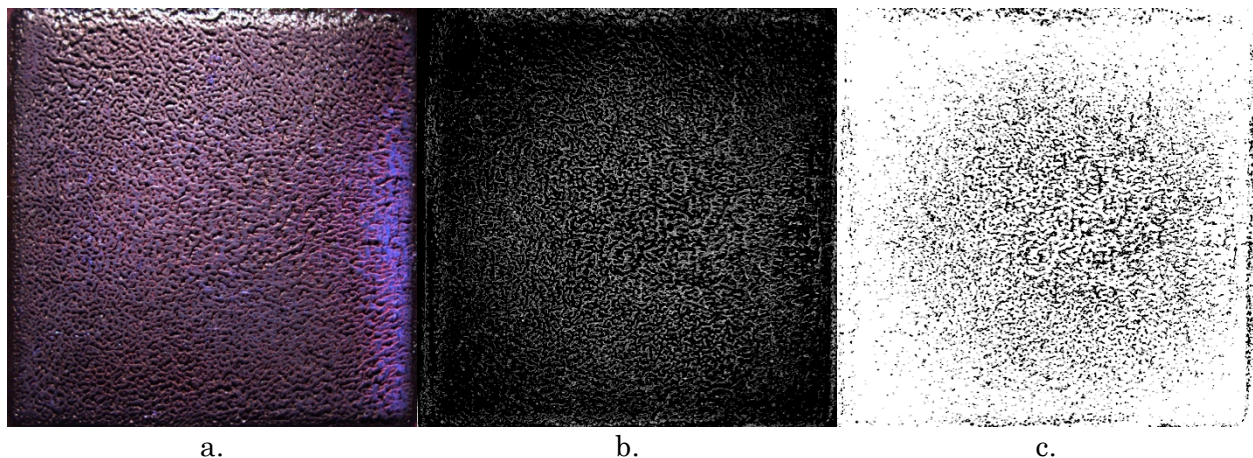


Figure 89. Edge detection and image fusing approach: a. 100-layer 2-toner sample illuminated from the top; b. edges detected and fused from 8 images; c. compensation image after applying morphological operators

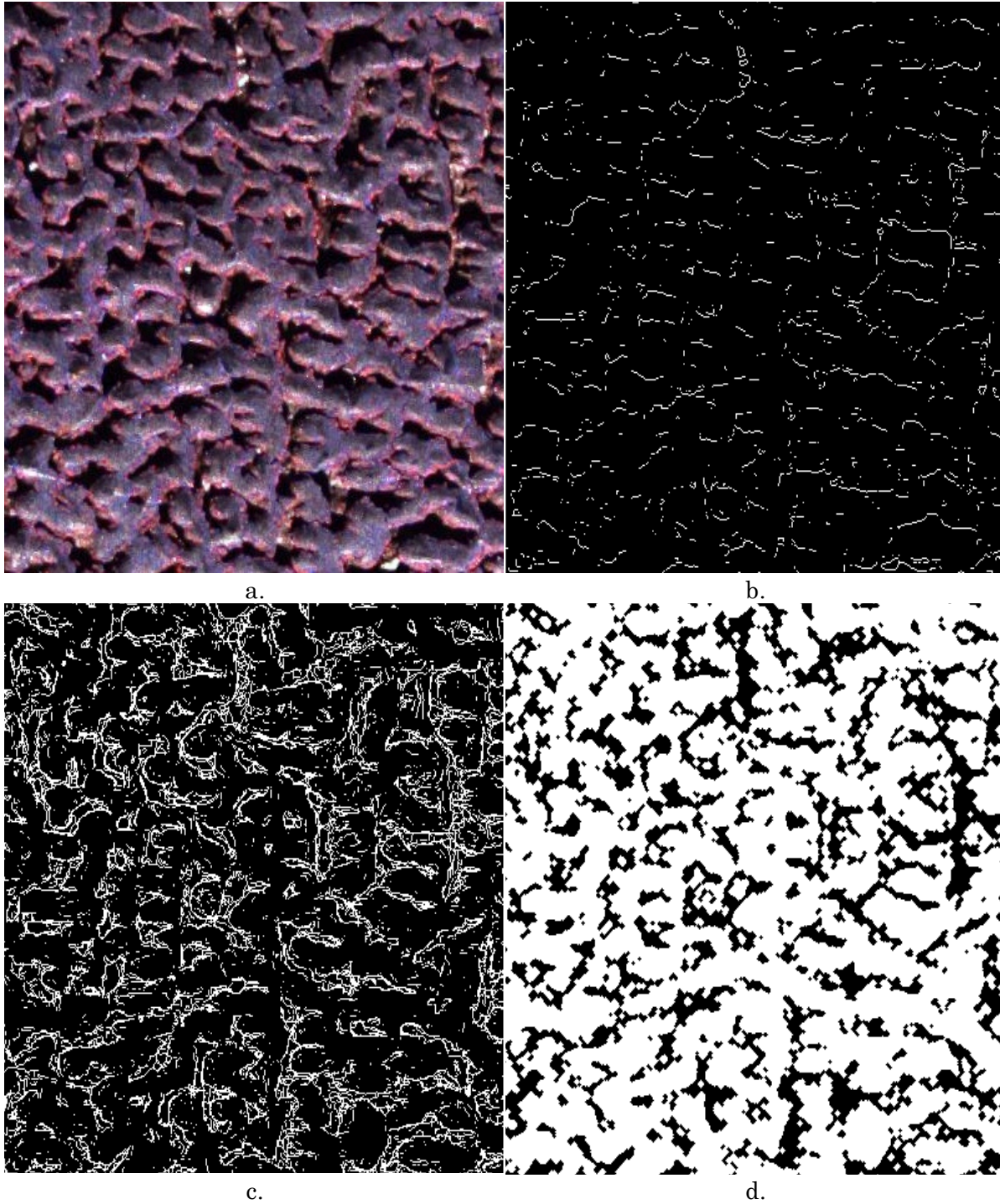


Figure 90. Detailed image of the edge detection approach: a. original image illuminated from the bottom; b. edges detected for this image only; c. edges from 8 images (8 illumination angles) fused; d. compensation image after applying morphological operators.

Fusing the results from the edge detection on eight images with distinct illumination angles indeed highlights any contours in the surface; however, it was difficult to generate a

compensation image from it. The use of morphological operators helped filling out the regions of interest but also decreased the level of detail or the fidelity of the shape of the defects detected. Nonetheless, the compensation image generated through this method seems to provide a first order approximation to the desired compensation for the EP3D printing process.

Overall, these approaches are encouraging since they showed that using a single camera and different illumination conditions would be beneficial to extract the surface variations. More development is needed in order to reliably use any of the approaches for feedback to the control system.

8.4. GelSight

The company GelSight is an early stage spinoff from MIT that promotes a new technology for surface imaging using an elastomeric sensor that conforms to the surface of the object to measure (see section 2.4.5). After reaching out to them, they generously agreed to collaborate with us imaging several samples. Five samples were sent for imaging: 25-layers preliminary sample, 30-layers fused face up, 30-layers fused face down, 30-layers using belt material as interface, and 100-layers 1-toner fused face down.

The samples were imaged using a bench configuration (beta system) that has a DSLR camera with a 18 MP sensor and a 65 mm macro lens, providing a resolution of 4.25 μm per pixel, and measurement region of 22.3 mm x 14.9 mm. Additionally 8 mm x 8 mm crops were provided to show details of the surface and the final outcome of their system is a 3D model of the surface. Sample images are shown in Figure 92 and in Appendix D.

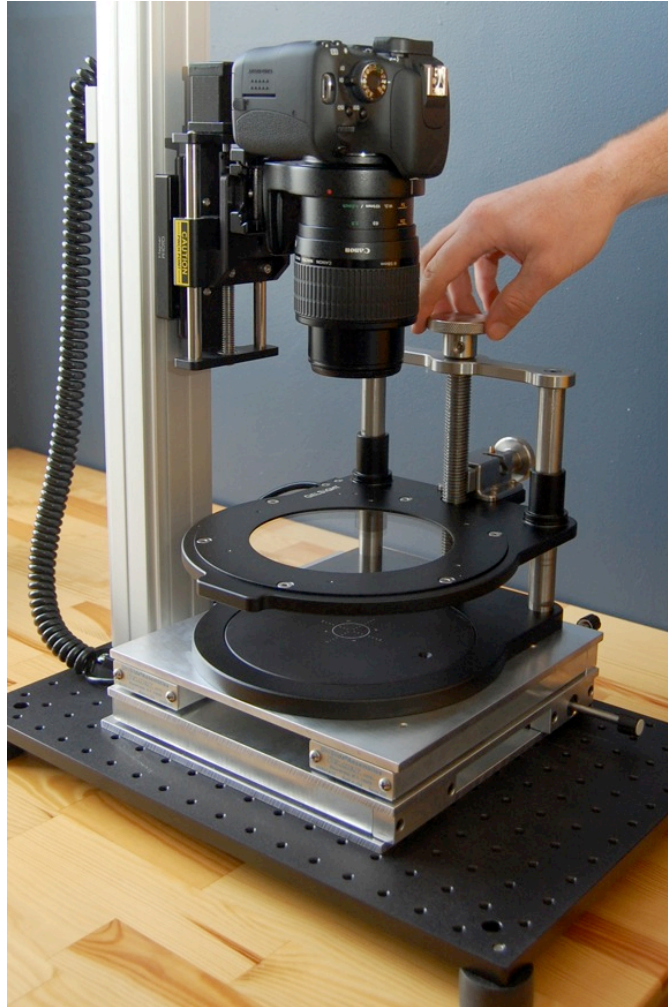


Figure 91. GelSight Benchtop Beta System, from [96]

The samples were selected as representatives of the sample generation methodology and very distinct features can be seen in all of them. It seems clear that the fusing methodology (fused face up vs. fused face down), as well as the intermediate substrate (silicon coated Mylar vs. HP Indigo belt) affect how the structure forms and leaves a permanent mark on the surface, particularly evident in the 30-layer sample that used the belt material (see appendix D.4).

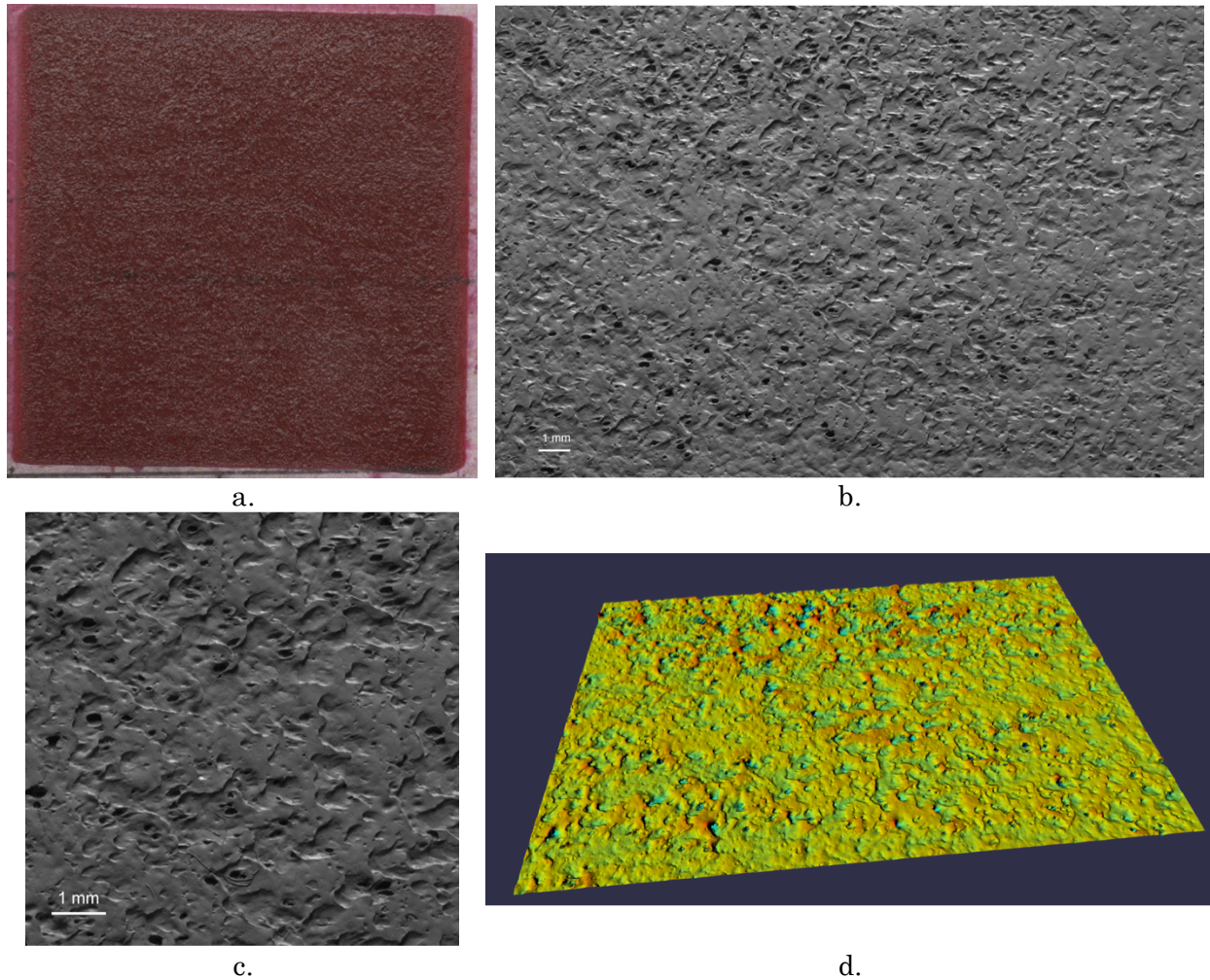


Figure 92. a. 30-layer sample fused face up imaged with a flatbed scanner; b. 22.3 x 14.9 mm section of the 30-layer sample imaged using GelSight, c. 8 x 8 mm detail, d. 3D reconstruction of the detail area

The technique implemented by GelSight provides great detail of the surface and eliminates the sensing issues related to the optical properties of the surface including the color. The area imaged using this configuration did not cover the entire printed sample but there is no reason why the device could not be adapted to requirements of the EP3D printing process. The 3-dimensional reconstruction of the surface seems accurate but it should be validated against another instrument or a reference sample.

8.5. Conclusion

Measuring the surface has proven to be an important issue to resolve towards the control of the EP3D printing process. Contact profilometers provide only a line of measurement data and potentially disrupt the sample while taking the measurement, making it less than ideal

for measuring the entire sample. Several imaging approaches have been tested with encouraging results. A single image approach served to identify areas where more material was needed when the defects (i.e. holes, and cracks) were large; however, when the defects were less noticeable, the segmentation became more difficult.

Two approaches to use multiple images were tested, first using the reflectance transformation imaging (RTI) and then extracting edges from images with different illuminations and fusing them into a single image to determine contours of the surface. Both approaches seem promising. The first used the open software promoted by the Cultural Heritage Imaging (CHI) nonprofit organization that is meant only as a visualization aid. Further research into the PTM model that is generated throughout this process may yield more useful information for its application in EP3D printing. The second approach was computationally simpler and relied on the different illumination angles to highlight different sections of the contours on the surface. It provided a good result identifying areas where more material is needed but did not provided further depth information.

The last approach explored was using the sensing system called GelSight from an early stage spinoff company from MIT. The imaging technique relies on a coated gel to conform to the surface of interest and imaging the coated surface that is well characterized to extract the geometry of the underlying object. The results obtained were very promising, the images are very detailed, the resolution was appropriate to capture all the features on the surface and a 3D model is constructed from the information gathered from six illumination angles. This type of result would be ideal for a control system since there would be detailed information of the status of the surface at all points in a timely manner since capturing the images and processing them is done in a matter of seconds. Further collaboration with this company is desired in order to explore the application of their technology in an automated implementation of the EP3D printing process.

Chapter 9. CONCLUSIONS AND FUTURE WORK

This research has explored the application of Electrophotographic printing for additive manufacturing. The creation of multilayer structures through EP has been seen as a promising technology due to the characteristics that have made laser printers and digital copiers prevalent in the office space: reliability, high speed, low cost, and good resolution.

Previous attempts had reported several challenges that had impeded the commercialization of EP3D printing, mainly the difficulty to transfer more material as the structure grows thicker, the appearance of surface defects that form as the number of layers increase, establishing the appropriate materials to use, and the automation of the process.

9.1. Contributions to the state of the art

This work contributed to overcome the first two challenges of EP3D printing: transferring new layers reliably and achieving a smooth surface. Firstly, a methodology was established to circumvent the limitation to deposit more material. New layers were printed on an intermediate substrate and later transferred onto the existing structure using rheological methods (applying heat and pressure); this strategy worked significantly better than using electrostatics as in most EP document printing and other EP3D printing approaches.

Having a working methodology, the following challenge was approached in several stages that are summarized in the following sections:

9.1.1. Surface defects characterization

The surface defects were characterized by two experimental approaches: exploring the main factors involved in the process, and by taking detailed layer-by-layer measurements. The exploration of which factors to control was based on the observations from preliminary trials in which the following were varied:

- base substrates
- the use of gradient transitions

- the use of multiple colors (i.e. different materials)
- the use of different halftoning levels

The experimental approach demonstrated that the surface degraded as more layers and more material was accumulated. The base substrate did not have a significant effect on the final surface roughness but played an important role for the curling of the sample. A significant difference on the surface roughness was detected between the leading and trailing edge of the samples.

Similarly, an experiment was conducted creating two 30-layer samples in which measurements were taken after each layer: one transfusing with the hard (heated) roller in contact with the top of the structure, and one with the soft (pressure) roller. The results showed that a more compliant transfusing interface was desirable to produced a smoother surface. The measurements showed that the surface defects (holes and cracks) became wider and deeper as more layers accumulated. These measurements also allowed the process to be characterized as a low frequency booster and to identify the cause of the differences in roughness between the leading and trailing edges as a dynamic response of the fuser to the sample entering the fuser rollers.

9.1.2. Modeling of EP3D printing for control

The experiments described above led to the development of a model of the EP3D printing process that reproduced the main features of the surface structure and shed light into how to control the surface quality. The model captures the stochastic nature of the EP process, the averaging action of the fusing process, and the influence of the compliance of the transfuse interface in the ultimate surface roughness as many layers accumulate.

This model provided a platform to test other conditions, explore the evolution of the surface for higher number of layers, evaluate control strategies, and ultimately have a better understanding of the EP3D printing process. Having a simulation capability also alleviated the experimental burden of creating EP3D printed samples, which consumed significant time and resources to be completed.

9.1.3. Development of preliminary control strategy for EP3D printing

In pursuit of the goal to achieve a smoother surface, a passive approach to control was tested by using a more compliant interface that conformed better to the surface while

transfusing. Although a smoother surface was achieved, the new interface material did not have good release properties, making the transfer of material less efficient. The process also became significantly slower because each layer needed to be preheated in an oven before it could be fused and afterwards the interface required thorough cleaning to remove the remaining toner.

A feedback control was designed to have a smarter approach to prevent surface defects. The control strategy relies on getting the status of the surface and establishing the areas that require more material. This approach was designed and tested using the simulation model developed for the EP3D printing process. However, it was not implemented on the current system due to the lack of good sensing of the surface and a reliable method for positioning the layers in order to achieve good registration. The results showed that achieving surface roughness smoother than the surface roughness of the initial substrate was possible, which would be more than acceptable for most applications that can be envisioned for this 3D printing technology.

9.1.4. Surface imaging for compensation of defects

Alternatives for measurement were also explored, particularly the imaging approaches to extract surface maps from multiple images of the EP3D printed sample with different illumination angles. Simple image processing approaches seemed to work to detect areas where more material is needed, especially when the defects are noticeable and there is enough contrast to separate the top of the surface from the holes and cracks by thresholding.

Other methods, such as the use of GelSight, proved effective in detecting the defects and extracting a three-dimensional model of the structure; however, the field of view was limited to an area of 22.3 x 14.9 mm (13.3% of the 50 x 50 mm sample). Nonetheless, there is great potential for this technology in an application like EP3D printing since it circumvents optical properties that tend to introduce noise and uncertainty in the measurements, and it is able to capture very subtle features of the surface, not easily detected with other methods.

The multiple illumination angles and single detector configuration not only provided good results but seems easy to translate into a commercial implementation of the EP3D printing

process, due to the simplicity of the architecture and the economical advantage of having multiple light sources versus multiple detectors or a tightly controlled change of focus plane. In the end, image-based sensing seems to be ideal to provide feedback that enables the control of the surface quality of the EP3D prints. The different methods explored in this work served as proof of concepts and provided the confidence to assure that the features that form in EP3D prints can be sensed with an image-based sensing system.

9.2. Areas for future work

Overall, the research conducted has provided a better understanding on the EP3D printing process and has pointed out solution paths for the challenges reported in literature to commercialize EP3D printing. However, much work still remains before that can be realized. Some of the areas where further contribution can be made in the near future are:

1. Understand further the root causes of the surface defects
2. Relax constraints and assumption of the simulation model
3. Extend the simulation model of the EP3D printed surface to 3D
4. Test different materials for the intermediate substrate
5. Explore materials for printing and their properties
6. Develop and validate a 3D surface map through image processing techniques
7. Implement the feedback control strategy
8. Automate the transfuse process

In the following sections each one of these areas is expanded for more details, and concludes with more general implications for further work on EP3D printing.

9.2.1. Understand further the root causes of surface defects

The surface defects observed in EP3D printing have been studied to understand how to minimize them or how to compensate for them; however, the root causes of those defects still requires further investigation. The simulation model developed shed some light into how the features appeared and expanded as more layers were aggregated, how the fusing process played a key role into the arrangement of the particles in the 3D structure, and from the DOE study, it seemed clear that the base substrate was not a significant factor in the ultimate appearance of the print. Similar studies may be needed to establish the role of

the interface surface, the surfaces of the components involved in the fusing process, the temperature, speed and pressure used, among others.

The fusing conditions have remained at fairly constant levels that seemed appropriate from previous experience with traditional document printing, and the initial testing for EP3D printing; however, it is unclear if some of the initiating defects occur due to local cold or hot offset mechanisms or whether those fusing conditions should be changed as the printed structure becomes thicker.

Furthermore, other fusing methods should be tested to determine if a more desirable surface is obtained. A stamp-based fusing test-bed is available at the PRISM lab that could be used and can be seen in Figure 19.c. This particular test-bed has the capability of fusing an area of 50 mm x 50 mm with a heated plunge, but also has a chamber that can be heated to allow for preheating of the sample or to control the cool down process. A photonic sintering device (housed in the Brinkman lab at RIT) is a non-contact alternative that can also be explored. This device has a high intensity lamp, which provides an energy beam that sinters the particles but may also produce a light induced transfer mechanism. Initial tests were done which did showed some success fusing the toner particles to the Mylar sheet used as intermediate substrate. However, other tests melted the Mylar and evaporated the toner particles indicating that a more detailed study is required to use this technology with EP3D printing.

9.2.2. Relaxation of constraints and assumptions of simulation

The simulation model was developed under several assumptions/constraints that are not realistic for the current implementation of the EP3D printing process, mainly: constant particle size, perfect alignment of particles to the sampling grid, and perfect layer registration. The relaxation of these assumptions/constraints may provide a closer reproduction of the process.

The particle size it is not constant across the entire set of particles developed; a particle size distribution would be more appropriate to model the particles. Manufacturers know this distribution and usually the spread is tightly controlled to achieve the desired quality of prints; nonetheless, assuming a constant particle size is just an approximation that simplifies the model and facilitates the simulation.

Similarly, it is unreal to think that all the toner particles follow perfectly a sampling grid equal to the particle size. The particles are arranged at slightly different locations leaving small gaps between them. Moreover, as shown in Figure 61 the particles are not perfectly stacked on top of each other when a layer is developed; particles stick on top of each other at different contact angles, some of them roll on top of the other as they are transferred, etc. Those effects introduce more variability and require more detailed treatment in the simulation. Currently, a random ballistic deposition model is being developed, in which there is a closer look at how particles align and form a structure as they are deposited by the action of a force. This model could complement the EP3D printing model not only at the development stage but also at the transfusing step where significant restructuring takes place. This would increase tremendously the computational complexity of the simulation but with increasing computing capabilities, it may be feasible to examine the structure at this level.

Perhaps the most noticeable effect that has been ignored so far in the simulation is the registration between layers. The manual process that has been used so far to construct EP3D prints do not allow for very good registration. This needs to be tackled in two fronts: the simulation model should capture registration errors to evaluate the admissible range for the system, but also the EP3D process should be automated to guarantee certain level of registration between layers and repeatability that enables the accurate reproduction of the intended geometry.

9.2.3. 3D extension of the simulation model

Up to this point the simulation model has been based on profiles of the EP3D print, mainly because the method available to validate the model has been profilometer readings. The natural next step in this line is to extend the model to provide three-dimensional models of the EP3D print. In principle, this could be accomplished by stacking a series of profiles for the entire width of the print; however, additional considerations must be taken into account:

- The averaging action of the fuser captured with the Gaussian low-pass filter would need to be extended to two dimensions since each point would be affected by (and affecting) its neighbors both in the direction of travel (x) and the cross-direction (y).

- The nip width instead of a length becomes an area of contact between the sample and the fuser rollers. The response of the rollers would be determined by the average of what the sample looks like under the nip.
- The edges on both extremes of the direction across from travel would be affected by the fuser differently than the center of the sample; just as the leading and trailing edges of the sample are affected by the response of the rollers to the change in displacement, the compression of the roller push the edges into the center of the sample, rounding and smoothing the edges.

All these considerations impose a much higher computational cost and would make the simulation last longer by several orders of magnitude.

9.2.4. Testing different materials for intermediate substrate

The passive approach to control indicated that a more compliant interface indeed helps to produce a smoother surface; however, the transfer efficiency decreased significantly and the process became much more labor intensive, requiring preheat of each layer and cleaning afterwards. Nevertheless, the concept of a more compliant interface is still desirable and should be explored further by testing different materials that may have better heat transfer properties and better release properties.

Furthermore, it would be useful to have an active surface which could conform to the surface in contact and its stiffness could be addressed point by point. This type of actuator would enable a more direct control on the transfuse process and ultimately on the height that each individual point of the surface would achieve.

9.2.5. Explore materials for printing and their properties

The studies within this thesis on the EP3D printing process have been conducted with HP emulsion aggregated toner because of availability and convenience; however, it is well known that toner may not be the most desirable material to create 3D structures. Toner has been engineered for other purposes, it is brittle and the particle size has been selected for the reproduction of images in document printing.

Those properties are not necessarily the most desirable for 3D printing. The 3D structures should be created from materials that align with the intended performance; bigger particles

might speed the process up yet still provide an acceptable resolution. It is necessary to examine what that acceptable resolution is depending on the application.

Additionally, with toner, significant curling was observed. It seems like both the fusing method (roller) and the interaction between the particles as the structure cools down may be responsible for the curling of the sample. Toner (and other plastics) would tend to compress and soften as they are heated and pressure has been applied, and the entire structure would tend to become denser as some particles would flow to fill gaps; afterwards they would tend to recover some of its original shape and release stresses, changing the structure and producing curling. From the DOE study it was suggested that a thicker/stiffer base substrate was desirable; however, it may be important to test other strategies to minimize those effects. A wider or bimodal particle size distribution may produce a denser structure to begin with, leaving less room for structure changes, which may lead to less curling.

Similarly, it may be advisable to control the heating and cool down process of the existing structure, new layer, and new structure after transfusing. Preheating the structure may facilitate the adhesion of the new particles and obtain a more dense structure. Likewise, with the more compliant interface (HP indigo transfuse belt) it was seen that preheating the new layer facilitated the transfuse process and produced a smoother surface (also attributed to the more compliant interface); therefore, preheating the new layer may be advisable even for interfaces that could work without that step. Lastly, allowing the sample to cool down more gradually may release some of the internal stresses and in turn minimize the curling effect.

Perhaps a combination of strategies may be the ultimate solution. As an example, the process could consist of:

- preheating both the sample and the new layer,
- fusing the sample with pressure only,
- fusing the sample with a second pass of heat and pressure, and
- cooling the structure down gradually.

It is important to consider these options and to establish improved strategies for the selection of materials, process parameters and applications for the 3D print.

9.2.6. Develop and validate a 3D surface map through image processing techniques

The development of sensing capability for the evaluation of the surface has been part of the research objectives since the beginning of this work. The current setup and the image processing algorithms could be refined much further towards extracting a three dimensional map of the surface.

More importantly, the results require validation. Currently, digital microscopes and optical profilers are alternatives to surface measurements of an entire area instead of line profiles like the ones obtained with the contact profilometer. A digital microscope can extract 3D models of the surface when coupled with motorized stands and high-end controllers and is being considered for acquisition by the lab. Additionally, Professor Andres Carrano at University of Auburn (formerly at RIT) has shown interest in pursuing problems of surface sensing and characterization, and is willing to collaborate in analyzing the case of EP3D prints with an optical profiler that may serve to validate the results of other sensing techniques.

Similarly, the dialogue established with GelSight has opened the door for further exploration of either incorporating their sensing capability into the EP3D printing process, or developing a similar strategy much more specific for the type of materials and the type of information that may be useful for the control of the EP3D printing process.

9.2.7. Implementation of feedback control

The initial testing for a feedback control strategy has proven to be effective to mitigate the formation of significant surface defects in the simulation models. The next step would be to implement this strategy; however, further advances in the experimental setup would be required, such as: an automated transfusing process to provide better registration, and a sensing capability to estimate the state of the surface (discussed in the previous section).

The automation of the transfuse process entails connecting the two phases of the EP3D printing process, printing of a layer and fusing it to the existing structure. Up until this point, the first part of the process has been done with the HP color LaserJet 4700 with the fuser removed, and the second part with the off-line fuser available in the lab. The manual intervention consists of transporting the printed layer on the intermediate substrate,

placing it on top of the structure under construction, feeding both through the fuser, and peeling off the intermediate substrate to reveal the newer structure. Eliminating all these stages requires significant design effort but some of the possibilities to consider are:

- Be able to print directly on the intermediate substrate without having to rely other elements such as paper or transparencies to trick the printer.
- Make the intermediate substrate a drum or a belt to enable direct transfer of the printed layer to the top of the structure under construction.
- Create the EP3D print in a platform that would adjust to the changes in height of the structure
- Enable further displacement on the fuser rollers to permit much higher structures to be fed through.
- Feed the structure under construction and the intermediate substrate through the fuser automatically
- Clean or discard the intermediate substrate to prepare for a new layer to be printed.
- Integrate sensing capabilities to evaluate the surface of the structure under construction.

The linear test-bed available in the PRISM lab (see Figure 60) has been envisioned as a good starting point for its flexibility; however, a programmable exposure station is needed to generate images that may serve to create layers.

9.2.8. Automate the transfuse process

Clearly, there are still many challenges to overcome and many aspects to consider before automating the EP3D printing process. Further testing can be done with a manual setup, even for the control system, but ultimately the process needs to be automated in order to become an alternative within the additive manufacturing space.

The transfuse process involves printing each layer on an intermediate substrate that may need to be a moving platform, a belt or drum to be able to repeat the process layer after layer. Transfuse belts exist, in fact a transfuse belt from a HP Indigo printer was used as a more compliant interface but further testing is needed to determine the appropriate material for the intermediate substrate (see section 9.2.4).

To guarantee layer registration micro-actuators may be needed to position the new layer and the existing structure appropriately in conjunction with a sensing strategy such as those reported in section 2.3 that used image processing. However, the first step should be to have a repeatable and reliable process and evaluate how critical the layer registration is before investing significant resources in a tightly controlled layer positioning system that may turn out to be excessive.

Appendix A. SIMULATION CODE

A.1. Static Simulation of EP Development Process

The static model summarized in section 2.1.2.1 was simulated using Matlab to verify the results reported in literature. The code developed is as follow:

```
%% Static Model for Solid Area Toner Development
%% Initialization Variables

qtm = 35;      % toner charge density [uC/g]
L = 1.25;      % Gap btw Mag. brush roll and photoreceptor [mm]
l = 0.1;       % Active development gap [mm]
Ltg = 1.20;    % Trim bar gap [mm]
Vb = 55;       % Velocity of brush [mm/s] 55 in/s
Vpc = 40;      % Velocity of photoreceptor [mm/s] 40 in/s
Vr = Vb/Vpc;   % Velocity ratio btw brush and photoreceptor
N = 2;         % Number of rolls
tpc = 30;      % thickness of photoreceptor [μm]
tt = 20;       % toner layer thickness [μm]
kpc = 3;       % Photoreceptor dielectric constant
kt = 1.5;      % Toner dielectric constant
td1 = 5.5;     % Toner diameter [μm]
td2 = 10;      % Toner diameter [μm]
kdev = 5;      % Developer dielectric constant (developer=toner+carrier)
Vbias = 575;   % Bias voltage [V]
Vlow = 75;     % Image discharge voltage [V]
Vdev = Vbias-Vlow;
eps = 0.885;   % Permittivity
Cdev = log10(1E-8); % Developer Conductivity
Ccen = log10(1E-9); % center conductivity
delta = log10(4); % delta
fn = 0.8;     % Neutralization fraction
Pd = 4;       % Developer mass density
Pf = 0.65;    % Developer packing fraction
Ke = 1.2;

C = [0:0.1:8]; % Active toner concentration [%] *****

Kins = eps*N*Vr/((tpc/kpc)+(tt/2/kt)+(1000*(L-l)/kdev)); % insulating constant
Kcond = eps*fn/((tpc/kpc)+(tt/2/kt)); % conducting constant
x = (Cdev-Ccen)/delta;
Ksad = ((exp(x)-exp(-x))/(exp(x)+exp(-x)))*(Kcond-Kins)/2+(Kcond+Kins)/2;
MdA = Pd*Pf*L*100; % Developer Mass/area on the roll [mg/cm2]
Csad = Ksad*fn*Vdev*100/(MdA*I*N*Vr*qtm/Ltg); % Toner Supply neutralization limit
Kcondve = Ke*I*qtm*td1; % Electrostatic conductive constant
```

```

Kinsve = Ke*L*qlm*td2;          % Electrostatic insulating constant

% Magnetic threshold voltage [V]
Vmagthr = ((exp(x)-exp(-x))/(exp(x)+exp(-x)))*(Kcondve-Kinsve)/2+(Kcondve+Kinsve)/2;
Vdevel = Vdev-Vmagthr;
if Vdevel<0
    Vdevel=0;
end

% Developed Solid Area Mass per unit Area
DMA = Ksad*Vdevel*(1-exp(-C/Csad))/qlm; %[mg/cm2]
QtA = DMA*qlm;          % Toner Charge per area [uC/cm2]

% Plot Development Curve
figure(1), plot(C,DMA)
title('Solid Area Development'), ylim([0 0.801])
xlabel('Toner Concentration [%]'), ylabel('Developed Mass per unit Area [mg/cm^2]')

```

A.2. Simulation of the EP3D printing process

The following code simulates the EP3D printing process with specific parameters for the fuser test-bed used:

```

%% One dimensional profile (considering pressure variation) version 2
% compression depends on the force applied by the roller on the surface

% % Fusing system modeling [lbf,in,s]
% Pa=25; % air pressure [psi]
% Wm=250; % motor roller speed [rpm]
% % T=180; % temperature of hot roller [C] - not considered in the model
%
% Vl=(Wm/30)*(3.3125*pi)*(1/60); % linear velocity through fuser [in/s]
% F=2*(Pa*pi*(2.5^2 - 0.75^2)/4)*((3.775+2.165)/2.165)*0.8; % Force on roller [lbf]
%
% m=13/(32*12); % mass [lbf]/g[in/s^2]
% k=(5*2*12.25*0.8/0.003); % Pressure roller spring constant [lbf/in]
% b=30; % Damping constant [lbf/in/s]

% Fusing system modeling [SI]

Pa=25*6894.757293168; % air pressure [Pa]
Wm=250; % motor roller speed [rpm]
% T=180; % temperature of hot roller [C] - not considered in the model

Vl=(Wm/30)*(3.3125*pi)*(25.4E-3/60); % linear velocity through fuser [m/s]
F=2*(Pa*pi*((2.5*25.4E-3)^2 - (0.75*25.4E-3)^2)/4)*((3.775+2.165)/2.165)*0.8; % Force on roller [N]

m=13*0.45359237; % mass [Kg]
k=(5*2*12.25*0.8/0.001)*(4.448222/25.4E-3)/6000; % Pressure roller spring constant [N/m] *
b=8*m/(25/73.42); % Damping constant [N/m/s] b=8*m/ts, ts=20mm/Vl(@500rpm)

```

```

p_size=5E-6; % particle size 5 microns
substrate=8E-3*25.4E-3; % base substrate thickness
nipwidth=12e-3; % nip width 12 mm

% Second order dynamic model
% x1 = vertical position of roller, x2 = vertical speed of roller
% u1 = Force by air pressure, u2 = sample profile
% y1 = Force applied by the roller to the sample; y2 = x1

A=[0 1; -k/m -b/m];
B=[0 0; 1/m k/m];
C=[k 0; 1 0];
D=[0 -k; 0 0];
x0=[F/k 0];

sys1=ss(A,B,C,D);

% Simulation parameters

P=0.95; % Probability of transfer
%k_comp=0.7; % compression factor when fusing
maxcomp=0.4; % maximum compression
mincomp=0.7; % minimum compression
compdepth=35E-6;

thres=36E-6; % threshold for complainece
dt=p_size/Vl; % t=x/Vl
substdimx=101E-3; % Substrate dimension x
pstartx=21E-3; % position of 3D print on substrate (Sample2=18, Sample3=21)
pdimx=50E-3-p_size; % 3D print dimension x **it has to be <10000
npoints = 9999;
nlayers = 30;

Tfinal=substdimx/Vl;
t=0:dt:Tfinal;
dim=size(t,2);

u=zeros(dim,2,nlayers);
y=zeros(dim,2,nlayers);

Z=zeros(npoints,nlayers+1);
Z=normrnd(substrate,3.6E-6,[npoints,1]); % base substrate

H=fspecial('gaussian',[5 1],1);

for i=2:nlayers+1
    X=normrnd(3,1,[npoints,1]);
    u(:,i-1)=F*ones(dim,2);
    u(1:round(pstartx/p_size)+1,2,i-1)=-substrate*ones(round(pstartx/p_size)+1,1);
    Zmean=mean(Z(:,i-1)+X*p_size);

```

```

u(round(pstartx/p_size)+2:round((pstartx+pdimx)/p_size)+1,2,i-1)=-Z(:,i-1);
u(round((pstartx+pdimx)/p_size)+2:dim,2,i-1)=-substrate*ones(dim-round((pstartx+pdimx)/p_size)-
1,1);

[y(:,i-1),t,xss]=lsim(sys1,u(:,i-1),t,x0);

Zmax=max(Z(:,i-1)+X*p_size);
%delta=Zmax-Zmean;
fmax=max(y(round(pstartx/p_size)+2:round((pstartx+pdimx)/p_size)+1,1,i-1));

Zmin=min(Z(:,i-1)+X*p_size);
deltamin=Zmax-Zmin;
if deltamin>thres
    fmin=min(y(round(pstartx/p_size)+2:round((pstartx+pdimx)/p_size)+1,1,i-1));
else
    fmin=k*(y(1,2,i-1)+(Zmax-thres));
end
fmax=(fmax-fmin)*0.95+fmin;

for j=1:npoints
    if j<=round(nipwidth/2/p_size)
        Zmax=max(Z(1:j+round(nipwidth/2/p_size),i-1)+X(1:j+round(nipwidth/2/p_size))*p_size);
    elseif j<round(pdimmx/p_size)-round(nipwidth/2/p_size)
        Zmax=max(Z(j-round(nipwidth/2/p_size):j+round(nipwidth/2/p_size),i-1)+X(j-
round(nipwidth/2/p_size):j+round(nipwidth/2/p_size))*p_size);
    else
        Zmax=max(Z(j-round(nipwidth/2/p_size):round(pdimmx/p_size),i-1)+X(j-
round(nipwidth/2/p_size):round(pdimmx/p_size))*p_size);
    end
    delta=Zmax-(Z(j,i-1)+X(j)*p_size);
    %delta=(Z(j,i-1)+X(j)*p_size)-Zmean;

    if (rand<P)&&(delta<thres)
        Ptrans=1;
        F1=y(j+round(pstartx/p_size)+1,1,i-1);
        if F1>fmax
            k_comp=maxcomp;
        elseif F1<fmin
            k_comp=mincomp;
        else
            k_comp=mincomp+((maxcomp-mincomp)/(fmax-fmin))*(F1-fmin);
        end
        %k_comp=(delta*(maxcomp-mincomp)/thres)+maxcomp;
    else
        Ptrans=0; k_comp=1;
    end
    Z(j,i)=X(j)*p_size*k_comp*Ptrans+(0.95+0.05*k_comp)*compdepth+Z(j,i-1)-compdepth;
end

Z(:,i)=imfilter(Z(:,i),H,'symmetric');

end

```

```

figure(1)
plot(p_size*[1:9999],1E6*Z(1:9999,[1:nlayers+1]))
xlabel('position [m]'), ylabel('height [\num]')
title('Simulation of EP3D profile with perfect registration')

y1(:,.)=y(:,1,:); y2(:,.)=y(:,2,:);
u1(:,.)=u(:,1,:); u2(:,.)=u(:,2,:);
figure(2)
subplot(3,1,1); plot(1e3*t*Vl,[y1(:,[1,5:5:nlayers])]);
title(' Force profile applied on sample'), ylabel(' Force [N]'), xlim([0 1e3*substdimx])
legend(string([1:5:26,30].:)), legend('show')
legend('Location','East'),set(legend,'YDir','reverse')
subplot(3,1,2);
plot(1e3*t*Vl,-1e6*u2(:,[1,5:5:nlayers]));
title(' Profile of a sample'), ylabel(' Height [\num]'), xlim([0 1e3*substdimx])
legend(string([1:5:26,30].:)), legend('show')
legend('Location','East'),set(legend,'YDir','reverse')
subplot(3,1,3); plot(1e3*t*Vl,1e6*(y2(:,[1,5:5:nlayers])-x0(1)));
title(' Response of roller'),ylabel(' z_1 [\num]')
xlabel(' Position in the direction of travel [mm]'), xlim([0 1e3*substdimx])
legend(string([30,26:-5:1].:)), legend('show')
legend('Location','East'),%set(legend,'YDir','reverse')

% Measurement equivalency
measxstart=50E-3-pstartx; % measurement location along x leading edge
%measxstart=substdimx-50E-3-pstartx; % measurement location along x trailing edge
measlength=16E-3; % measurement lenght

Zmeas=Z(round(measxstart/p_size):-1:round((measxstart-measlength)/p_size),:); % leading edge
%Zmeas=Z(round(measxstart/p_size):1:round((measxstart+measlength)/p_size),:); % trailing edge
X1=mean(Zmeas);
Ra=mean(abs(Zmeas-ones(round(measlength/p_size)+1,1)*X1));
Rq=std(Zmeas);
figure(11), plot(0:nlayers,1E6*[Ra]),hold on,plot(0:30, 1E6*S3LRa,'r'), hold off
xlabel('Layer'), ylabel('Ra (Surface roughness) [\num]'),
title(' Ra comparison'),% for sample fused face up trailing edge')
legend('simulated data','fused face dwn. ld.ed.'), legend('Location','NorthWest')
%figure(7), plot(0:30,[Rq' S2TRq']), title('Rq comparison')

figure(3)
plot(1E3*p_size*[1:401],1E6*Zmeas(2101:2501,[1:nlayers+1])) %round(measlength/p_size)
xlabel('Position [mm]'), ylabel('Height [\num]'), xlim([0 2])
title(' Section of the simulation of EP3D profile for sample fused face down leading edge')
legend(string(:,.)), legend('show')
legend('Location','EastOutside'),set(legend,'YDir','reverse')

```

A.3. Simulation of feedback control strategy applied to the EP3D printing process

The following code simulates the feedback control strategy described in section 7.2.

```
%% One dimensional profile (considering pressure variation) version 2 + feedback control
% compression depends on the force applied by the roller on the surface

% % Fusing system modeling [lbf,in,s]
% Pa=25; % air pressure [psi]
% Wm=250; % motor roller speed [rpm]
% % T=180; % temperature of hot roller [C] - not considered in the model
%
% Vl=(Wm/30)*(3.3125*pi)*(1/60); % linear velocity through fuser [in/s]
% F=2*(Pa*pi*(2.5^2 - 0.75^2)/4)*((3.775+2.165)/2.165)*0.8; % Force on roller [lbf]
%
% m=13/(32*12); % mass [lbf]/g[in/s^2]
% k=(5*2*12.25*0.8/0.003); % Pressure roller spring constant [lbf/in]
% b=30; % Damping constant [lbf/in/s]

% Fusing system modeling [SI]

Pa=25*6894.757293168; % air pressure [Pa]
Wm=250; % motor roller speed [rpm]
% T=180; % temperature of hot roller [C] - not considered in the model

Vl=(Wm/30)*(3.3125*pi)*(25.4E-3/60); % linear velocity through fuser [m/s]
F=2*(Pa*pi*((2.5*25.4E-3)^2 - (0.75*25.4E-3)^2)/4)*((3.775+2.165)/2.165)*0.8; % Force on roller [N]

m=13*0.45359237; % mass [Kg]
k=(5*2*12.25*0.8/0.001)*(4.448222/25.4E-3)/6000; % Pressure roller spring constant [N/m] *
b=8*m/(25/73.42); % Damping constant [N/m/s] b=8*m/ts, ts=20mm/Vl(@500rpm)

p_size=5E-6; % particle size 5 microns
substrate=8E-3*25.4E-3; % base substrate thickness
nipwidth=12e-3; % nip width 12 mm

% Second order dynamic model
% x1 = vertical position of roller, x2 = vertical speed of roller
% u1 = Force by air pressure, u2 = sample profile
% y1 = Force applied by the roller to the sample; y2 = x1

A=[0 1; -k/m -b/m];
B=[0 0; 1/m k/m];
C=[k 0; 1 0];
D=[0 -k; 0 0];
x0=[F/k 0];

sys1=ss(A,B,C,D);
```

```

% Simulation parameters

P=0.95; % Probability of transfer
%k_comp=0.7; % compression factor when fusing
maxcomp=0.4; % maximum compression
mincomp=0.7; % minimum compression
compdepth=35E-6;

thres=36E-6; % threshold for complainece
dt=p_size/Vl; % t=x/Vl
substdimx=101E-3; % Substrate dimension x
pstartx=21E-3; % position of 3D print on substrate (Sample2=18, Sample3=21)
pdimx=50E-3-p_size; % 3D print dimension x **it has to be <10000
npoints = 9999;
nlayers = 30;

Tfinal=substdimx/Vl;
t=0:dt:Tfinal;
dim=size(t,2);

u=zeros(dim,2,nlayers);
y=zeros(dim,2,nlayers);

Z=zeros(npoints,nlayers+1);
Z=normrnd(substrate,3.6E-6,[npoints,1]); % base substrate

H=fspecial('gaussian',[5 1],1);

for i=2:nlayers+1
    X=normrnd(3,1,[npoints,1]);
    u(:,i-1)=F*ones(dim,2);
    u(1:round(pstartx/p_size)+1,2,i-1)=-substrate*ones(round(pstartx/p_size)+1,1);
    Zmean=mean(Z(:,i-1)+X*p_size);
    u(round(pstartx/p_size)+2:round((pstartx+pdimx)/p_size)+1,2,i-1)=-Z(:,i-1);
    u(round((pstartx+pdimx)/p_size)+2:dim,2,i-1)=-substrate*ones(dim-round((pstartx+pdimx)/p_size)-1,1);

    [y(:,i-1),t,xss]=lsim(sys1,u(:,i-1),t,x0);

    Zmax=max(Z(:,i-1)+X*p_size);
    %deltamax=Zmax-Zmean;
    fmax=max(y(round(pstartx/p_size)+2:round((pstartx+pdimx)/p_size)+1,1,i-1));

    Zmin=min(Z(:,i-1)+X*p_size);
    deltamin=Zmax-Zmin;
    if deltamin>thres
        fmin=min(y(round(pstartx/p_size)+2:round((pstartx+pdimx)/p_size)+1,1,i-1));
    else
        fmin=k*(y(1,2,i-1)+(Zmax-thres));
    end
    fmax=(fmax-fmin)*0.95+fmin;

```



```

for j=1:npoints
    if j<=round(nipwidth/2/p_size)
        Zmax=max(Z(1:j+round(nipwidth/2/p_size),i-1)+X(1:j+round(nipwidth/2/p_size))*p_size);
    elseif j<round(pdimg/p_size)-round(nipwidth/2/p_size)
        Zmax=max(Z(j-round(nipwidth/2/p_size):j+round(nipwidth/2/p_size),i-1)+X(j-
round(nipwidth/2/p_size):j+round(nipwidth/2/p_size))*p_size);
    else
        Zmax=max(Z(j-round(nipwidth/2/p_size):round(pdimg/p_size),i-1)+X(j-
round(nipwidth/2/p_size):round(pdimg/p_size))*p_size);
    end
    delta=Zmax-(Z(j,i-1)+X(j)*p_size);
    %delta=(Z(j,i-1)+X(j)*p_size)-Zmean;

    if (rand<P)&&(delta<thres)
        Ptrans=1;
        F1=y(j+round(pstartx/p_size)+1,1,i-1);
        if F1>fmax
            k_comp=maxcomp;
        elseif F1<fmin
            k_comp=mincomp;
        else
            k_comp=mincomp+((maxcomp-mincomp)/(fmax-fmin))*(F1-fmin);
        end
        %k_comp=(delta*(maxcomp-mincomp)/thres)+maxcomp;
    else
        Ptrans=0; k_comp=1;
    end
    Z(j,i)=X(j)*p_size*k_comp*Ptrans+(0.95+0.05*k_comp)*compdepth+Z(j,i-1)-compdepth;
end

Z(:,i)=imfilter(Z(:,i),H,'symmetric');

thcomp=15E-6;
Zmax=max(Z(:,i));
for j=1:npoints
    if (Zmax-Z(j,i))>thcomp
        Xcomp(j,i-1)=1;
    else
        Xcomp(j,i-1)=0;
    end
end

Xcomp(:,i-1)=Xcomp(:,i-1).*normrnd(3,1,[npoints,1]);%*****
ucomp(:,i-1)=F*ones(dim,2);
ucomp(1:round(pstartx/p_size)+1,2,i-1)=-substrate*ones(round(pstartx/p_size)+1,1);
Zmean=mean(Z(:,i)+Xcomp(:,i-1)*p_size);
ucomp(round(pstartx/p_size)+2:round((pstartx+pdimg)/p_size)+1,2,i-1)=-Z(:,i);
ucomp(round((pstartx+pdimg)/p_size)+2:dim,2,i-1)=-substrate*ones(dim-
round((pstartx+pdimg)/p_size)-1,1);

[ycomp(:,i-1),t,xss]=lsim(sys1,ucomp(:,i-1),t,x0);

```

```

Zmax=max(Z(:,i)+Xcomp(:,i-1)*p_size);
%delta_max=Zmax-Zmean;
fmax=max(ycomp(round(pstartx/p_size)+2:round((pstartx+pdimx)/p_size)+1,1,i-1));

Zmin=min(Z(:,i)+Xcomp(:,i-1)*p_size);
deltamin=Zmax-Zmin;
if deltamin>thres
    fmin=min(ycomp(round(pstartx/p_size)+2:round((pstartx+pdimx)/p_size)+1,1,i-1));
else
    fmin=k*(ycomp(1,2,i-1)+(Zmax-thres));
end
fmax=(fmax-fmin)*0.95+fmin;

for j=1:npoints
    if j<=round(nipwidth/2/p_size)
        Zmax=max(Z(1:j+round(nipwidth/2/p_size),i)+Xcomp(1:j+round(nipwidth/2/p_size),i-1)*p_size);
    elseif j<round(pdimx/p_size)-round(nipwidth/2/p_size)
        Zmax=max(Z(j-round(nipwidth/2/p_size):j+round(nipwidth/2/p_size),i)+Xcomp(j-round(nipwidth/2/p_size):j+round(nipwidth/2/p_size),i-1)*p_size);
    else
        Zmax=max(Z(j-round(nipwidth/2/p_size):round(pdimx/p_size),i)+Xcomp(j-round(nipwidth/2/p_size):round(pdimx/p_size),i-1)*p_size);
    end
    delta=Zmax-(Z(j,i)+Xcomp(j,i-1)*p_size);
    %delta=(Z(j,i-1)+X(j)*p_size)-Zmean;

    if (rand<P)&&(delta<thres)
        Ptrans=1;
        F1=ycomp(j+round(pstartx/p_size)+1,1,i-1);
        if F1>fmax
            k_comp=maxcomp;
        elseif F1<fmin
            k_comp=mincomp;
        else
            k_comp=mincomp+((maxcomp-mincomp)/(fmax-fmin))*(F1-fmin);
        end
        %k_comp=(delta*(maxcomp-mincomp)/thres)+maxcomp;
    else
        Ptrans=0; k_comp=1;
    end
    Z(j,i)=Xcomp(j,i-1)*p_size*k_comp*Ptrans+(0.95+0.05*k_comp)*compdepth+Z(j,i)-compdepth;
end

Z(:,i)=imfilter(Z(:,i),H,'symmetric');

end

figure(1)
plot(p_size*[1:9999],1E6*Z(1:9999,[1:nlayers+1]))
xlabel('position [m]'), ylabel('height [\nmum]')
title('Simulation of EP3D profile with perfect registration')

```

```

%% Measurement equivalency
measxstart=50E-3-pstartx; % measurement location along x leading edge
%measxstart=substdimx-50E-3-pstartx; % measurement location along x trailing edge
measlength=16E-3; % measurement length

% layer=30;
Zmeas=Z(round(measxstart/p_size):-1:round((measxstart-measlength)/p_size),:); % leading edge
%Zmeas=Z(round(measxstart/p_size):1:round((measxstart+measlength)/p_size),:); % trailing edge
X1=mean(Zmeas);
Ra=mean(abs(Zmeas-ones(round(measlength/p_size)+1,1)*X1));
Rq=std(Zmeas);

figure(11), plot(0:nlayers,1E6*[Ra']),hold on,plot(0:30, 1E6*S3LRa','r'), hold off
xlabel('Layer'), ylabel('Ra (Surface roughness) [\mum]'),
title(' Ra comparison'),% for sample fused face up trailing edge')
legend('simulated data','fused face dwn. ld.ed.'), legend('Location','NorthWest')
%figure(7), plot(0:30,[Rq' S2TRq']), title('Rq comparison')

```

A.4. Light direction estimation from reflecting sphere

The following code was developed to estimate light direction from a sphere to aid the image processing techniques explored in section 8.3:

```

%% Load image file
Im=imread('ball-test-RGB.tif');

%% select region for ball 1
[BW,xv1,yv1]=roipoly(Im);
xv1=round(xv1);
yv1=round(yv1);

xmin=min(xv1);
xmax=max(xv1);
ymin=min(yv1);
ymax=max(yv1);

Ball1=Im(ymin:ymax,xmin:xmax,:);
figure(2), imshow(Ball1)

%% Get the center of sphere, radius and point of reflection
Rmin=round((xmax-xmin)/2)-70;
Rmax=round((xmax-xmin)/2);

[center1,radius1]=imfindcircles(Ball1,[Rmin,Rmax],'ObjectPolarity','dark','EdgeThreshold',0.15)
viscircles(center1, radius1,'EdgeColor','b');

% Display the calculated center
hold on, plot(center1(:,1),center1(:,2),'b+', 'LineWidth',2); hold off;

```

```

Rmin=round((xmax-xmin)/25);
Rmax=round((xmax-xmin)/10);

[center_ref1,radius_ref1]=imfindcircles(Ball1,[Rmin,Rmax],'ObjectPolarity','bright')
viscircles(center_ref1, radius_ref1,'EdgeColor','r');

% Display the calculated center
hold on; plot(center_ref1(:,1),center_ref1(:,2),'r+', 'LineWidth',2); hold off;

%% Calculate light direction
dirxy1=center_ref1-center1;
z_ref1=sqrt(radius1^2-(dirxy1(1))^2-(dirxy1(2))^2)+radius1;
dir1=[dirxy1 z_ref1]/norm([dirxy1 z_ref1])

```

A.5. Edge detection and image fusing for compensation image

The following code was used to extract the edges from 8 images with different illumination angles and combined to create a binary compensation image.

```

%% Read images from distinct illumination angles
I1=imread('test3-000.jpg');
I2=imread('test3-045.jpg');
I3=imread('test3-090.jpg');
I4=imread('test3-135.jpg');
I5=imread('test3-180.jpg');
I6=imread('test3-225.jpg');
I7=imread('test3-270.jpg');
I8=imread('test3-315.jpg');
figure(1), imshow(I1(700:1100,1000:1400,:))

%% Edge detection
tr=0.165;
I1e=edge(rgb2gray(I1),'sobel',tr);
I2e=edge(rgb2gray(I2),'sobel',tr);
I3e=edge(rgb2gray(I3),'sobel',tr);
I4e=edge(rgb2gray(I4),'sobel',tr);
I5e=edge(rgb2gray(I5),'sobel',tr);
I6e=edge(rgb2gray(I6),'sobel',tr);
I7e=edge(rgb2gray(I7),'sobel',tr);
I8e=edge(rgb2gray(I8),'sobel',tr);
%%
figure(2), imshow(I1e(700:1100,1000:1400))

%% Image fusing
for i=1:2048
    for j=1:2448
        Ifused(i,j)=(I1e(i,j) | I2e(i,j) | I3e(i,j) | I4e(i,j) | I5e(i,j) | I6e(i,j) | I7e(i,j) | I8e(i,j));
    end
end

```

```

    end
end

figure(3), imshow(Ifused(700:1100,1000:1400))

%% Apply morph operators to generate compensation image
se = strel('disk',2);
Ifused1=imclose(Ifused,se);
se = strel('disk',1);
Ifused1=imerode(Ifused1,se);
se = strel('disk',1);
Ifused1=imdilate(Ifused1,se);
% se = strel('disk',1);
% Ifused1=imerode(Ifused1,se);
% se = strel('disk',1);
% Ifused1=imdilate(Ifused1,se);

Ifused1=~Ifused1;

% se = strel('disk',1);
% Ifused1=imerode(Ifused1,se);

% se = strel('disk',1);
% Ifused1=imclose(Ifused1,se);
% se = strel('disk',1);
% Ifused1=imdilate(Ifused1,se);

figure(4), imshow(Ifused1(700:1100,1000:1400))

%% Save output files
imwrite(Ifused,'test3-fused.jpg');
imwrite(Ifused1,'test3-morphed.jpg');

```

Appendix B. RESULTS OF DOE ANALYSIS

This section compiles the graphs and tables resulting of the DOE analysis for the experiments covered in section 5.3.

B.1. Ra – Leading edge

Table 11. Analysis of Variance for Ra(1) [μm], using Adjusted SS for Tests

Source	DF	Seq SS	Adj SS	Adj MS	F	P
Layers (x10)	2	1195.75	1195.75	597.88	52.28	0.000
Substrate	2	27.76	27.76	13.88	1.21	0.305
Colors/Materials	1	188.99	188.99	188.99	16.53	0.000
Halftoning	1	628.00	628.00	628.00	54.92	0.000
Graded	1	33.19	33.19	33.19	2.90	0.094
Substrate*Colors/Materials	2	13.98	13.98	6.99	0.61	0.546
Substrate*Halftoning	2	1.11	1.11	0.56	0.05	0.953
Substrate*Graded	2	69.71	69.71	34.85	3.05	0.056
Colors/Materials*Halftoning	1	68.60	68.60	68.60	6.00	0.018
Colors/Materials*Graded	1	0.01	0.01	0.01	0.00	0.980
Halftoning*Graded	1	5.60	5.60	5.60	0.49	0.487
Error	55	628.96	628.96	11.44		
Total	71	2861.66				
S = 3.38166 R-Sq = 78.02% R-Sq(adj) = 71.63%						
Unusual Observations for Ra(1) [μm]						
Obs	Ra(1) [μm]	Fit	SE Fit	Residual	St Resid	
5	4.2220	10.8507	1.6432	-6.6287	-2.24 R	
21	5.8480	12.0100	1.6432	-6.1620	-2.08 R	
53	27.5490	20.3048	1.6432	7.2442	2.45 R	
R denotes an observation with a large standardized residual.						

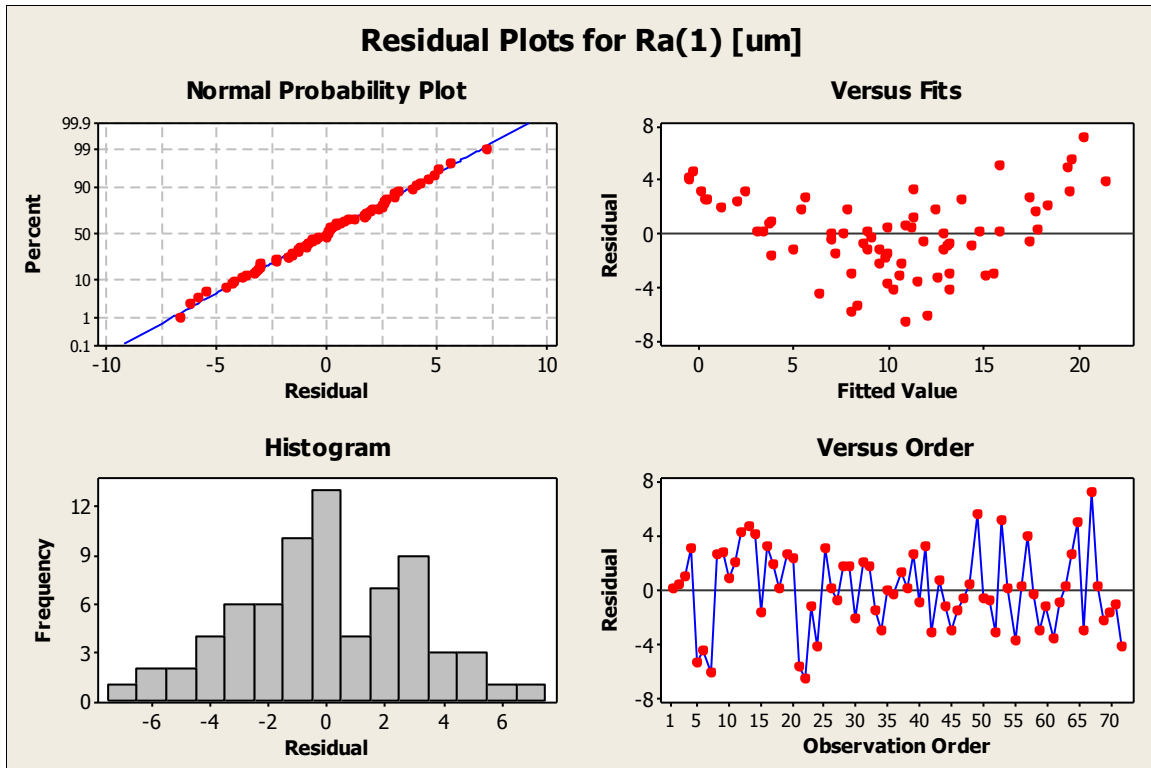


Figure 93. Residual plots for Ra - leading edge

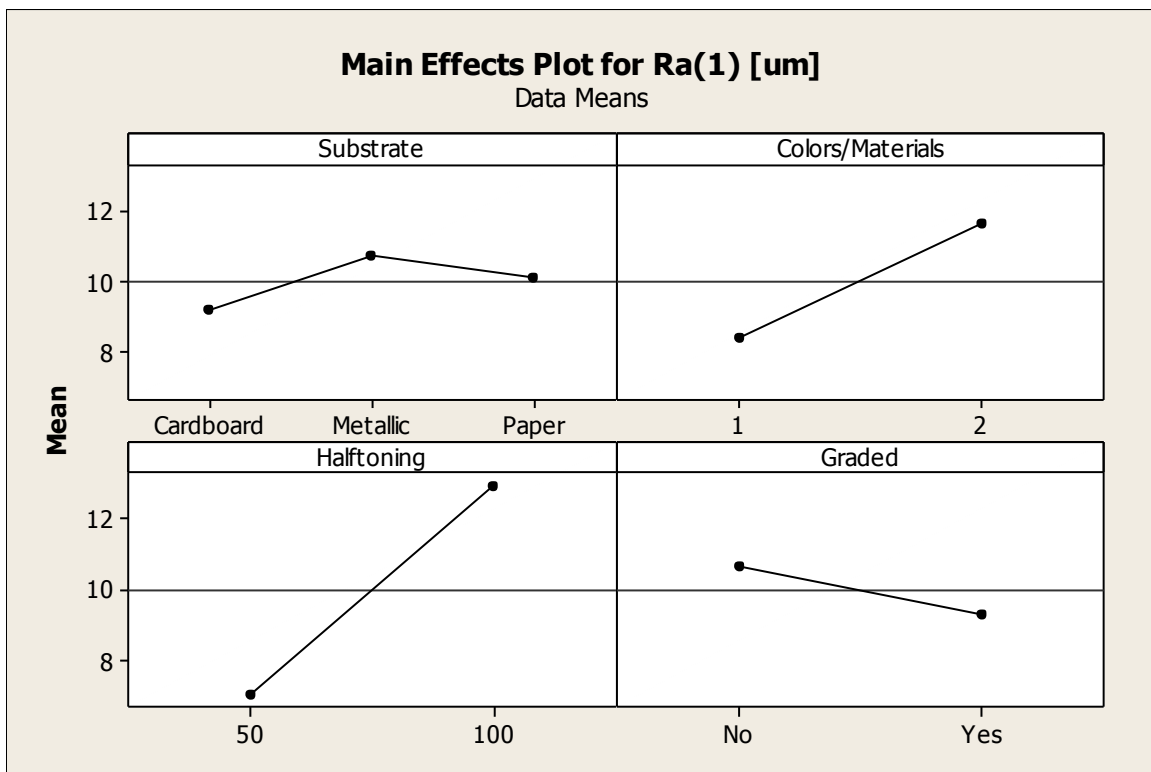


Figure 94. Main effects plot for Ra - leading edge

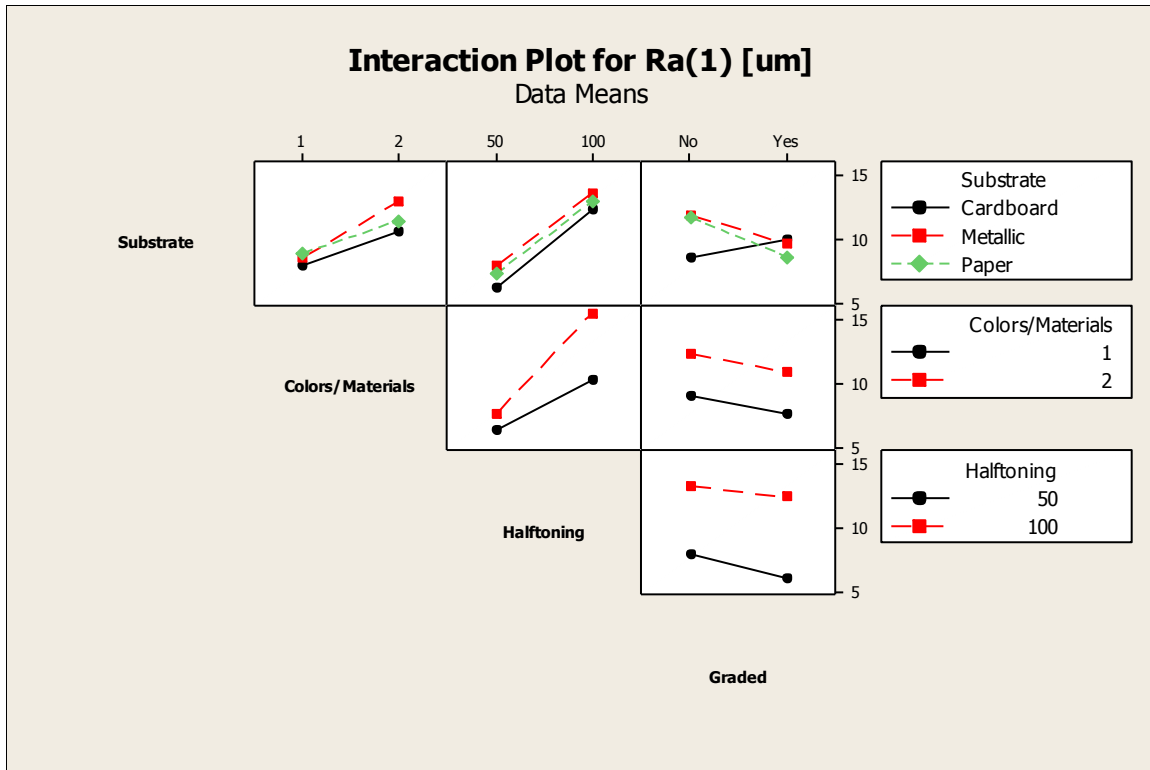


Figure 95. Interaction plot for Ra - leading edge

B.2. Rq – Leading edge

Table 12. Analysis of Variance for Rq(1) [μm], using Adjusted SS for Tests

Source	DF	Seq SS	Adj SS	Adj MS	F	P
Layers (x10)	2	2289.98	2289.98	1144.99	48.49	0.000
Substrate	2	28.62	28.62	14.31	0.61	0.549
Colors/Materials	1	433.35	433.35	433.35	18.35	0.000
Halftoning	1	1510.54	1510.54	1510.54	63.97	0.000
Graded	1	123.01	123.01	123.01	5.21	0.026
Substrate*Colors/Materials	2	42.68	42.68	21.34	0.90	0.411
Substrate*Halftoning	2	1.40	1.40	0.70	0.03	0.971
Substrate*Graded	2	70.37	70.37	35.18	1.49	0.234
Colors/Materials*Halftoning	1	142.68	142.68	142.68	6.04	0.017
Colors/Materials*Graded	1	6.00	6.00	6.00	0.25	0.616
Halftoning*Graded	1	0.91	0.91	0.91	0.04	0.845
Error	55	1298.72	1298.72	23.61		
Total	71	5948.24				

S = 4.85933 R-Sq = 78.17% R-Sq(adj) = 71.81%

Unusual Observations for Rq(1) [μm]

Obs	Rq(1) [μm]	Fit	SE Fit	Residual	St Resid
5	6.3400	16.9065	2.3612	-10.5665	-2.49 R
13	3.0890	12.6420	2.3612	-9.5530	-2.25 R
21	7.8710	17.5288	2.3612	-9.6578	-2.27 R
53	41.6950	30.2716	2.3612	11.4234	2.69 R

R denotes an observation with a large standardized residual.

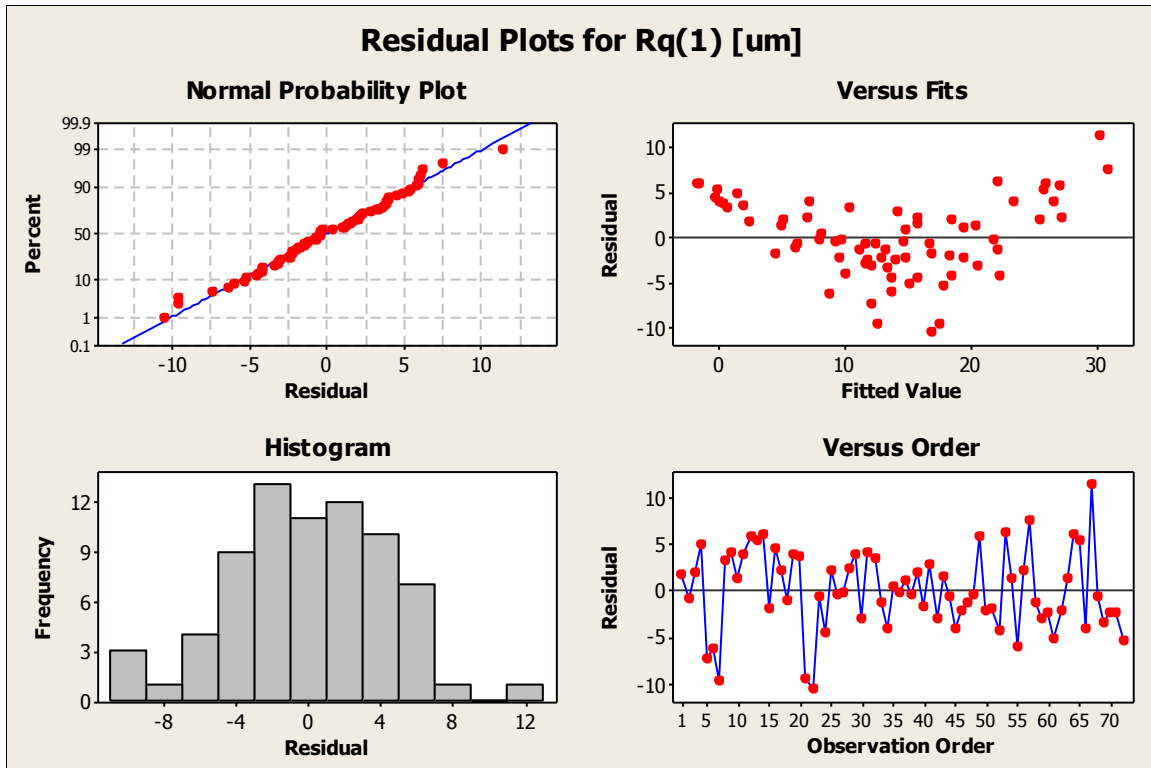


Figure 96. Residual plots for Rq - leading edge

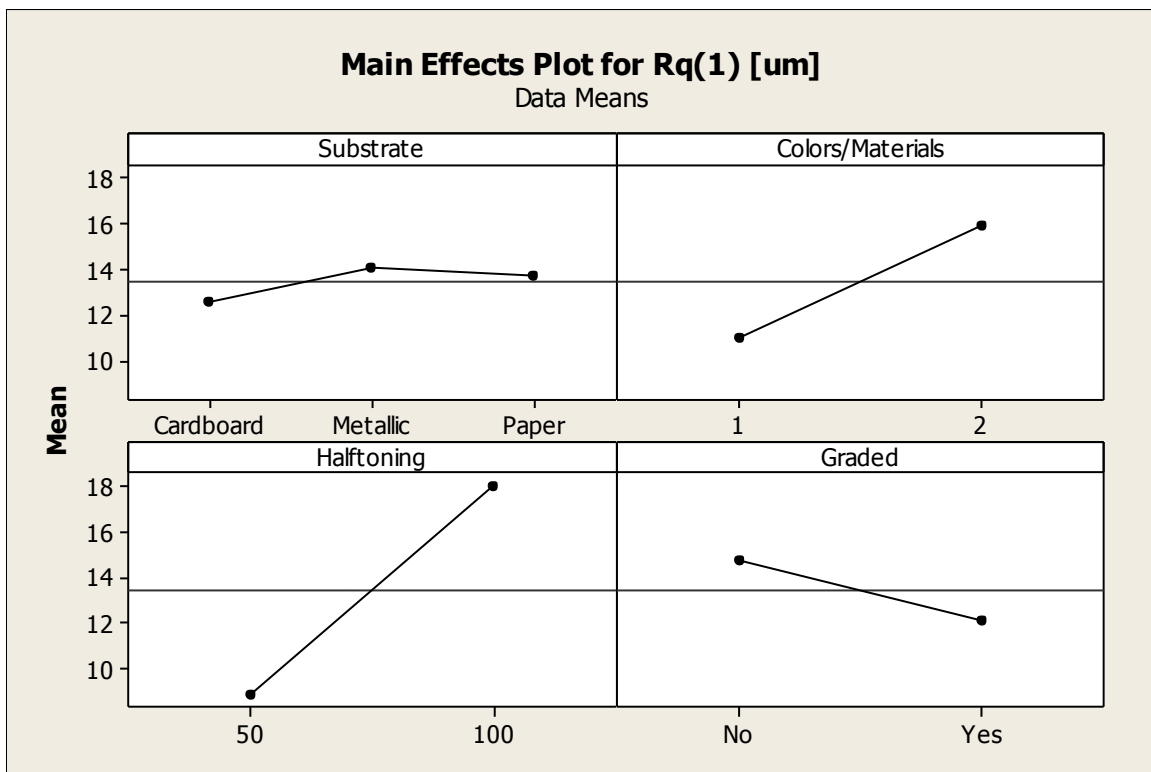


Figure 97. Main effects plot for Rq - leading edge

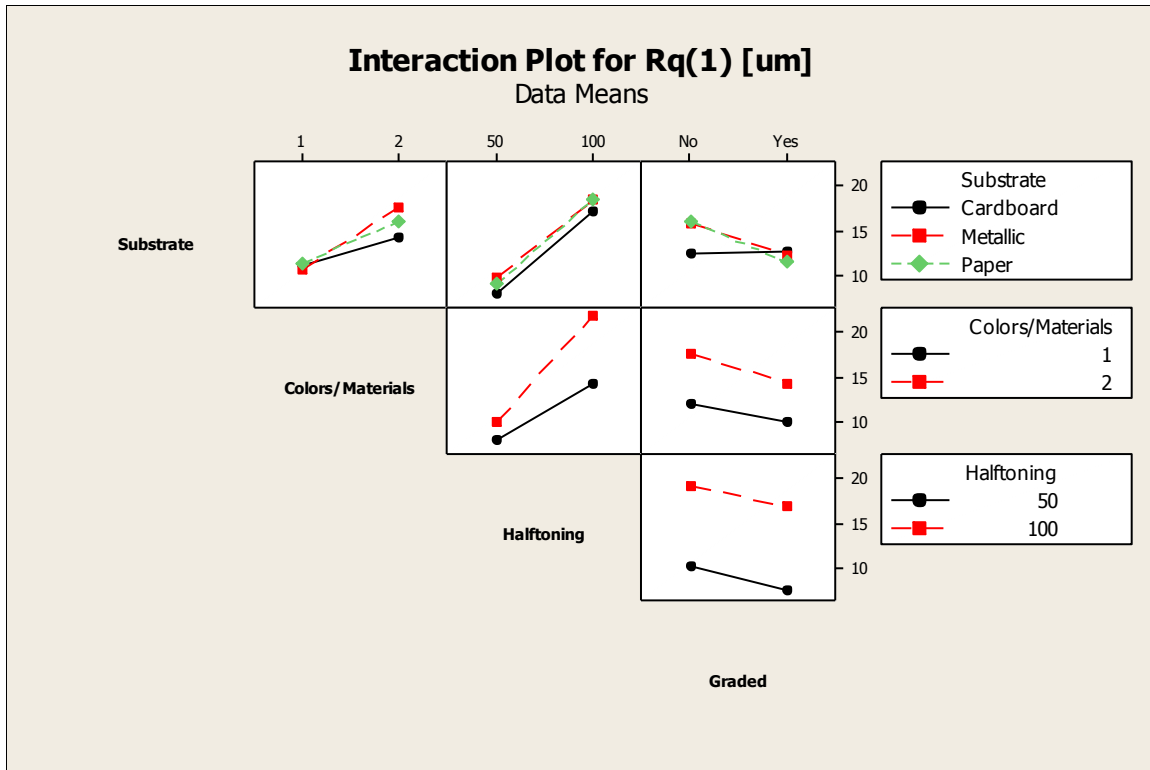


Figure 98. Interaction plot for Rq - leading edge

B.3. Ra – Trailing edge

Table 13. Analysis of Variance for Ra(2) [μm], using Adjusted SS for Tests

Source	DF	Seq SS	Adj SS	Adj MS	F	P
Layers (x10)	2	314.373	314.373	157.187	31.45	0.000
Substrate	2	40.545	40.545	20.272	4.06	0.023
Colors/Materials	1	4.621	4.621	4.621	0.92	0.341
Halftoning	1	82.638	82.638	82.638	16.53	0.000
Graded	1	19.032	19.032	19.032	3.81	0.056
Substrate*Colors/Materials	2	2.650	2.650	1.325	0.27	0.768
Substrate*Halftoning	2	5.532	5.532	2.766	0.55	0.578
Substrate*Graded	2	11.035	11.035	5.517	1.10	0.339
Colors/Materials*Halftoning	1	0.784	0.784	0.784	0.16	0.694
Colors/Materials*Graded	1	7.159	7.159	7.159	1.43	0.237
Halftoning*Graded	1	37.723	37.723	37.723	7.55	0.008
Error	55	274.906	274.906	4.998		
Total	71	801.000				
S = 2.23569 R-Sq = 65.68% R-Sq(adj) = 55.70%						
Unusual Observations for Ra(2) – R denotes an observation with a large standardized residual.						
Obs	Ra(2) [μm]	Fit	SE Fit	Residual	St Resid	
14	13.1460	5.5677	1.0863	7.5783	3.88 R	
53	14.2990	9.8154	1.0863	4.4836	2.29 R	
57	13.7790	9.1309	1.0863	4.6481	2.38 R	
65	6.9800	11.1526	1.0863	-4.1726	-2.14 R	

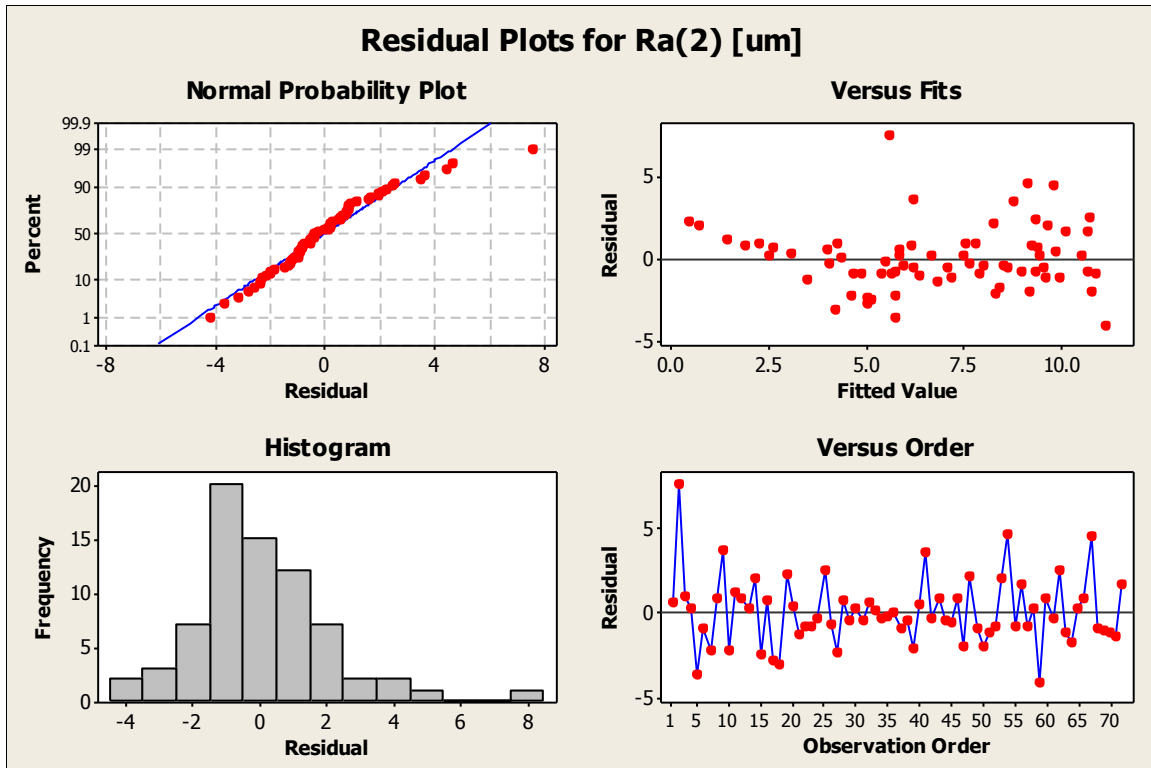


Figure 99. Residual plots for Ra - trailing edge

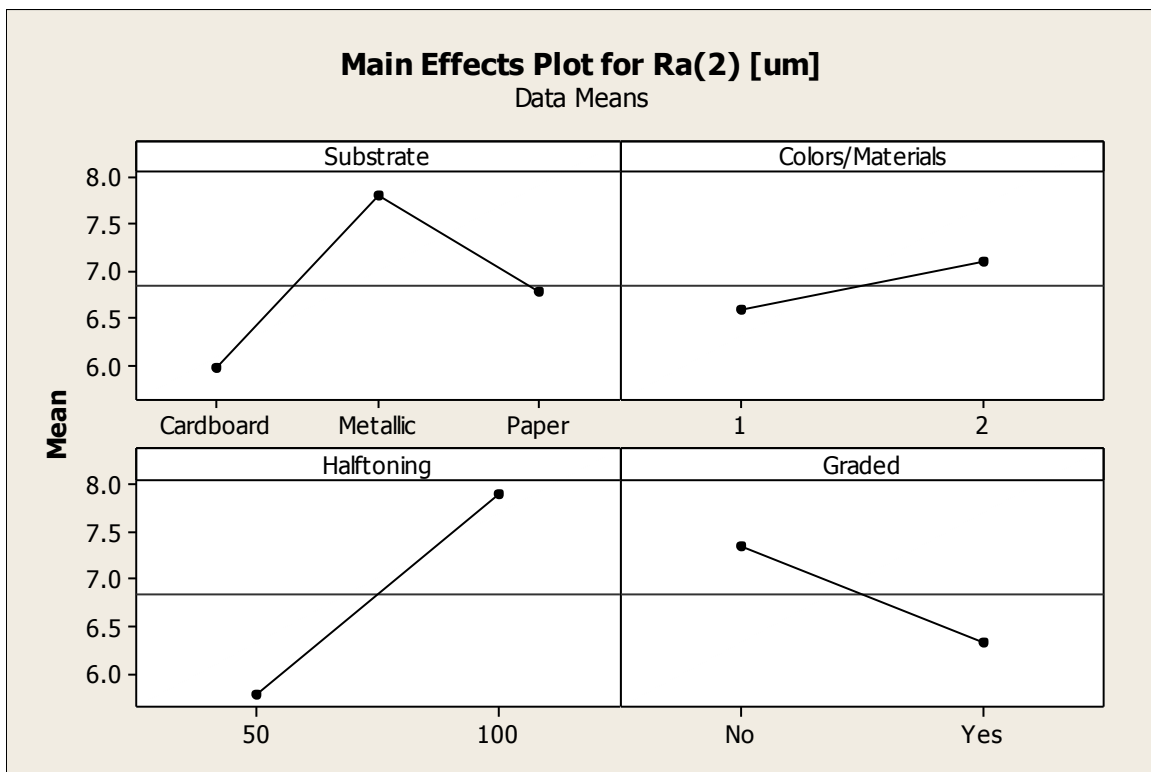


Figure 100. Main effects plot for Ra - trailing edge

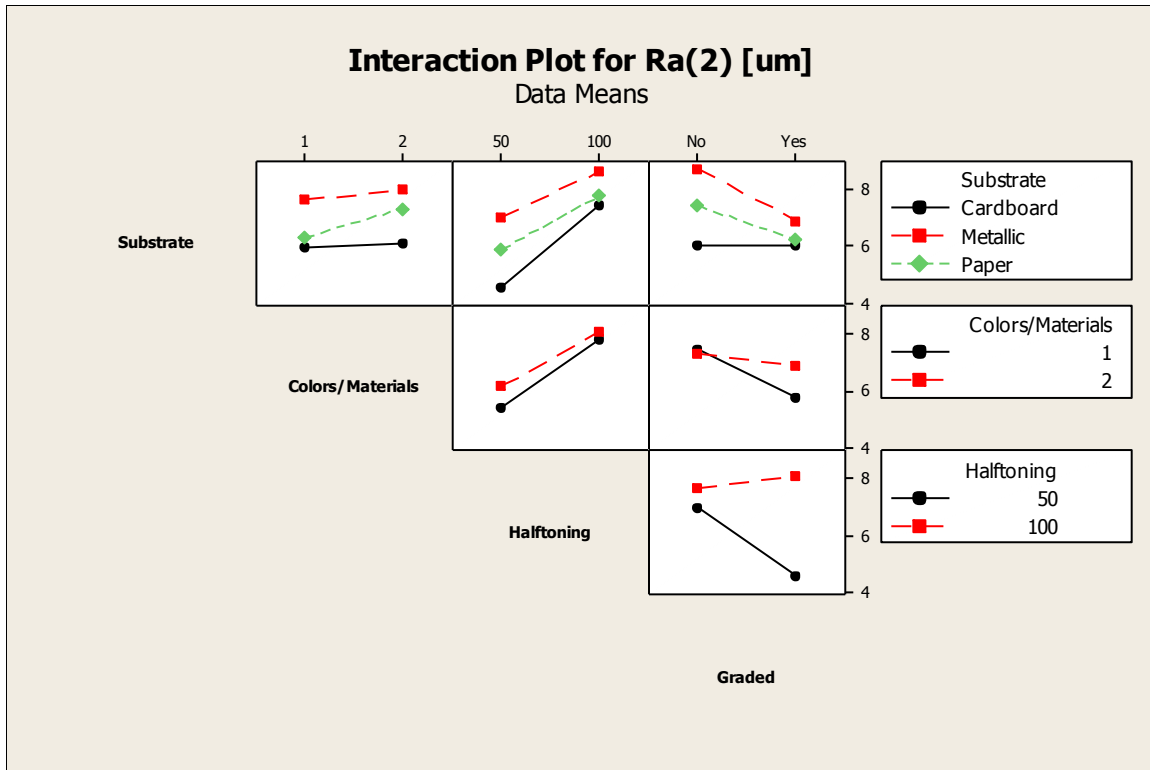


Figure 101. Interaction plots for Ra - trailing edge

B.4. Rq – Trailing edge

Table 14. Analysis of Variance for Rq(2) [μm], using Adjusted SS for Tests

Source	DF	Seq SS	Adj SS	Adj MS	F	P
Layers (x10)	2	565.126	565.126	282.563	34.59	0.000
Substrate	2	50.334	50.334	25.167	3.08	0.054
Colors/Materials	1	10.715	10.715	10.715	1.31	0.257
Halftoning	1	242.323	242.323	242.323	29.67	0.000
Graded	1	51.494	51.494	51.494	6.30	0.015
Substrate*Colors/Materials	2	5.731	5.731	2.865	0.35	0.706
Substrate*Halftoning	2	5.203	5.203	2.601	0.32	0.729
Substrate*Graded	2	22.487	22.487	11.243	1.38	0.261
Colors/Materials*Halftoning	1	1.268	1.268	1.268	0.16	0.695
Colors/Materials*Graded	1	11.499	11.499	11.499	1.41	0.241
Halftoning*Graded	1	43.845	43.845	43.845	5.37	0.024
Error	55	449.255	449.255	8.168		
Total	71	1459.280				
S = 2.85802 R-Sq = 69.21% R-Sq(adj) = 60.26%						
Unusual Observations for Rq(2) [μm]						
Obs	Rq(2) [μm]	Fit	SE Fit	Residual	St Resid	
6	2.6200	7.7871	1.3887	-5.1671	-2.07 R	
14	15.8790	7.4170	1.3887	8.4620	3.39 R	
53	21.9350	14.3080	1.3887	7.6270	3.05 R	
57	19.8490	13.0112	1.3887	6.8378	2.74 R	
R denotes an observation with a large standardized residual.						

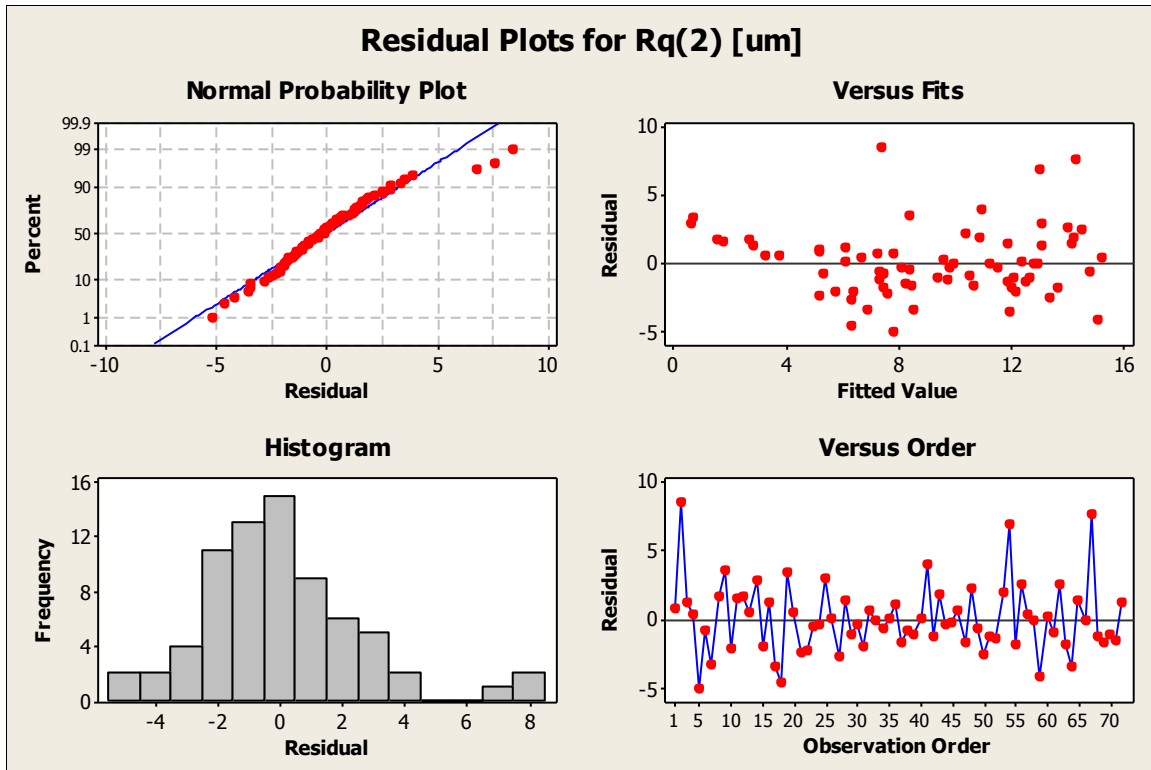


Figure 102. Residual plots for Rq - trailing edge

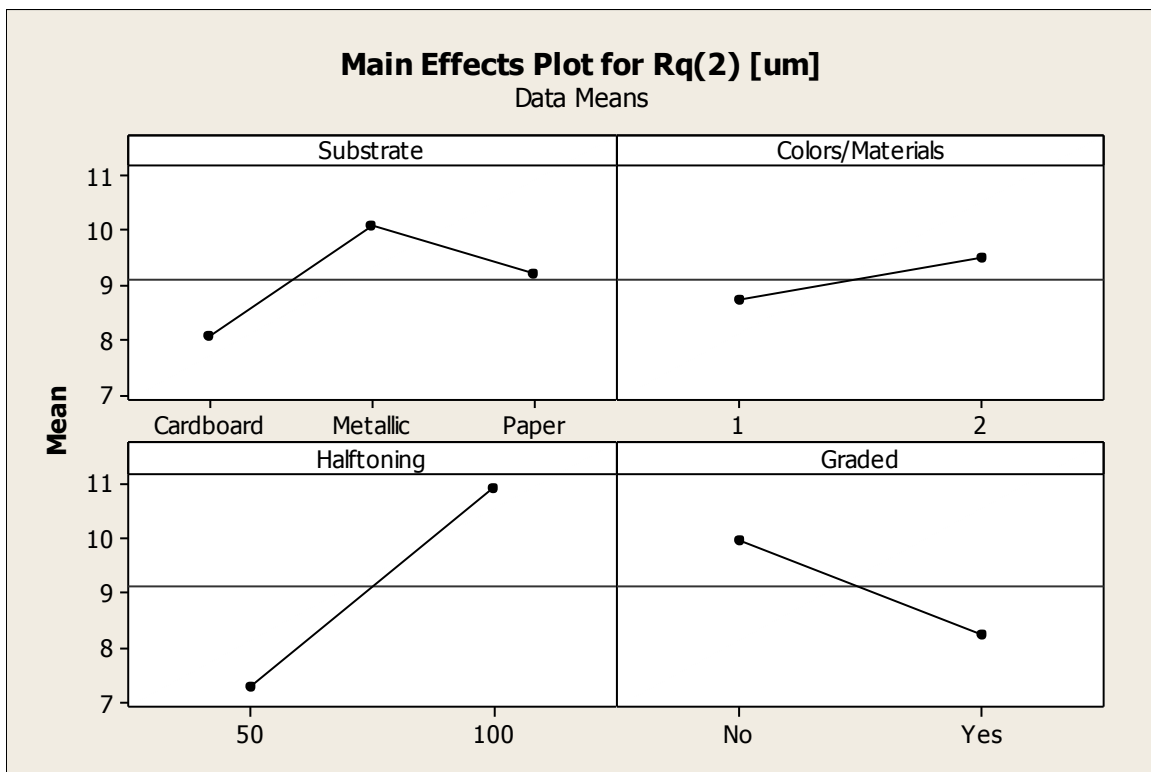


Figure 103. Main effects plot for Rq - trailing edge

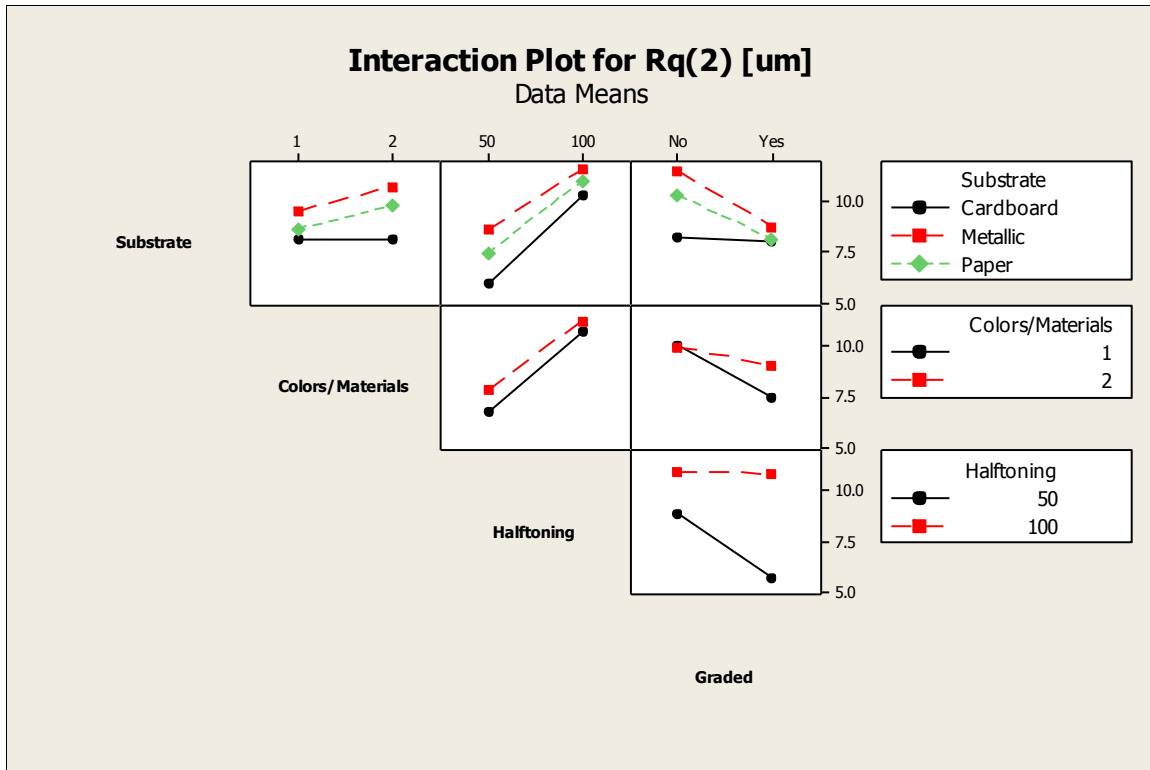


Figure 104. Interaction plots for Rq - trailing edge

B.5. Unfiltered profile Pa – Leading edge

Table 15. Analysis of Variance for Pa(1) [μm], using Adjusted SS for Tests

Source	DF	Seq SS	Adj SS	Adj MS	F	P
Layers (x10)	2	2170.02	2170.02	1085.01	46.74	0.000
Substrate	2	56.81	56.81	28.40	1.22	0.302
Colors/Materials	1	336.06	336.06	336.06	14.48	0.000
Halftoning	1	1114.53	1114.53	1114.53	48.02	0.000
Graded	1	96.89	96.89	96.89	4.17	0.046
Substrate*Colors/Materials	2	35.17	35.17	17.58	0.76	0.474
Substrate*Halftoning	2	3.54	3.54	1.77	0.08	0.927
Substrate*Graded	2	79.97	79.97	39.98	1.72	0.188
Colors/Materials*Halftoning	1	109.37	109.37	109.37	4.71	0.034
Colors/Materials*Graded	1	5.67	5.67	5.67	0.24	0.623
Halftoning*Graded	1	1.33	1.33	1.33	0.06	0.811
Error	55	1276.66	1276.66	23.21		
Total	71	5286.01				

S = 4.81788 R-Sq = 75.85% R-Sq(adj) = 68.82%

Unusual Observations for Pa(1) [μm]

Obs	Pa(1) [μm]	Fit	SE Fit	Residual	St Resid
5	5.6220	14.4838	2.3411	-8.8618	-2.10 R
21	7.8460	17.1417	2.3411	-9.2957	-2.21 R
69	42.7920	30.4240	2.3411	12.3680	2.94 R
70	36.8530	25.9339	2.3411	10.9191	2.59 R

R denotes an observation with a large standardized residual.

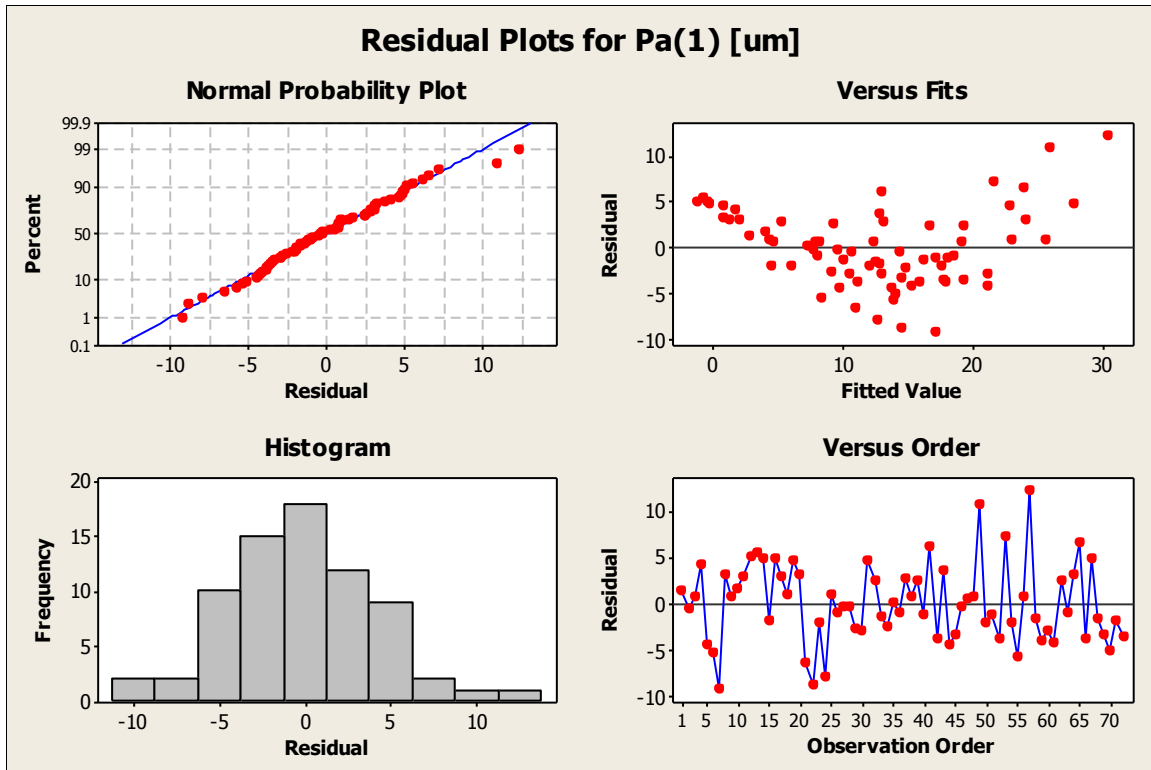


Figure 105. Residual plots for Pa - leading edge

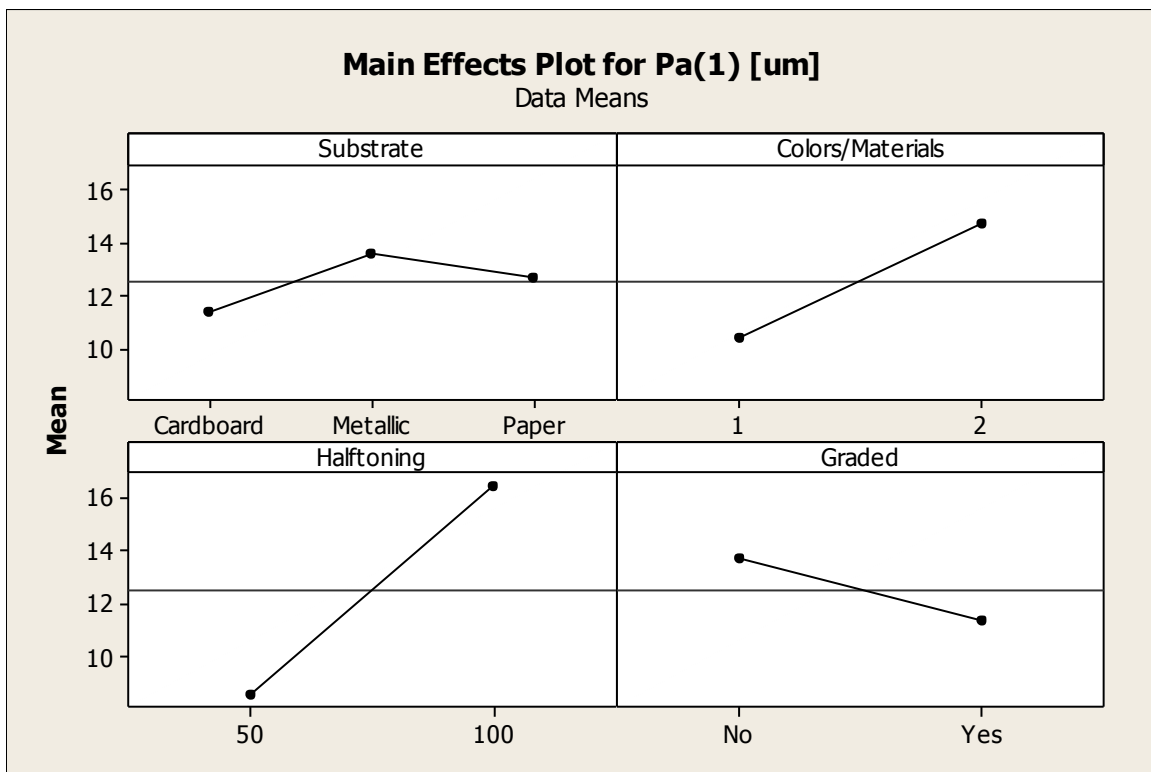


Figure 106. Main effects plot for Pa - leading edge

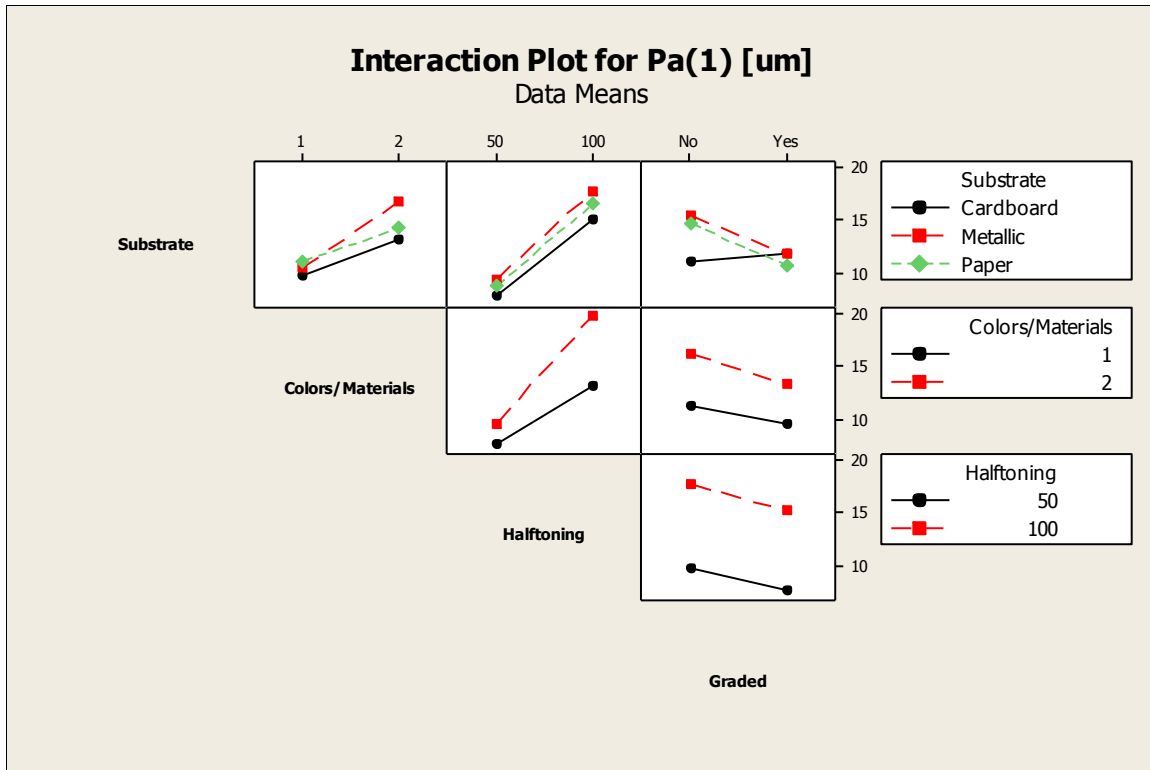


Figure 107. Interaction plot for Pa - leading edge

B.6. Pq – Leading edge

Table 16. Analysis of Variance for Pq(1) [μm], using Adjusted SS for Tests

Source	DF	Seq SS	Adj SS	Adj MS	F	P
Layers (x10)	2	3734.09	3734.09	1867.05	49.28	0.000
Substrate	2	37.65	37.65	18.83	0.50	0.611
Colors/Materials	1	621.59	621.59	621.59	16.41	0.000
Halftoning	1	2206.35	2206.35	2206.35	58.23	0.000
Graded	1	175.75	175.75	175.75	4.64	0.036
Substrate*Colors/Materials	2	59.51	59.51	29.75	0.79	0.461
Substrate*Halftoning	2	0.99	0.99	0.50	0.01	0.987
Substrate*Graded	2	74.95	74.95	37.48	0.99	0.378
Colors/Materials*Halftoning	1	192.68	192.68	192.68	5.09	0.028
Colors/Materials*Graded	1	14.41	14.41	14.41	0.38	0.540
Halftoning*Graded	1	0.49	0.49	0.49	0.01	0.910
Error	55	2083.83	2083.83	37.89		
Total	71	9202.31				
S = 6.15531 R-Sq = 77.36% R-Sq(adj) = 70.77%						
Unusual Observations for Pq(1) [μm]						
Obs	Pq(1) [μm]	Fit	SE Fit	Residual	St Resid	
5	7.4520	19.4891	2.9909	-12.0371	-2.24 R	
21	9.9070	21.8076	2.9909	-11.9006	-2.21 R	
69	53.3840	39.2561	2.9909	14.1279	2.63 R	
70	46.3130	33.8439	2.9909	12.4691	2.32 R	
R denotes an observation with a large standardized residual.						

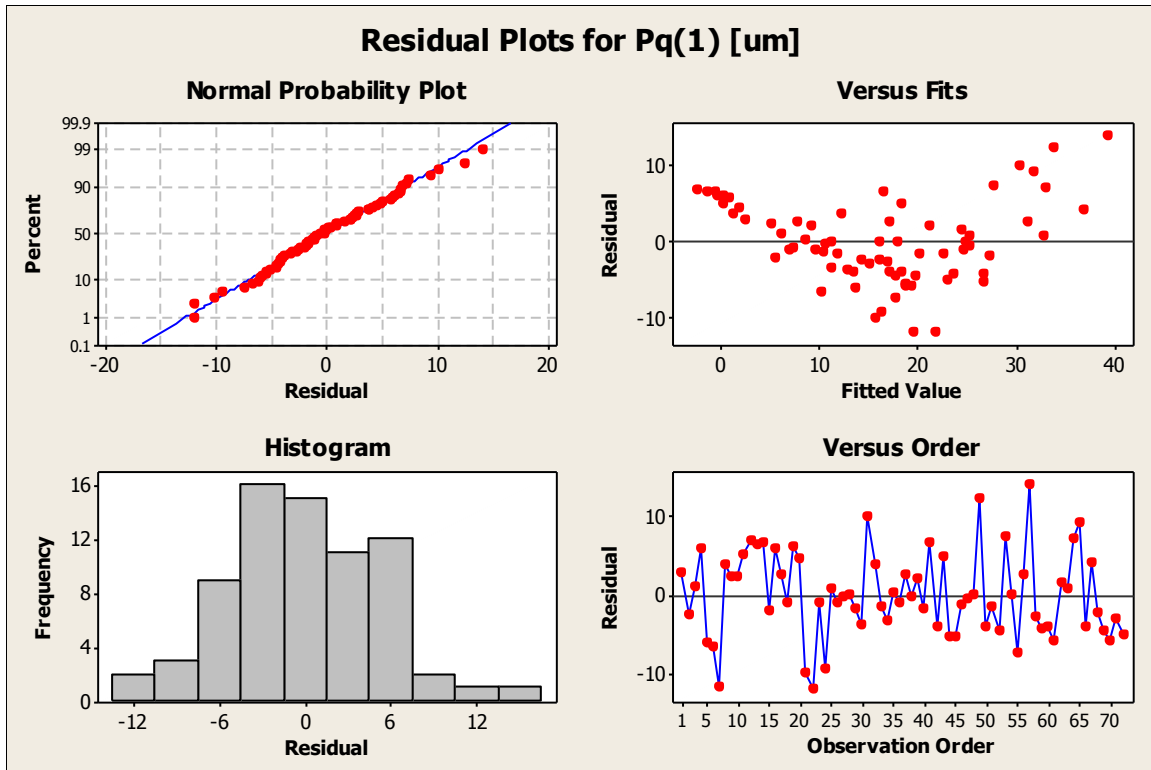


Figure 108. Residual plots for Pq - leading edge

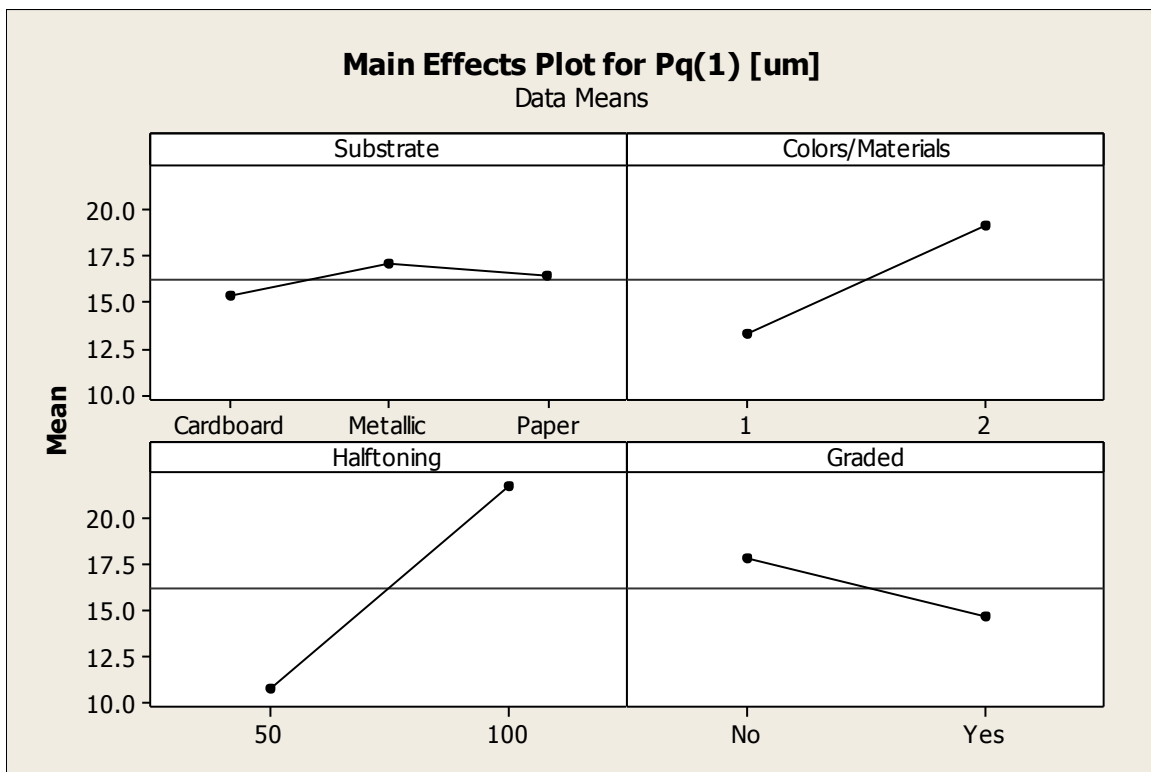


Figure 109. Main effects plot for Pq - leading edge

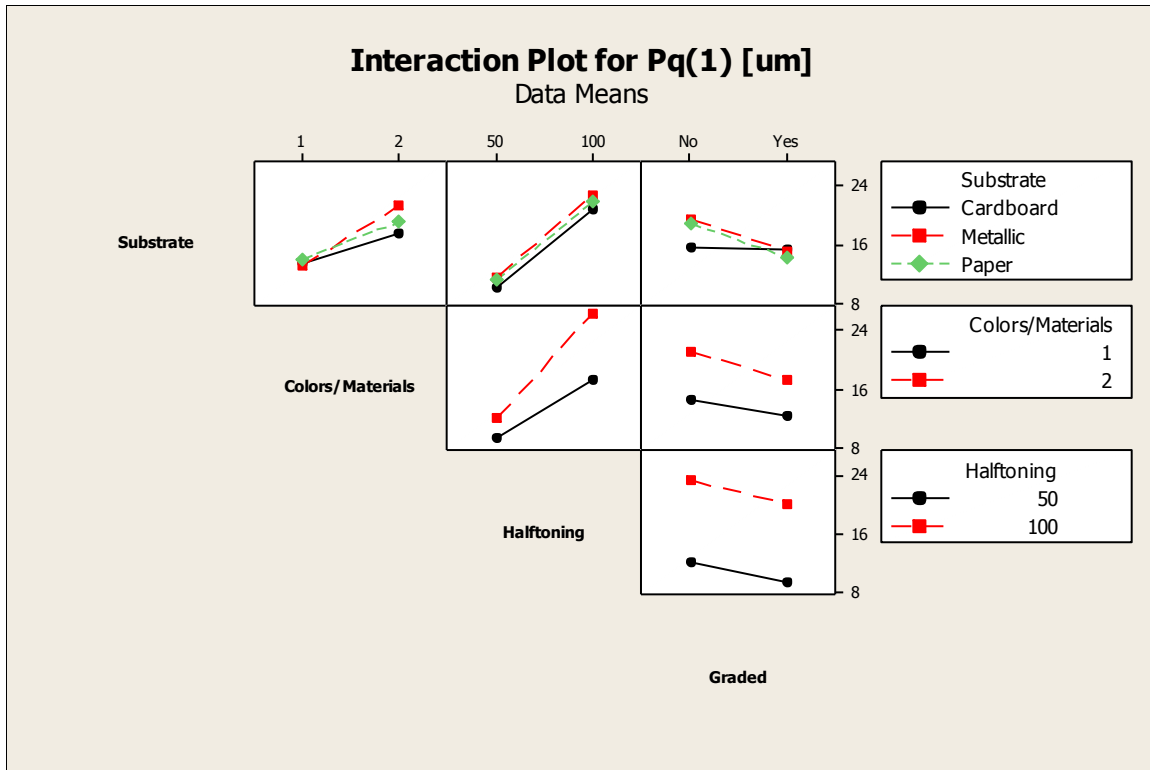


Figure 110. Interaction plot for Pq - leading edge

B.7. Pa – Trailing edge

Table 17. Analysis of Variance for Pa(2) [μm], using Adjusted SS for Tests

Source	DF	Seq SS	Adj SS	Adj MS	F	P
Layers (x10)	2	702.11	702.11	351.05	22.66	0.000
Substrate	2	54.89	54.89	27.44	1.77	0.180
Colors/Materials	1	107.36	107.36	107.36	6.93	0.011
Halftoning	1	316.47	316.47	316.47	20.43	0.000
Graded	1	55.95	55.95	55.95	3.61	0.063
Substrate*Colors/Materials	2	19.23	19.23	9.62	0.62	0.541
Substrate*Halftoning	2	12.94	12.94	6.47	0.42	0.661
Substrate*Graded	2	51.80	51.80	25.90	1.67	0.197
Colors/Materials*Halftoning	1	44.17	44.17	44.17	2.85	0.097
Colors/Materials*Graded	1	0.23	0.23	0.23	0.01	0.904
Halftoning*Graded	1	13.67	13.67	13.67	0.88	0.352
Error	55	852.01	852.01	15.49		
Total	71	2230.83				
S = 3.93588 R-Sq = 61.81% R-Sq(adj) = 50.70%						
Unusual Observations for Pa(2) [μm]						
Obs	Pa(2) [μm]	Fit	SE Fit	Residual	St Resid	
53	39.5070	20.0937	1.9125	19.4133	5.64 R	
R denotes an observation with a large standardized residual.						

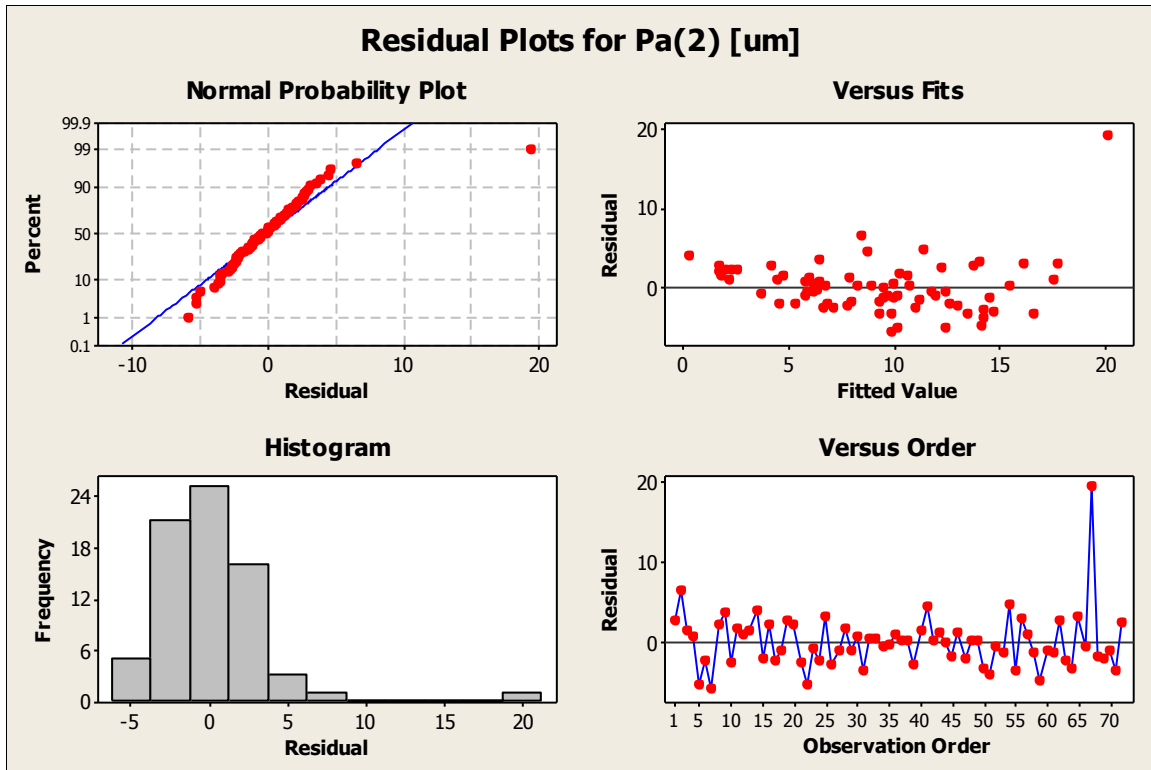


Figure 111. Residual plots for Pa - trailing edge

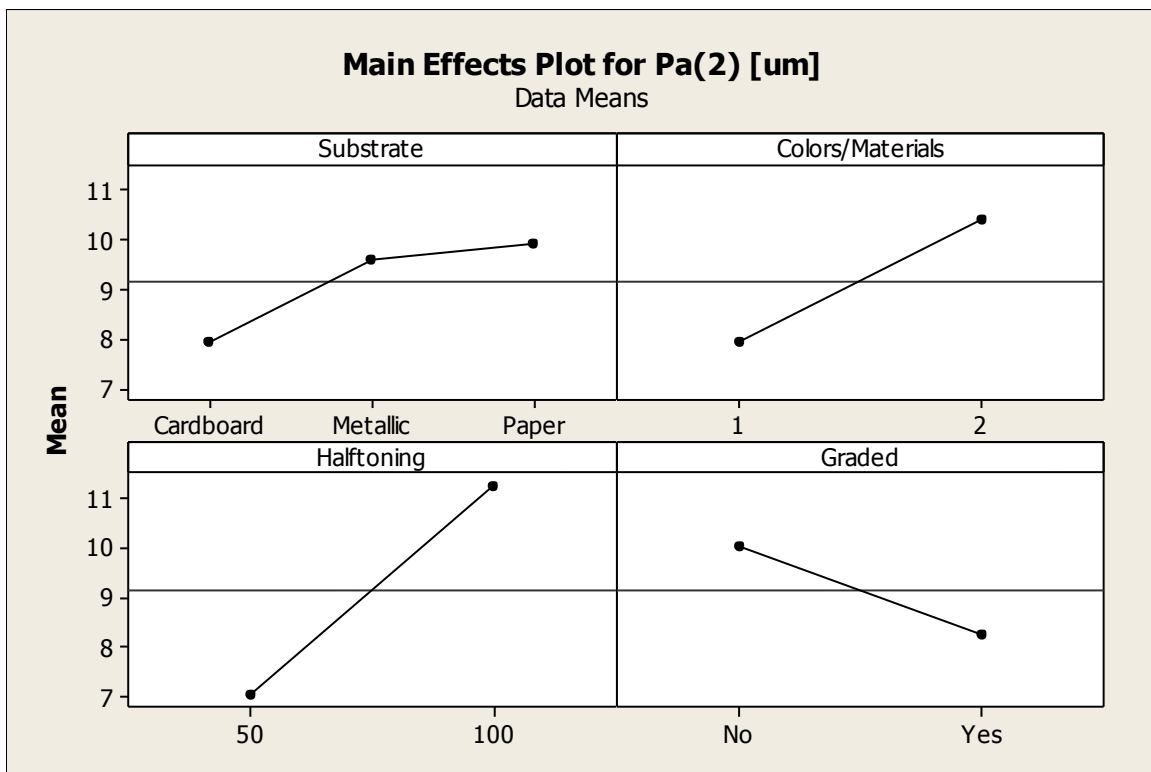


Figure 112. Main effects plot for Pa - trailing edge

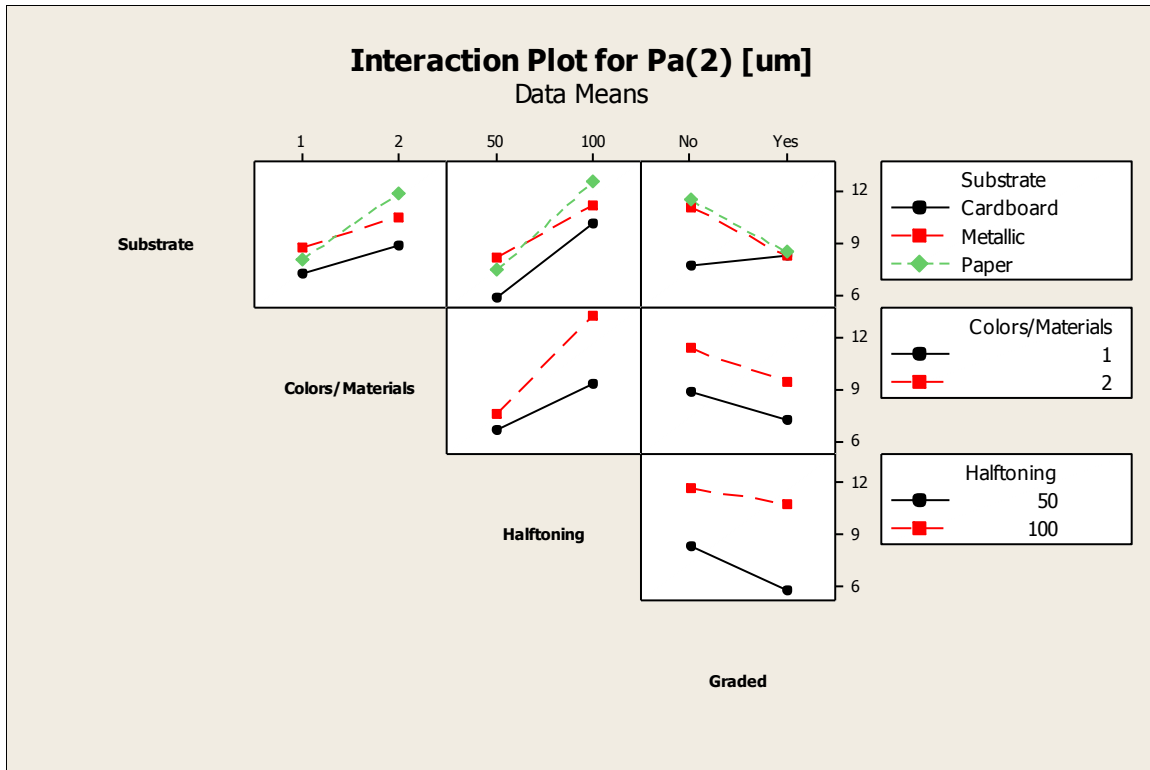


Figure 113. Interaction plot for Pa - trailing edge

B.8. Pq – Trailing edge

Table 18. Analysis of Variance for Pq(2) [μm], using Adjusted SS for Tests

Source	DF	Seq SS	Adj SS	Adj MS	F	P
Layers (x10)	2	1139.08	1139.08	569.54	23.28	0.000
Substrate	2	78.05	78.05	39.03	1.60	0.212
Colors/Materials	1	161.96	161.96	161.96	6.62	0.013
Halftoning	1	614.54	614.54	614.54	25.12	0.000
Graded	1	122.33	122.33	122.33	5.00	0.029
Substrate*Colors/Materials	2	24.62	24.62	12.31	0.50	0.607
Substrate*Halftoning	2	16.97	16.97	8.49	0.35	0.708
Substrate*Graded	2	87.24	87.24	43.62	1.78	0.178
Colors/Materials*Halftoning	1	48.74	48.74	48.74	1.99	0.164
Colors/Materials*Graded	1	0.01	0.01	0.01	0.00	0.988
Halftoning*Graded	1	13.70	13.70	13.70	0.56	0.457
Error	55	1345.39	1345.39	24.46		
Total	71	3652.63				
S = 4.94587 R-Sq = 63.17% R-Sq(adj) = 52.45%						
Unusual Observations for Pq(2) [μm]						
Obs	Pq(2) [μm]	Fit	SE Fit	Residual	St Resid	
53	51.0010	25.9253	2.4033	25.0757	5.80 R	
R denotes an observation with a large standardized residual.						

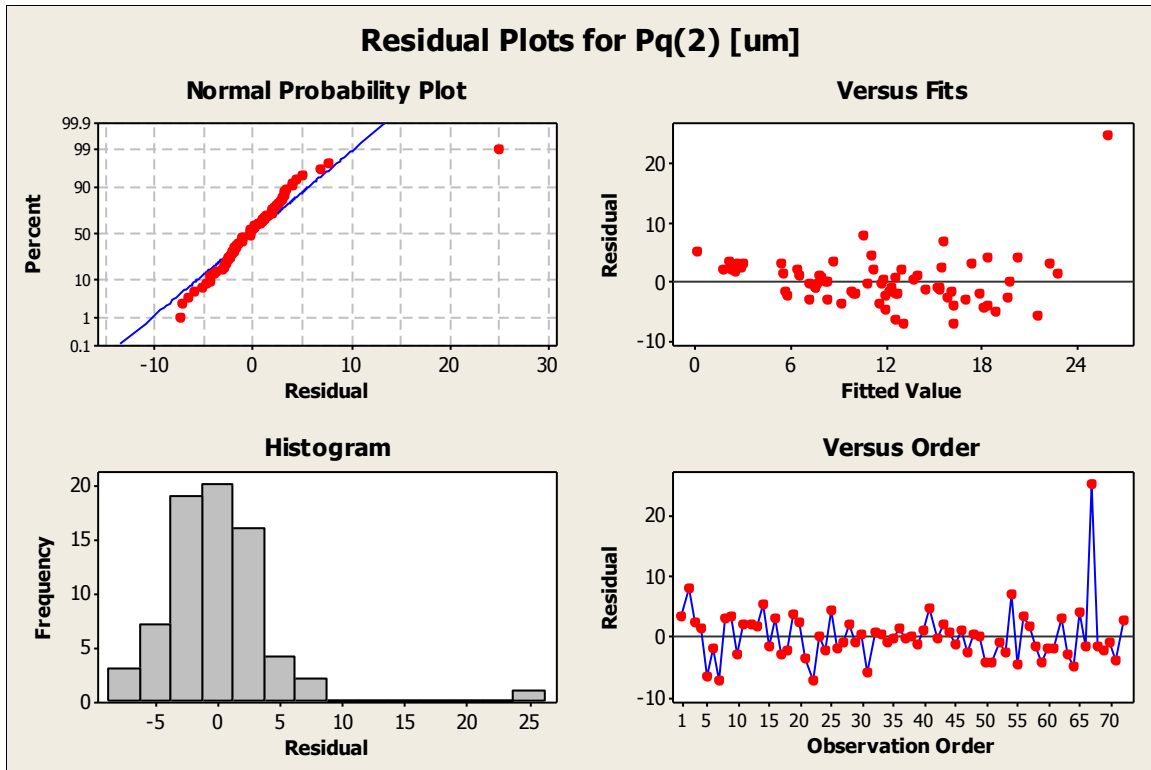


Figure 114. Residual plots for Pq - trailing edge

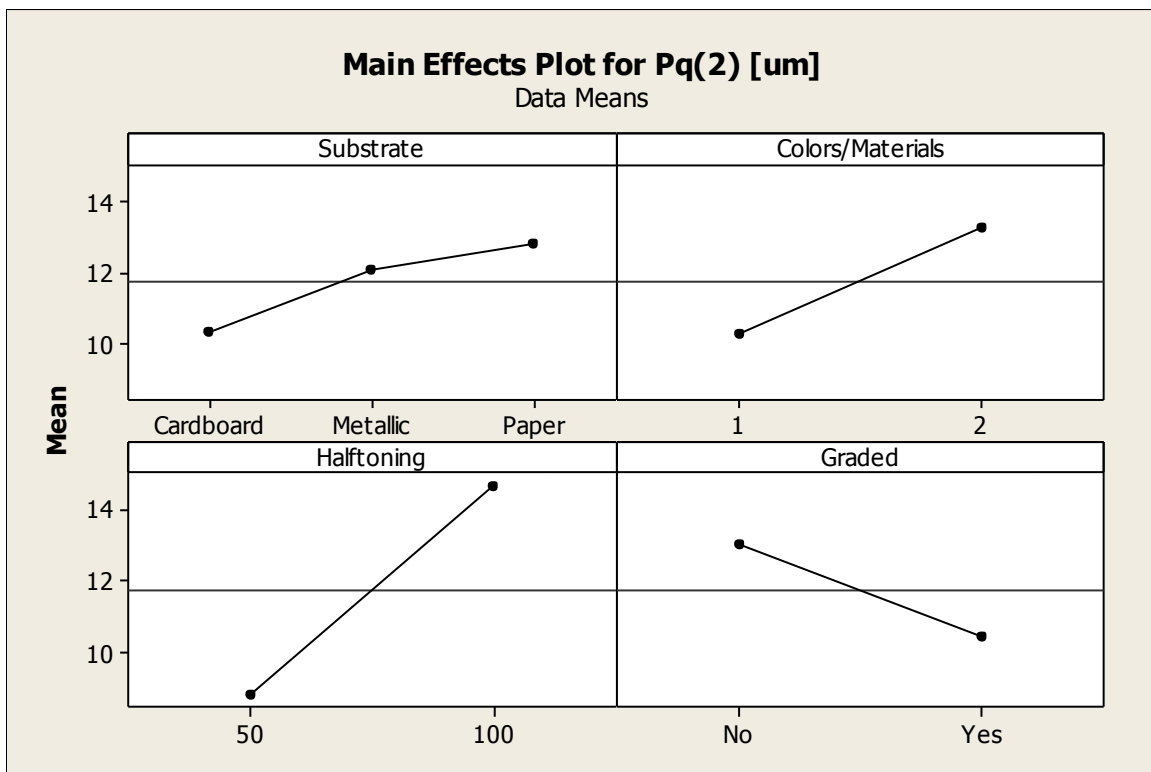


Figure 115. Main effects plot for Pq - trailing edge

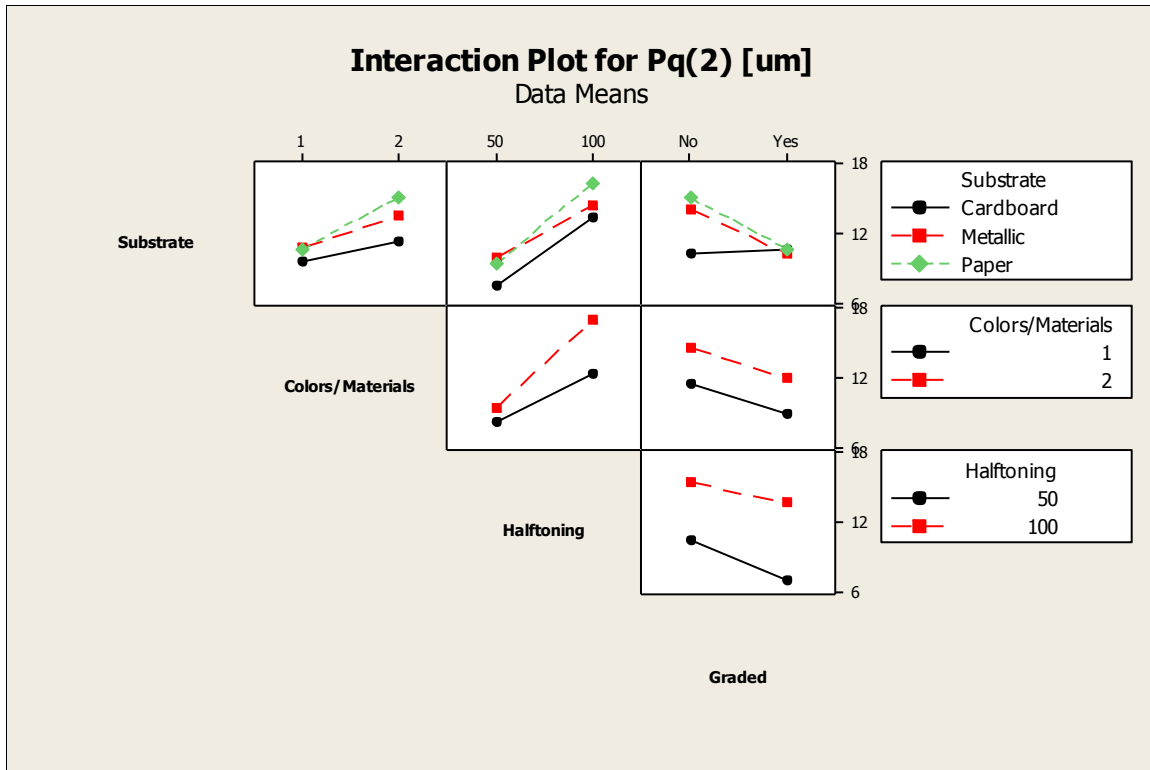


Figure 116. Interaction plot for Pq - trailing edge

B.9. Height at curling

Table 19. Analysis of Variance for Height at curling [in], using Adjusted SS

Source	DF	Seq SS	Adj SS	Adj MS	F	P
Layers (x10)	2	0.19971	0.19971	0.09986	5.51	0.007
Substrate	2	0.57470	0.57470	0.28735	15.85	0.000
Colors/Materials	1	0.46561	0.46561	0.46561	25.68	0.000
Halftoning	1	0.29287	0.29287	0.29287	16.15	0.000
Graded	1	0.04993	0.04993	0.04993	2.75	0.103
Substrate*Colors/Materials	2	0.27502	0.27502	0.13751	7.58	0.001
Substrate*Halftoning	2	0.12108	0.12108	0.06054	3.34	0.043
Substrate*Graded	2	0.04736	0.04736	0.02368	1.31	0.279
Colors/Materials*Halftoning	1	0.01003	0.01003	0.01003	0.55	0.460
Colors/Materials*Graded	1	0.00130	0.00130	0.00130	0.07	0.790
Halftoning*Graded	1	0.02880	0.02880	0.02880	1.59	0.213
Error	55	0.99741	0.99741	0.01813		
Total	71	3.06382				
S = 0.134665 R-Sq = 67.45% R-Sq(adj) = 57.98%						
Unusual Observations for Height at curling [in]						
Obs	Curl[in]	Fit	SE Fit	Residual	St Resid	
2	0.70700	0.44187	0.06544	0.26513	2.25 R	
4	0.09100	0.41165	0.06544	-0.32065	-2.72 R	
5	1.00600	0.74332	0.06544	0.26268	2.23 R	
R denotes an observation with a large standardized residual.						

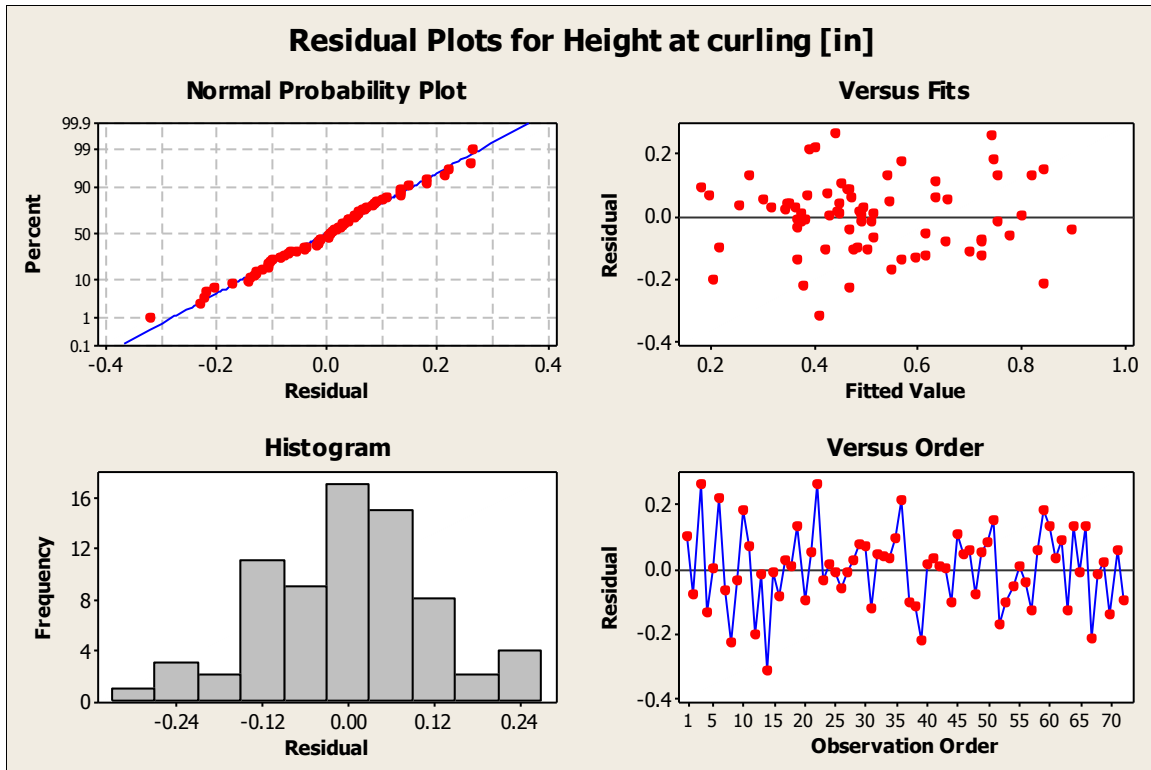


Figure 117. Residual plots for Height at curling

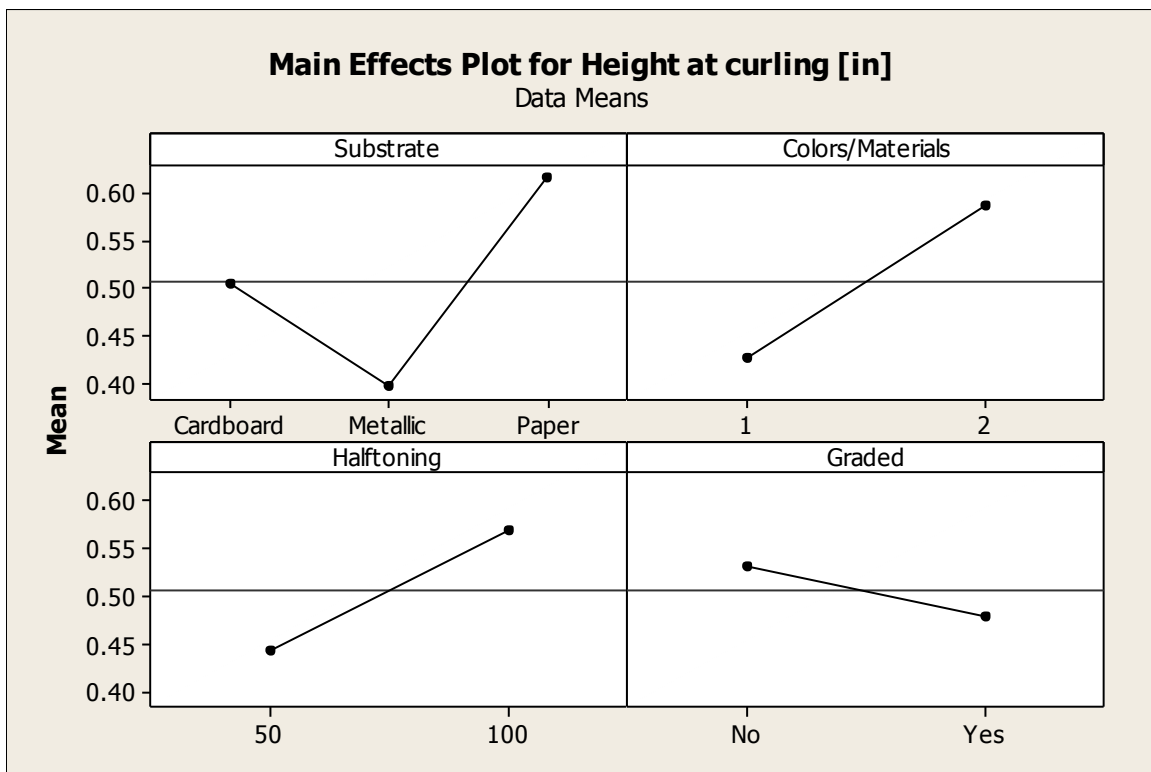


Figure 118. Main effects plot for Height at curling

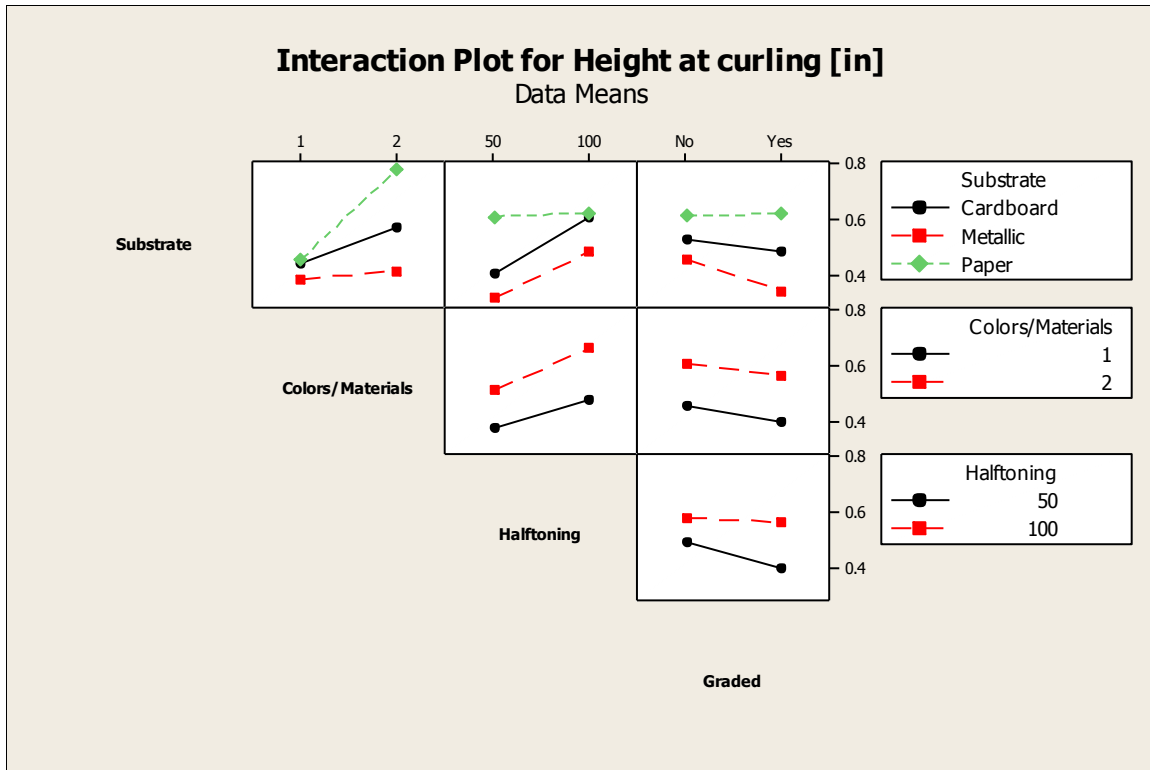


Figure 119. Interaction plot for Height at curling

B.10. Material Transferred

Table 20. Analysis of Variance for Material Transferred [g], using Adjusted SS

Source	DF	Seq SS	Adj SS	Adj MS	F	P
Layers (x10)	2	0.000066	0.000066	0.000033	0.99	0.377
Substrate	2	0.000183	0.000183	0.000092	2.74	0.073
Colors/Materials	1	0.036302	0.036302	0.036302	1085.43	0.000
Halftoning	1	0.106514	0.106514	0.106514	3184.80	0.000
Graded	1	0.019837	0.019837	0.019837	593.13	0.000
Substrate*Colors/Materials	2	0.000034	0.000034	0.000017	0.51	0.602
Substrate*Halftoning	2	0.000079	0.000079	0.000040	1.18	0.314
Substrate*Graded	2	0.000002	0.000002	0.000001	0.04	0.966
Colors/Materials*Halftoning	1	0.008075	0.008075	0.008075	241.45	0.000
Colors/Materials*Graded	1	0.002430	0.002430	0.002430	72.66	0.000
Halftoning*Graded	1	0.000217	0.000217	0.000217	6.48	0.014
Error	55	0.001839	0.001839	0.000033		
Total	71	0.175580				
S = 0.00578313 R-Sq = 98.95% R-Sq(adj) = 98.65%						
Unusual Observations for Material Transferred [g]						
Obs	Material [g]	Fit	SE Fit	Residual	St Resid	
13	0.205500	0.191069	0.002810	0.014431	2.85 R	
37	0.174600	0.189165	0.002810	-0.014565	-2.88 R	
69	0.173600	0.185236	0.002810	-0.011636	-2.30 R	
70	0.119100	0.136972	0.002810	-0.017872	-3.54 R	
R denotes an observation with a large standardized residual.						

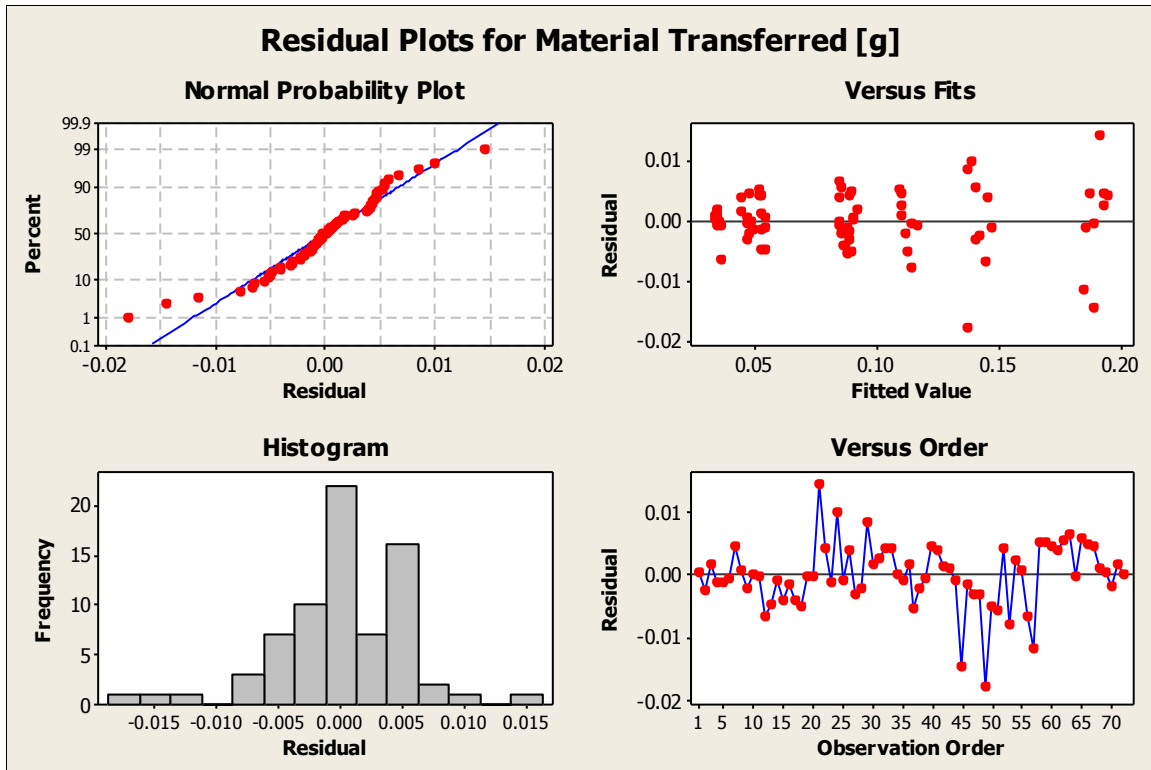


Figure 120. Residual plots for Material transferred

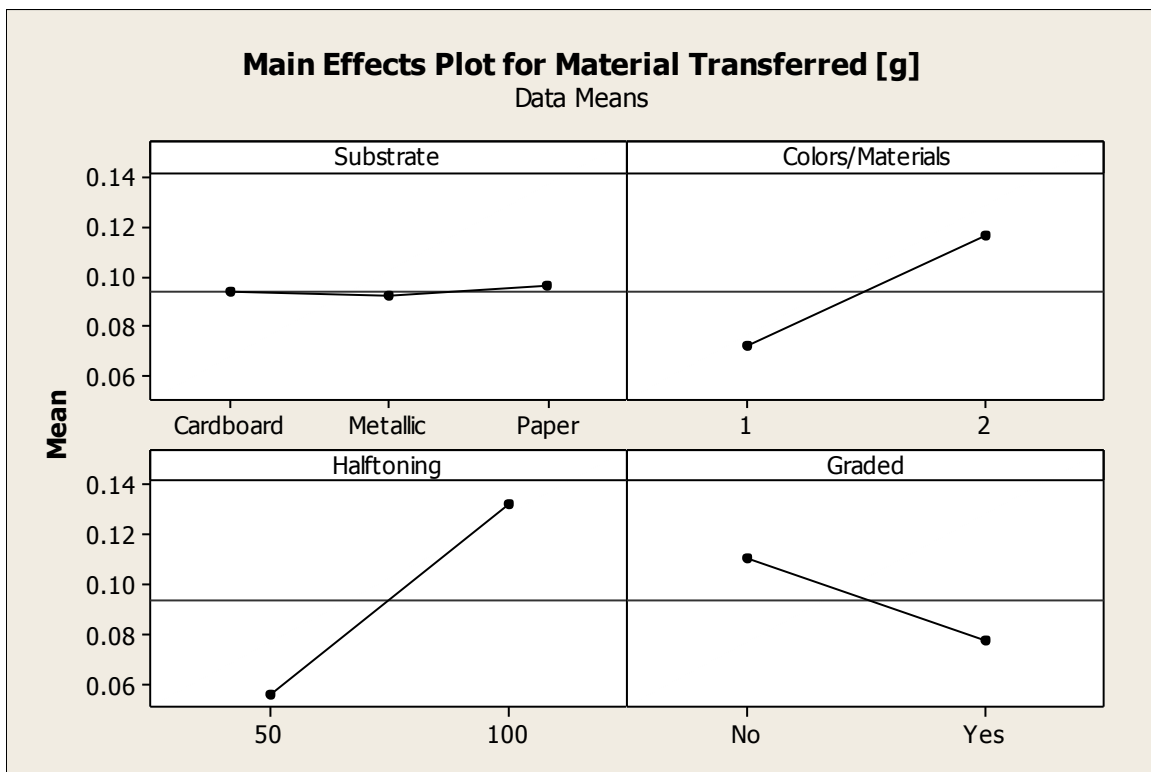


Figure 121. Main effects plot for Material transferred

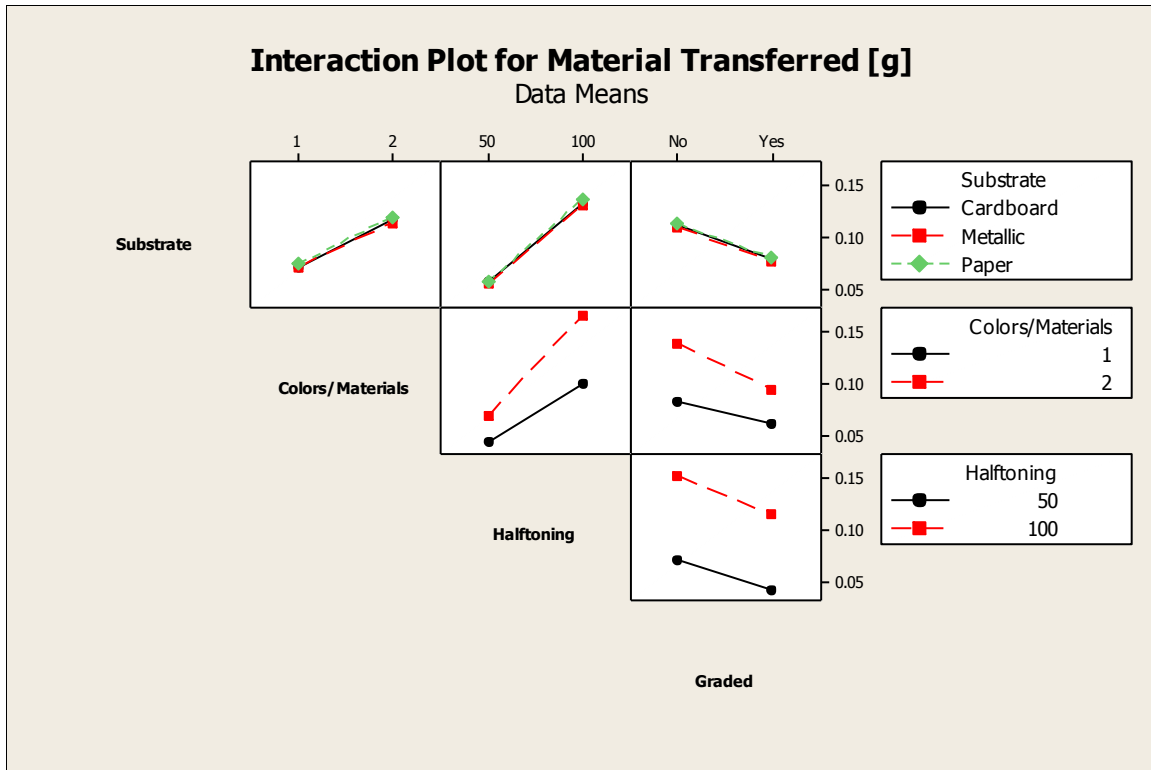


Figure 122. Interaction plot for Material transferred

B.11. Surface quality

Table 21. Analysis of Variance for Surface quality [qual], using Adjusted SS

Source	DF	Seq SS	Adj SS	Adj MS	F	P
Layers (x10)	2	40.5278	40.5278	20.2639	28.27	0.000
Substrate	2	2.0278	2.0278	1.0139	1.41	0.252
Colors/Materials	1	2.3472	2.3472	2.3472	3.27	0.076
Halftoning	1	25.6806	25.6806	25.6806	35.82	0.000
Graded	1	1.6806	1.6806	1.6806	2.34	0.131
Substrate*Colors/Materials	2	0.6944	0.6944	0.3472	0.48	0.619
Substrate*Halftoning	2	0.1944	0.1944	0.0972	0.14	0.873
Substrate*Graded	2	1.0278	1.0278	0.5139	0.72	0.493
Colors/Materials*Halftoning	1	3.1250	3.1250	3.1250	4.36	0.041
Colors/Materials*Graded	1	0.1250	0.1250	0.1250	0.17	0.678
Halftoning*Graded	1	0.1250	0.1250	0.1250	0.17	0.678
Error	55	39.4306	39.4306	0.7169		
Total	71	116.9861				

S = 0.846711 R-Sq = 66.29% R-Sq(adj) = 56.49%

Unusual Observations for Surface quality [qual]

Obs	Quality [qual]	Fit	SE Fit	Residual	St Resid
3	6.00000	8.22222	0.41143	-2.22222	-3.00 R
5	9.00000	7.05556	0.41143	1.94444	2.63 R
20	7.00000	8.63889	0.41143	-1.63889	-2.21 R
62	7.00000	5.26389	0.41143	1.73611	2.35 R

R denotes an observation with a large standardized residual.

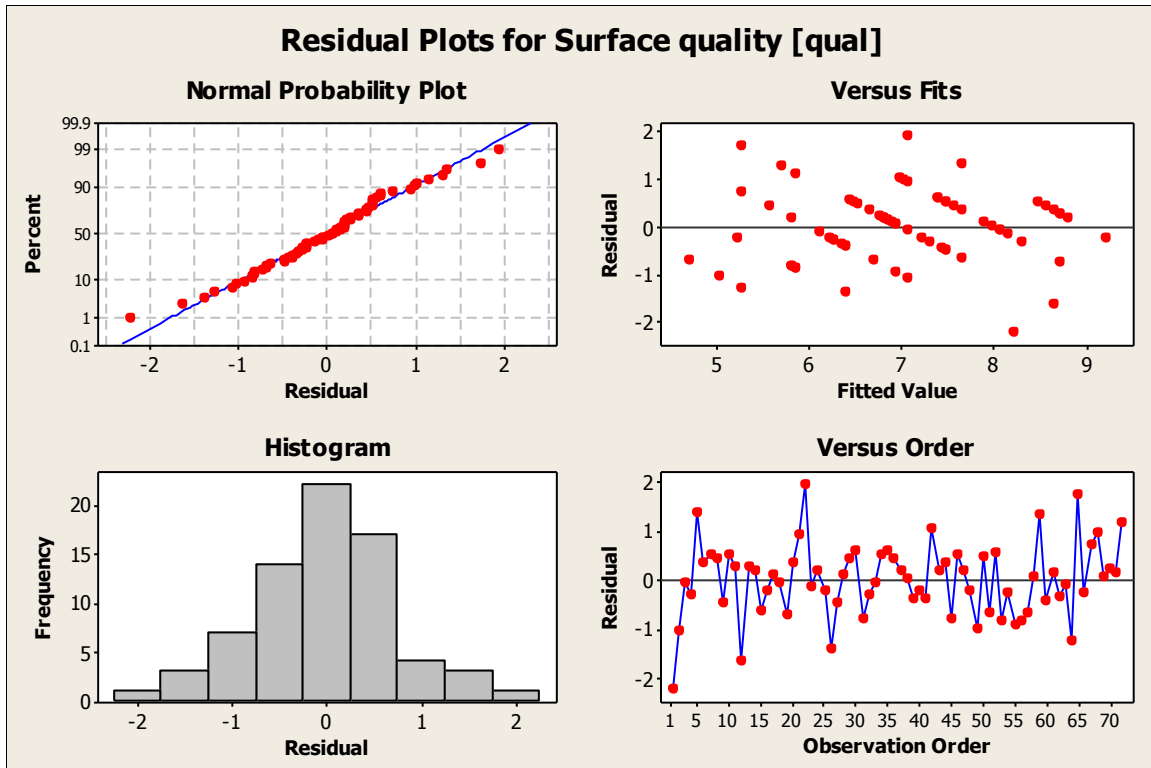


Figure 123. Residual plots for Surface quality

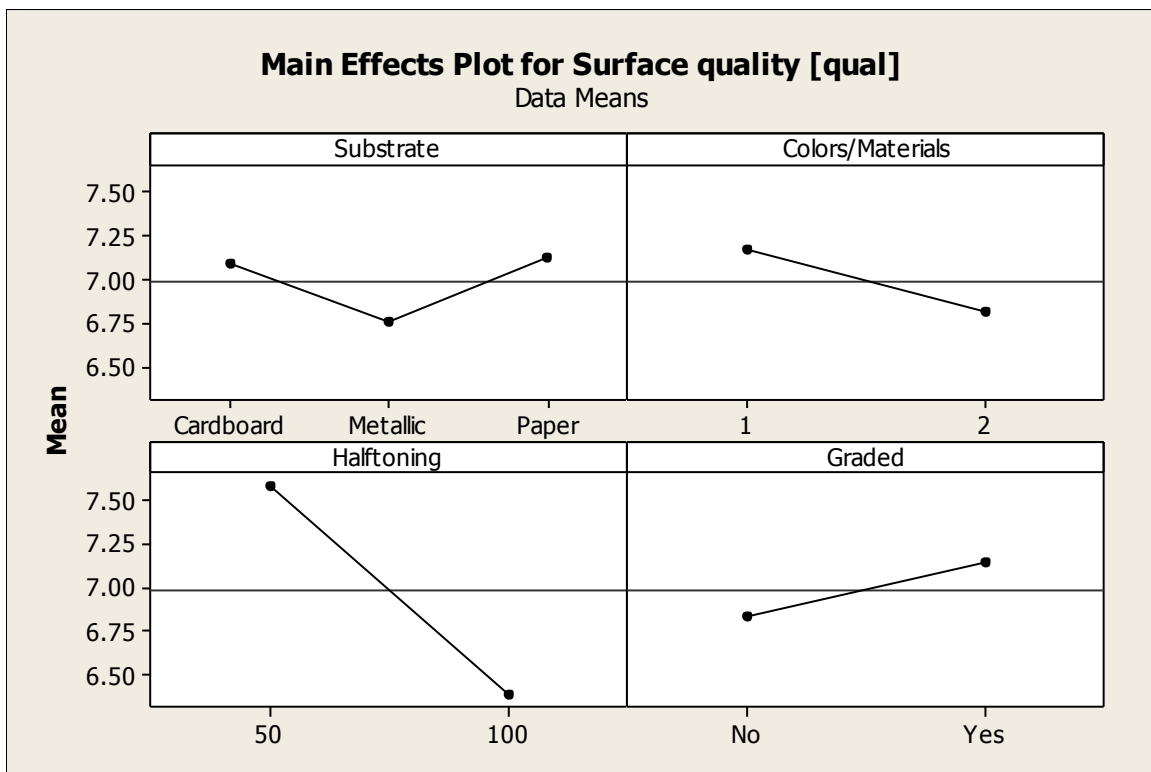


Figure 124. Main effects plot for Surface quality

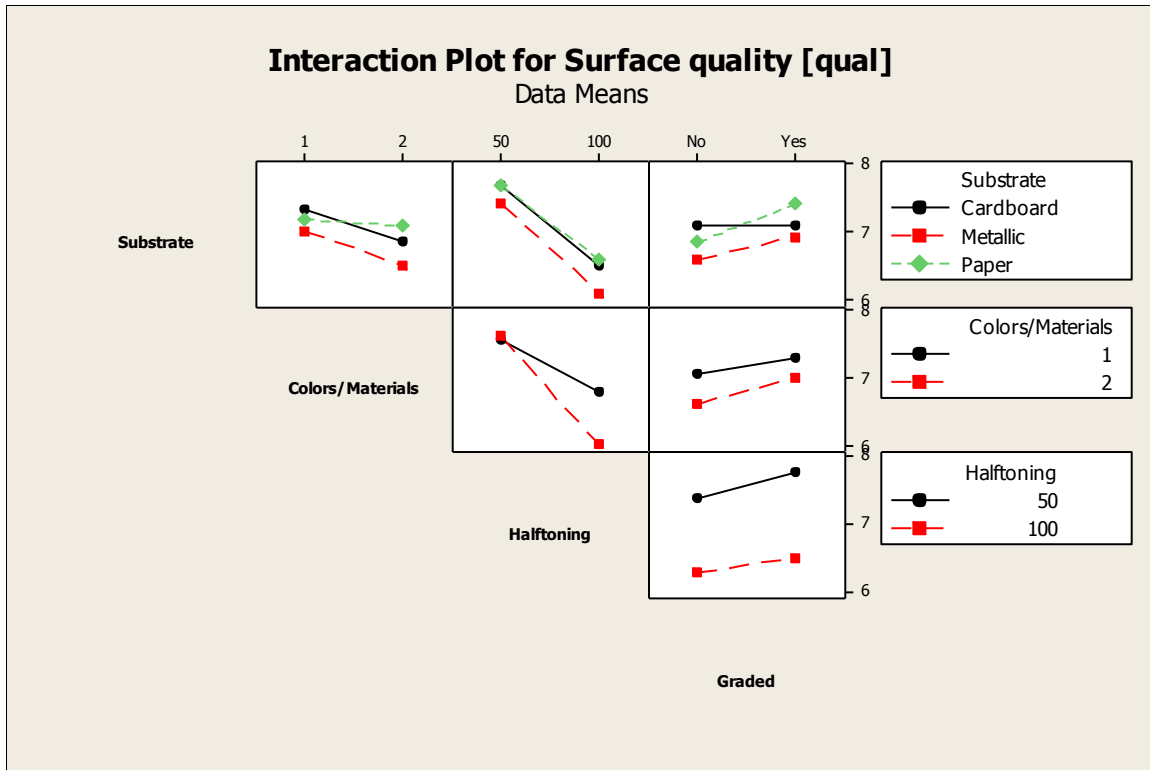


Figure 125. Interaction plot for Surface quality

B.12. Height Adjusted to discount base substrate

Table 22. Analysis of Variance for Height Adj. [mil], using Adjusted SS

Source	DF	Seq SS	Adj SS	Adj MS	F	P
Layers (x10)	2	261.444	261.444	130.722	68.77	0.000
Substrate	2	2.965	2.965	1.483	0.78	0.463
Colors/Materials	1	56.889	56.889	56.889	29.93	0.000
Halftoning	1	260.681	260.681	260.681	137.15	0.000
Graded	1	32.000	32.000	32.000	16.84	0.000
Substrate*Colors/Materials	2	0.007	0.007	0.003	0.00	0.998
Substrate*Halftoning	2	0.340	0.340	0.170	0.09	0.915
Substrate*Graded	2	0.438	0.438	0.219	0.12	0.892
Colors/Materials*Halftoning	1	21.125	21.125	21.125	11.11	0.002
Colors/Materials*Graded	1	18.000	18.000	18.000	9.47	0.003
Halftoning*Graded	1	2.347	2.347	2.347	1.23	0.271
Error	55	104.542	104.542	1.901		
Total	71	760.778				

S = 1.37868 R-Sq = 86.26% R-Sq(adj) = 82.26%

Unusual Observations for Height Adj. [mil]

Obs	Height Adj	Fit	SE Fit	Residual	St Resid
13	4.0000	6.9583	0.6699	-2.9583	-2.46 R
21	3.5000	6.8333	0.6699	-3.3333	-2.77 R
61	16.0000	11.6250	0.6699	4.3750	3.63 R
69	14.0000	11.5000	0.6699	2.5000	2.07 R

R denotes an observation with a large standardized residual.

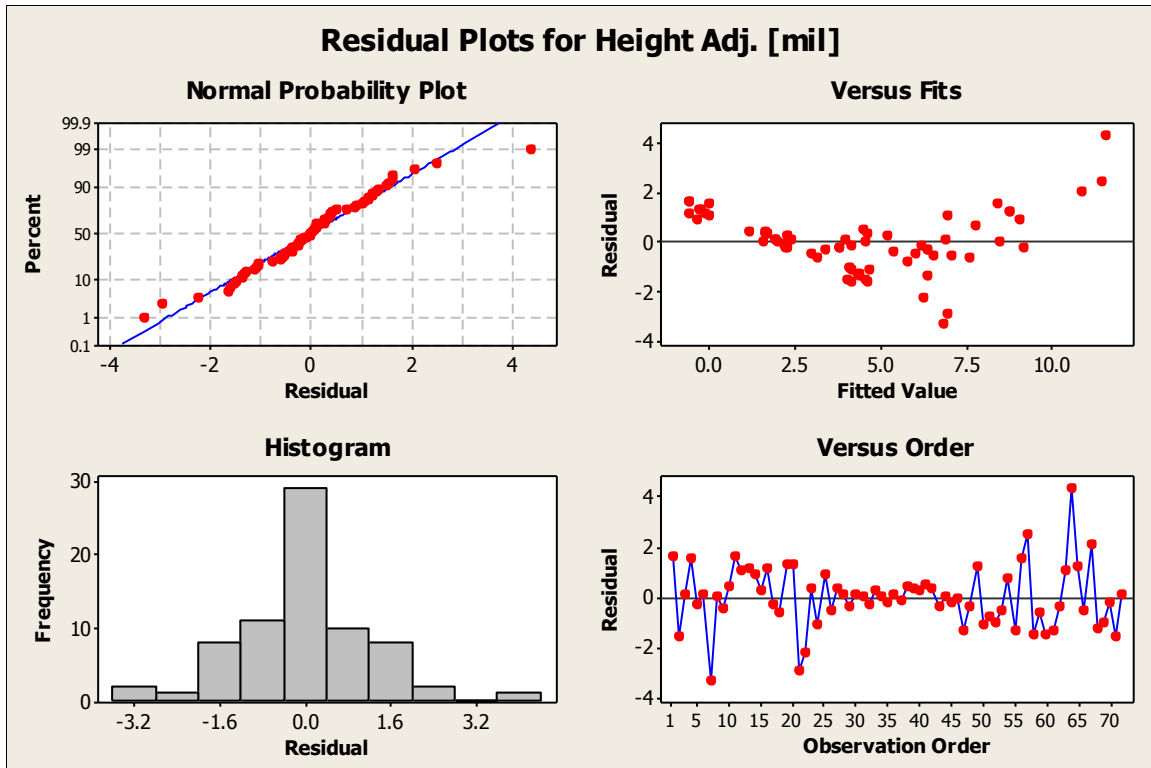


Figure 126. Residual plots for Height adjusted

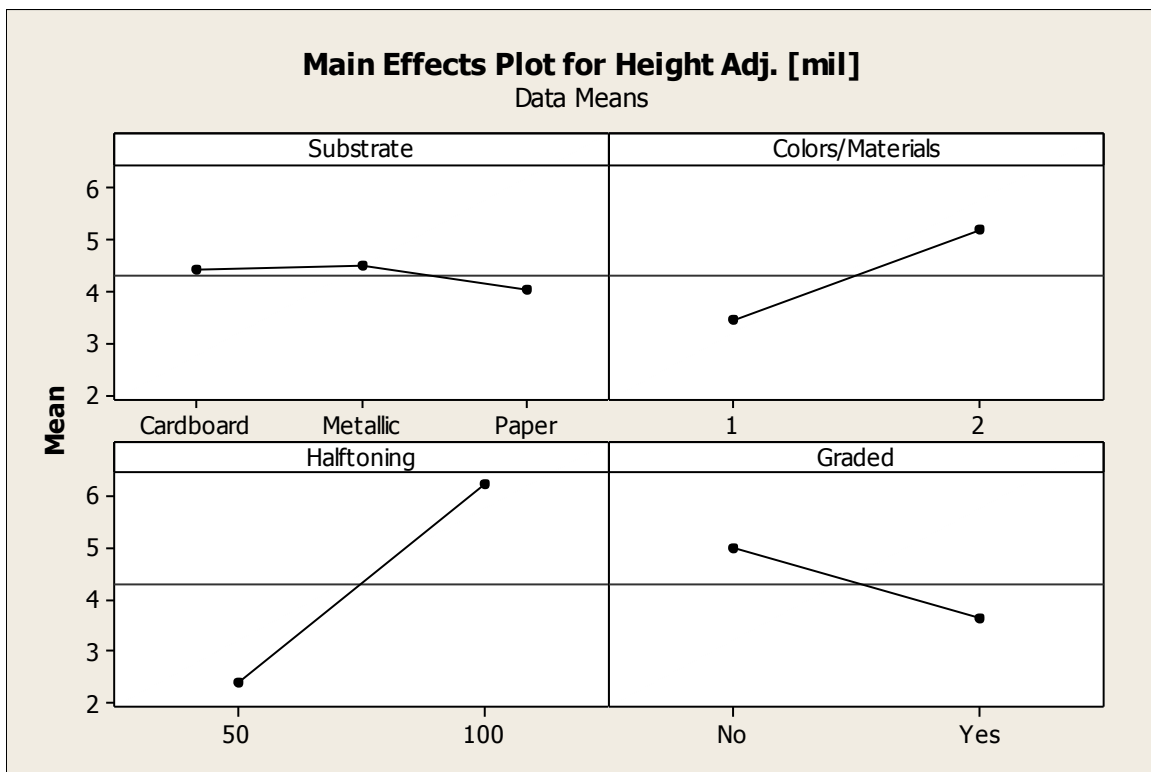


Figure 127. Main effects plot for Height adjusted

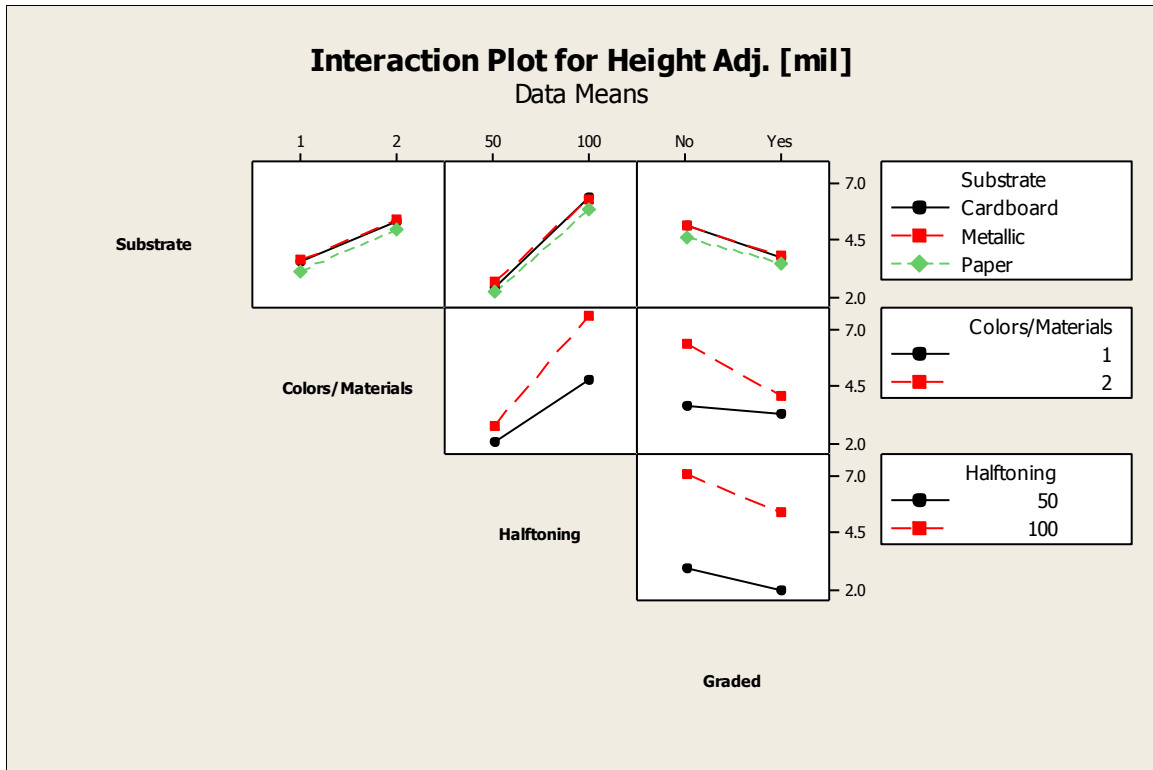


Figure 128. Interaction plot for Height adjusted

B.13. Analysis blocked by printed pattern

Due to uneven patterns printed, particularly the ones with one toner and graded transition, the analysis was blocked by printed pattern conditions (Toners (C/CM) – % Fill (100%/50%) – Use of Graded Transition (Yes/No)):

B.13.1. C-100%-Yes

Table 23. Analysis of Variance for Material Transferred [g], using Adjusted SS

Source	DF	Seq SS	Adj SS	Adj MS	F	P
Layers (x10)	2	0.0000333	0.0000333	0.0000167	0.75	0.527
Substrate	2	0.0000534	0.0000534	0.0000267	1.21	0.388
Error	4	0.0000883	0.0000883	0.0000221		
Total	8	0.0001750				
S = 0.00469905 R-Sq = 49.54% R-Sq(adj) = 0.00%						

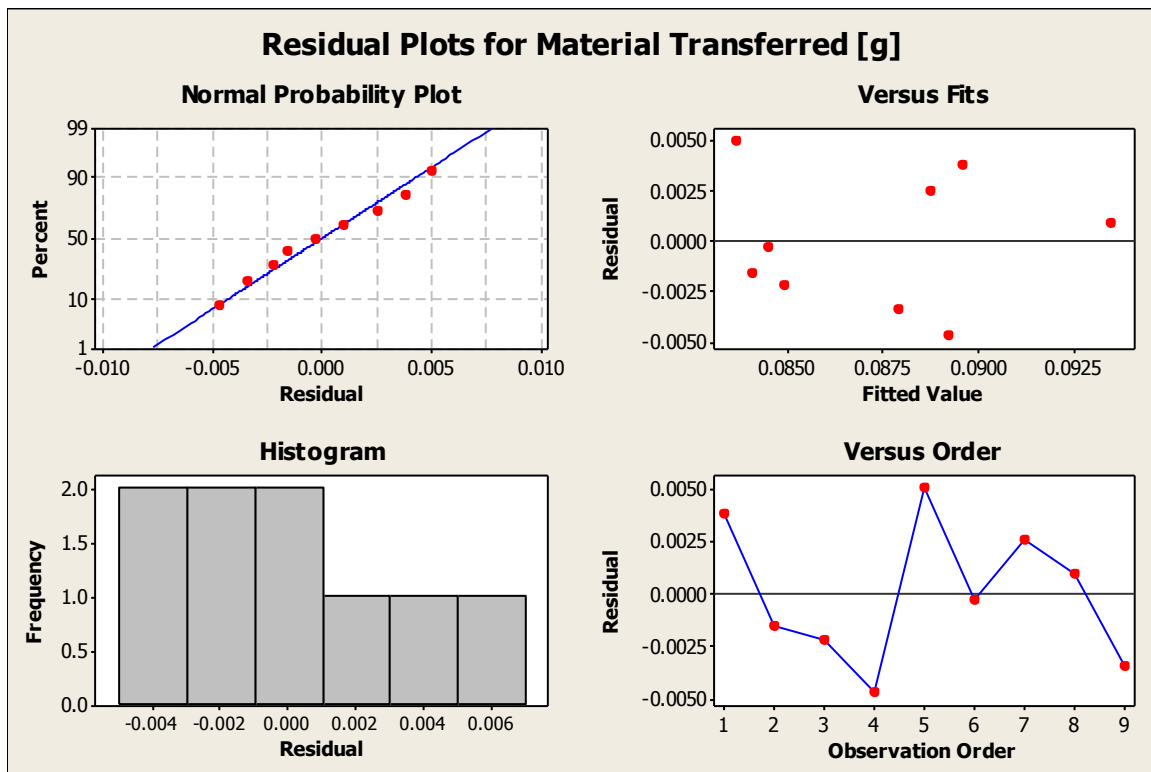


Figure 129. Residual plots for Material transferred

Table 24. Analysis of Variance for Height Adj. [mil], using Adjusted SS

Source	DF	Seq SS	Adj SS	Adj MS	F	P
Layers (x10)	2	35.0556	35.0556	17.5278	54.87	0.001
Substrate	2	1.3889	1.3889	0.6944	2.17	0.230
Error	4	1.2778	1.2778	0.3194		
Total	8	37.7222				
S = 0.565194 R-Sq = 96.61% R-Sq(adj) = 93.23%						

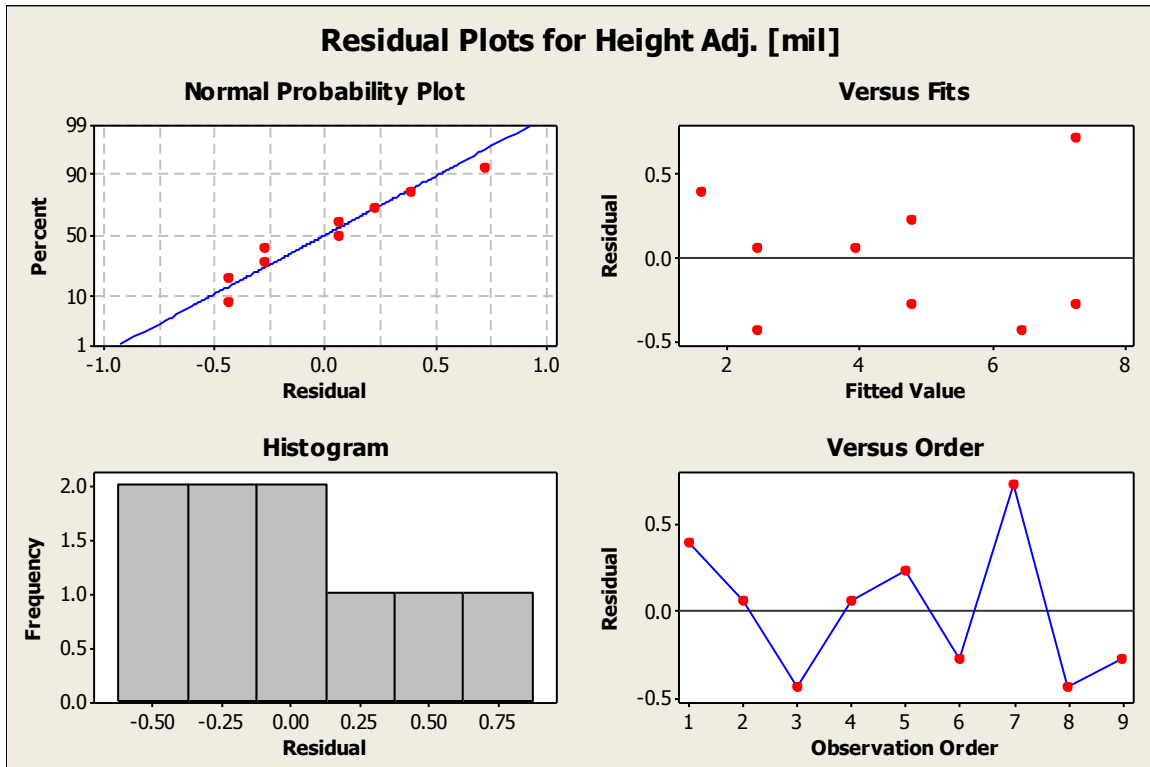


Figure 130. Residual plot for Height Adjusted

B.13.2. CM-100%-Yes

Table 25. Analysis of Variance for Material Transferred [g], using Adjusted SS

Source	DF	Seq SS	Adj SS	Adj MS	F	P
Layers (x10)	2	0.0002055	0.0002055	0.0001028	0.95	0.461
Substrate	2	0.0000615	0.0000615	0.0000307	0.28	0.768
Error	4	0.0004347	0.0004347	0.0001087		
Total	8	0.0007017				

S = 0.0104250 R-Sq = 38.05% R-Sq(adj) = 0.00%

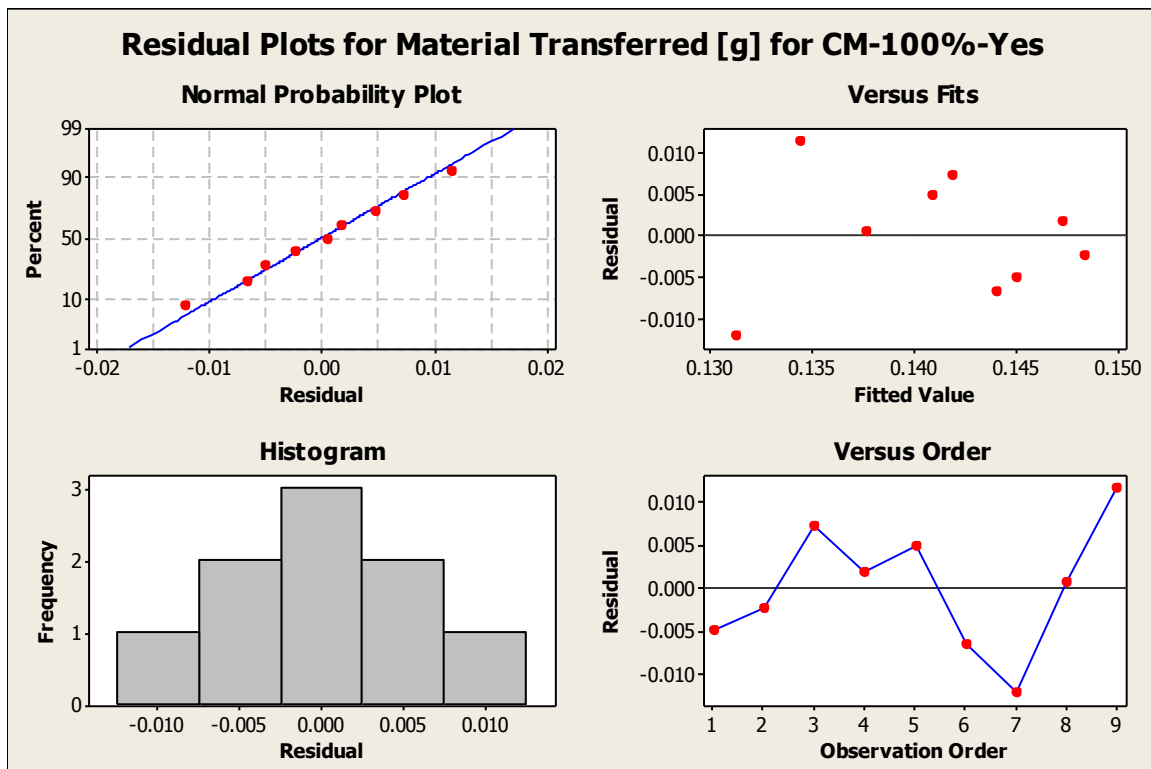


Figure 131. Residual plot for Material transferred

Table 26. Analysis of Variance for Height Adj. [mil], using Adjusted SS

Source	DF	Seq SS	Adj SS	Adj MS	F	P
Layers (x10)	2	75.500	75.500	37.750	302.00	0.000
Substrate	2	0.500	0.500	0.250	2.00	0.250
Error	4	0.500	0.500	0.125		
Total	8	76.500				
S = 0.353553 R-Sq = 99.35% R-Sq(adj) = 98.69%						

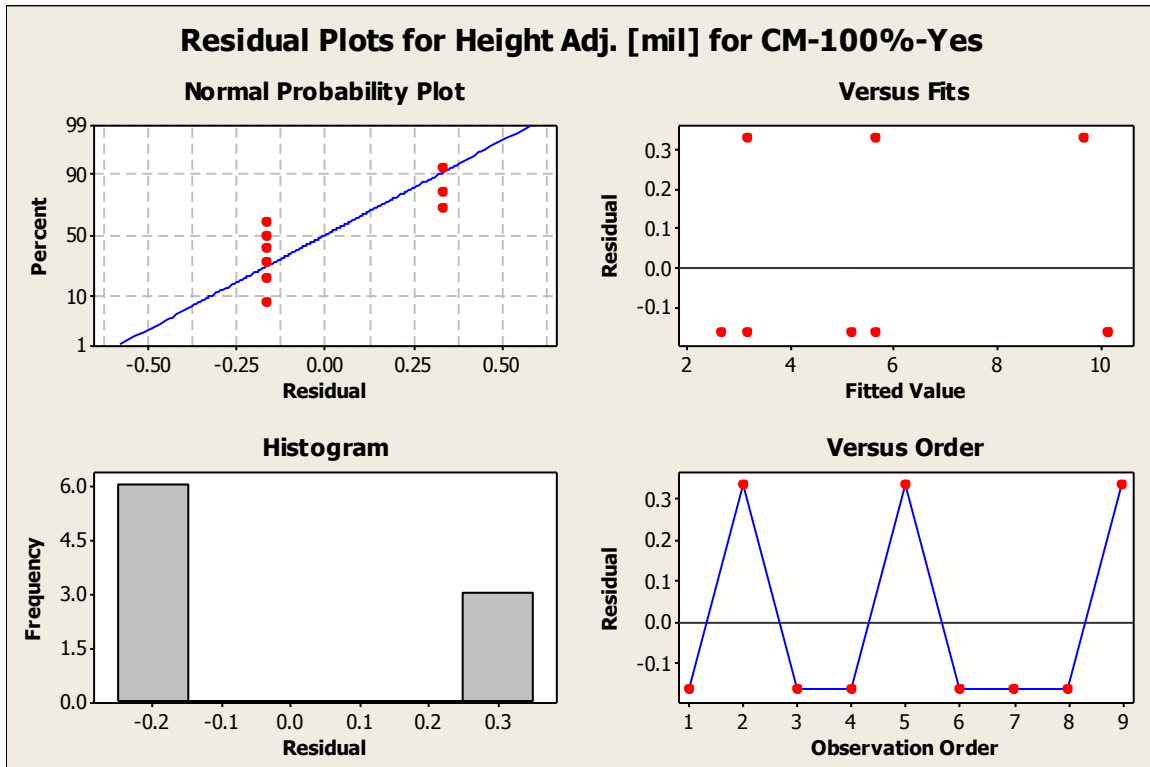


Figure 132. Residual plots for Height adjusted

B.13.3. C-50%-Yes

Table 27. Analysis of Variance for Material Transferred [g], using Adjusted SS

Source	DF	Seq SS	Adj SS	Adj MS	F	P
Layers (x10)	2	0.0000036	0.0000036	0.0000018	0.43	0.679
Substrate	2	0.0000110	0.0000110	0.0000055	1.30	0.366
Error	4	0.0000168	0.0000168	0.0000042		
Total	8	0.0000313				
S = 0.00204966 R-Sq = 46.40% R-Sq(adj) = 0.00%						

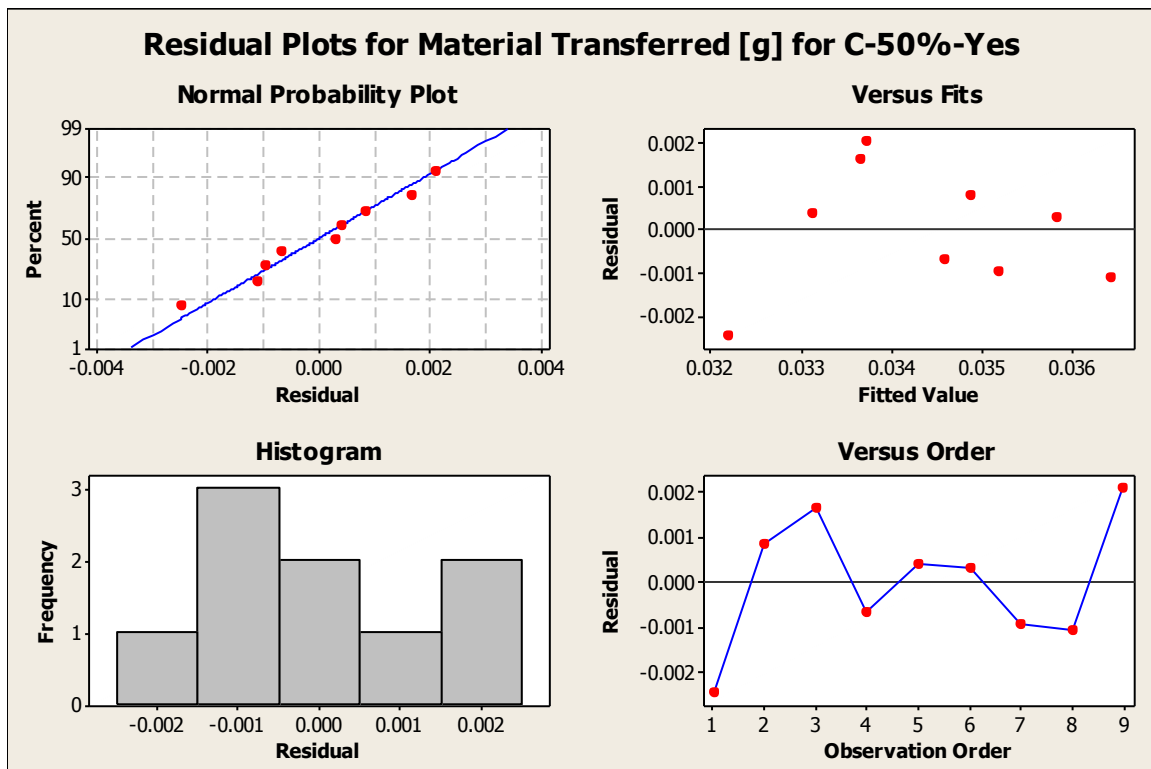


Figure 133. Residual plots for Material transferred

Table 28. Analysis of Variance for Height Adj. [mil], using Adjusted SS

Source	DF	Seq SS	Adj SS	Adj MS	F	P
Layers	2	7.0556	7.0556	3.5278	127.00	0.000
(x10)	2	0.0556	0.0556	0.0278	1.00	0.444
Substrate	4	0.1111	0.1111	0.0278		
Error	8	7.2222				
Total						
S = 0.353553 R-Sq = 98.46% R-Sq(adj) = 96.92%						
Unusual Observations for Height Adj. [mil]						
Obs	Height Adj.	Fit	SE Fit	Residual	St Resid	
1	0.50000	0.72222	0.12423	-0.22222	-2.00 R	
R denotes an observation with a large standardized residual.						

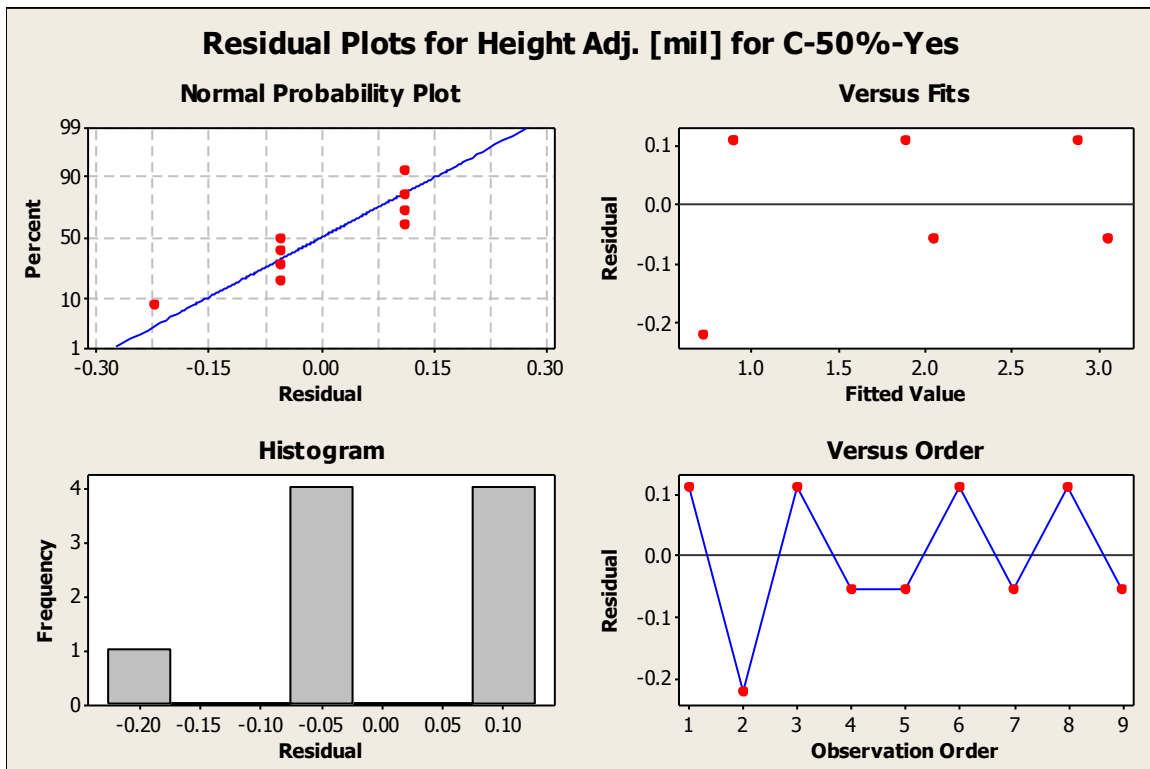


Figure 134. Residual plots for Height adjusted

B.13.4. CM-50%-Yes

Table 29. Analysis of Variance for Material Transferred [g], using Adjusted SS

Source	DF	Seq SS	Adj SS	Adj MS	F	P
Layers (x10)	2	0.0000236	0.0000236	0.0000118	3.76	0.120
Substrate	2	0.0000067	0.0000067	0.0000033	1.06	0.426
Error	4	0.0000126	0.0000126	0.0000031		
Total	8	0.0000429				

S = 0.00177232 R-Sq = 70.70% R-Sq(adj) = 41.41%

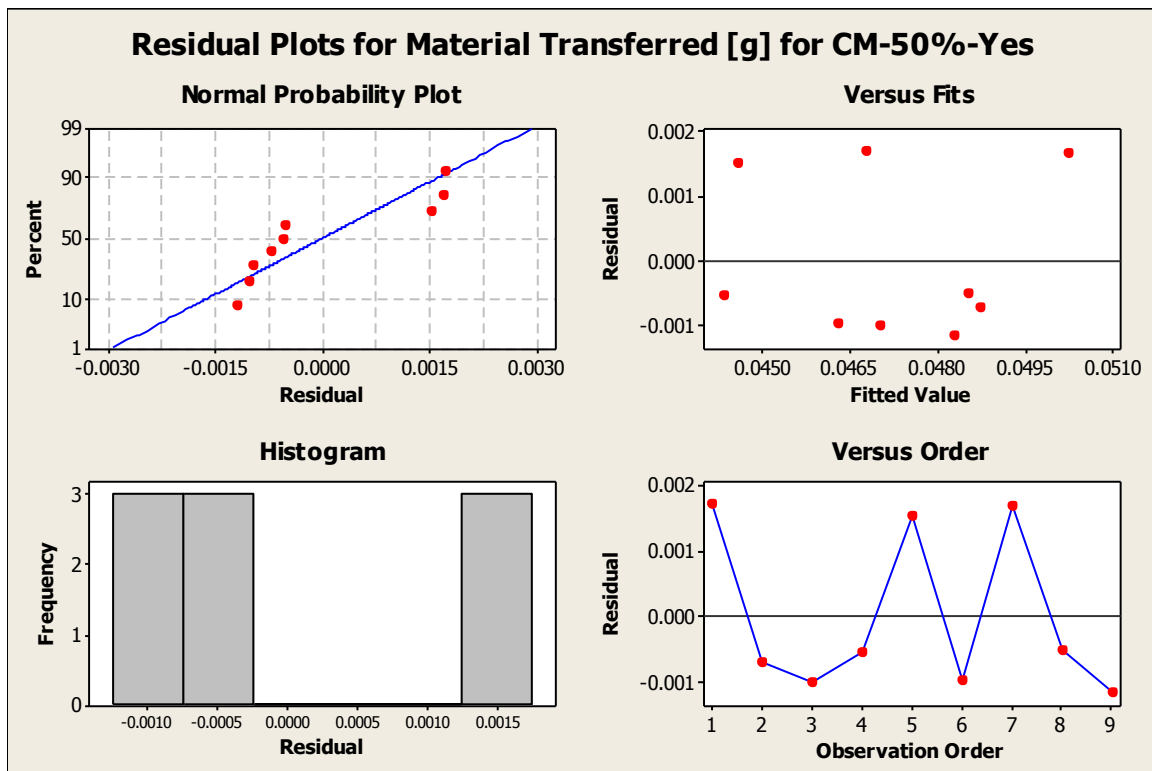


Figure 135. Residual plots for Material transferred

Table 30. Analysis of Variance for Height Adj. [mil], using Adjusted SS

Source	DF	Seq SS	Adj SS	Adj MS	F	P
Layers (x10)	2	6.0556	6.0556	3.0278	109.00	0.000
Substrate	2	0.2222	0.2222	0.1111	4.00	0.111
Error	4	0.1111	0.1111	0.0278		
Total	8	6.3889				
S = 0.166667 R-Sq = 98.26% R-Sq(adj) = 96.52%						

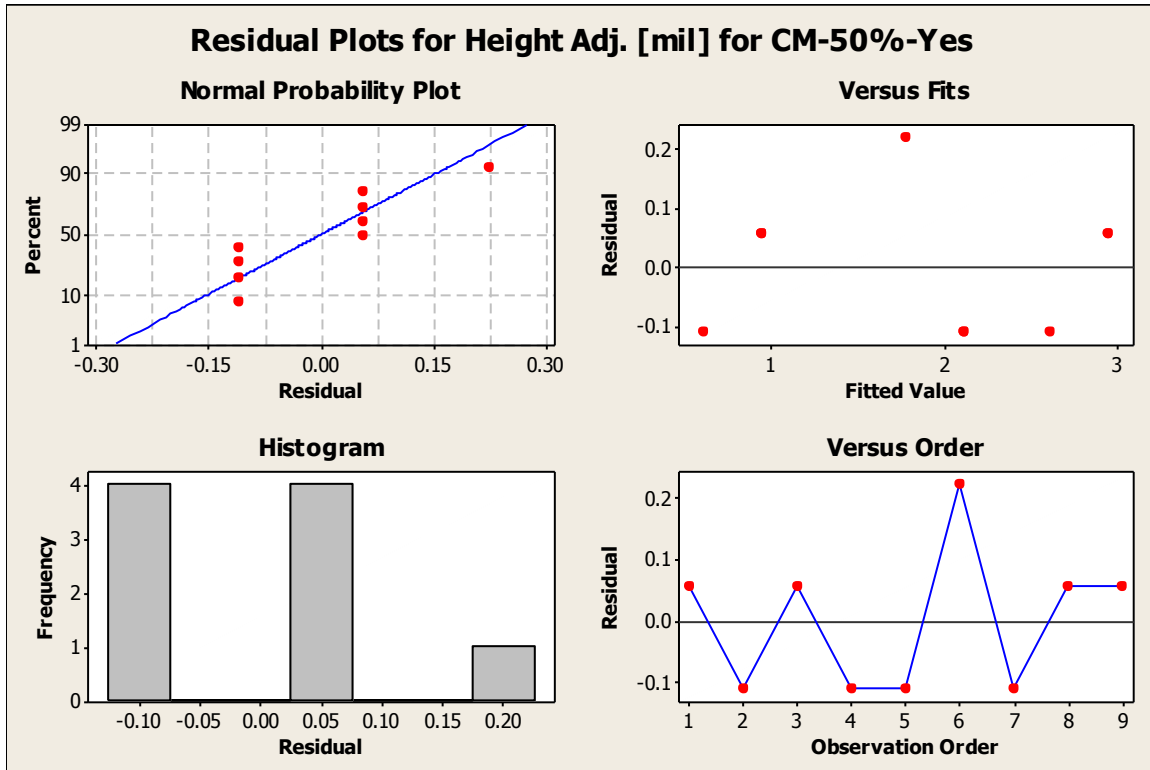


Figure 136. Residual plots for Height adjusted

B.13.5. C-100%-No

Table 31. Analysis of Variance for Material Transferred [g], using Adjusted SS

Source	DF	Seq SS	Adj SS	Adj MS	F	P
Layers (x10)	2	0.0000098	0.0000098	0.0000049	0.27	0.774
Substrate	2	0.0000084	0.0000084	0.0000042	0.23	0.802
Error	4	0.0000718	0.0000718	0.0000180		
Total	8	0.0000900				
S = 0.00423688 R-Sq = 20.23% R-Sq(adj) = 0.00%						

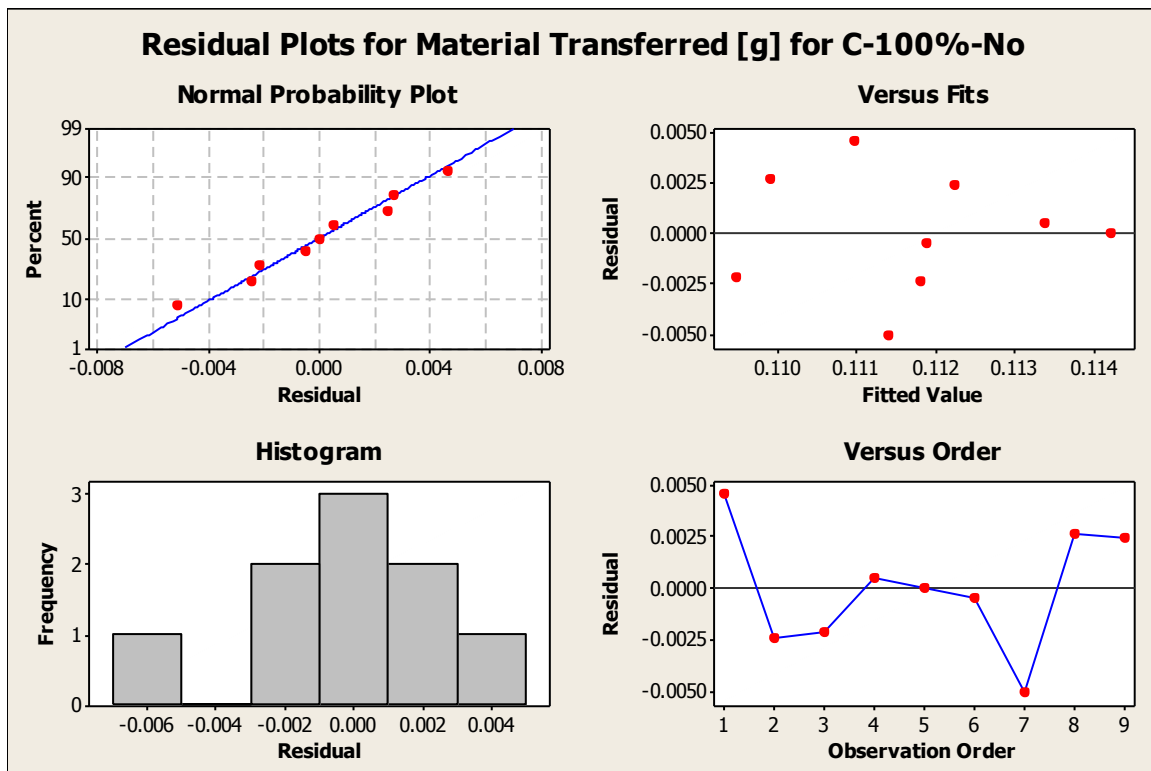


Figure 137. Residual plots for Material transferred

Table 32. Analysis of Variance for Height Adj. [mil], using Adjusted SS

Source	DF	Seq SS	Adj SS	Adj MS	F	P
Layers (x10)	2	35.1667	35.1667	17.5833	42.20	0.002
Substrate	2	0.6667	0.6667	0.3333	0.80	0.510
Error	4	1.6667	1.6667	0.4167		
Total	8	37.5000				
S = 0.645497 R-Sq = 95.56% R-Sq(adj) = 91.11%						

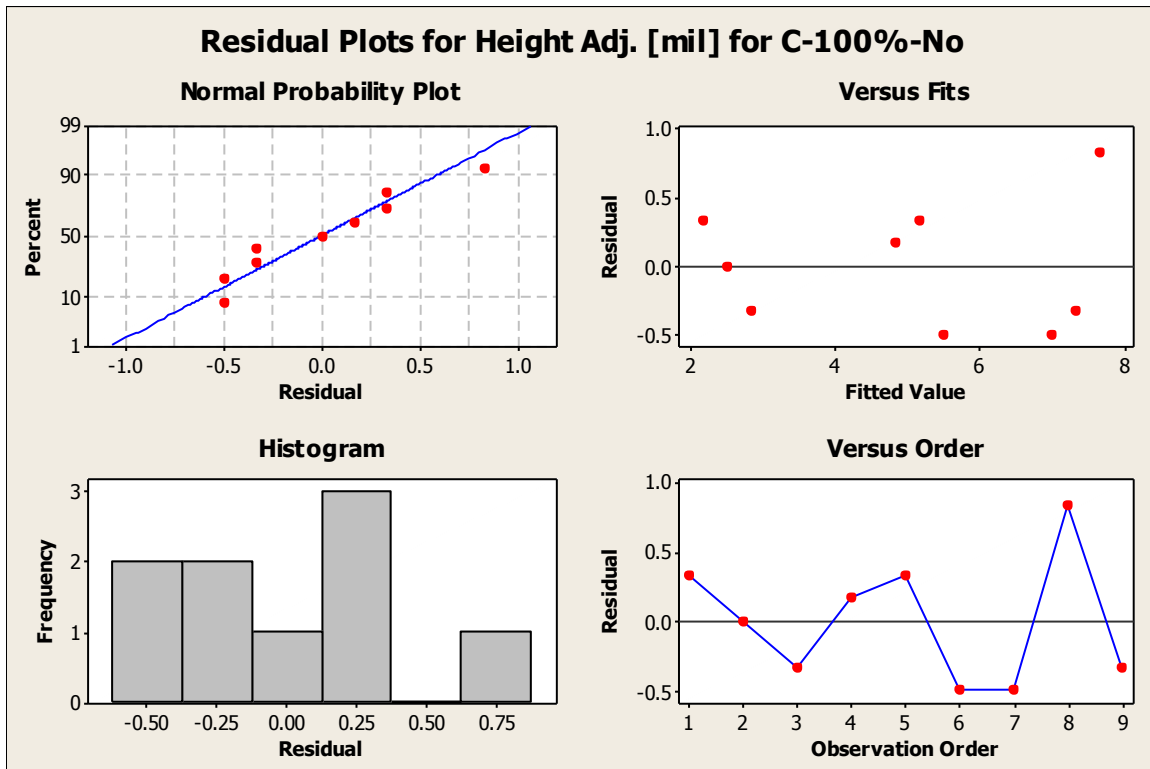


Figure 138. Residual plots for Height adjusted

B.13.6. CM-100%-No

Table 33. Analysis of Variance for Material Transferred [g], using Adjusted SS

Source	DF	Seq SS	Adj SS	Adj MS	F	P
Layers (x10)	2	0.0003516	0.0003516	0.0001758	2.31	0.216
Substrate	2	0.0002967	0.0002967	0.0001484	1.95	0.257
Error	4	0.0003049	0.0003049	0.0000762		
Total	8	0.0009532				
S = 0.00873057 R-Sq = 68.01% R-Sq(adj) = 36.03%						

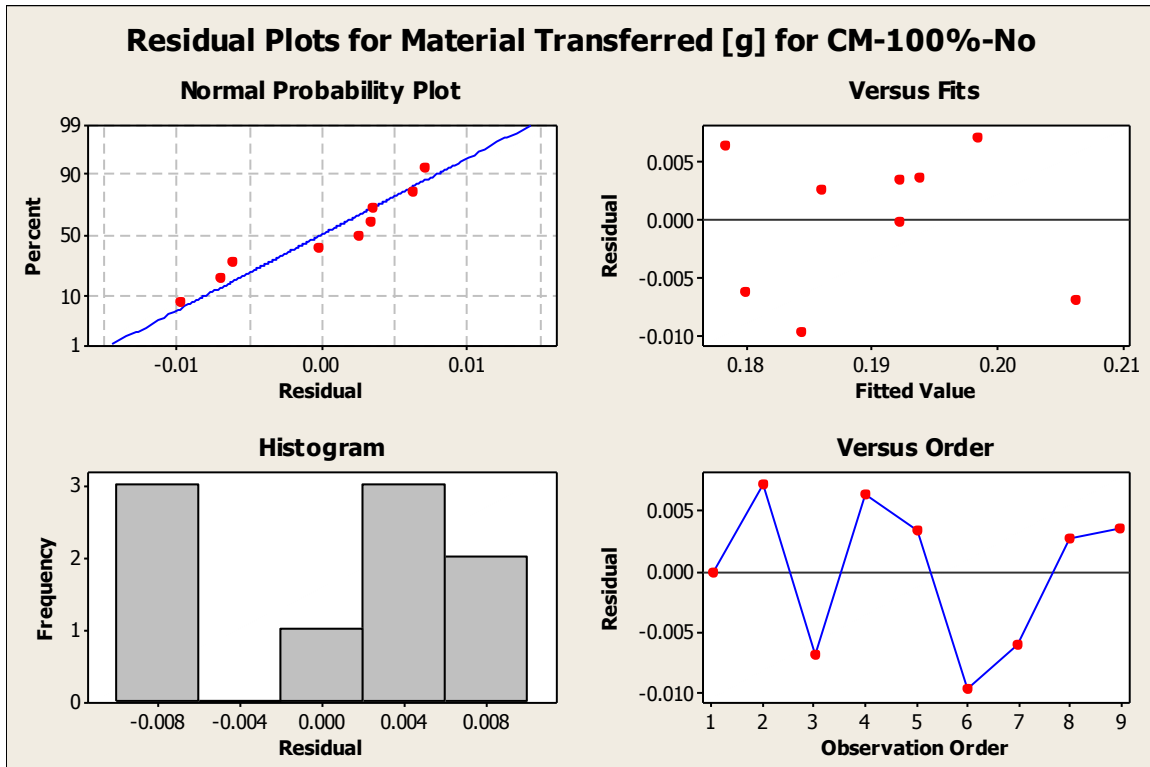


Figure 139. Residual plots for Material transferred

Table 34. Analysis of Variance for Height Adj. [mil], using Adjusted SS

Source	DF	Seq SS	Adj SS	Adj MS	F	P
Layers (x10)	2	165.389	165.389	82.694	83.86	0.001
Substrate	2	2.056	2.056	1.028	1.04	0.432
Error	4	3.944	3.944	0.986		
Total	8	171.389				
S = 0.993031 R-Sq = 97.70% R-Sq(adj) = 95.40%						

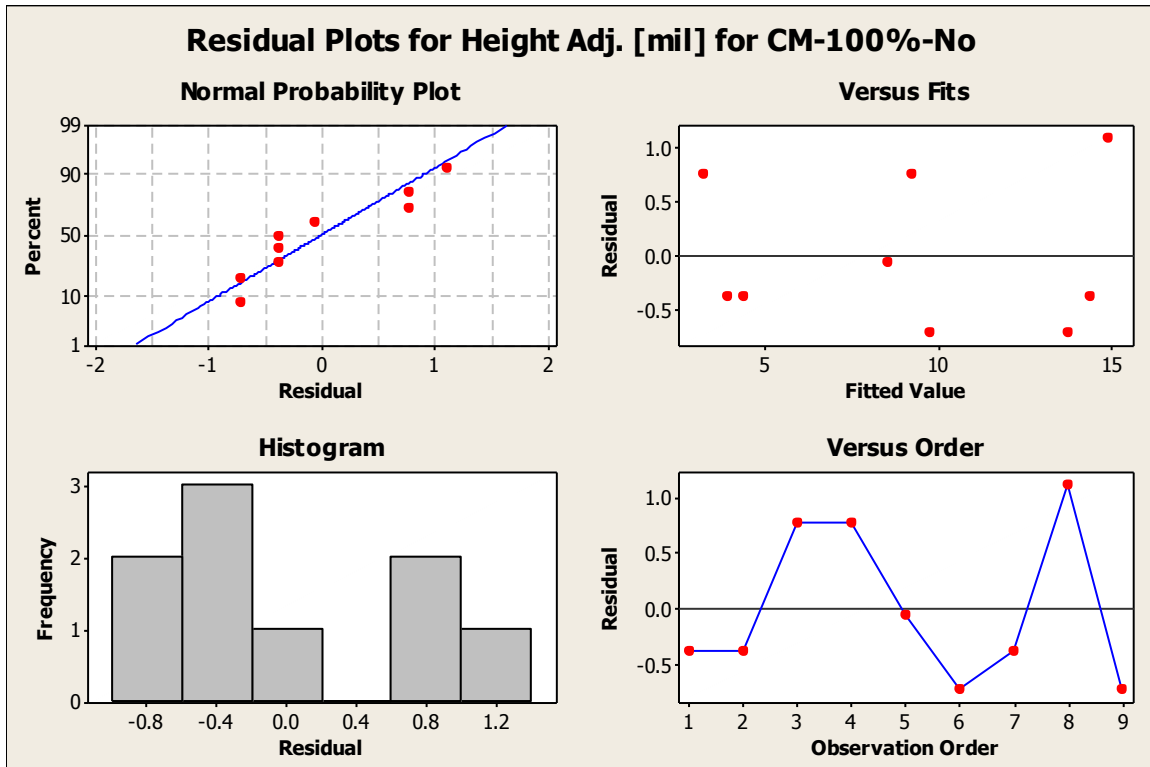


Figure 140. Residual plots for Height adjusted

B.13.7. C-50%-No

Table 35. Analysis of Variance for Material Transferred [g], using Adjusted SS

Source	DF	Seq SS	Adj SS	Adj MS	F	P
Layers (x10)	2	0.0000033	0.0000033	0.0000017	0.08	0.923
Substrate	2	0.0000108	0.0000108	0.0000054	0.26	0.781
Error	4	0.0000819	0.0000819	0.0000205		
Total	8	0.0000960				
S = 0.00873057 R-Sq = 68.01% R-Sq(adj) = 36.03%						

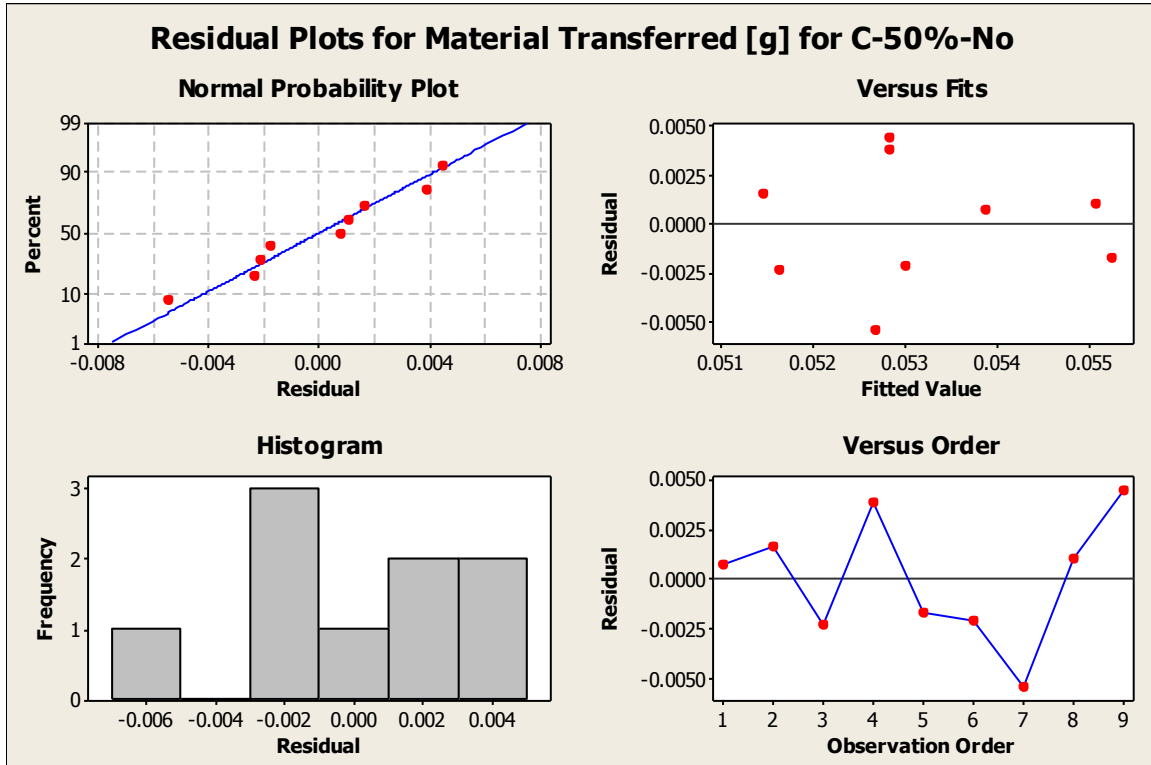


Figure 141. Residual plots for Material transferred

Table 36. Analysis of Variance for Height Adj. [mil], using Adjusted SS

Source	DF	Seq SS	Adj SS	Adj MS	F	P
Layers (x10)	2	6.0000	6.0000	3.0000	**	
Substrate	2	0.5000	0.5000	0.2500	**	
Error	4	0.0000	0.0000	0.0000		
Total	8	6.5000				
S = 1.333031E-16 R-Sq = 100.00% R-Sq(adj) = 100.00%						
** Denominator of F-test is zero or undefined.						

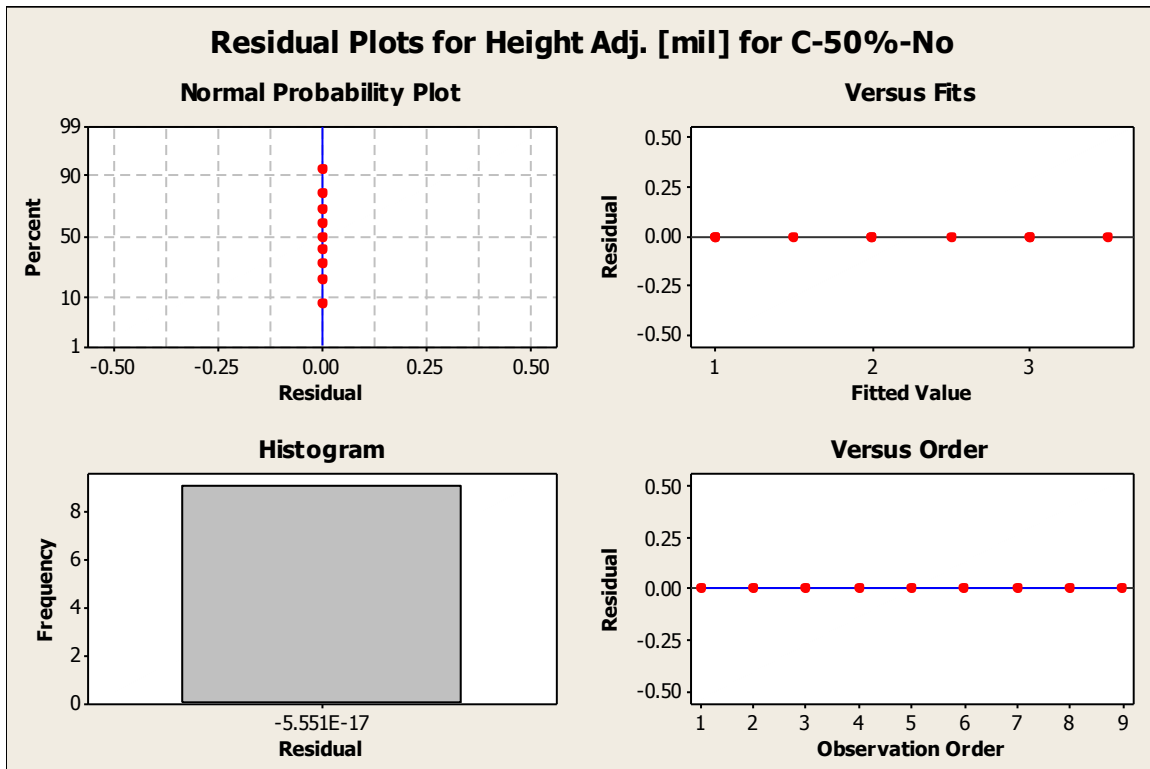


Figure 142. Residual plots for Height adjusted

B.13.8. CM-50%-No

Table 37. Analysis of Variance for Material Transferred [g], using Adjusted SS

Source	DF	Seq SS	Adj SS	Adj MS	F	P
Layers (x10)	2	0.0000125	0.0000125	0.0000063	0.37	0.714
Substrate	2	0.0000255	0.0000255	0.0000127	0.75	0.530
Error	4	0.0000681	0.0000681	0.0000170		
Total	8	0.0001061				
S = 0.00412587 R-Sq = 35.81% R-Sq(adj) = 0.00%						

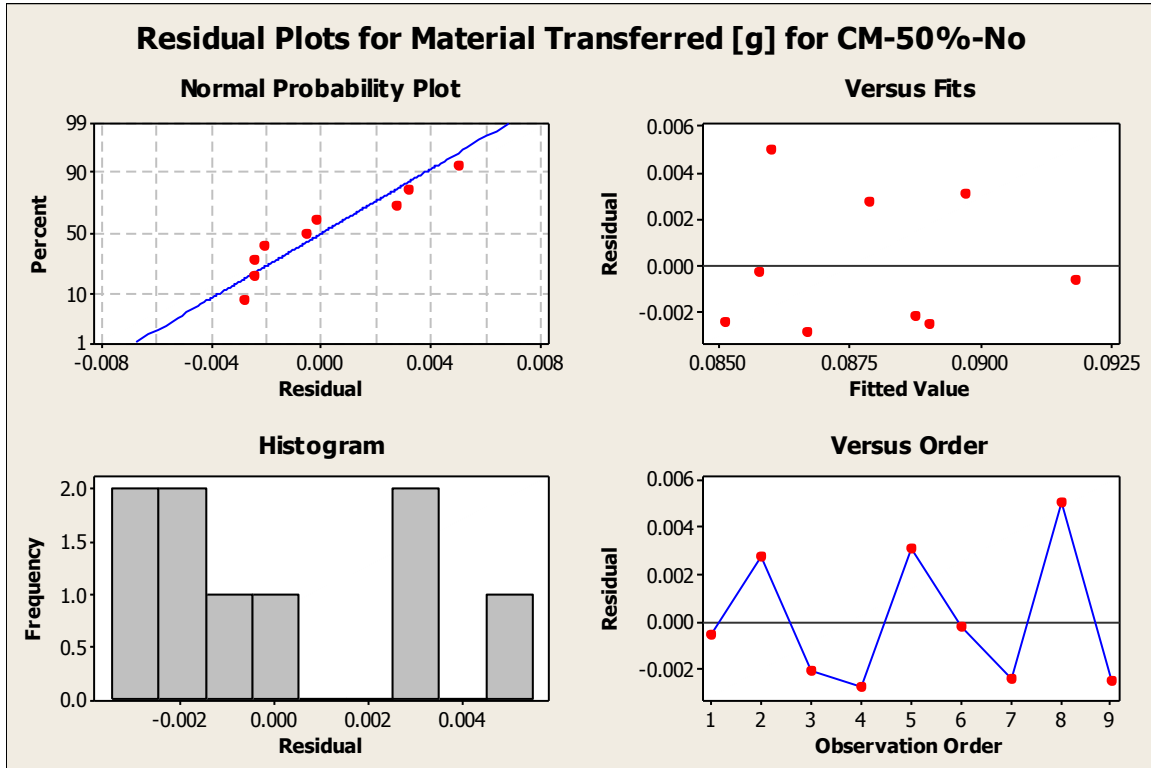


Figure 143. Residual plots for Material transferred

Table 38. Analysis of Variance for Height Adj. [mil], using Adjusted SS

Source	DF	Seq SS	Adj SS	Adj MS	F	P
Layers (x10)	2	24.0556	24.0556	12.0278	173.20	0.000
Substrate	2	1.0556	1.0556	0.5278	7.60	0.043
Error	4	0.2778	0.2778	0.0694		
Total	8	25.3889				
S = 0.263523 R-Sq = 98.91% R-Sq(adj) = 97.81%						

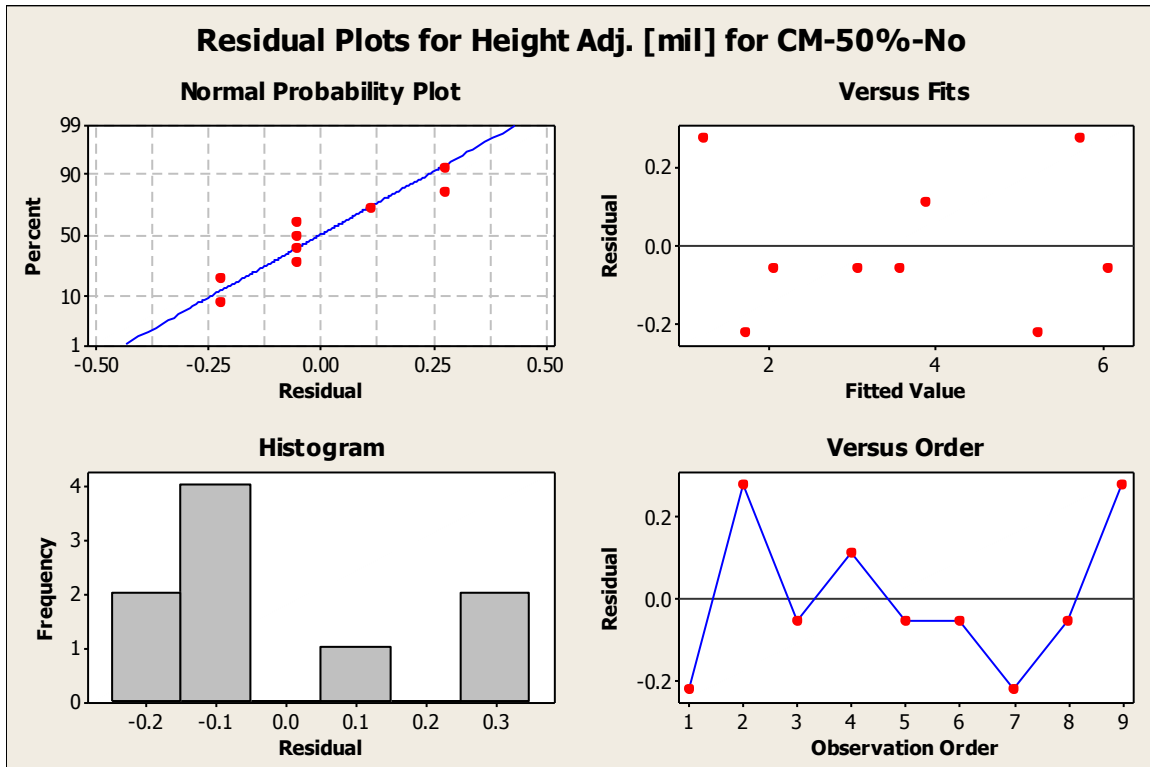


Figure 144. Residual plots for Height adjusted

Appendix C. PLOTS AND RAW DATA FROM LAYER-BY-LAYER ANALYSIS

ANALYSIS

This section contains the plots and summary of the measurements captured for the layer-by-layer analysis on the two 30-layer samples.

C.1. Sample fused face up – leading edge

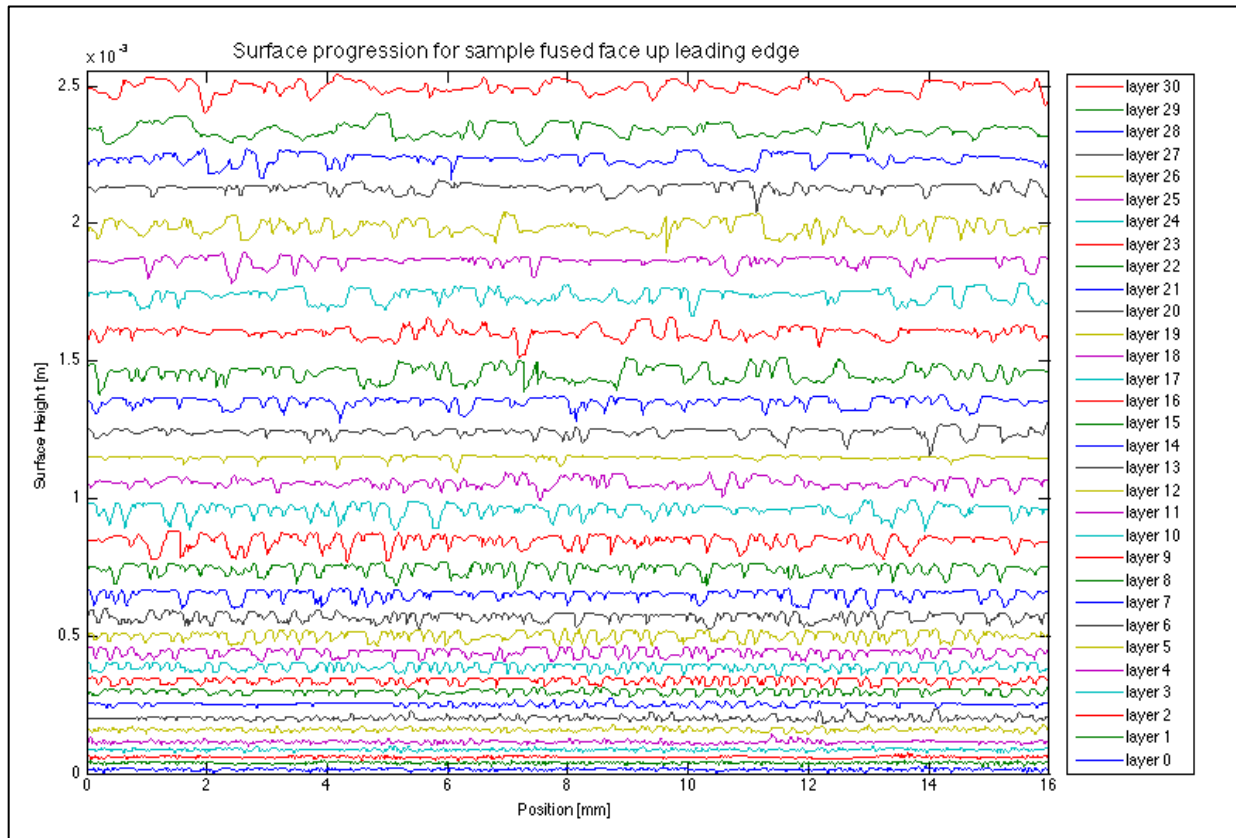


Figure 145. Plot of measurements at each layer (shifted up to avoid overlap)

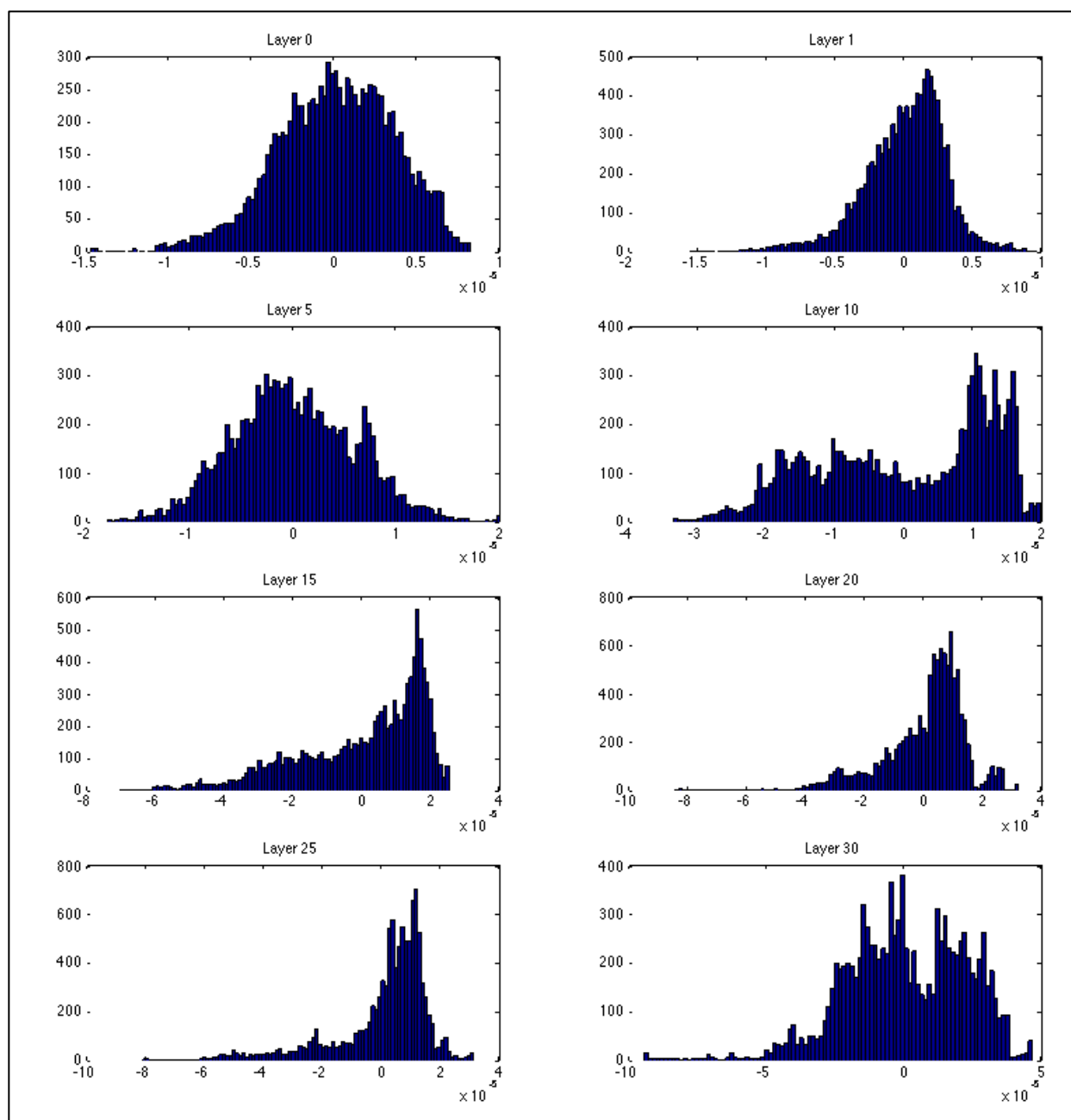


Figure 146. Histogram of measurements at layers 0 (base substrate), 1, 5, 10, 15, 20, 25, and 30

C.2. Sample fused face up – trailing edge

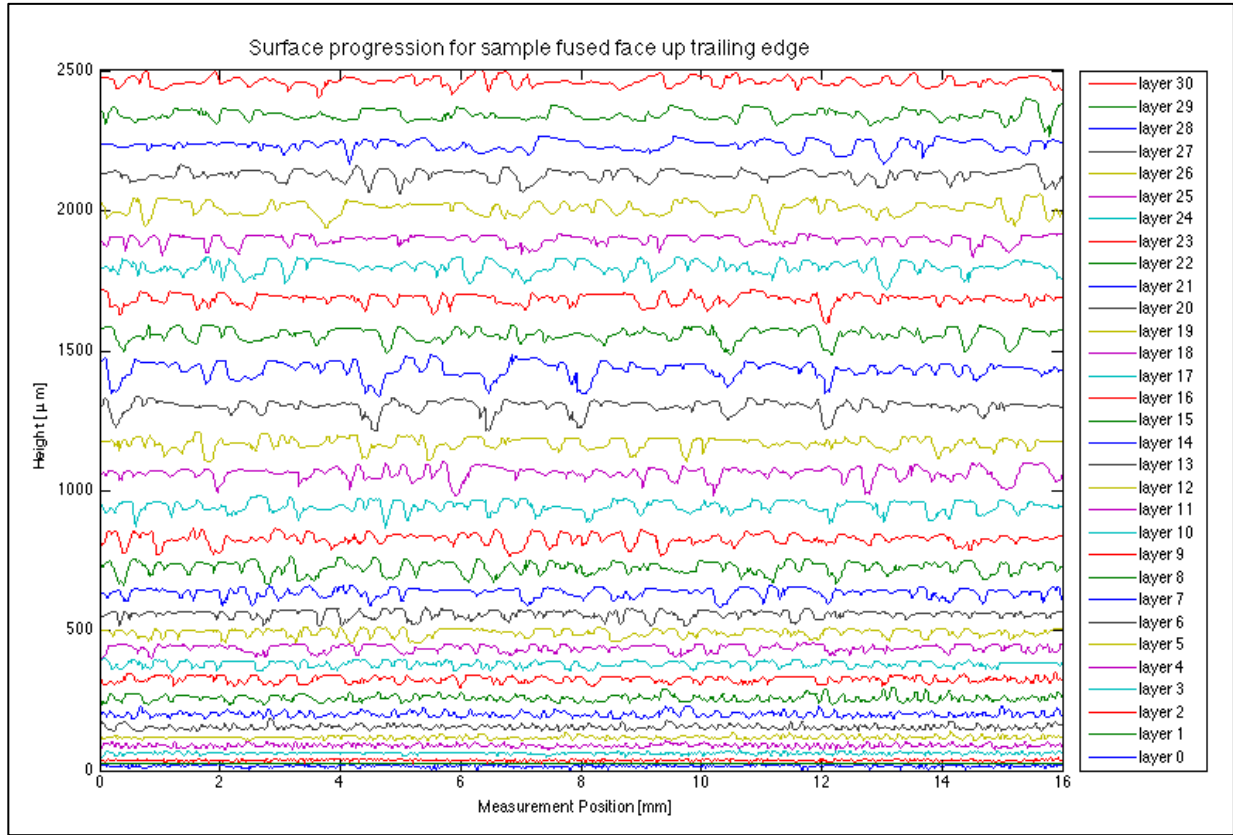


Figure 147. Plot of measurements at each layer (shifted up to avoid overlap)

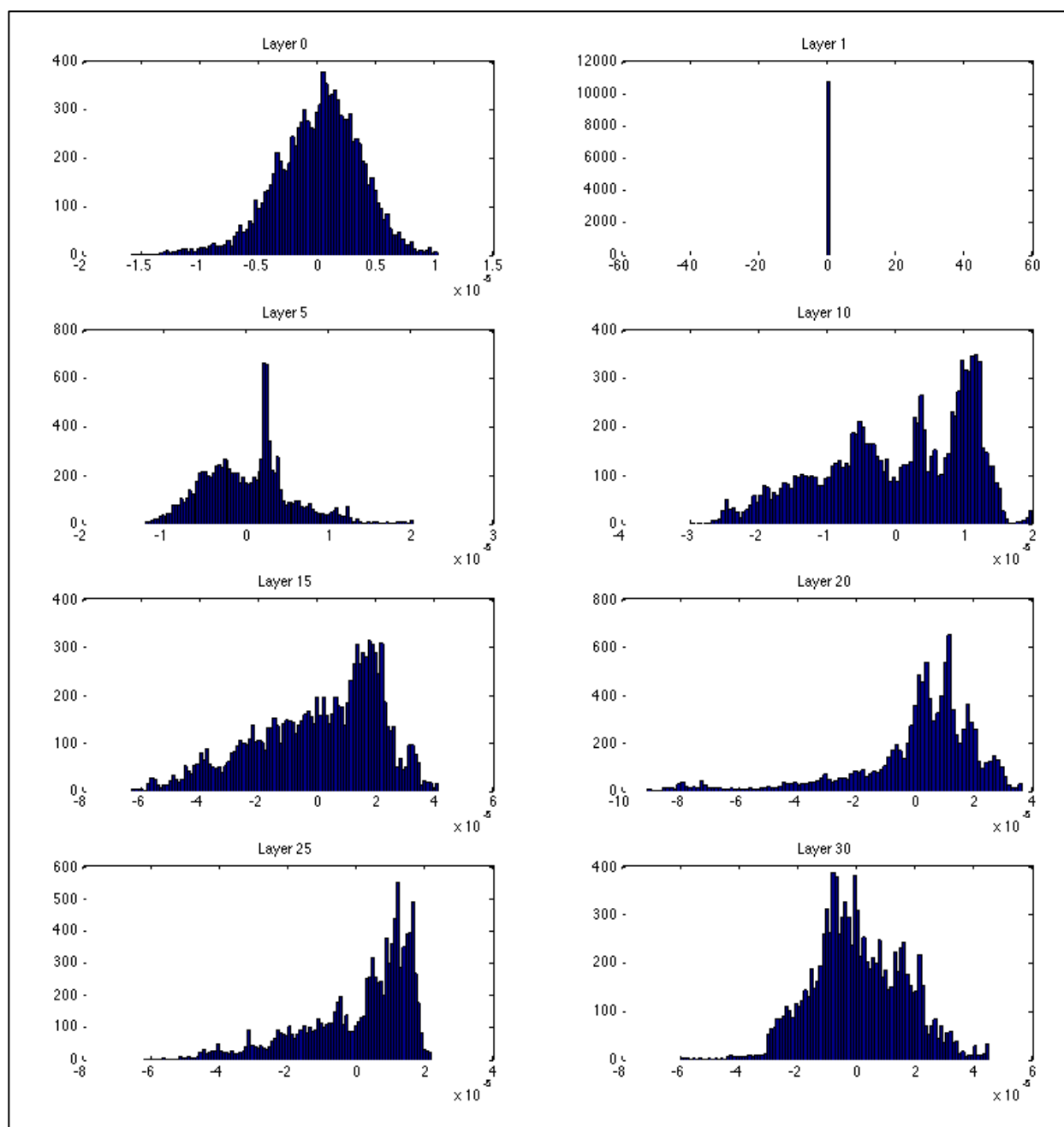


Figure 148. Histogram of measurements at layers 0 (base substrate), 1, 5, 10, 15, 20, 25, and 30

C.3. Sample fused face down – leading edge

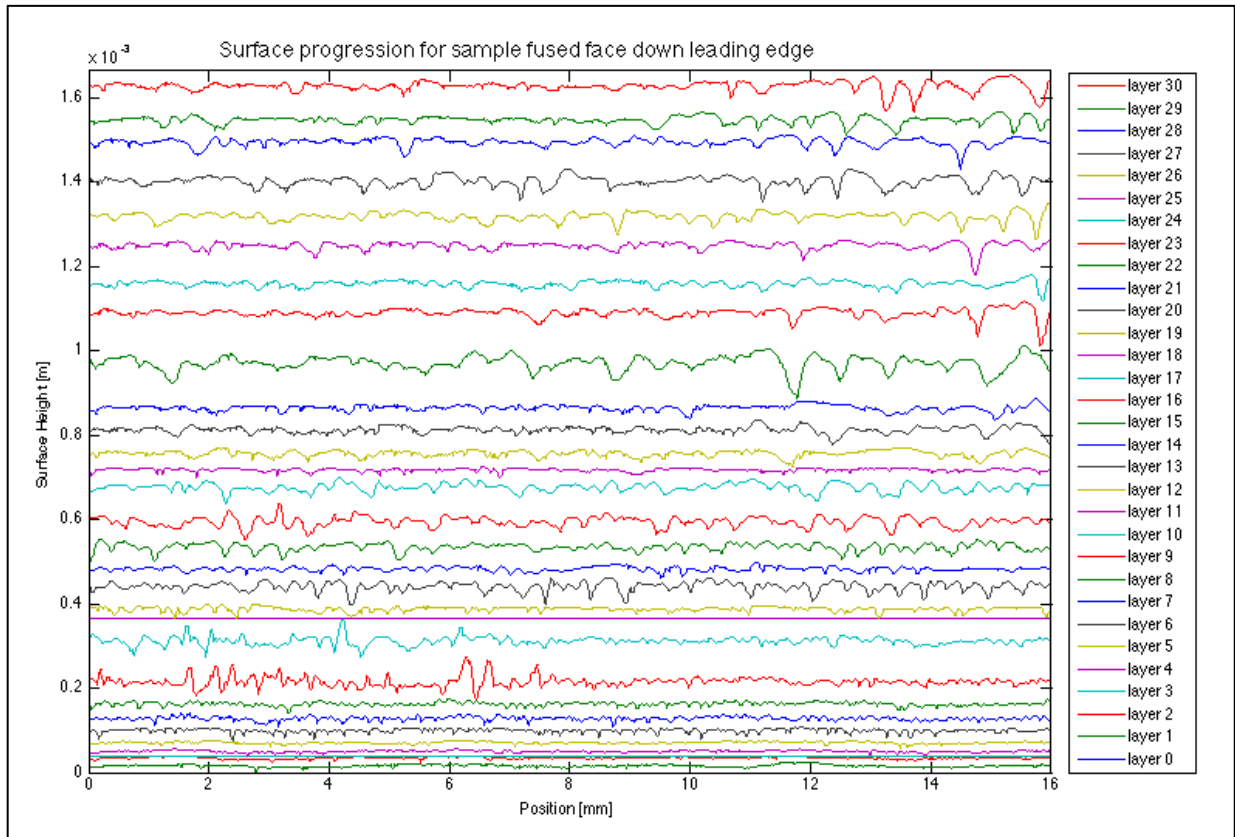


Figure 149. Plot of measurements at each layer (shifted up to avoid overlap)

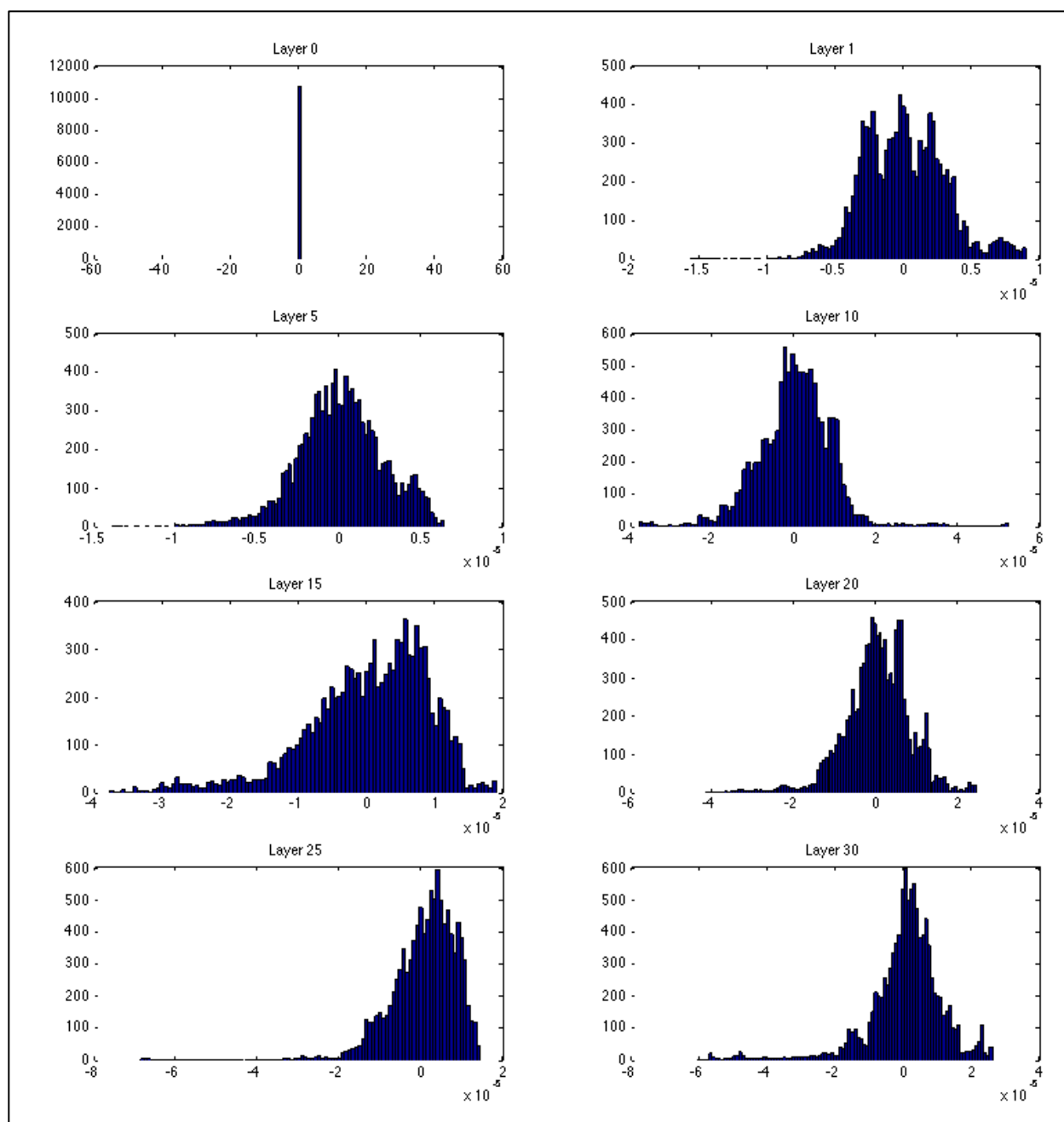


Figure 150. Histogram of measurements at layers 0 (base substrate), 1, 5, 10, 15, 20, 25, and 30

C.4. Sample fused face down – trailing edge

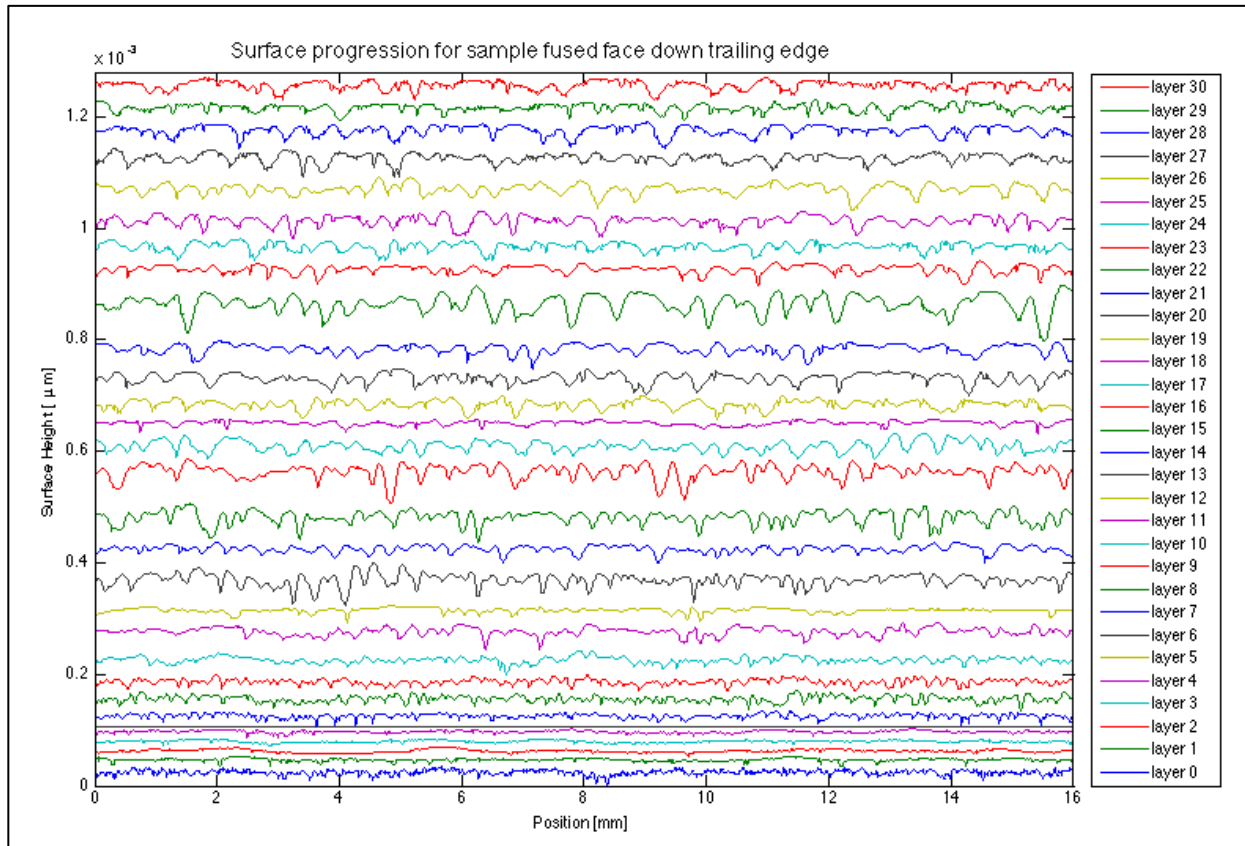


Figure 151. Plot of measurements at each layer (shifted up to avoid overlap)

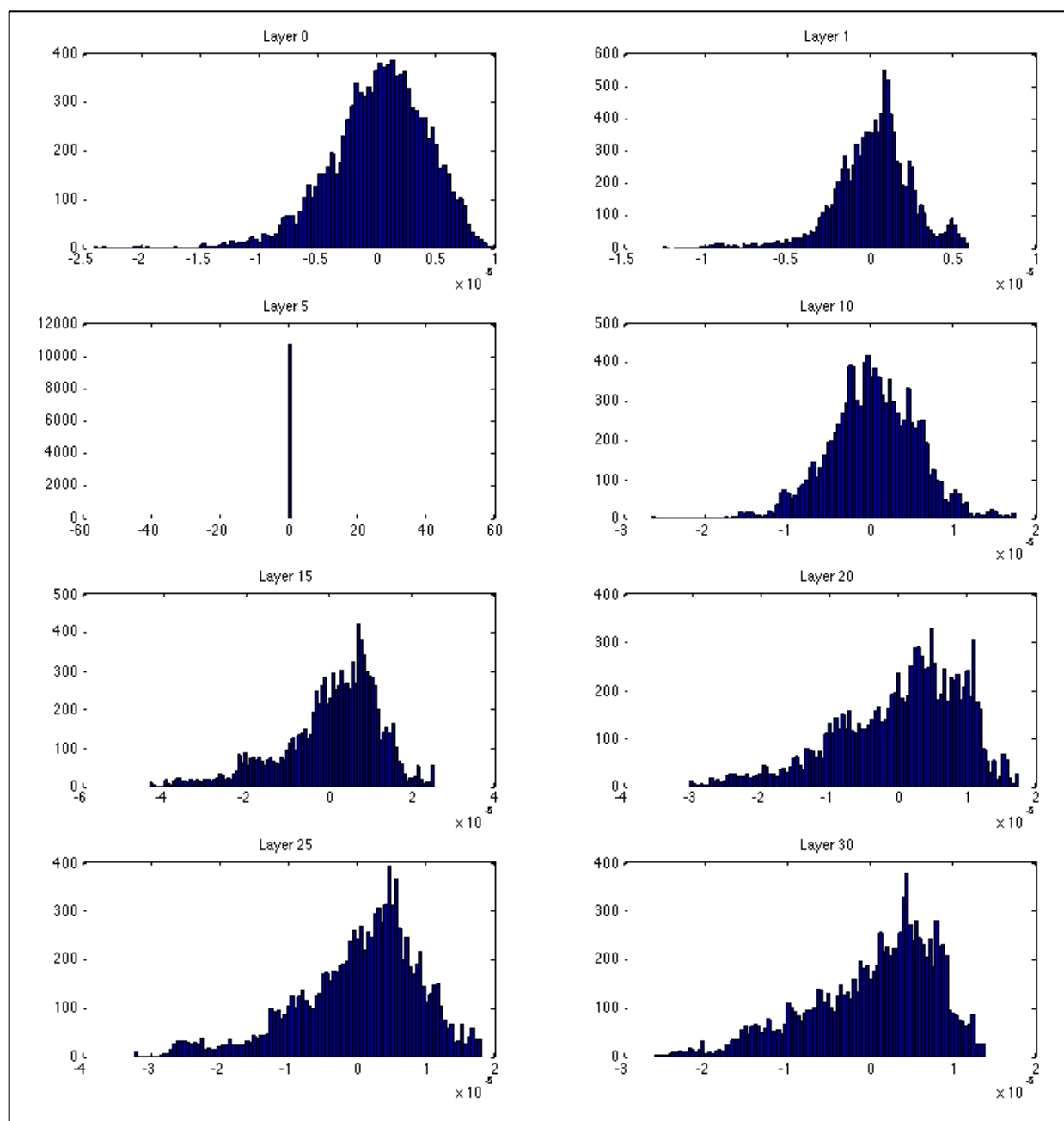


Figure 152. Histogram of measurements at layers 0 (base substrate), 1, 5, 10, 15, 20, 25, and 30

C.5. Compiled raw measurements

Table 39. Measurements for sample fused face up

Layer #	Mylar Sheet [g]	Printed Sheet [g]	After transfer [g]	Initial Material to transfer	Material transferred [g]	Material remaining [g]	Ra readings [μm]	
							trailing edge	leading edge
0							2.847	2.888
1	0.5226	0.5345	0.5247	0.0119	0.0098	0.0021	1.826	2.322
2	0.5096	0.5206	0.5115	0.0110	0.0091	0.0019	2.24	2.268
3	0.5134	0.5247	0.5166	0.0113	0.0081	0.0032	2.868	3.009
4	0.513	0.5238	0.5164	0.0108	0.0074	0.0034	4.918	3.72
5	0.5112	0.5228	0.5138	0.0116	0.0090	0.0026	4.237	4.799
6	0.5109	0.5226	0.5142	0.0117	0.0084	0.0033	6.217	5.751
7	0.5101	0.5211	0.5131	0.0110	0.0080	0.0030	7.379	4.698
8	0.5143	0.5254	0.5171	0.0111	0.0083	0.0028	8.815	7.776
9	0.5147	0.5259	0.5172	0.0112	0.0087	0.0025	9.519	9.276
10	0.5191	0.5299	0.5225	0.0108	0.0074	0.0034	8.972	11.169
11	0.5109	0.5227	0.5133	0.0118	0.0094	0.0024	10.325	12.013
12	0.51	0.5213	0.5122	0.0113	0.0091	0.0022	10.897	13.354
13	0.5123	0.5238	0.5163	0.0115	0.0075	0.0040	10.433	12.906
14	0.5147	0.5259	0.5173	0.0112	0.0086	0.0026	12.537	13.411
15	0.5123	0.5246	0.5155	0.0123	0.0091	0.0032	17.468	15.118
16	0.5173	0.5285	0.5209	0.0112	0.0076	0.0036	14.861	18.071
17	0.5124	0.5243	0.5163	0.0119	0.0080	0.0039	16.226	17.184
18	0.5145	0.526	0.516	0.0115	0.0100	0.0015	16.25	12.669
19	0.5142	0.5256	0.5174	0.0114	0.0082	0.0032	15.445	4.158
20	0.5133	0.5244	0.5137	0.0111	0.0107	0.0004	15.336	10.886
21	0.5201	0.5312	0.5209	0.0111	0.0103	0.0008	22.173	13.818
22	0.5196	0.5304	0.521	0.0108	0.0094	0.0014	17.795	22.982
23	0.5146	0.5255	0.515	0.0109	0.0105	0.0004	14.427	14.922
24	0.5097	0.5207	0.5124	0.0110	0.0083	0.0027	17.396	18.674
25	0.5191	0.5302	0.5195	0.0111	0.0107	0.0004	12.929	12.142
26	0.5242	0.535	0.5242	0.0108	0.0108	0.0000	19.393	20.525
27	0.5193	0.5302	0.5205	0.0109	0.0097	0.0012	14.7	11.262
28	0.5122	0.5236	0.514	0.0114	0.0096	0.0018	14.173	15.692
29	0.5176	0.5292	0.5187	0.0116	0.0105	0.0011	14.958	19.478
30	0.5203	0.5315	0.5234	0.0112	0.0081	0.0031	12.729	17.829

Table 40. Measurements for sample fused face down

Layer #	Mylar Sheet [g]	Printed Sheet [g]	After transfer [g]	Initial Material to transfer	Material transferred [g]	Material remaining [g]	Ra readings [μm]	
							trailing edge	leading edge
0							3.278	3.296
1	0.5142	0.5259	0.5148	0.0117	0.0111	0.0006	1.811	2.403
2	0.5061	0.5175	0.5061	0.0114	0.0114	0.0000	2.145	1.79
3	0.5141	0.5255	0.5145	0.0114	0.0110	0.0004	1.725	1.885
4	0.5134	0.5247	0.5134	0.0113	0.0113	0.0000	1.714	1.832
5	0.5174	0.5287	0.5176	0.0113	0.0111	0.0002	1.841	2.054
6	0.5153	0.5265	0.5154	0.0112	0.0111	0.0001	2.899	3.362
7	0.5158	0.5274	0.5162	0.0116	0.0112	0.0004	3.026	3.516
8	0.5158	0.5275	0.5161	0.0117	0.0114	0.0003	4.543	3.5
9	0.5148	0.5256	0.5146	0.0108	0.0110	-0.0002	3.994	7.91
10	0.5189	0.5301	0.5191	0.0112	0.0110	0.0002	4.26	6.886
11	0.5124	0.5237	0.5124	0.0113	0.0113	0.0000	5.484	7.635
12	0.5148	0.5258	0.5148	0.0110	0.0110	0.0000	2.884	4.132
13	0.5163	0.5275	0.5169	0.0112	0.0106	0.0006	8.159	8.279
14	0.5099	0.5213	0.5104	0.0114	0.0109	0.0005	4.851	4.012
15	0.5154	0.5268	0.5157	0.0114	0.0111	0.0003	9.215	7.084
16	0.5119	0.523	0.5119	0.0111	0.0111	0.0000	9.575	9.116
17	0.5122	0.5235	0.5124	0.0113	0.0111	0.0002	7.736	7.751
18	0.5104	0.5215	0.5108	0.0111	0.0107	0.0004	3.108	2.739
19	0.5132	0.5239	0.5132	0.0107	0.0107	0.0000	6.058	5.727
20	0.5159	0.527	0.5161	0.0111	0.0109	0.0002	7.36	6.109
21	0.5183	0.5294	0.5183	0.0111	0.0111	0.0000	6.845	5.246
22	0.5209	0.5324	0.522	0.0115	0.0104	0.0011	13.34	13.18
23	0.5187	0.5301	0.5191	0.0114	0.0110	0.0004	5.634	7.237
24	0.5158	0.5273	0.516	0.0115	0.0113	0.0002	6.058	5.798
25	0.5118	0.5235	0.5123	0.0117	0.0112	0.0005	6.974	6.48
26	0.5105	0.5217	0.5113	0.0112	0.0104	0.0008	6.989	7.665
27	0.5135	0.5249	0.5138	0.0114	0.0111	0.0003	6.388	9.747
28	0.5123	0.5236	0.5124	0.0113	0.0112	0.0001	6.878	6.919
29	0.5134	0.5242	0.5136	0.0108	0.0106	0.0002	5.205	6.815
30	0.5096	0.5208	0.5098	0.0112	0.0110	0.0002	6.264	7.824

Appendix D. IMAGES CAPTURED BY GELSIGHT

The following images were captured by GelSight using the bench configuration of their device for surface imaging; resulting images were 5202 x 3465 pixels at a resolution of 4.25 μm per pixel for a total sampling region of 22.3 x 14.9 mm.

D.1. 25-layer sample

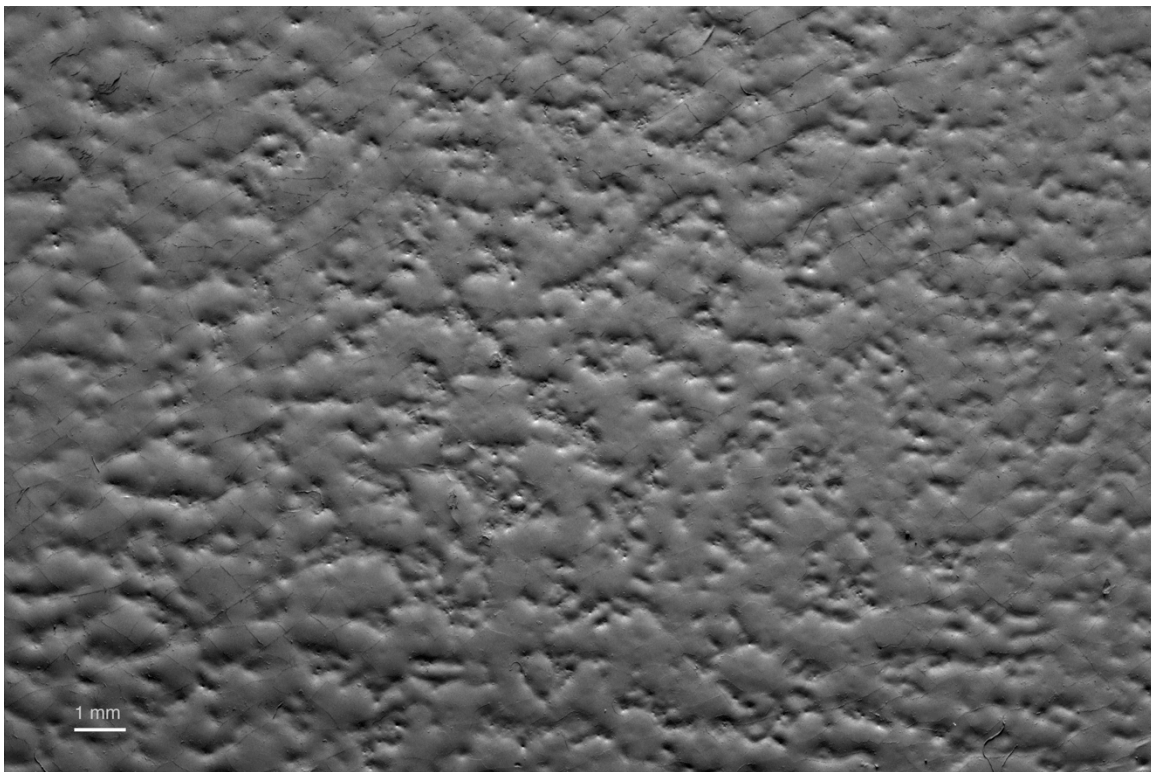


Figure 153. 22.3 x 14.9 mm section of the sample

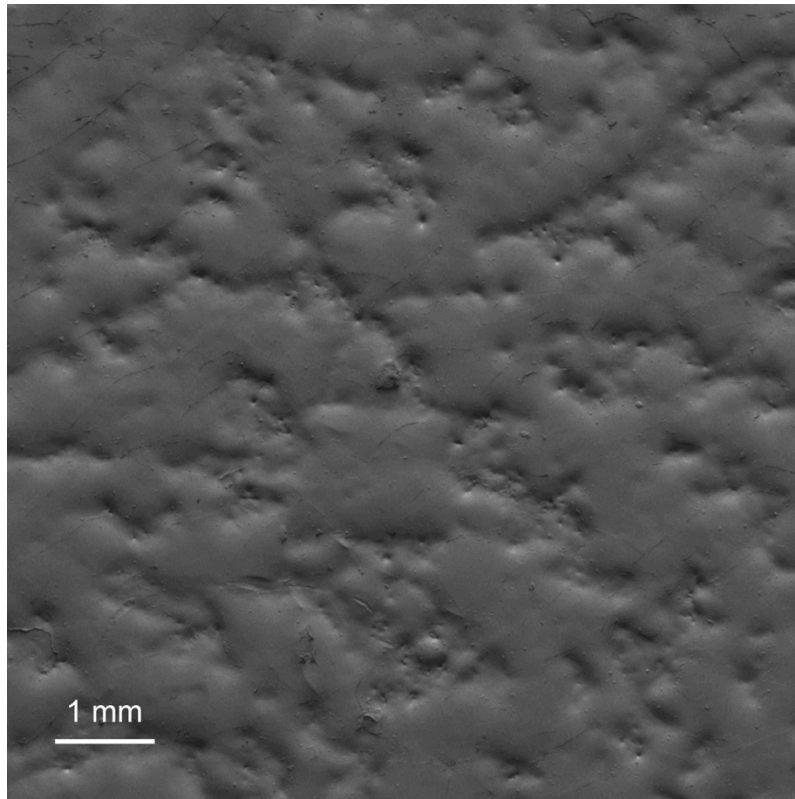


Figure 154. 8 x 8 mm detail of the sample

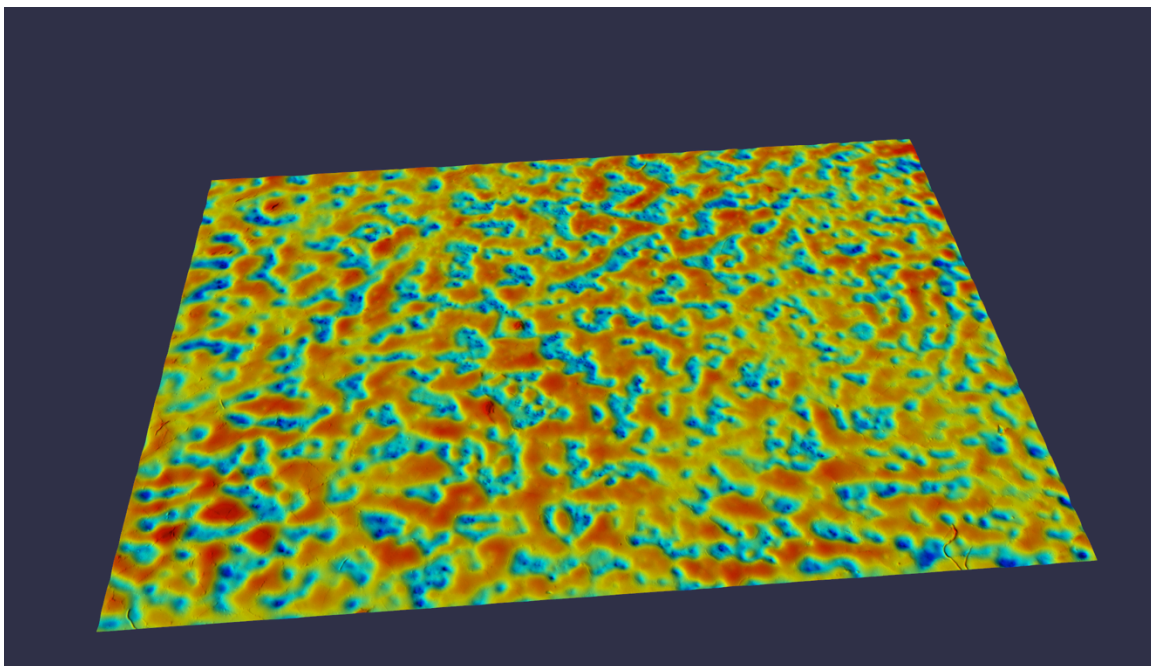


Figure 155. 3D reconstruction of the detail of the sample

D.2. 30-layer sample fused face up

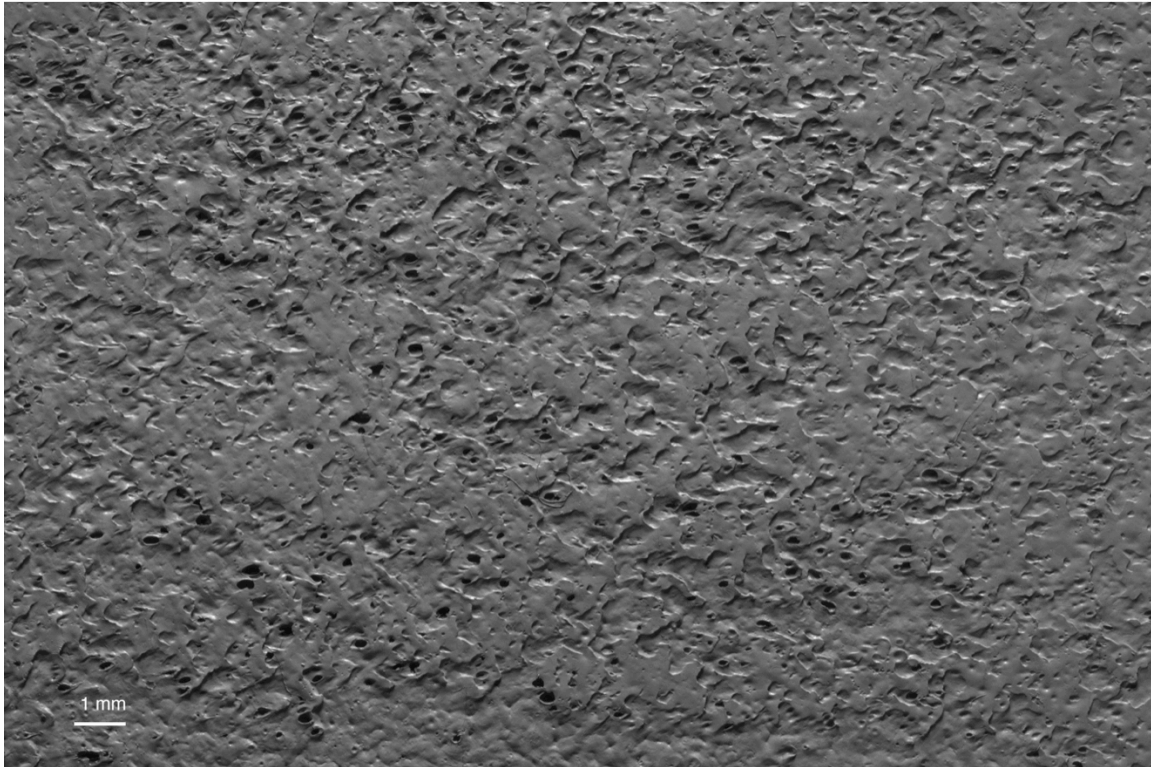


Figure 156. 22.3 x 14.9 mm section of the sample

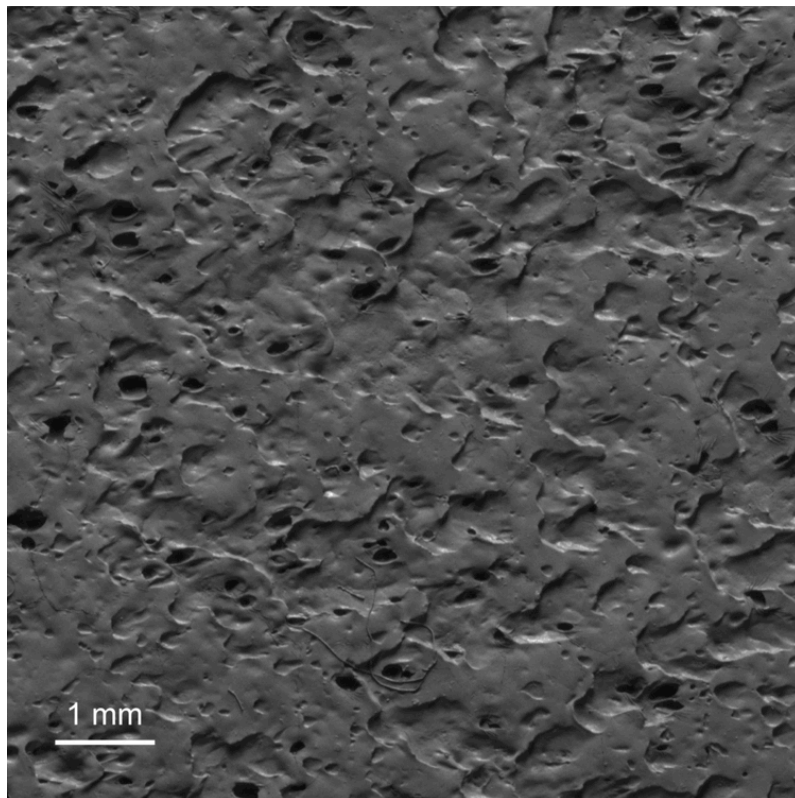


Figure 157. 8 x 8 mm detail of the sample

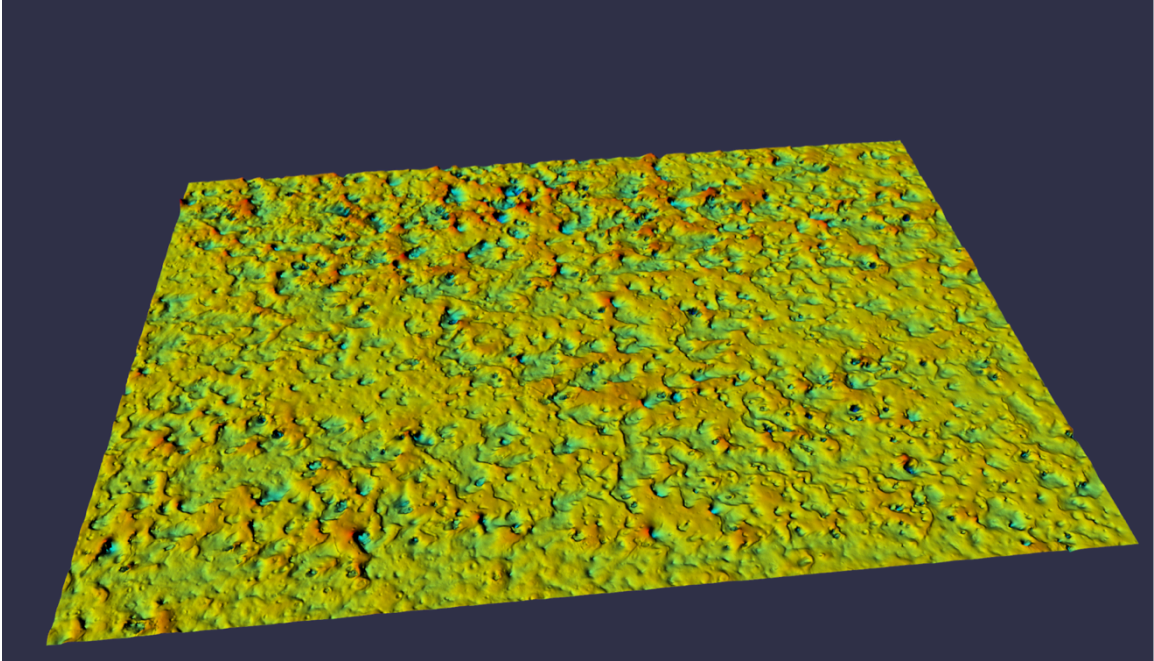


Figure 158. 3D reconstruction of the detail of the sample

D.3. 30-layer sample fused face down

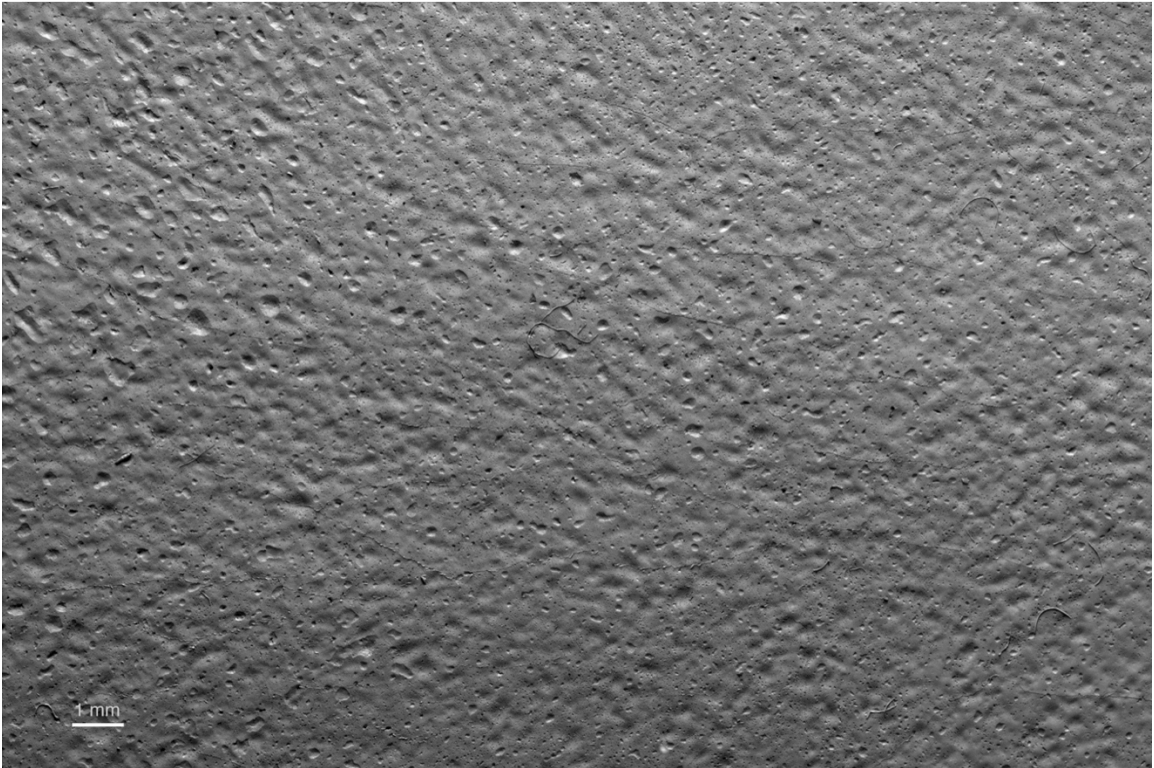


Figure 159. 22.3 x 14.9 mm section of the sample

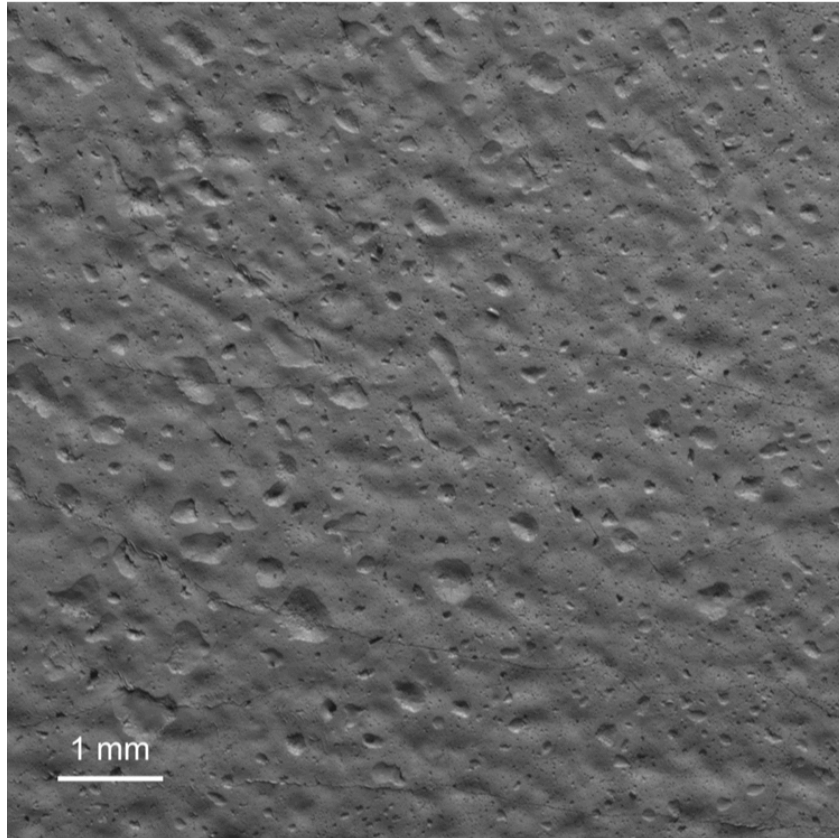


Figure 160. 8 x 8 mm detail of the sample

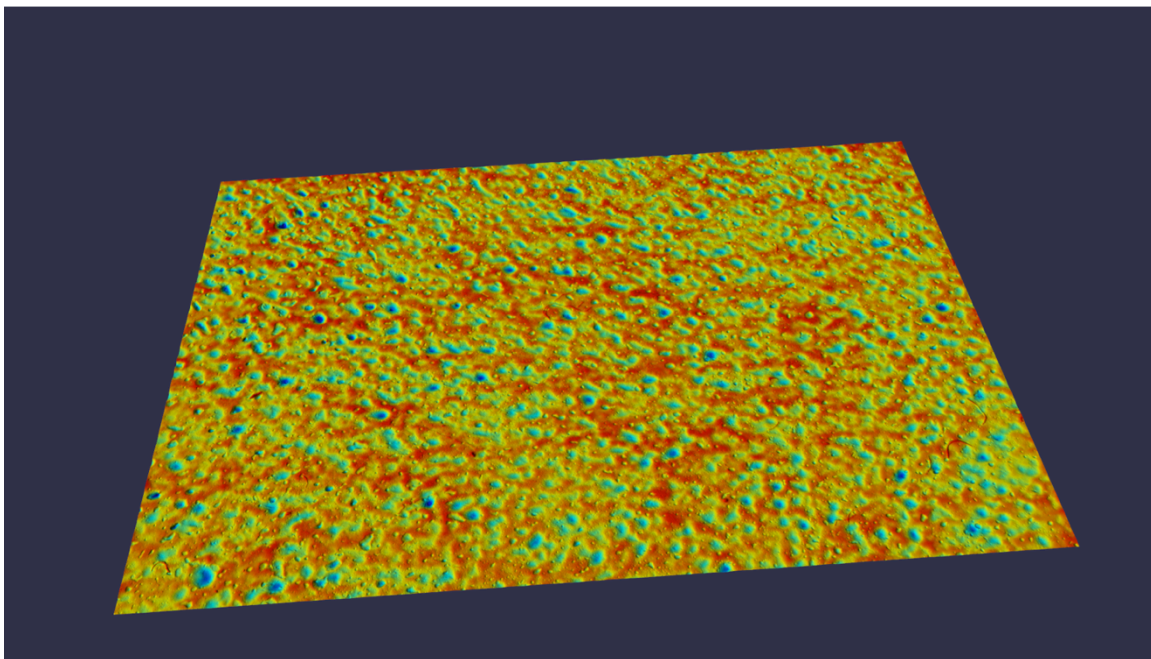


Figure 161. 3D reconstruction of the detail of the sample

D.4. 30-layer sample belt interface



Figure 162. 22.3 x 14.9 mm section of the sample

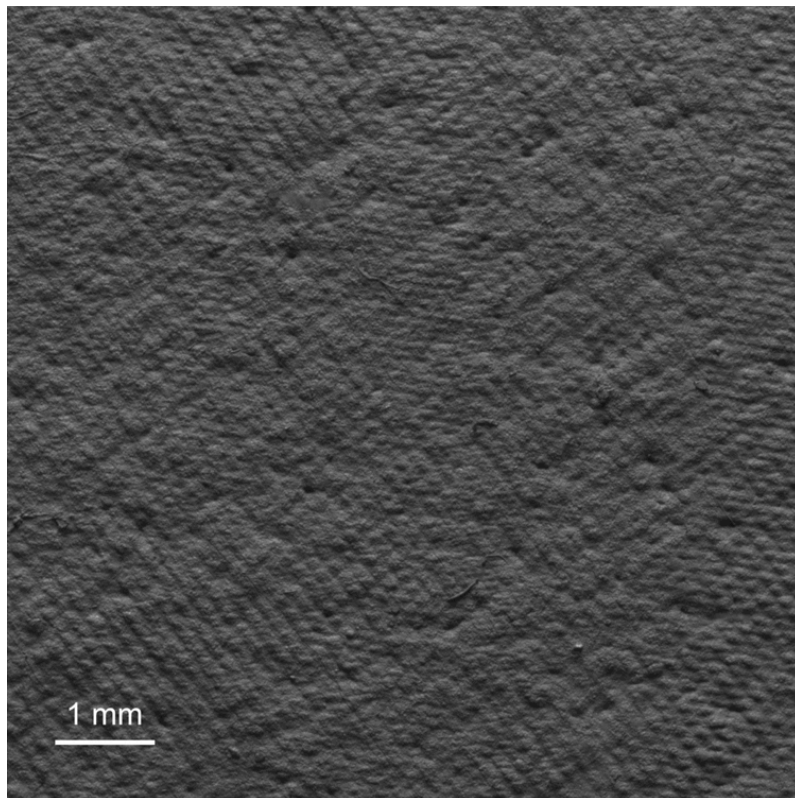


Figure 163. 8 x 8 mm detail of the sample

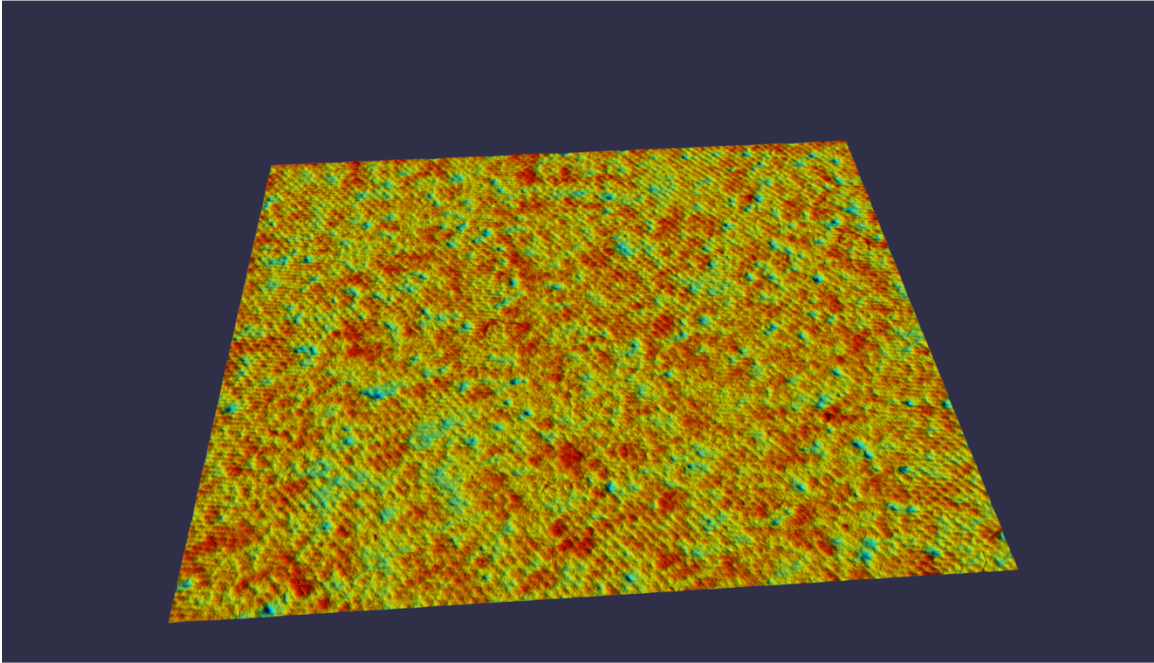


Figure 164. 3D reconstruction of the detail of the sample

D.5. 100-layer 1-toner sample

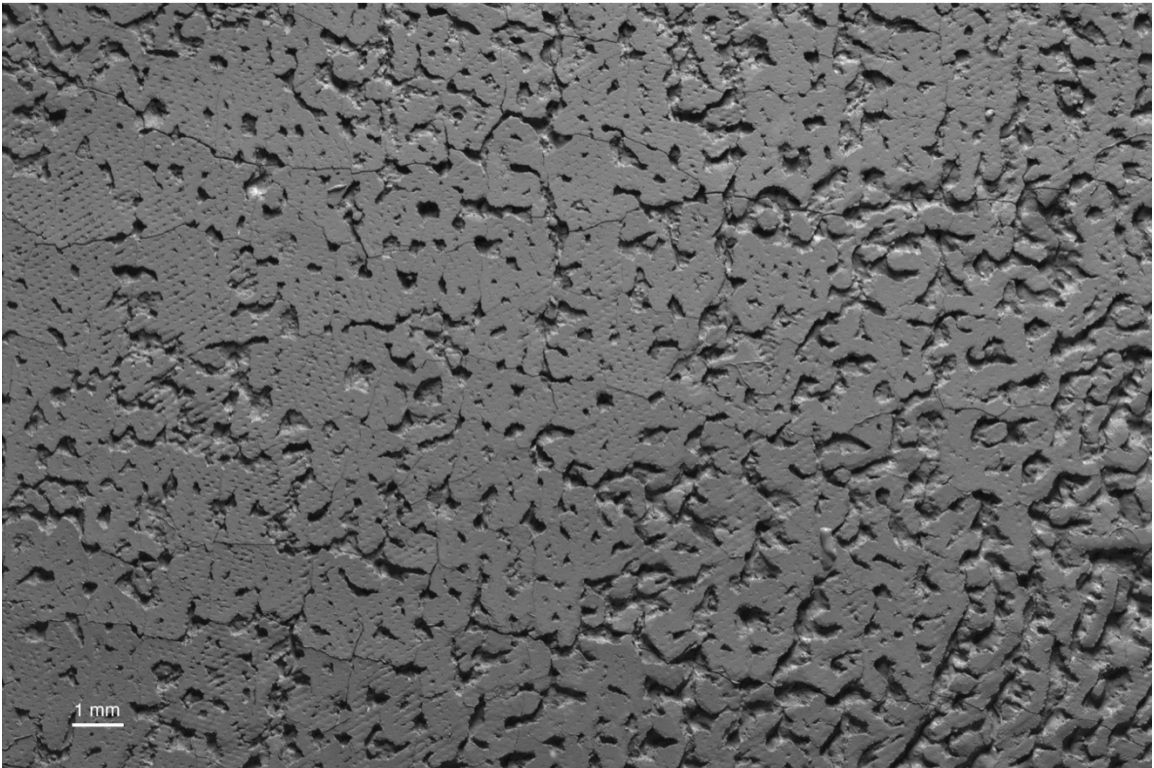


Figure 165. 22.3 x 14.9 mm section of the sample

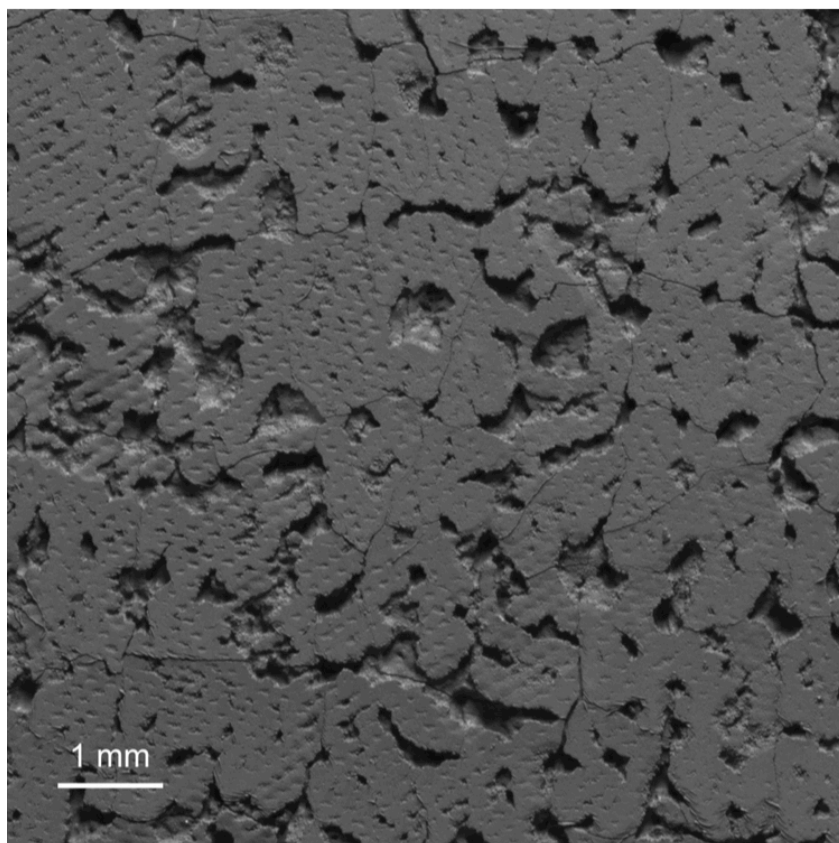


Figure 166. 8 x 8 mm detail of the sample

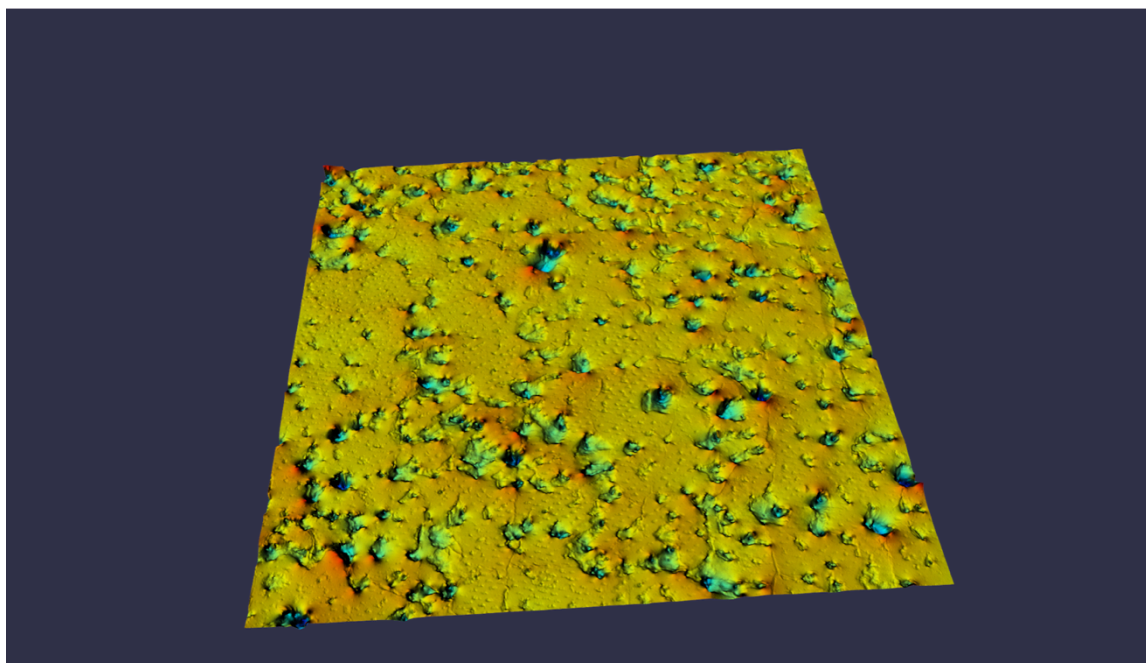


Figure 167. 3D reconstruction of the detail of the sample

BIBLIOGRAPHY

- [1] J. B. Jones, G. J. Gibbons, and D. I. Wimpenny, "Transfer Methods toward Additive Manufacturing by Electrophotography," in *NIP 27 and Digital Fabrication*, Minneapolis, MN, 2011, pp. 180 - 184.
- [2] D. K. Bynum, "Automated manufacturing system using thin sections," U.S. Patent 5088047, 1992.
- [3] A. V. Kumar and H. Zhang, "Electrophotographic powder deposition for freeform fabrication," in *10th Solid Freeform Fabrication Symposium*, 1999.
- [4] D. Cormier, J. Taylor, and H. West, "An Investigation of Selective Coloring with 3-D Laser Printing," *Journal of Manufacturing Processes*, vol. 4, pp. 148-152, 2002.
- [5] A. V. Kumar and A. Dutta, "Electrophotographic Layered Manufacturing," *Journal of Manufacturing Science and Engineering*, vol. 126, pp. 571-576, 2004.
- [6] D. I. Wimpenny, S. Banerjee, and J. B. Jones, "Laser Printed Elastomeric Parts and their Properties," in *Solid Freeform Fabrication Symposium*, Austin, TX, 2009.
- [7] J. Knapp, "Challenges associated with control of toner deposition for 3D printing," M. Esterman, Ed., ed: e-mail, 2012.
- [8] Y. Hoshino, K. Li, D. J. Karunanayake, and T. Hasegawa, "Review of Toner-Based Printing Technologies and Fundamentals of Toner Charging Mechanism," *Journal of Imaging Science and Technology*, vol. 54, pp. 050201-5, 2010.
- [9] R. M. Schaffert, *Electrophotography*, 2nd ed. London: Focal Press, 1975.
- [10] A. V. Kumar, "Solid Freeform Fabrication using Powder Deposition," U.S. Patent 6066285, 2000.
- [11] D. Cormier, J. Taylor, K. Unnanon, P. Kulkarni, and H. West, "Experiments in Layered Electro-Photographic Printing," in *2000 Solid Freeform Fabrication Proceedings*, Austin, TX, 2000, pp. 267-274.
- [12] A. Kumar Das, "An Investigation on the Printing of Metal and Polymer Powders Using Electrophotographic Solid Freeform Fabrication " Master of Science, Department of Mechanical and Aerospace Engineering University of Florida, Gainesville, FL, 2004.
- [13] J. B. Jones, D. I. Wimpenny, G. J. Gibbons, and C. Sutcliffe, "Additive manufacturing by electrophotography: Challenges and successes," presented at the NIP 26 and Digital Fabrication, Austin, Texas, 2010.
- [14] R. Zhang, P.-S. Tsai, J. E. Cryer, and M. Shah, "Shape-from-shading: a survey," *Pattern Analysis and Machine Intelligence, IEEE Transactions on*, vol. 21, pp. 690-706, 1999.
- [15] S. K. Nayar and Y. Nakagawa, "Shape from focus," *Pattern Analysis and Machine Intelligence, IEEE Transactions on*, vol. 16, pp. 824-831, 1994.
- [16] T. Chen, M. Goesele, and H.-P. Seidel, "Mesostructure from Specularity," in *Computer Vision and Pattern Recognition, 2006 IEEE Computer Society Conference on*, 2006, pp. 1825-1832.
- [17] M. K. Johnson, F. Cole, A. Raj, and E. H. Adelson, "Microgeometry capture using an elastomeric sensor," *ACM Trans. Graph.*, vol. 30, pp. 1-8, 2011.

- [18] L. B. Schein, *Electrophotography and Development Physics*, Revised 2nd. ed. Morgan Hill: Laplacian Press, 1992.
- [19] M. F. Molaire, "Aqueous Surface-Smoothing Layer Compositions for High-Quality Photoreceptors," presented at the NIP23 and Digital Fabrication, Anchorage, AK, 2007.
- [20] D. Mahalko. (2007, 01/18/2013). *Laser Printer - Writing*. Available: http://en.wikipedia.org/wiki/File:LaserPrinter-Writing_-_ReplaceJPG.png
- [21] Canon. (2013, 1/25/2013). *Creation of Revolutionary Printing Technologies through Imagination & Perspiration*. Available: http://www.canon.com/technology/approach/history/print_tech.html
- [22] J. Knapp, "Xerographic Development: Sub-System Challenges & Example Solutions," ed: Xerox, 2008.
- [23] F. Liu, G. T. Chiu, E. S. Hamby, and Y. Eun, "Modeling and Control of a Hybrid Two-Component Development Process for Xerography," *Control Systems Technology, IEEE Transactions on*, vol. 19, pp. 531-544, 2011.
- [24] Konica-Minolta. (2012, 01/31/2013). *Colour Production Print Systems: From start to finish, consistent quality for professional results - bizhub PRESS C7000/C6000*. Available: http://www.konicaminolta.in/business/production/c7000_c6000/feature01.html
- [25] Mondri. (2013, 01/31/2013). *Color Laser Printer - Transfer belt system*. Available: http://www.mondigroup.com/paper_new/EN/color_copy_professional/Color_Laser_Printing/Printing_process/Transfer_belt_system/transfer_belt_system.aspx
- [26] B. Chaffin, A. Holden, and A. Paris, "Effect of Fusing Parameters on Print Gloss," *Journal of Imaging Science*, vol. 54, pp. 60406-1-60406-8, 2010.
- [27] M. Anzai and N. Hoshi, "Prediction of Deposit Toner Mass by Improved Toner Flow Model for Dual Component Magnetic Brush Development," in *NIP14: International Conference on Digital Printing Technologies*, Toronto, ON, Canada, 1998, pp. 462-465.
- [28] F. Takeda, K. Sakamoto, and K. Kobayashi, "Model for a mono-component development process using edge enhancement effects of floating electrodes," *IEEE Transactions on Industry Applications*, vol. 24, pp. 256-261, 1988.
- [29] P. Ramesh, "Modeling and Control of Toner Material State in Two Component Development Systems," *Journal of Imaging Science and Technology*, vol. 53, pp. 41206-1-41206-5, 2009.
- [30] E. Gross and P. Ramesh, "Xerographic Printing System Performance Optimization by Toner Throughput Control," *Journal of Imaging Science and Technology*, vol. 53, pp. 41207-1-41207-5, 2009.
- [31] A. V. Kumar and A. Dutta, "Investigation of an electrophotography based rapid prototyping technology," *Rapid Prototyping Journal*, vol. 9, pp. 95 - 103, 2003.
- [32] A. V. Kumar, A. Dutta, and J. E. Fay, "Solid freeform fabrication by electrophotographic printing," in *2003 Solid Freeform Fabrication Proceedings*, 2003, pp. 39-49.
- [33] S. Banerjee, "Development of a novel toner for electrophotography based additive manufacturing process," PhD, De Montfort University, Leicester, 2011.
- [34] H. Godbole, "Characterization of Color, Gloss and Mechanical Performance of 3D Printed Structures," Master of Science, Industrial Engineering, RIT, Rochester, NY, 2012.

- [35] J. B. Jones, D. I. Wimpenny, and G. J. Gibbons, "The Influence of Residual Toner Charge on 3D Laser Printed Objects," presented at the NIP 28 and Digital Fabrication, Quebec, Canada, 2012.
- [36] J. B. Jones, *et al.*, "Printed Circuit Boards by Selective Deposition and Processing," *Nanoscale*, vol. 22, p. 23, 2011.
- [37] D. Buttner, K. Kruger, A. Schonberger, D. Jung, and B. Zobrist, "Laser Printing of Conductive Silver Lines," presented at the NIP26 and Digital Fabrication, Austin, TX, 2010.
- [38] J. B. Jones, D. Büttner, R. Chudasama, D. Wimpenny, and K. Krüger, "Laser Printing Circuit Boards and Electronics," *Journal of Imaging Science and Technology*, vol. 56, pp. 40503-1-40503-11, 2012.
- [39] Kodak. (2009, 11/18/2013). *KODAK Dimensional Printing System Sparks Customer Excitement - Press Release - Kodak Graphic Communications Group*. Available: http://graphics.kodak.com/us/en/about_gcg/news/2009/090629a.htm
- [40] Kodak. (2009, 11/18/2013). *Fifth Imaging Unit Solutions - Kodak Graphic Communications Group*. Available: http://graphics.kodak.com/us/en/product/printers_presses/comm_sheet/digital_color/fifth_imaging/default.htm
- [41] Kodak, "Kodak NexPress Intelligent Dimensional Coating Solution," ed: Eastman Kodak Company, 2013.
- [42] Kodak. (2013, 11/18/2013). *KODAK NEXPRESS 2500 Digital Production Color Press - Kodak Graphic Communications Group*. Available: http://www.graphics.kodak.com/gb/en/product/printers_presses/comm_sheet/digital_color/nexpress/recon/2500/default.htm
- [43] printdirectory.org. (2007, *Kodak NexPress - Detail*. Available: <http://www.printdirectory.org/detail/link-638.html>
- [44] D. L. Bourell, M. C. Leu, and D. W. Rosen, "Roadmap for Additive Manufacturing Identifying the Future of Freeform Processing ", ed. Austin, TX: The University of Texas at Austin, 2009.
- [45] A. L. Cooke and S. P. Moylan, "Process Intermittent Measurement for Powder-Bed Based Additive Manufacturing," presented at the 22nd International SFF Symposium - An Additive Manufacturing Conference, Austin, TX, 2011.
- [46] M. Gatto and R. A. Harris, "Non-destructive analysis (NDA) of external and internal structures in 3DP," *Rapid Prototyping Journal*, vol. 17, pp. 128-137, 2011.
- [47] S. Arimoto, S. Kawamura, and F. Miyazaki, "Bettering operation of Robots by learning," *Journal of Robotic Systems*, vol. 1, pp. 123-140, 1984.
- [48] D. A. Bristow, M. Tharayil, and A. G. Alleyne, "A survey of iterative learning control," *Control Systems, IEEE*, vol. 26, pp. 96-114, 2006.
- [49] Y. Wang, F. Gao, and F. J. Doyle Iii, "Survey on iterative learning control, repetitive control, and run-to-run control," *Journal of Process Control*, vol. 19, pp. 1589-1600, 2009.
- [50] J.-X. Xu, Y. Chen, T. H. Lee, and S. Yamamoto, "Terminal iterative learning control with an application to RTPCVD thickness control," *Automatica*, vol. 35, pp. 1535-1542, 1999.
- [51] G. Gauthier and B. Boulet, "Terminal Iterative Learning Control design with singular value decomposition decoupling for thermoforming ovens," in *2009 American Control Conference (ACC)*, 2009, pp. 1640-1645.

- [52] S. Tong Duy and A. Hyo-Sung, "Terminal iterative learning control with multiple intermediate pass points," in *2011 American Control Conference (ACC)*, 2011, pp. 3651-3656.
- [53] S. Owen. (1999, 11/14/2013). *Phong Model - Specular Reflection*. Available: http://www.siggraph.org/education/materials/HyperGraph/illumine/specular_highlights/phong_model_specular_reflection.htm
- [54] S. Owen. (1999, 11/14/2013). *Diffuse Reflection*. Available: http://www.siggraph.org/education/materials/HyperGraph/illumine/diffuse_reflection.htm
- [55] B. T. Phong, "Illumination for computer generated pictures," *Communications of the ACM*, vol. 18, pp. 311-317, 1975.
- [56] V. P. Fesenkov, "Photometric Investigations of the Lunar Surface," *Astronomicheskii Zh.*, vol. 5, pp. 219-234, 1929.
- [57] T. Rindfleisch, "Photometric Method for Lunar Topography," *Photometric Eng.*, vol. 32, pp. 262-276, 1966.
- [58] B. Horn, "Obtaining shape from shading information," in *The Psychology of Computer Vision*, P. Winston, Ed., ed New York: McGraw-Hill, 1975, pp. 115-155.
- [59] B. K. P. Horn, "Shape from Shading: A Method for Obtaining the Shape of a Smooth Opaque Object from One View," PhD, Electrical Engineering, M.I.T., 1970.
- [60] K. Ikeuchi and B. K. P. Horn, "Numerical Shape from Shading and Occluding Boundaries," *Artificial Intelligence*, vol. 17, pp. 141-184, 1981.
- [61] B. K. P. Horn and M. J. Brooks, "Shape and Source from Shading," in *International Joint Conference on Artificial Intelligence*, 1985, pp. 932-936.
- [62] B. K. P. Horn, "Height and Gradient from Shading," *International Journal of Computer Vision*, vol. 5, pp. 37-75, 1990.
- [63] P. Dupuis and J. Oliensis, "Direct Method for Reconstructing Shape from Shading" in *Computer Vision and Pattern Recognition*, 1992, pp. 453-458.
- [64] J. Oliensis and P. Dupuis, "A Global Algorithm for Shape from Shading," in *International Conference in Computer Vision*, Berlin, Germany, 1993, pp. 692-701.
- [65] A. P. Pentland, "Local Shading Analysis," *IEEE Transactions on Pattern Analysis and Machine Intelligence*, vol. 6, pp. 170-187, 1984.
- [66] C. H. Lee and A. Rosenfeld, "Improved Methods of Estimating Shape from Shading Using the Light Source Coordinate System," *Artificial Intelligence*, vol. 26, pp. 125-143, 1985.
- [67] A. P. Pentland, "Shape Information from Shading: A Theory about Human Perception," in *International Conference in Computer Vision*, 1988, pp. 404-413.
- [68] P. S. Tsai and M. Shah, "Shape from Shading Using Linear Approximation," *Image and Vision Computing Journal*, vol. 12, pp. 487-498, 1994.
- [69] E. Prados and O. Faugeras, "Shape From Shading," in *Handbook of Mathematical Models in Computer Vision*, N. Paragios, et al., Eds., ed: Springer US, 2006, pp. 375-388.
- [70] E. Prados and O. Faugeras, "'Perspective Shape from Shading' and Viscosity Solutions," in *9th International Conference on Computer Vision*, 2003, pp. 826-831.
- [71] E. Prados, F. Camilli, and O. Faugeras, "A Viscosity Solution Method for Shape-from-Shading without Image Boundary Data," *ESAIM: Mathematical Modelling and Numerical Analysis*, vol. 40, pp. 393-412, 2006.
- [72] E. Prados and O. Faugeras, "Shape From Shading: a well-posed problem?," in *IEEE Conference on Computer Vision and Pattern Recognition*, 2005, pp. 870-877.

- [73] H. Jin, D. Cremers, D. Wang, E. Prados, A. Yezzi, and S. Soatto, "3-D Reconstruction of Shaded Objects from Multiple Images Under Unknown Illumination," *International Journal of Computer Vision*, vol. 76, pp. 245-256, 2008.
- [74] K.-J. Yoon, E. Prados, and P. Sturm, "Generic Scene Recovery Using Multiple Images," in *Scale Space and Variational Methods in Computer Vision*. vol. 5567, X.-C. Tai, *et al.*, Eds., ed: Springer Berlin Heidelberg, 2009, pp. 745-757.
- [75] K.-J. Yoon, E. Prados, and P. Sturm, "Joint Estimation of Shape and Reflectance using Multiple Images with Known Illumination Conditions," *International Journal of Computer Vision*, vol. 86, pp. 192-210, 2010.
- [76] E. Prados, N. Jindal, and S. Soatto, "A Non-local Approach to Shape from Ambient Shading," in *Scale Space and Variational Methods in Computer Vision*. vol. 5567, X.-C. Tai, *et al.*, Eds., ed: Springer Berlin Heidelberg, 2009, pp. 696-708.
- [77] W. Chenglei, B. Wilburn, Y. Matsushita, and C. Theobalt, "High-quality shape from multi-view stereo and shading under general illumination," in *2011 IEEE Conference on Computer Vision and Pattern Recognition (CVPR)*, 2011, pp. 969-976.
- [78] S. K. Nayar, "Shape from Focus," The Robotics Institute, Carnegie Mellon University, Pittsburgh, PA 1989.
- [79] M. Noguchi and S. K. Nayar, "Microscopic shape from focus using active illumination," in *Proceedings of the 12th IAPR International Conference on Pattern Recognition*, 1994, pp. 147-152.
- [80] S.-O. Shim, A. S. Malik, and T.-S. Choi, "Accurate shape from focus based on focus adjustment in optical microscopy," *Microscopy Research and Technique*, vol. 72, pp. 362-370, 2009.
- [81] R. Minhas, A. Adeel Mohammed, and Q. M. Jonathan Wu, "Shape from focus using fast discrete curvelet transform," *Pattern Recognition*, vol. 44, pp. 839-853, 2011.
- [82] I. Lee, M. Tariq Mahmood, and T.-S. Choi, "Adaptive window selection for 3D shape recovery from image focus," *Optics & Laser Technology*, vol. 45, pp. 21-31, 2013.
- [83] S. Pertuz, D. Puig, and M. A. Garcia, "Analysis of focus measure operators for shape-from-focus," *Pattern Recognition*, vol. 46, pp. 1415-1432, 2013.
- [84] G. Healey and T. O. Binford, "Local shape from specularities," *Computer Vision, Graphics, and Image Processing*, vol. 42, pp. 62-86, 1988.
- [85] A. Blake and H. Bulthoff, "Shape from Specularities: computation and psychophysics," *Philosophical Transactions of the Royal Society of London B*, vol. 331, pp. 237-252, 1991.
- [86] Y. Francken, T. Cuyppers, T. Mertens, J. Gielis, and P. Bekaert, "High quality mesostructure acquisition using specularities," in *Computer Vision and Pattern Recognition, 2008. CVPR 2008. IEEE Conference on*, 2008, pp. 1-7.
- [87] Y. Adato, Y. Vasilyev, O. Ben-Shahar, and T. Zickler, "Toward a Theory of Shape from Specular Flow," in *IEEE International Conference on Computer Vision*, 2007.
- [88] R. W. Fleming, A. Torralba, and E. H. Adelson, "Specular reflections and the perception of shape," *Journal of Vision*, vol. 4, 2004.
- [89] Cultural_Heritage_Imaging. (2012, 01/30/2013). *Reflectance Transformation Imaging (RTI)*. Available: <http://culturalheritageimaging.org/Technologies/RTI/>
- [90] T. Malzbender, D. Gelb, and H. Wolters, "Polynomial texture maps," presented at the SIGGRAPH 2001, Los Angeles, CA, 2001.
- [91] M. K. Johnson and E. H. Adelson, "Retrographic sensing for the measurement of surface texture and shape," in *CVPR 2009*, Miami, FL, 2009, pp. 1070-1077.

- [92] A. J. Rojas Arciniegas and M. Esterman, "Exploring Surface Defects on EP-based 3D Printed Structures," *Journal of Imaging Science and Technology*, vol. Under Review, 2013.
- [93] A. Boschetto, V. Giordano, and F. Veniali, "3D roughness profile model in fused deposition modelling," *Rapid Prototyping Journal*, vol. 19, pp. 240 - 252, 2013.
- [94] A. J. Rojas Arciniegas and M. Esterman, "Characterization and modeling of surface defects in EP3D printing," *Rapid Prototyping Journal*, vol. Under Review, 2013.
- [95] R. C. Gonzalez and R. E. Woods, *Digital Image Processing*, 3rd ed.: Prentice Hall, 2007.
- [96] B. Yost, "GelSight Measurements - RIT EP 3D Printed Samples," GelSight Inc. 2013.